15th International Meeting on Thermodiffusion

May 29th – June 1st, 2023 – Tarragona (Spain)

IMT 15

Book of Abstracts

IMT15 Abstract Book

Editor-in-Chief:
Dr. Diana Dubert

Editors:
Prof. Xavier Ruiz Martí
Prof. Fina Gavaldà Mastínez
Prof. Jaume Masons Bosch

ISBN 978-84-1365-081-4
The book is available on IMT15 webpage:
https://wwwa.fundacio.urv.cat/congressos/imt-2023/

Committees

Organizing Committee

Diana Dubert (Chair)
Departament de Química Física I Inorgànica , URV, Tarragona, Spain

Xavier Ruiz Martí
Departament de Química Física I Inorgànica, URV, Tarragona, Spain

Fina Gavaldà Martínez
Departament de Química Física I Inorgànica, URV, Tarragona, Spain

Jaume Massons Bosch
Departament de Química Física I Inorgànica, URV, Tarragona, Spain

Maria José Simón Olmos
Departament d'Enginyeria Mecànica, URV, Tarragona, Spain

M. Mounir Bou-Ali
Mondragón Unibertsitatea, Spain

Valentina Shevtsova
IKERBASQUE, Basque Foundation for Science, Bilbao, Spain and Mondragón Unibertsitatea, Spain

Antoni Perez-Poch
Universitat Politècnica de Catalunya, Barcelona, Spain

International Scientific Committee

Prof. Dr. M. Mounir Bou-Ali
Mondragón Unibertsitatea, Spain

Prof. Miguel Rubi
University of Barcelona, Spain

Prof. Valentina Shevtsova
IKERBASQUE, Basque Foundation for Science, Bilbao, Spain and Mondragón Unibertsitatea, Spain

Prof. Fernando Bresme
Imperial College, UK

Prof. Guillaume Galliero
Université de Pau et des Pays de l'Adour, France

Prof. Werner Köhler
Bayreuth Universität, Germany

Prof. Manfred Lücke
Universität des Saarlandes, Germany

Prof. Tatyana Lyubimova
Russian Academy of Science

Prof. Francois Montel
TOTAL R&D, Pau, France

Prof. Marisol Ripoll *Forschungszentrum Jülich, Germany*

Prof. Velisa Vesovic
Imperial College, UK

Prof. Simone Wiegand
Forschungszentrum Jülich, Germany

Prof. Kader Mojtabi
Institut Mécanique des Fluides de Toulouse, France

Table of content

Click on the title to access the abstract

INVITED LECTURES

TOPIC 01THEORETICAL, EXPERIMENTAL AND NUMERICAL METHODS TO INVESTIGATE THERMODIFFUSION IN BINARY, TERNARY AND MULTICOMPONENT MIXTURES

Oral communications

Poster

TOPIC 02- NON EQUILIBRIUM THERMODYNAMICS OF FLUIDS UNDER THERMAL STRESS

Oral Communications

TOPIC 03 - NON-EQUILIBRIUM FLUCTUATIONS IN THERMALLY INHOMOGENEOUS FLUIDS

Oral Communications

Poster

TOPIC 04 - MACROMOLECULAR SOLUTIONS, AIRBORNE PARTICLES, COLLOIDAL SUSPENSIONS, AND BIOLOGICAL FLUIDS: THE THERMOPHORESIS CASE

Oral Communications

TOPIC 05 - THERMODIFFUSION IN POROUS MEDIA AND ENHANCED OIL RECOVERY

Oral Communications

Poster

TOPIC 06 - SORET-DRIVEN HYDRODYNAMIC INSTABILITIES AND CONVECTIVE PATTERNS

Oral Communications

Poster

TOPIC 07- THERMODIFFUSION EFFECTS IN CRYSTAL GROWTH AND POLYMER PROCESSING

TOPIC 08- THERMODIFFUSION IN MICROGRAVITY

Oral Communications

Poster

TOPIC 09 - THERMODIFFUSION IN BIOLOGICAL TRANSPORT

Oral Communications

TOPIC 10 - PHASE CHANGE MATERIALS (PCM)

Oral Communications

Poster

TOPIC 11- APPLICATIONS OF THERMAL DIFFUSION

Oral Communications

Poster

Invited Lectures

Thermal Diffusion in Multicomponent Mixtures including H_2O-CO_2-Salts from Molecular Simulations

Abbas Firoozabadi, Rice University

Thermal diffusion is known to affect species segregation and separation in a wide range of problems including in the subsurface. This presentation will cover the formulations that will facilitate proper measurements, molecular simulations, and large-scale calculations in relation to mixture including subsurface CO_2-H_2O-Salt systems.

In laboratory measurement of thermal diffusion factor, the effect of thermodynamic factor is neglected. In both binary mixtures as well as in ternary and higher mixtures, thermodynamic factor may have a large effect.

In ternary and higher mixtures, the Fickian diffusion coefficients may be required in evaluation of thermal diffusion factors. Molecular simulations can be used in estimation of thermal diffusion factors. In molecular simulations, a temperature gradient is established through non-equilibrium which has a number of subtleties. The implementation should be made carefully.

CO_2 can be found in brine in the subsurface. CO_2 permanent storage in the subsurface is the most promising method to prevent emission to the atmosphere. The long-term distribution of CO_2 in the subsurface brine is of high interest. CO_2 and brines may form complicated molecular structures. Some aspects of the problem in non-isothermal conditions will conclude the presentation.

Thermodiffusion of polymer solutions in mixed solvents

W. Köhler[1], D. Sommermann[1], M. Schraml[1]

[1]Physikalisches Institut, Universität Bayreuth, Germany, werner.koehler@uni-bayreuth.de

Introduction

Diffusion and Thermodiffusion in polymer solutions have revealed a number of unexpected characteristics, such as the molar mass independence of the thermodiffusion coefficient (Schimpf et al. 1989), the speeding-up of diffusion with increasing polymer concentration in the semidilute regime (Adam et al. 1985, Rauch et al. 2003), and the insensitivity of the Soret coefficient to the glass transition at high polymer concentrations (Rauch et al. 2002). Little is known about thermodiffusion of ternary mixtures with polymers, e.g., a polymer dissolved in a binary solvent as represented by one of the DCMIX4 samples (Mialdun et al. 2020) and studied in a nonequilibrium fluctuations experiment (García-Fernández et al. 2019).

Thermodiffusion in ternary mixtures has extensively been studied during the DCMIX microgravity campaign both in space and in the laboratory using, besides the thermogravitational column method, different two-color optical techniques. It has become clear that a major obstacle in all these experiments is the difficult inversion of the frequently ill-conditioned optical contrast factor matrix. In our contribution we explain how the inversion problem can be avoided in the case of strongly asymmetric ternary mixtures, such as polymers or colloids in mixed solvents. These systems typically show bimodal dynamics with well-separated diffusion eigenvalues. A natural choice, which needs to be justified by the results, is the assignment of the fast mode to the solvent and the slow mode to the polymer dynamics. This automatically fixes the directions of the diffusion eigenvectors in the space of the two independent composition variables and, thus, the diagonalization transformation of the diffusion matrix.

In our contribution we analyse experiments within the framework usually employed for ternary mixtures. We show, how the ternary problem can be reduced to an effective binary one and we determine the diffusion and Soret coefficients for all components both for the asymptotic steady state and for the individual modes. These results are compared to data for binary reference systems, where possible. Using the transformation recently proposed by Ortiz de Zárate (Ortiz de Zárate 2020), transformation-invariant Soret coefficients are obtained.

Experiment

Experiments were performed on solutions of polystyrene (PS) of M_w = 4880 g/mol dissolved in the mixed solvent toluene (Tol) and cyclohexane (cHex). The composition in mass fractions was 0.040/0.480/0.480 (PS/Tol/cHex). Measurements were carried out by means of 2-color optical beam deflection (2-OBD). Further details are described in Ref. (Sommermann et al. 2022).

Results

Let us take PS (c_1) and Tol (c_2) as the independent concentrations and cHex (c_3) as the dependent one. Fig. 1 shows a sketch of the concentration changes of all three components during the fast and the slow mode.

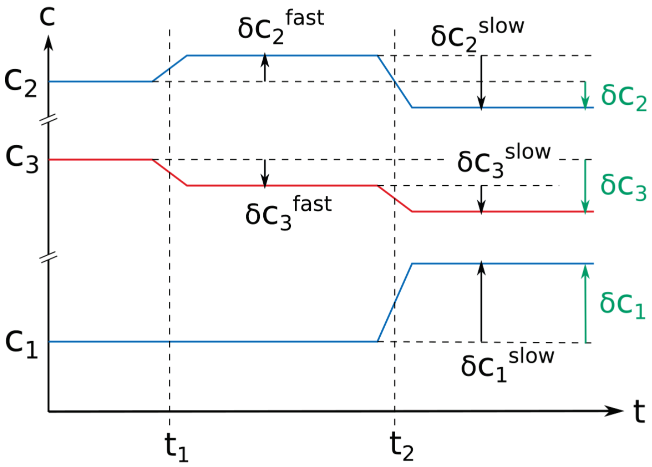

Figure 1: sketch of the concentration changes during the fast and the slow mode for the case of r = c3/c2 = 0.5. Figure from Ref. (Sommermann et al. 2022).

The identification of the concentration shifts associated with the two modes leads to the diffusion eigenvectors

$$\underline{v}_1 = \begin{pmatrix} 0 \\ 1 \end{pmatrix} \,, \quad \underline{v}_2 = \frac{1}{\sqrt{1+(1+r)^2}} \begin{pmatrix} 1+r \\ -1 \end{pmatrix}$$

where $r = c_3/c_2$ is the concentration ratio of the two solvents. The diffusion eigenvectors yield the diagonalization transformation matrix and, with the diffusion eigenvalues $\hat{D}_i$, the diffusion matrix

$$\underline{\underline{D}} = \underline{\underline{V}} \begin{pmatrix} \hat{D}_1 & 0 \\ 0 & \hat{D}_2 \end{pmatrix} \underline{\underline{V}}^{-1} = \begin{pmatrix} \hat{D}_2 & 0 \\ \frac{\hat{D}_1 - \hat{D}_2}{1+r} & \hat{D}_1 \end{pmatrix}$$

Since the two diffusion eigenvalues are rather different, the off-diagonal element D_{21} is of similar magnitude as the diagonal ones.

The theory has been worked out in detail in Ref. (Sommermann et al. 2022). Starting with the four amplitudes M_{ij} and the two diffusion eigenvalues extracted from a 2-OBD experiment, it allows to compute not only the diffusion matrix but also the total Soret coefficients of the three components for the asymptotic steady state separation and also the partial Soret coefficients for the two modes individually.

The biggest advantage of our pseudo-binary approach is the avoidance of the inversion of the two-color contrast factor matrix and the comparability of the errors to the ones usually observed for binary systems. This huge increase of accuracy is shown in Fig. 2 for the two primed Soret coefficients of the independent components PS and Tol. The scattered points show results from Monte Carlo simulations, where all experimental quantities have been subjected to realistic statistical errors.

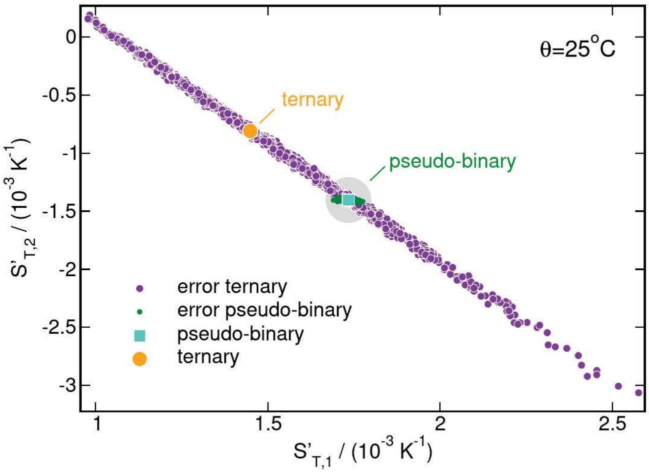

Figure 2: Monte Carlo simulations of the effect of experimental error on the primed Soret coefficients of PS (1) and Tol (2) for the cases of the conventional ternary evaluation and the new pseudo-binary method. Figure from Ref. (Sommermann et al. 2022)

All results can be found in Ref. (Sommermann et al. 2022) and will be given in the presentation. As an example, Tab. 1 shows the transformation-invariant Soret coefficients according to Ortiz de Zárate (Ortiz de Zárate et al. 2020) of the two independent components PS and Tol together with the partial Soret coefficients for the two modes. The agreement is perfect.

	units	20 °C	25 °C	30 °C	35 °C	σ
$S_{T,1}$	$10^{-3}\,\mathrm{K}^{-1}$	46.3	44.0	41.9	39.6	2.5
$S_{T,2}$	$10^{-3}\,\mathrm{K}^{-1}$	-2.36	-2.24	-2.15	-2.09	0.15
$S_{T,2}^{\mathrm{fast}}$	$10^{-3}\,\mathrm{K}^{-1}$	-2.46	-2.33	-2.24	-2.17	0.4
$S_{T,3}^{\mathrm{fast}}$	$10^{-3}\,\mathrm{K}^{-1}$	2.46	2.33	2.24	2.17	0.4
$S_{T,1}^{\mathrm{slow}}$	$10^{-3}\,\mathrm{K}^{-1}$	47.5	45.2	43.0	40.6	2.5

Table 1: Transformation-invariant Soret coefficients (top two rows) and partial Soret coefficients for the fast and the slow mode.

Finally, the viscosity-scaled thermophoretic mobility of the polymer, which can be calculated from the partial Soret coefficient of the slow mode and the corresponding diffusion eigenvalue, agrees with the universal value for ηD_T observed for binary polymer solutions (Stadelmaier et al. 2009).

Conclusions

The inversion of optical 2-color experiments for the investigation of diffusion and thermodiffusion in ternary systems has proven notoriously difficult without additional a priori assumptions. For certain systems with well-separated diffusion eigenvalues, reasonable assumptions about the directions of the diffusion eigenvectors essentially eliminate these problems and increase the accuracy for ternary systems to the one known from binaries. A natural attribution of the two modes seems feasible for well-separated dynamics as observed for polymers or colloids in binary solvents at moderate concentrations. With increasing polymer or colloid concentration, the interparticle interaction between entities of the large species becomes more dominant and the attribution of the diffusion eigenvectors more difficult. So far, only the dilute to moderately semidilute case has been worked out.

Acknowledgements

The work was supported by Deutsche Forschungsgemeinschaft (DFG, KO1541/13-1) and by Deutsches Zentrum für Luft- und Raumfahrt (DLR) (Grant 50WM2147).

References

M. Adam, M. Delsanti, Dynamical behavior of semidilute polymer solutions in a θ solvent: quasi-elastic light scattering experiments, Macromolecules, 18, 1760 (1985)

L. García-Fernández, P. Fruton, H. Bataller, J. M. Ortiz de Zárate, F. Croccolo, Coupled non-equilibrium fluctuations in a polymeric ternary mixture. Eur. Phys. J. E 42: 124 (2019)

A. Mialdun, M. M. Bou-Ali, M. Braibanti, F. Croccolo, A. Errarte, J. M. Ezquerro, J. J. Fernandez, L. Garcia Fernandez, Q. Galand, Y. Gaponenko, F. Gavalda, W. Köhler, T. Lyubimova, J. M. Ortiz de Zárate, J. Rodriguez, X. Ruiz, I. I. Ryzhkov, V. Shevtsova, S. van Vaerenbergh, V. Yasnou, H. Bataller, Data quality assessment of diffusion coefficient measurements in ternary mixtures 4 (DCMIX4) experiment, *Acta Astronaut*., 176, 204 (2020)

J. M. Ortiz de Zárate, J. V. Sengers, Frame-invariant Fick diffusion matrices of multicomponent fluid mixtures, *Phys. Chem. Chem. Phys*., 22, 17597 (2020)

J. Rauch, W. Köhler, Collective and thermal diffusion in dilute, semidilute, and concentrated solutions of polystyrene in toluene, *J. Chem. Phys*., 119, 11977 (2003)

J. Rauch, W. Köhler, Diffusion and thermal diffusion of semidilute to concentrated solutions of polystyrene in toluene in the vicinity of the glass transition, *Phys. Rev. Lett*., 88, 185901 (2002)

M. E. Schimpf, J. C. Giddings, Characterization of thermal diffusion in polymer solutions by thermal field-flow fractionation: dependence of polymer and solvent parameters, *J. Polym. Sci.: Part B: Polym. Phys*., 27, 1317 (1989)

D. Sommermann, M. Schraml, W. Köhler, Thermodiffusion of polymer solutions and colloidal dispersions in mixed solvents, *J. Chem. Phys*., 157, 194903 (2022)

D. Stadelmaier, W. Köhler, Thermal Diffusion of Dilute Polymer Solutions: the Role of Chain Flexibility and the

Effective Segment Size, *Macromolecules*, 42, 9147 (2009)

Scientific outcome from microgravity experiments and beyond

V. Shevtsova,[1,2] W. Koehler[3], M. M. Bou-Ali[1], A. Mialdun[4]

[1]Fluid Mechanics Group, Mondragon University, Mondragon, Spain, mbouali@mondragon.edu
[2]Ikerbasque, Basque Foundation for Science, Bilbao, Spain, x.vshevtsova@mondragon.edu
[3]Physikalisches Institut, Bayreuth University, Bayreuth, Germany, werner.koehler@uni-bayreuth.de
[4]CREST, ATM, CP-165/43, Brussels University (ULB), Brussels, Belgium, Aliaksndr.Mialdun@ulb.be

Introduction

In recent years, there has been a growing interest in mass and thermodiffusion in multicomponent mixtures, with a particular focus on ternary mixtures. The application of optical techniques has significantly improved the quality of mass and diffusion experiments, starting with binary liquid mixtures and expanding to ternary mixtures. Additionally, the resurgence of interest in thermodiffusion is attributed to the availability of convection-free experiments.

The first microgravity experiment related to thermodiffusion was conducted in 1992 during the EUREKA mission, where the Soret coefficient was measured in 20 binary organic mixtures and aqueous solutions (Van Vaerenbergh et al., 1995). While the experiment was only partly successful, experiments related to measuring Soret coefficients have been regularly conducted in orbit since then.

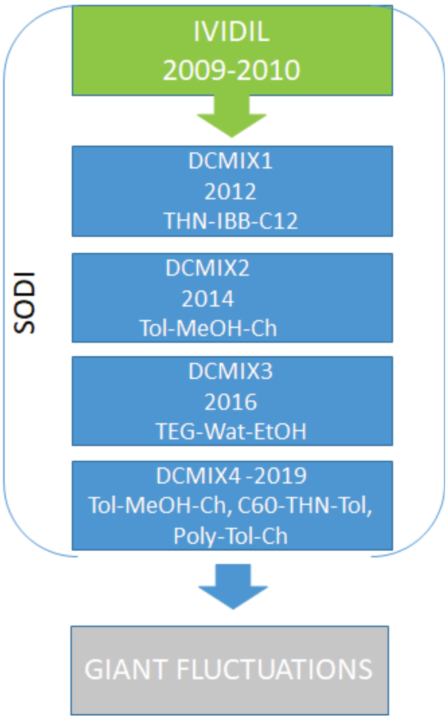

Figure 1: (inside blue frame) The outline of the Soret experiments carried out on the ISS in the SODI (Selected Opticals Diagnostic Instrument. (outside blue frame) Future experiment.

Figure 1 illustrates experiments conducted in the SODI (Selectable Optical Diagnostic Instrument) on the International Space Station (ISS), equipped with a two-wavelength interferometer to measure Soret and diffusion coefficients in ternary mixtures.

The first experiment, IVIDIL (Influence Vibration on Diffusion in Liquids), demonstrated the feasibility of conducting experiments on the ISS and paved the way for ternary experiments.

The DCMIX project is perhaps the most important collaboration in this area in recent years, in which teams from various countries have worked with ESA and Roscosmos to measure ternary liquid mixtures aboard the ISS. The DCMIX project also provided a valuable basis for the current GIANT FLUCTUATIONS project, which aims to investigate fluctuations in ternary systems subjected to temperature and Soret-induced concentration gradients under microgravity.

The **outcome** of the DCMIX project is **not only the measured coefficients**; the amount of fundamental knowledge gained is much more significant. Aside from the measured coefficients, the DCMIX project resulted in numerous fundamental discoveries and breakthroughs during the experiment preparation and result processing stages. These findings are separated into two categories: *generic* (global) and *experiment-dependent*. The ‘*generic*’ results present a kind of scientific breakthroughs related to the Soret experiment in ternary mixtures, but independent of the particular DCMIX experiment. The ‘*experiment-dependent*’ results are new and interesting findings specific to the DCMIX mixture under consideration.. Due to space limitation only ‘*generic*’ results are shortly presented here.

‘*Generic*’ results

1. The first ever benchmark between ground and microgravity results as well as the first benchmark for ternary mixtures (Bou-Ali et al., 2015).

2. Understanding the importance of the condition number for ternary and higher mixtures (Shevtsova et al., 2011).

Optical methods, such as phase-shifting interferometry utilized in SODI, detect concentration changes in a sample using measurements of the refractive index (n). The conversion requires contrast factors, which are derivatives of n with concentration and temperature. In ternary mixtures, the 2x2 matrix composed of the contrast factors can be ill-conditioned, limiting the mixture compositions that can be measured. This also applies to the thermogravitational column, where the derivatives of the refractive index and density are considered.

3. Revelation and insight into the asymmetric nature of error propagation in the Soret experiment.

a) The error bar forms a very elongated ellipsoid instead of an isotropic cloud around the solution (Mialdun et al., 2018).

b) Not all three Soret coefficients in a ternary mixture are obtained with the same accuracy. The individual uncertainties depend on the orientation of the error ellipsoid within the Gibbs triangle and its projections onto the three axes (Triller et al., 2019).

4. New methodologies for processing large amounts of raw data from the Soret experiment, even partially corrupted by laser instabilities.

a) Suggestion of an optimal multi-step path to process results with a smaller uncertainty (Mialdun et al., 2018).

b) A robust data evaluation method that maps the SODI experiment to an equivalent OBD experiment and does not rely on phase stepping (Sommermann et al., 2019).

5. Introduction of the Soret vector for component separation and the new relationship between binary and ternary coefficients on the Gibbs triangle.

a) The Soret vector on the Gibbs triangle elucidates the essential features of Soret-driven separation in ternary mixtures as a whole (Mialdun et al., 2021).

b) Sign changes along the binary boundaries and the existence of a singular point in the ternary Gibbs diagram, where all Soret coefficients vanish simultaneously (Schraml et al., 2021).

The Soret vector, as defined in Figure 2, offers several advantages: (i) to predict the Soret sign of a ternary mixture from knowledge of the Soret coefficients in binary subsystems; (ii) to control the consistency of measured coefficients; (iii) to determine the regions and components causing the greatest separation; and (iv) to identify the regions where Soret separation is inaccessible for optical techniques or gravitationally unstable.

The peculiarity of the singular point in the ternary Gibbs diagram is that a mixture of this composition will remain homogeneous in the presence of a temperature gradient.

Conclusions

The DCMIX project has significantly increased knowledge about ternary mixtures. Microgravity experiments have played a key role in that.

Microgravity experiments define crucial experimental cornerstones that are complemented by a large number of ground experiments.

Microgravity experiments permitted a consolidation of strong international science teams. The tests on-board the ISS were an essential motivation.

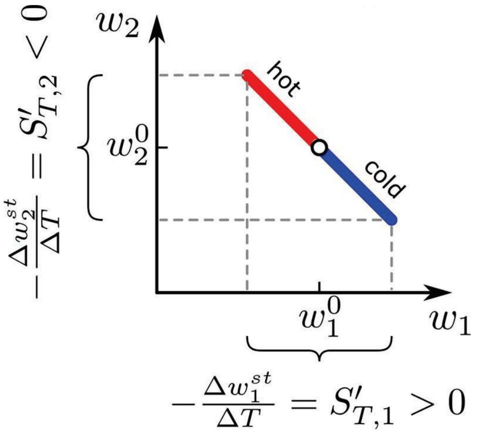

Figure 2: Concept of the Soret vector in a ternary mixture wich is defined by its component as $\mathbf{S}_T' = S_{T1}' \mathbf{e}_1 + S_{T2}' \mathbf{e}_2$ where $\mathbf{e}_i$ is the unit vector along the axis w_i. The coordinates of the blue (red) part of the vector corresponding to the concentration change due to temperature decrease (increase). The two half-vectors, symmetrically located around the mean concentration, do visually show how the concentration evolution with temperature difference.

References

S. Van Vaerenbergh, J.C. Legros, J.Ch. Dupin, First results of Soret coefficient measurement experiment, *Adv. Space Res*, **16** (1), 69-81 (1995)

M.M. Bou-Ali et al., Benchmark values for the Soret, thermodiffusion and molecular diffusion coefficients of the ternary mixture tetralin+isobutylbenzene+n-dodecane with 0.8-0.1-0.1 mass fraction, Eur. Phys. J. E **38**, 30 (2015)

Shevtsova V., Sechenyh V., Nepomnyashchy A., Legros J.C., Analysis of the application of optical two wavelength techniques to measurement of the Soret coefficients in ternary mixtures, *Philsophical Magazine*, **91**, 3498-3518 (2011)

A. Mialdun, I. Ryzhkov, O. Khlybov, T. Lyubimova, and V. Shevtsova, Measurement of Soret coefficients in a ternary mixture of toluene–methanol–cyclohexane in convection-free environment, *J. Chem. Physics* **148**, 044506 (2018)

T. Triller, D. Sommermann, M. Schraml, F. Sommer, E. Lapeira, M.M. Bou-Ali, and W. Koehler*,* The Soret effect in ternary mixtures of water+ethanol+triethylene glycol of equal mass fractions: Ground and microgravity experiments, Eur. Phys. J. E **42**, 27 (2019)

D. Sommermann, T. Triller, W. Koehler A robust data evaluation method for the DCMIX microgravity experiments, *Microgravity Sci. Technol.* **31**, 465–474 (2019).

A. Mialdun, M. Bou-Ali, V. Shevtsova, Soret vector for description of multicomponent mixtures, Scientific report, **11**, 17735 (2021)

M. Schraml, H. Bataller, C. Bauer, M. M. Bou-Ali, F. Croccolo, E. Lapeira, A. Mialdun, P. Moeckel, A. T. Ndjaka, V. Shevtsova, and W. Koehler, The Soret coefficients of the ternary system water/ethanol/triethylene glycol and its corresponding binary mixtures, *Eur. Phys. J. E* **44**, 128 (2021)

Diffusion in liquid mixtures

A. Vailati[1]

[1]Dipartimento di Fisica “A. Pontremoli”, Università degli Studi di Milano, Milano, Italy, alberto.vailati@unimi.it

Abstract

Recently, several European scientists have contributed to a joint effort led by the European Space Agency aimed at the identification of the priorities for future research in space in the field of Soft Matter and Biophysics (Vailati et al. 2021).

In this work we present an overview some of the aspects that make the investigation of diffusion in liquid mixtures in Space still a challenging and promising field of research, of strategic relevance for space exploration, due to its applicative importance for the processing of fuels, food, and other materials needed for the sustainability of long-term space travels.

In the past and present years, the investigation of diffusion in liquid mixtures has largely benefitted from the opportunity of performing experiments under reduced gravity conditions using sounding rockets and Low Earth Orbit platforms, such as the International Space Station (Braibanti et al. 2019). Until now, diffusive mixing has been mainly investigated at the macroscopic scale. Its investigation at the mesoscopic scale is becoming increasingly important for the understanding of mass transfer in confined systems, such as complex fluids, soft matter, biological systems, porous media, and microfluidic devices. Microgravity conditions provide the opportunity of investigating the effect of external fields on diffusive mixing in the absence of the convective flows induced by buoyancy on Earth (Vailati et al. 2011), with applicative relevance to the processing of liquids in space (Vailati et al. 2020).

Even though microgravity experiments are still of primary relevance for the fundamental understanding of diffusion in complex fluids, the significance of these studies is shifting in the direction of investigating diffusion in multi-component mixtures under hypergravity and reduced gravity conditions, a topic of great relevance for long-term space exploration missions, where the ability of processing materials in the liquid state will represent a strategic habilitating factor (Vailati et al. 2023).

Acknowledgements

Work supported by the European Space Agency

References

(Braibanti et al. 2019) M. Braibanti, P.-A Artola, P. Baaske, H. Bataller, J -P. Bazile, M. M. Bou-Ali, D. S. Cannell, M. Carpineti, R. Cerbino, F. Croccolo, J. Diaz, A Donev 10, A. Errarte, J. M. Ezquerro, A. Frutos-Pastor, Q. Galand, G. Galliero, Y. Gaponenko, L. García-Fernández, J. Gavaldá, F. Giavazzi, M. Giglio, C. Giraudet, H. Hoang, E. Kufner, W. Köhler, E. Lapeira, A. Laverón-Simavilla, J -C. Legros, I. Lizarraga, T. Lyubimova, S. Mazzoni, N. Melville, A. Mialdun, O. Minster, F. Montel, F. J. Molster, J. M. Ortiz de Zárate, J. Rodríguez, B. Rousseau, X. Ruiz, I. I. Ryzhkov, M. Schraml, V. Shevtsova, C. J. Takacs, T. Triller, S. Van Vaerenbergh, A. Vailati, A. Verga, R. Vermorel, V. Vesovic, V. Yasnou, S. Xu, D. Zapf, K. Zhang, European Space Agency experiments on thermodiffusion of fluid mixtures in space, *European Physycal Journal E Soft Matter,* 42, 86 (2019).

(Vailati et al 2011) A. Vailati, R. Cerbino, S. Mazzoni, C. J. Takacs, D. S. Cannell, M. Giglio Fractal fronts of diffusion in microgravity. *Nature Communications* 2, 290 (2011)

(Vailati et al. 2020) A. Vailati, P. Baaske, H. Bataller, S. Bolis, M. Braibanti, M. Carpineti, R. Cerbino, F. Croccolo, J-L. Dewandel, A. Donev, L. García-Fernández, F. Giavazzi, R. Haslinger, S. Hens, M. Knauer, W. Köhler, E. Kufner, J. M. Ortiz de Zárate, J. Peeters, C. J. Schwarz, I. Silkina, S. Xu & D. Zapf, Giant Fluctuations Induced by Thermal Diffusion in Complex Liquids. *Microgravity Science and. Technology,* 32, 873 (2020).

(Vailati et al. 2021) A. Vailati, A. De Wit, D. Maes, S. Veesler, J. Gavira, E. Zaccarelli, C. S. Iorio, L. Liggieri, B. Dollet, M. Cloitre, T. Hellweg, R. Höhler, G. Volpe, H. Löwen, R. Golestanian, M. Sperl, M. Ben Amar, P. Ciarletta, P. Haas, J. Blum, G. Wurm, H. Thomas, M. Thoma, Soft Matter and Biophysics, *ESA SciSpacE White Papers* (2021)

(Vailati et al. 2023) A. Vailati, H. Bataller, M. M. Bou-Ali, M. Carpineti, R. Cerbino, F. Croccolo, S. U. Egelhaaf, F. Giavazzi, C. Giraudet, G. Guevara-Carrion, D. Horváth, W. Köhler, A. Mialdun, J. Porter, K. Schwarzenberger, V. Shevtsova & A. De Wit, Diffusion in Liquid Mixtures, *npj Microgravity*, 9, 1 (2023)

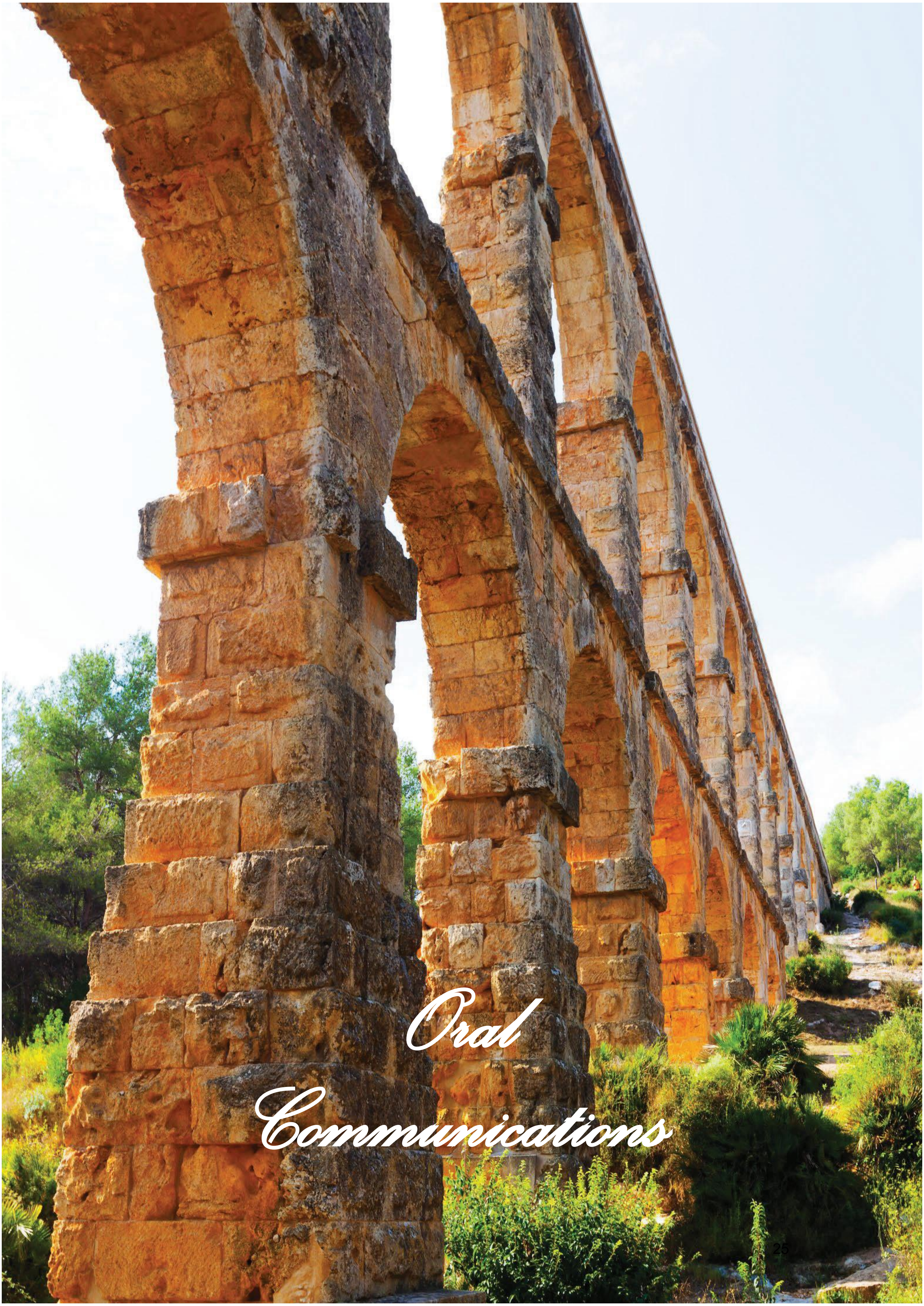

Oral Communications

Complex time dependent patterns in the Soret regime

A. Alonso[1], I. Mercader[1], O. Batiste[1]

[1]Departament de Física, Universitat Politècnica de Catalunya, Spain (arantxa.alonso@upc.edu, oriol.batiste@upc.edu, maria.isabel.mercader@upc.edu)

Introduction

In the present work we investigate the influence of variations of the aspect ratio of the cell, Γ, on the patterns arising in a slightly inclined cylindrical container heated from below for binary mixtures. In the presence of the shear mechanism induced by inclination, superimposed to the thermodiffusive effects, oscillatory superhighway convection (SHC) patterns coexist with the large-scale shear flow (LSF) (Figure 1). SHC patterns show a number of parallel thermal lanes, each containing aligned coherent structures that counter-propagate in adjacent lanes. LSF patterns generate a linear concentration profile across the cell. Both families of solutions are stable.

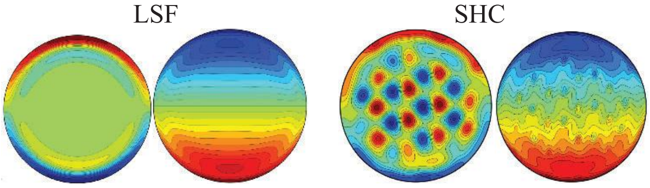

Figure 1: Temperature and concentration contour plots for coexisting stable LSF and SHC states.

The oscillatory SHC patterns arise in the Soret regime, where concentration gradients contribute significantly to the dynamics, and were first observed experimentally (Croccolo et al. 2013) and later obtained numerically (Alonso et al. 2018). Some of the complex patterns obtained in a Γ=5 cell were analysed in detail in Alonso et al. 2022.

We will present and analyze the spatio-temporal features of the patterns appearing in the Soret regime for values of the aspect ratio of Γ=5.2, 5.3, 5.4. When the value of Γ is changed, SHC-like patterns continue to arise, but their spatio-temporal properties differ considerably: symmetric and non-symmetric periodic orbits, modulated solutions with two and three frequencies, and chaotic solutions are some of the patterns that we obtain in wide regions of the parameter space.

Equations and numerical tools

We consider the Boussinesq binary-fluid convection in a cylindrical cell of height H and radius R, inclined an angle α with respect to the horizontal. The cylinder is heated from below, with a temperature difference between the lids equal to ΔT. The whole boundary is impermeable and non-slip, with fixed temperature at the lids, while the lateral wall is assumed to be thermally insulated. The governing equations of the problem reflect the incompressibility condition, the mass and heat conservation laws, and the Navier-Stokes equations in the Boussinesq approximation.

The resulting system of nondimensional equations depends on the inclination angle α, the aspect ratio $\Gamma=R/H$, and four dimensionless parameters, the Rayleigh number Ra, the separation ratio S, the Prandtl σ and Lewis numbers τ. Equations and boundary conditions are equivariant under the group of symmetries that contains the transformations $\{I, R_1, R_2, R_3\}$. I stands for the identity, R_1 is a reflection with respect to the middle longitudinal vertical plane, R_2 is a point symmetry with respect to the center of the cylinder, and R_3 is the composition of the previous transformations. The nondimensionalized system of equations and boundary conditions is solved numerically using the algorithm described in Mercader et al. 2010. More details about the derivation of the equations, symmetries, and the numerical method can be found in some previous works in the same or related configurations (Alonso et al. 2018, 2022).

To gain insight of the spatio-temporal properties of the patterns obtained by DNS we use a post-processing tool known as higher order dynamic mode decomposition (HODMD) (LeClainche & Vega 2017). This method decomposes the thermal and concentration fields as Fourier-like expansions that can be obtained from a set of spatially discretized snapshots, which are portraits of the system for equispaced values of time. The use of HODMD allows to discard transient dynamics and facilitates identifying the spatio-temporal nature of the solutions

Main results

We take as reference values for the simulations those of the experiment of Croccolo et al. 2013, where a isobutylbenzene–n-dodecane at 50% weight fraction binary mixture is used. The nondimensional parameters for this mixture are $S=0.13$, $\tau=0.011$, and $\sigma=16$.

We focus here in the results corresponding to a Γ~5.3 aspect ratio cell. Unlike in the Γ~5 cell, no stable periodic solutions are obtained in this case. The SHC-like patterns that arise are modulated quasi-periodic or chaotic solutions composed of 9 convective lanes, stable solutions with different number of lanes are not found in the explored region of the parameter space. In contrast, stable 8- and 9-lane periodic solutions are observed for the Γ=5.2 cell. Modulated 9- and 10-lane solutions coexist in the Γ=5.4 cell.

Figures 2 and 3 show the time series in nondimensional time units (1 n.t.u. corresponds to 20s) for the kinetic energy of a few selected solutions obtained in the range Ra=(1596,1620). The time dependence of these solutions differs substantially. Figure 4 shows the averaged Nusselt number (top) and the frequencies associated to the pattern obtained by FFT (bottom) as a function of Ra.

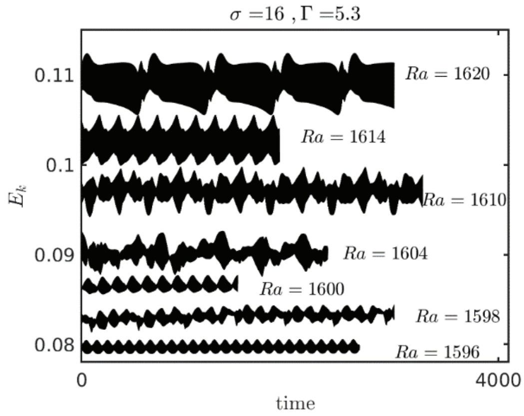

Figure 2: Kinetic energy as a function of time for modulated SHC states obtained for different values of *Ra* in a Γ=5.3 cell.

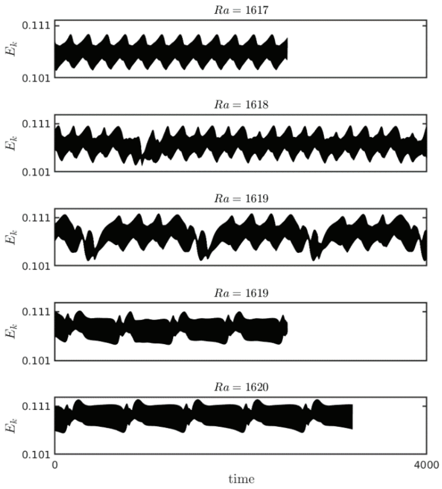

Figure 3: Kinetic energy as a function of time: hysteretic behaviour, different types of modulated SHC can coexist (*Ra*=1619).

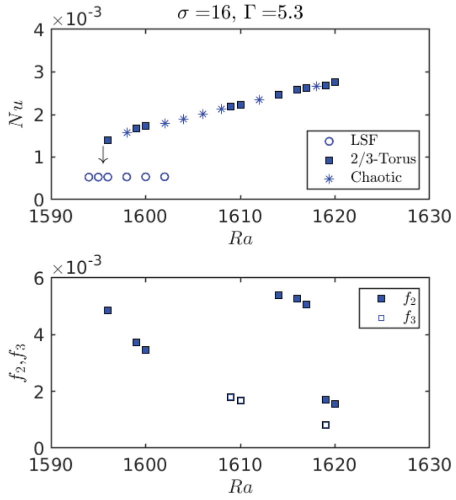

Figure 4: Averaged Nusselt number (top) and frequencies of the solutions (bottom) as a function of the Rayleigh number. Only the frequencies of the modulations are included, the large frequency (*f*=0.24) of the basic SHC pattern is not shown.

Solutions for *Ra*=1596,1600,1614,1620 are exemples of different types of quasiperiodic orbits. For all of the them, the modulation spans for a long time compared with the period of basic SHC solution. The period of the fast frequency associated to the basic SHC pattern is T_b=4.17 n.t.u.=83 s. For *Ra*=1596 the periods of the modulation is around T_{m1}=100 n.t.u.=0.5h, and it raises as *Ra* increases. For the largest modulations the periods are around T_{m1}=666 n.t.u.=3.7 h (*Ra*=1620). Figure 5 shows the phase portrait in two symmetric points *(x,y)* and *(x,-y)* for two types of quasi-periodic SHC solutions: a R_1-symmetric QP orbit (*Ra*=1600) and a non-symmetric QP orbit (*Ra*=1614).

Solutions for *Ra*=1598,1612,1618 and *Ra*=1602-1608 are chaotic orbits, and solutions such as the one obtained for Ra=1619 (third plot in Figure 3) add a still larger modulation to the one already present (T_{m2}=1333 n.t.u.=7.4 h). The system exhibits hysteretic behaviour for certain ranges of *Ra* values. As an example, Figure 3 includes two different stable solutions obtained for the same value of *Ra*, *Ra*=1619.

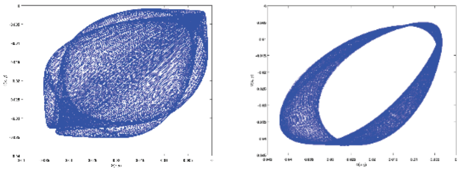

Figure 5: Phase portrait in two symmetric points *(x,y)* and *(x,-y)* for two types of quasi-periodic SHC solutions: a symmetric QP orbit (Ra=1600, left) and a non-symmetric QP orbit (Ra=1614, right).

Conclusions

We present and analyse the spatio-temporal features of relevant patterns arising in an inclined cylinder in the Soret regime for aspect ratios around *Γ*=5. The reconstructions of periodic SHC solutions provided by HODMD suggest that they originate from a Hopf instability of the basic steady pattern of longitudinal rolls. Subsequent bifurcations give rise to several types of modulated solutions of slowly varying amplitudes, which can be quasiperiodic and chaotic orbits. Lengthy computations are required to establish precisely the spatiotemporal nature of the SHC-like patterns.

Acknowledgements

This work is supported by the Spanish Ministry of Science and Innovation under Grant No. PID2020-114043GB-I00.

References

F. Croccolo, F. Scheffold, A. Vailati, Effect of marginal inclination on pattern formation in a binary liquid mixture under thermal stress, *Phys. Rev. Lett.* 111, 014502, (2013)

A. Alonso, I. Mercader, O. Batiste, Time-dependent patterns in quasivertical cylindrical binary convection, *Phys. Rev. E* 97, 023108, (2018)

A. Alonso, I. Mercader, O. Batiste, J.M. Vega, Analyzing slightly inclined cylindrical binary fluid convection via higher order dynamic mode decomposition, *SIAM J. Appl. Dyn. Syst.* 21(3), 2148-2186, (2022)

I. Mercader, O. Batiste, A. Alonso, An efficient spectral code for incompressible flows in cylindrical geometries, *Computers & Fluids* 39, 215-224, (2010)

S. Le Clainche, J.M. Vega, Higher order dynamic mode, *SIAM J. Appl. Dyn. Syst.* 16, 882-925, (2017)

Diffusion and thermodiffusion of supercritical CO2 mixtures: A molecular simulation study

G. Guevara-Carrion[1], D. Saric[1], J. Vrabec[1]

[1]Thermodynamics, Technical University of Berlin, Germany, email: g.guevara@tu-berlin.de

Introduction

Supercritical carbon dioxide (CO_2) mixtures are essential for numerous environmental, power and chemical industry applications. Although thermophysical properties of CO_2 and some of its binary mixtures are well-known, the knowledge of their transport properties is insufficient. In fact, reliable data on diffusion, and particularly, on thermodiffusion of CO_2 mixtures are scarce, especially in the extended critical region, where anomalous behavior of these properties has been observed experimentally and with molecular simulation (Guevara-Carrion et al. 2019, Chatwell et al. 2021).

Besides experimental techniques, molecular modeling and simulation is a powerful tool for the prediction of dynamic properties of fluids, but also for the understanding of microscopic interactions that lead to the observed diffusion and thermodiffusion processes. In this work, we present the results of a molecular simulation study on diffusion and thermodiffusion of seven binary supercritical carbon dioxide (scCO_2) mixtures with hydrogen, methane, ethane, isobutane, benzene, toluene and naphthalene at concentrations near the infinite dilution limit. These mixtures were studied along the 9, 10 and 12 MPa isobars in the temperature range between 290 and 340 K. Because of pronounced density fluctuations in the extended critical region, molecular dynamics simulations are particularly challenging and require extensive sampling and large system sizes. Equilibrium molecular dynamics simulations and the Green-Kubo formalism were applied, employing simple, rigid, non-polarizable molecular models.

Fick and Maxwell-Stefan diffusion coefficients, as well as the related thermodynamic factor were investigated along the 9 MPa isobar for three solute mole fractions (0.5, 1.0 and 1.5 mol%). The Fick diffusion coefficient at infinite dilution was obtained by extrapolation of the intra-diffusion coefficient of the solute i to the infinite dilution limit, $D_{ij}^{\infty} = D_i^{x_j \to 1}$.

Diffusion

It was found that slight variations of temperature and pressure in the extended critical region may cause the density of these mixtures to halve, the shear viscosity to double and diffusion coefficients to rise strongly. This anomalous behavior of both thermodynamic and transport properties is particularly pronounced near the so-called Widom line. In contrast to the strong composition dependence of the Fick diffusion coefficient in the extended critical region, the Maxwell-Stefan diffusion coefficient shows a rather weak dependence on the solute mole fraction, cf. Fig. 1. This can be explained by the strong changes of thermodynamic factor, which account for the thermodynamic non-ideality of a mixture and is, per definition, zero at the critical point. Generally, the thermodynamic factor displays a well pronounced minimum near the Widom line of the studied mixtures, even with only 0.5 mol% of the solute present. For example, CO_2 + naphthalene reaches a thermodynamic factor value as low as $\Gamma = 0.45$ at $T = 320$ K along $p = 9$ MPa. This minimum can be related to large density fluctuations and the presence of clustering effects near the Widom line.

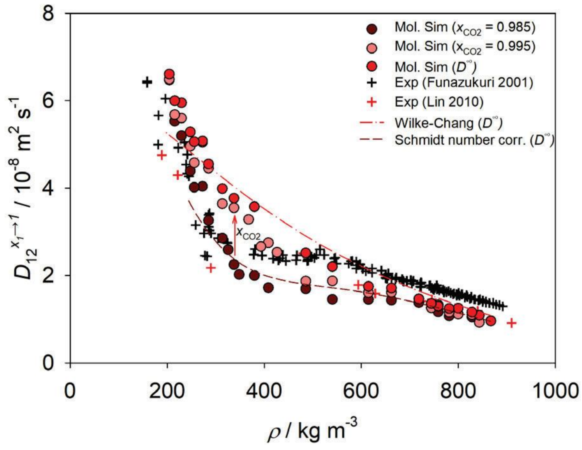

Figure 1: Density dependence of the Fick diffusion coefficient of benzene diluted on CO_2. Molecular simulation data for the Fick diffusion coefficient along the isobar p = 9 MPa are compared with experimental data and predictive equations (Wilke et al. 1955, Funazukuri et al. 2006).

Fig. 1 shows the density dependence of the sampled Fick diffusion coefficient along the $p = 9$ MPa isobar for the supercritical CO_2 mixed with benzene in comparison to the available experimental data at the same density, but at different temperatures and pressures. The anomalous slow-down of Fick diffusion near the Widom line observed through that experimental data is qualitatively replicated by simulation at a finite mole fraction. The observed diffusive slow-down becomes less pronounced with decreasing solute mole fraction and disappears at the infinite dilution limit, as the thermodynamic factor reaches the value of unity.

Molecular simulation data show a clear breakdown of the Stokes-Einstein relation, i.e. decoupling of diffusion and viscosity around the Widom temperature, where the transition from a high- to low-density fluid occurs, cf. Fig. 2. Furthermore, molecular simulation results indicate a strong correlation of the Fick diffusion coefficient on the self-diffusion coefficient of pure CO_2 and the molecular mass of the solute, cf. Fig. 3. This relation can be useful for the development of an empirical equation to access the Fick diffusion coefficient only based on the properties of pure $scCO_2$, the molecular mass of the solute and mixture density.

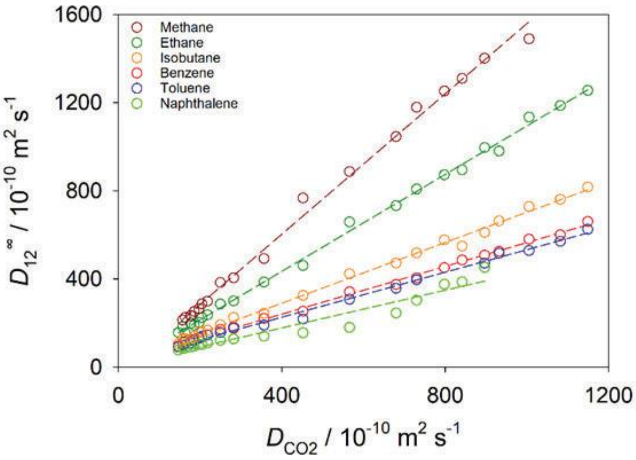

Figure 2: Dependence of the infinite dilution Fick diffusion coefficient on the self-diffusion coefficient of pure CO_2 for methane, ethane, isobutane, benzene, toluene and naphthalene diluted in $scCO_2$. Open symbols represent molecular simulation data along the 9 MPa isobar and temperatures between 290 K and 345 K. The lines are linear fits to the data.

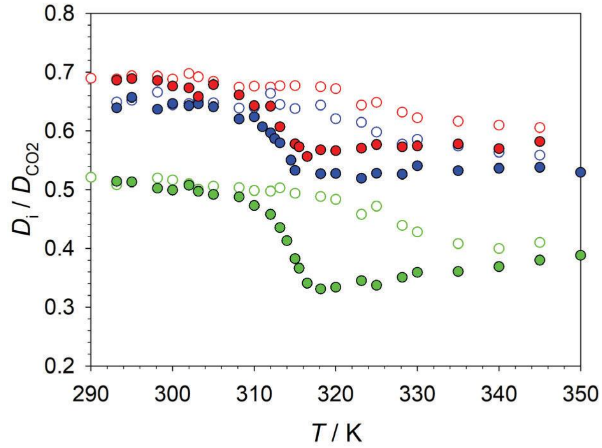

Figure 3: Ratio of the intra-diffusion coefficient of the solute to the solvent for CO_2 mixtures with 0.5 mol% of each benzene (red), toluene (blue) or naphthalene (green). Solid and open symbols represent the simulation data along the isobars $p = 9$ and 12 MPa, respectively.

Thermodiffusion

As a second-order effect, the mass flux induced by the Soret effect is relatively small and therefore challenging to evaluate with equilibrium molecular dynamics simulation. Nonetheless, this technique allows for the determination of the different contributions to the thermal diffusion coefficient, and thus to the understanding of the associated microscopic mechanisms. The Soret coefficient relates the thermal diffusion coefficient D^T to the Fick diffusion coefficient D_{ij}, $S^T = D^T/D_{ij}$. Therefore, it is expected that the Soret coefficient shows an anomalous behavior in the near-critical region, as observed for the Fick diffusion coefficient. First molecular simulation results for some of the studied CO_2 mixtures support this assumption with the sampled Soret coefficient showing a strong temperature dependence and anomalous behavior near the Widom line. Further, analysis of the different terms contributing to the thermal diffusion coefficient identified the enthalpic term as the main contribution. Thus, an accurate assessment of the partial molar enthalpies is essential for the calculation of the Soret coefficient employing equilibrium methods.

Conclusions

Molecular dynamics simulation techniques were employed for the determination and analysis of the Fick diffusion coefficient of binary mixtures of supercritical CO_2 and different solutes. In the near-critical region, it was found, even for highly diluted mixtures, that the thermodynamic factor may strongly differ from unity. These non-idealities induce an anomalous slow-down of the Fick diffusion coefficient in this region. Similarly, first simulation results suggest an anomalous behavior of the Soret coefficient in the near-critical region.

Acknowledgements

This work was funded by the Deutsche Forschungsgemeinschaft (DFG) under the grant VR 6/11. Molecular dynamics simulations were performed either on the Cray CS500 system at the Paderborn Center for Parallel Computing or on the HPE Apollo system at the High-Performance Computing Center Stuttgart (HLRS) contributing to the project MMHBF2.

References

G. Guevara-Carrion, S. Ancherbak, A. Mialdun, J. Vrabec, V. Shevtsova, Diffusion of methane in supercritical carbon dioxide across the Widom line. *Sci. Rep*. 9, 1–14 (2019).

R. Chat well, G. Guevara-Carrion, Y. Gaponenko, V. Shevtsova, J. Vrabec, Diffusion of the carbon dioxide–ethanol mixture in the extended critical region. *Phys. Chem. Chem. Phys*. 23, 3106–3115 (2021).

T. Funazukuri, C. Kong, S. Kagei, Infinite dilution binary diffusion coefficients of benzene in carbon dioxide by the Taylor dispersion technique at temperatures from 308.15 to 328.15 k and pressures from 6 to 30 MPa. *Int. J. Thermophys*. 22, 1643–1660 (2001).

R. Lin, L.L. Tavlarides, Diffusion coefficients of diesel fuel and surrogate compounds in supercritical carbon dioxide. *J. Supercrit. Fluids* 52, 47–55 (2010)

C. Wilke, P. Chang, Correlation of diffusion coefficients in dilute solutions. *AIChE J*. 1, 264–270 (1955).

T. Funazukuri, C. Kong, S. Kagei, Binary diffusion coefficients in supercritical fluids: Recent progress in measurements and correlations for binary diffusion coefficients. *J. Supercrit. Fluids* 38, 201–210 (2006).

Mixed convection in porous thermogravitational column

A. Mojtabi[1], K. Sioud[1,2], M-C. Charrier Mojtabi[1]

[1] Institut de Mécanique des Fluides de Toulouse, UMR CNRS INPT/UPS N 5502, Université de Toulouse, Toulouse, 31400, France.
[2]Institut Clément Ader (ICA), Université de Toulouse, CNRS-INSA-ISAE-Mines Albi-UPS, 31400 Toulouse, France

Introduction

Thermo-diffusion is a mass transport phenomenon which appears in multi-component mixtures subjected to a thermal gradient. This phenomenon is also called the Soret or Ludwig-Soret effect (1856). This effect leads to species separation of the fluid mixture. It was the subject of numerous works. This mass transport takes place towards the hot or cold walls, depending on the species involved, their thermodynamic characteristics and the thermal boundary conditions. The presence of convection and the Soret effect lead to another phenomenon called thermo-gravitational diffusion, resulting in greater species separation compared to the one obtained in pure thermodiffusion.

To increase the species separation, Khouzam et al. (2013) used mixed convection. Sioud et al. (2022) showed that the species separation obtained in spherical annular columns is more important than in the usual vertical thermogravitational column (TGC). Mojtabi et al. (2019) studied a new configuration of the horizontal porous layer by moving the cavity walls at constant and opposite velocity. Seta et al. (2020) studied the species separation stability for different mixtures with negative Soret coefficient, in a parallelepipedic thermogravitational microcolumn.

The present study deals with forced convection imposed to a binary fluid saturating a porous medium and flowing in a cavity whose vertical plates are maintained at constant and different temperatures.

This coupling leads to species separation continuously. This process could be used in multiple academic and industrial applications.

1. Mathematical formulation

In the present study, we consider a water-ethanol mixture (60.88% water) flowing through a parallelepipedic cavity, of $L = 2.5$ m length, $e = 6 \cdot 10^{-3}$m thickness and $H = 0{,}314$ m height with $e << H << L$, saturating a porous media of a porosity $\epsilon^* = 0.4$. Both lateral vertical walls are isothermal and maintained respectively at different temperatures as seen in **Fig.1**.

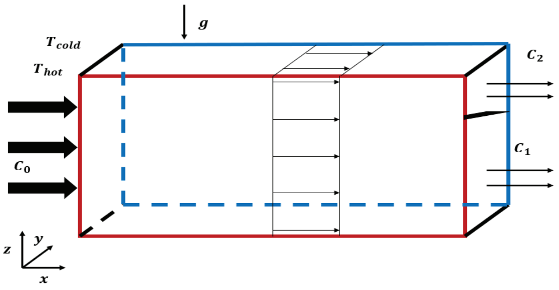

Figure 1: Schematic drawing of the studied cell.

.

This mixture is incompressible. We neglect viscous dissipation and Dufour effect.

The Boussinesq approximation is assumed to be valid; in the convection generating term, the density varies linearly with the local temperature and the local mass fraction.

The mathematical formulation of the physical problem is given by:

$$\begin{cases} \nabla . \boldsymbol{V} = 0 \\ \boldsymbol{V} = -\dfrac{K}{\mu}\left(\boldsymbol{\nabla} P - \rho_0[1 - \beta_T(T - T_0) - \beta_C(C - C_0)]\boldsymbol{g}\right) \\ (\rho c)^* \dfrac{\partial T}{\partial t} + (\rho c)_f \boldsymbol{V}.\nabla T = \lambda^* \, \nabla^2 T \\ \left(\epsilon^* \dfrac{\partial C}{\partial t} + \boldsymbol{V}.\, \nabla C\right) = \left(D^* \, \nabla^2 C + {D_T}^* C_0(1 - C_0)\nabla^2 T\right) \end{cases}$$

where D^* and ${D_T}^*$ are, respectively, the mass diffusion coefficient and the thermodiffusion coefficient of the denser component in porous media, $\boldsymbol{V}$ is the velocity of the fluid, T is the temperature and C is the mass fraction of the constituent of interest. We suppose that $C(1 - C) \approx C_0(1 - C_0)$.

In these equations, $(\rho c)^*$ and λ^* are, respectively, the effective heat capacity and the thermal conductivity of the porous medium, ϵ^*its porosity and K its permeability. μ and ρ_0 are the dynamic viscosity and the density, at $T = T_0$ of the saturating fuid.

The boundary conditions of the study are written as follows:

For velocity

$$\begin{cases} y = 0, e\,; \boldsymbol{V}.\boldsymbol{n} = 0 \\ z = 0, H\,; \boldsymbol{V}.\boldsymbol{n} = 0 \\ x = 0\,; \boldsymbol{V}.\boldsymbol{x} = u_{deb} \\ x = L\,; \dfrac{\partial \boldsymbol{V}}{\partial x} = \boldsymbol{0} \end{cases}$$

For temprerature

$$\begin{cases} y = 0 \;\; ; T = T_{hot} \\ y = e \;\; ; T = T_{cold} \\ x = 0\,;\; T = T_0 \\ x = L\,;\; \dfrac{\partial T}{\partial x} = 0 \\ z = 0, H\,;\; \dfrac{\partial T}{\partial z} = \dfrac{\partial C}{\partial z} = 0 \end{cases}$$

For mass fraction

$$\begin{cases} x = 0, C = C_0 \\ x = L;\; \frac{\partial C}{\partial x} = 0 \\ y = 0, e;\; D^* \frac{\partial C}{\partial y} + {D_T}^* C_0(1 - C_0)\frac{\partial T}{\partial y} = 0 \end{cases}$$

2. Analytical solution

In order to solve the corresponding problem analytically, when the flow reaches the massic established regime, the forgotten effect hypothesis (Platten et al. 2003) and parallel fow approximation (Mojtabi et al. 2019) were taken into consideration.

$$\begin{cases} \boldsymbol{V} = w(y)\boldsymbol{z} + u_{deb}\boldsymbol{x} \\ T = f(y) \\ C = mz + h(y) \end{cases}$$

m designates the mass fraction gradient along $\boldsymbol{z}$.

$$\begin{cases} T = \dfrac{T_{cold} - T_{hot}}{e} y + T_{hot} \\ w(y) = Kg\beta_T(T_{cold} - T_{hot})(2y - e)/24ev \\ h(y) = \dfrac{(T_{cold} - T_{hot})}{D^*} \left(\dfrac{mKg\beta_T(e^3 - 6ey^2 + 4y^3)}{24ev}\right) \\ \qquad -D_T{}^*C_0(1 - C_0)\left(\dfrac{y}{e} - \dfrac{1}{2}\right) \\ m = \dfrac{-10Kgv\beta_T D_T{}^* C_0(1 - C_0)(T_{cold} - T_{hot})^2}{(Keg\beta_T(T_{cold} - T_{hot}))^2 + 120(vD^*)^2} \end{cases}$$

3. Results and discussion

Numerical simulations are carried out with a finite elements method using COMSOL Multiphysics software and the results are compared to the analytical ones as seen for vertical velocity in fig.2 and mass fraction in fig.3. The evolution of the mass fraction at the bottom and top of the column as a function of time in x=L is given in fig.4

We observe a good agreement between numerical and analytical results in 2D. 3D numerical simulations are being developed to validate used assumptions.

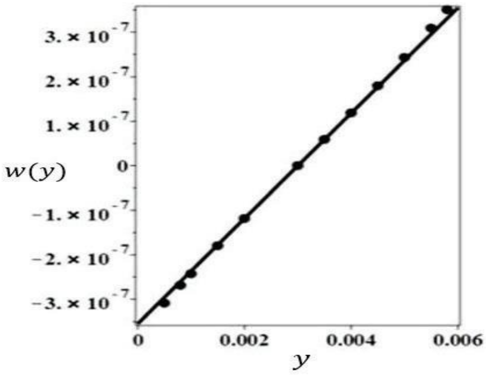

Figure 2: Numerical (dots) and analytical (line) of the vertical component of the velocity function of y

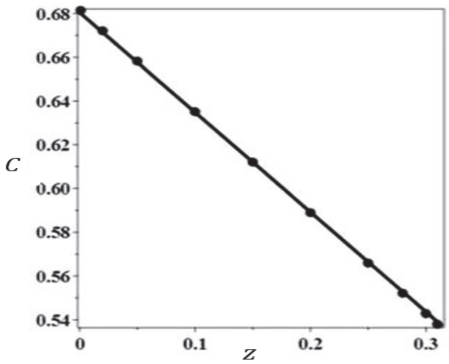

Figure 3: Numerical (dots) and analytical (line) mass fraction profile as a function of z for $x = L$

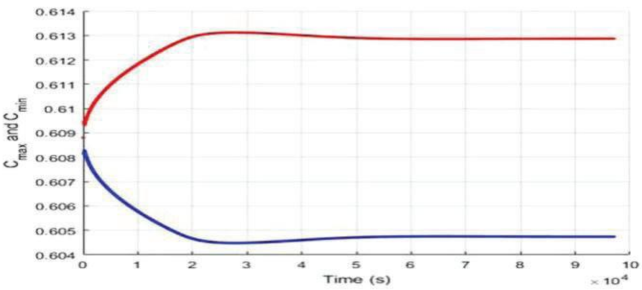

Figure 4: Evolution of the mass fraction at the bottom and top of the column as a function of time in x=L.

Conclusions

This work presents a new procedure allowing the species separation in a continuous way. For this, the binary fluid initially at a uniform concentration is introduced with a constant velocity through the vertical slot of the thermogravitational column at $x = 0$ and comes out through the opposite slot at $x = L$, once mass fraction equilibrium is reached.

It is possible to juxtapose and connect several similar columns to achieve complete species separation.

Also, the fact of using porous thermogravitional columns, makes it possible to significantly increase the quantity of separated product since the thickness e of the porous cavity can be 6 to 7 times greater than the one of a cavity with the binary fluid alone.

Acknowledgements

The authors acknowledge the support of CNES, the French National Space Agency, which provided access to results obtained in microgravity.

References

A. Khouzam, A. Mojtabi, M.C. Charrier-Mojtabi, B. Ouattara, Species separation of a binary mixture in the presence of mixed convection. Int. J. Therm. Sci. 73, 18–27 (2013).

A. Mojtabi, A. Khouzam, Y. Loujaine, M.C. Charrier-Mojtabi, Analytical and numerical study of Soret mixed convection in two-sided lid-driven horizontal cavity: optimal species separation. Int. J. Heat Mass Transf. 139, 1037–1046 (2019).

B. Seta, J. Gavalda, MM. Bou Ali, X. Ruiz, Stability analysis under thermogravitational effect, Int. J. of Thermal Sciences, V. 156, 106464, (2020)

C. Ludwig. Diffusion zwichen unfleigh erwarmten orten gleich zusammengesetz losungen. Akad. Wiss. Wien, Math Naturwiss, 20, pp. 539 (1856).

JK. Platten, MM. Bou Ali, JF. Dutrieux, Enhanced molecular separation in inclined columns, J. Of Physical Chemitry B,! 107, 42, 11763–11767, (2003).

K. Sioud, A. Abdennadher, S. Kaddeche, M.C. Charrier-Mojtabi, A. Mojtabi, Soret-Driven Convection Inside Concentric Porous Spheres Saturated by Binary Fluid: Comparison with Parallelepipedic Vertical Column, Transport in Porous Media, 145, 635–651, (2022).

Revised Enskog Theory for Mie fluids: A predictive model for transport properties in dense gases

V. G. Jervell[1], Ø. Wilhelmsen[1]

[1]Porelab, Department of Chemistry, Norwegian University of Science and Technology, Trondheim, Norway,
Vegard.g.jervell@ntnu.no, Oivind.wilhelmsen@ntnu.no

Introduction

The Enskog solutions to the Boltzmann equations have for many years provided a route to predicting the effects of thermal diffusion. By using more complex interaction potentials, predictions for dilute gases have become increasingly accurate for real fluids. However, for dense gases, predictions have thus far been limited to the use of the hard sphere potential.

The Revised Enskog Theory (RET) for multicomponent mixtures, developed by van Bejren and Ernst, uses the radial distribution function (rdf) at contact to account for the effects of increased density in hard sphere mixtures. By using Barker-Henderson perturbation theory to calculate the rdf at contact, we extend the Revised Enskog Theory to Mie fluids (RET-Mie).

Several equations of state have been developed on the basis of the Mie potential, and the parameters of the interaction potential have been regressed to pure-component equilibrium properties. Using these parameters as input, RET-Mie is fully predictive for transport properties.

Comparing the model to an extensive set of gas phase experiemental data (Vargaftik, 1975, Oost et al. 1969/1972), it is found that predicted thermal diffusion ratios are typically within 10-20 % of the reported measurements. It is also found that the predicted thermal diffusion factor differs by less than 15 % from simulation results for Lennard-Jones mixtures, even at densities significantly exceeding the critical density.

Theory

The Boltzmann equations for a multicomponent system consisting of particles with non-negligible covolume may, in the absence of external forces, be written as, (de Haro et al. 1983)

$$\left(\frac{\partial}{\partial t} + \frac{\partial}{\partial u_i}\right) f_i = \sum_j J_{ij}(f_i, f_j),$$

where u_i is the velocity of a particle of species *i*, f_i is the velocity distribution function (vdf) of species *i*, and

$$J_{ij} = \iiint \chi\left(r + \sigma_{ij}\right) f_i'(r) f_j'\left(r + \sigma_{ij}\right) - \chi\left(r - \sigma_{ij}\right) f_i'\left(r - \sigma_{ij}\right) f_j'(r)\, b\, db\, d\varepsilon\, du_j$$

is the streaming operator, which describes the effect of collisions on the vdfs. Here, χ is the radial distribution function, σ_{ij} is a length associated with the size of the particles, for hard spheres taken to be the particle diameter, and b and ε are the collision coordinates, as illustrated in Fig. 1.

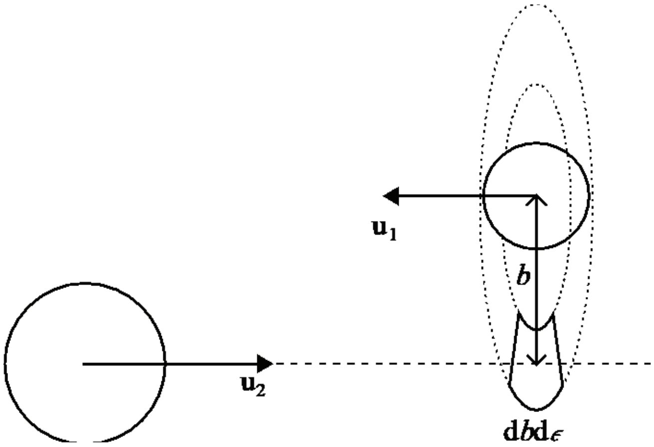

Figure 1: The coordinates describing a binary collision.

An approximate solution to this set of equations is found by means of the Enskog solution method. From these solutions, it becomes apparent that the "contact diameter", σ_{ij}, plays two distinct roles: That of modifying the frequency of collisions, through the rdf at contact, and that of enhancing transport as energy and momentum are transferred across a non-zero distance from one particle to the next during collisions.

We employ Barker-Henderson perturbation theory to evaluate the rdf at contact for particles interacting through a Mie (generalized Lennard-Jones) potential. Regarding the instantaneous transport between particles at the moment of collision, we propose a manner in which to find a reasonable distance that may be considered the "contact diameter" for colliding Mie particles. Thus, we may employ the RET to evaluate the transport coefficients of a dense, multicomponent mixture of Mie particles.

Mie potential parameters

All predictions in the current work have been made using potential parameters regressed to equilibrium properties. Calculation of transport properties thus requires no *a priori* knowledge about the transport properties of the investigated systems.

Implementation

The proposed model, RET-Mie, has been implemented as an Open-Source package, and may be found on GitHub under the ThermoTools project.

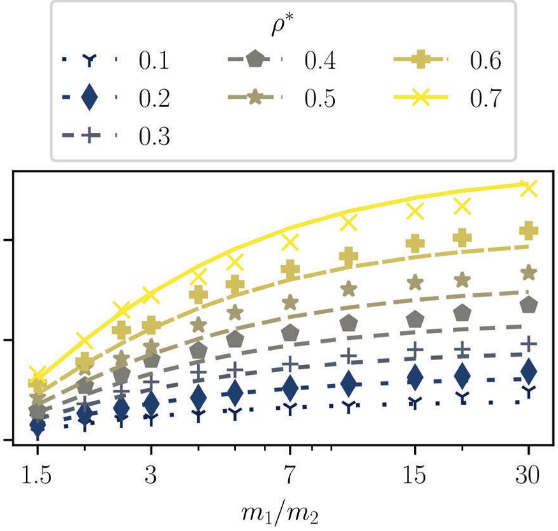

Figure 2: The thermal diffusion factor of several isotopic Lennard-Jones mixtures at $T^* = 2.0$. Predictions (lines) using RET-Mie. Marks are simulation results (Hoang and Galliero, 2022).

Results

The RET-Mie has been tested in its ability to reproduce the transport properties of a wide variety of systems. Not only thermal diffusion has beem examined, but also diffusion coefficients, shear viscosities and thermal conductivities.

As shown in Fig. 2, the predicted thermal diffusion factor of isotopic LJ mixtures is in good agreement with simulation results (Hoang and Galliero, 2022), even up to a reduced density of $\rho^* = 0.7$.

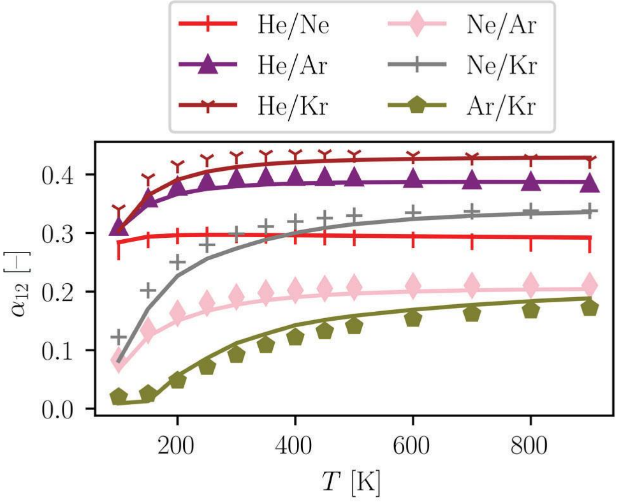

Figure 3: The thermal diffusion factor of several real mixtures, as predicted using RET-Mie (lines) and computed using *ab initio* potentials (marks) (Song et al. 2011).

Thermal diffusion factors were predicted for several real mixtures at temperatures ranging from 100 K to 1000 K, and compared to computations using *ab initio* quantum chemical potentials (Song et al. 2011). As shown in Fig. 3, the agreement with their computations is excellent.

Conclusions

The RET-Mie has so far shown itself to be a reliable model for predicting thermal diffusion coefficients, and other transport coefficients, without requiring any *a priori* knowledge about the transport properties of the system in question.

Several possible extensions, both involving molecules with internal energy, molecules with significantly non-spherical interaction potentials, and systems with significantly large thermal de Broglie wavelengths deserve further attention.

Acknowledgements

The authors acknowledge funding from the Research Council of Norway (RCN), the Center of Excellence Funding Scheme, Project No. 262644, PoreLab. Funding was also provided by the PredictCUI project coordinated by SINTEF Energy Research, and the authors acknowledge the contributions of Equinor, Gassco, Shell, and the PETROMAKS 2 programme of the Research Council of Norway (308770).

The authors also wish to thank Prof. S. Kjelstrup, Prof. D. Bedeaux, Prof. B. Hafskjold and Prof. H. Struchtrup for valuable discussions, insights and comments.

References

N. Vargaftik, *Tables on the Thermophysical Properties of Liquids and Gases*, 2nd ed. (Hemisphere Publishing Corporation, 1975)

W. Oost and A. de Vries, *Physica*, 41, 440 (1969)

W. Oost, J. Los, H. Cauwenbergh and W. Van Dael, *Physica*, 62, 409 (1972)

M. López de Haro, E. G. D. Cohen, and J. M. Kincaid, *The Journal of Chemical Physics* 78, 2746 (1983)

H. Hoang and G. Galliero, *The European Physical Journal E* 45, 42 (2022).

B. Song, X. Wang, J. Wu and Z. Liu, *Molecular Physics* 109, 1607 (2011)

Thermodiffusion of aqueous salt solutions: Hofmeister Series and overlapping hydration shells

S. Wiegand[1,2], S. Mohanakumar[3], W.J. Briels[1,4]

[1]IBI-4: Biomacromolecular Systems and Processes, Forschungszentrum Jülich GmbH,
D-52428 Jülich, Germany, s.wiegand@fz-juelich.de, [2]Chemistry Department – Physical Chemistry, University Cologne, D-50939
Cologne, Germany, [3]IBI-4: Biomacromolecular Systems and Processes, Forschungszentrum Jülich GmbH,
D-52428 Jülich, Germany, s.mohanakumar@fz-juelich.de, [4]University of Twente, Computational Chemical Physics, Postbus 217, 7500 AE
Enschede, The Netherlands, w.j.briels@utwente.nl

Motivation

Our study of ionic solutes is motivated by the most important practical application of thermodiffusion, where it is used to monitor protein-ligand reactions. Proteins are complex molecules that contain ionic as well as non-ionic groups. While non-ionic solutes in water have been extensively studied recently (Niether and Wiegand, 2019), ionic solutes' concentration and temperature dependence have not been investigated systematically. For non-ionic compounds, a strong correlation between thermodiffusion and hydration was found (Niether and Wiegand, 2019).

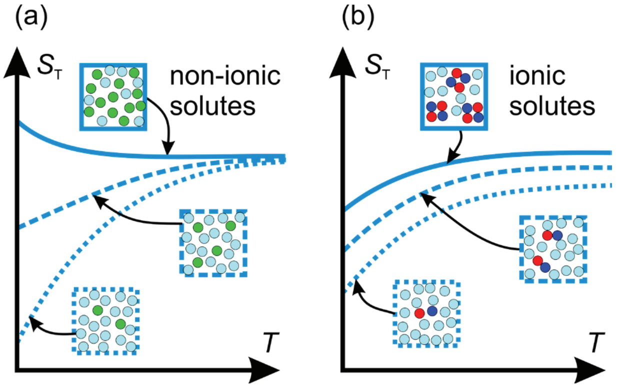

Figure 1: Schematic comparison of the temperature dependence of S_T for non-ionic and ionic solutes at different concentrations: low (dotted line), intermediate (dashed line), and high (solid line).

Comparison of non-ionic and ionic solutes

We found one striking difference between non-ionic and ionic solutes looking at the effect of concentration on the temperature dependence of the Soret coefficient S_T, as illustrated in Fig. 1 (Mohanakumar et al. 2021). For a typical non-ionic solute in water, the behavior of S_T changes from increasing with temperature to decreasing with temperature as the concentration increases. This is correlated with the hydration of the solutes which decreases as the concentration increases. Only very hydrophilic non-ionic solutes have S_T values that increase with temperature for all concentrations. In contrast, the Soret coefficients of ionic solutes show the typical temperature dependence of very hydrophilic solutes over the entire concentration range. For salts with a high degree of dissociation we might have a tightly bound first hydration layer, which leads to a highly hydrophilic entity. For less dissociated salts it might be explained by cluster formation of the salts with increasing concentrations. Even at high salt concentrations the clusters as a whole are hydrated at their surfaces by water, but the total exposure to water is less as the surface decreases when more ions are part of larger clusters.

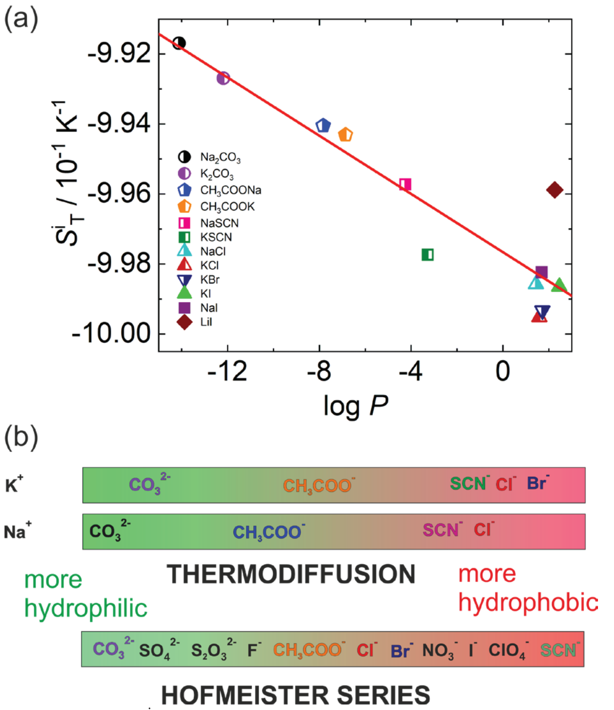

Figure 2: (a) S^i_T values of all studied systems plotted as function of log P. Note, that log P is the sum of an ionic and non-ionic contribution. First order polynomials of concentration and temperature have been used to fit the data using Eq.1. (b) Sequence of the anions based on S^i_T for the two investigated cations in comparison with the Hofmeister series.

Anion and Cation influence on S_T

We investigated systematically the concentration and temperature dependence of the thermodiffusion of aqueous solutions of various potassium and sodium salts (Mohanakumar et al. 2021, Mohanakumar et al. 2022a).

To describe the temperature and concentration dependence we used an empirical Ansatz suggested by Wittko and Köhler (Wittko and Köhler, 2007)

$$S_T(m,T) = \alpha(m)\beta(T) + S_T^i \tag{1}$$

With polynomial serial expansions for $\alpha(m)$ and $\beta(T)$

$$\begin{aligned}\alpha(m) &= \alpha_1 m + \alpha_2 m^2 + \alpha_3 m^3 + \cdots \\ \beta(m) &= 1 + b_1(T - T_0) + b_2(T - T_0)^2 + \cdots\end{aligned} \tag{2}$$

m is the molality, T_0 is an arbitrary reference temperature, set to $T_0 = 25°\text{C}$ and S_T^i is a temperature and concentration independent constant. Note, that we set $a_0 = 0$ as it is strongly coupled to S_T^i.

We could describe the temperature and concentration dependence of $\boldsymbol{S}_\mathbf{T}$ of various potassium and sodium salts in water using Eq.(1). In Figure 2(a) we display the adjustable parameter $\boldsymbol{S}_\mathbf{T}^{\boldsymbol{i}}$ as function of $\mathbf{log}\,\boldsymbol{P}$, with $\boldsymbol{P}$ being the ratio of the equilibrium concentration of the solute (salt) in octanol and in water. So, a negative $\mathbf{log}\,\boldsymbol{P}$ signifies stronger hydrophilicity. We find for all investigated salts a linear correlation between $\boldsymbol{S}_\mathbf{T}^{\boldsymbol{i}}$ and $\mathbf{log}\,\boldsymbol{P}$. This implies that also, for ionic solutes, hydrophilicity plays an important role. If we compare with the hydrophilicity scale of the Hofmeister series, we find a good agreement except for the thiocyanate anion, which should be, according to Hofmeister, the most hydrophobic anion. In brief, we can state that the hydration of the ions plays a significant role.

Overlapping hydration shells

Various salts in water exhibit non-monotonic variations of the Soret coefficient S_T with concentration, which is not understood on a microscopic level. We investigated the thermodiffusive properties of aqueous solutions of sodium iodide, potassium iodide and lithium iodide, using thermal diffusion forced Rayleigh scattering in a concentration range of 0.5 – 4 mole per kg of solvent and a temperature range of 15 to 45°C (Mohanakumar et al. 2022b). In all three cases S_T has a minimum at $m_\text{min} = 1$ mole per kg of solvent. We develop an intuitive picture in which the relevant objects are the fully hydrated salt molecules (FHP), including all water molecules that behave differently from bulk water. Our hypothesis is that these FHPs form a random close packing at m_min, which implies that the outer hydration shell start to touch as indicated in Figure 3. Preliminary, somewhat sketchy calculations indicate that indeed Soret coefficients begin to rise beyond m_min. Indications are given as to why the model will fail at large concentrations.

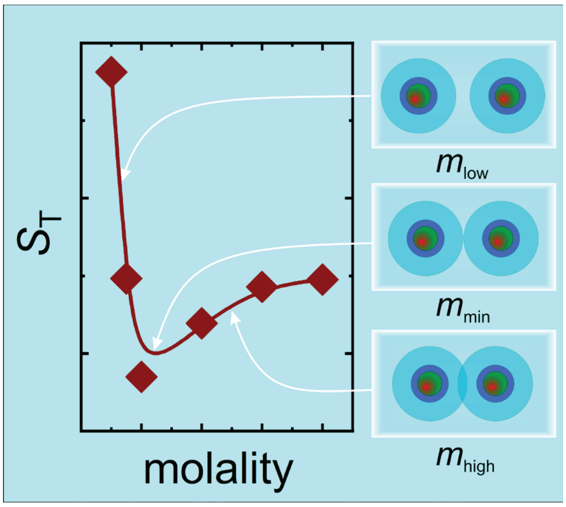

Figure 3: Hydrated salt molecules overlapping with increasing concentration. The green–red sphere represents the bare salt molecule, after adding the blue shell of strongly attached water molecules we get the salt particle (HSP), while after adding next the outer light blue shell of perturbed water we arrive at the hydrated salt molecule, called FHP. At concentrations above m_min the outer shells overlap as shown on the right side.

Conclusions

We have studied the thermophoretic properties of various salts in water over a range of temperatures and concentrations. Although the temperature dependence of the Soret coefficient of the ionic compounds does not change in the same pronounced way as function of their hydrophilicity observed for non-ionic solutes, we find a linear correlation between S_T^i and $\log P$. Most likely, the hydration shell of ionic solutes is more tightly bound to the ions than in the case of non-ionic solutes, so we find a similar temperature dependence of the Soret coefficient for all concentrations. Additionally, overlapping of the hydration shells might also be responsible for the occurrence of a minimum of S_T with concentration. However, this hypothesis needs to be quantified by computer simulations.

Acknowledgements

We thank Fernando Bresme, Jan Dhont and Jutta Luettmer-Strathmann for fruitful and helpful discussions.

References

D. Niether, S. Wiegand, Thermophoresis of biological and biocompatible compounds in aqueous solution, *J. Phys. Condens. Matter*, 31, 503003 (2019).

S. Mohanakumar, J. Luettmer-Strathmann, S. Wiegand, Thermodiffusion of aqueous solutions of various potassium salts, *J. Chem. Phys.*, 154, 84506 (2021).

S. Mohanakumar, S. Wiegand: Towards understanding specific ion effects in aqueous media using thermodiffusion *The Eur. Phys. J. E* 45(2), 10 (2022a).

G. Wittko, W. Köhler, On the temperature dependence of thermal diffusion of liquid mixtures, *Europhys. Lett.* 78, 46007 (2007).

S. Mohanakumar, H. Kriegs, W. J. Briels, S. Wiegand, Overlapping hydration shells in salt solutions causing non-monotonic Soret coefficients with varying concentration *PCCP* 24, 27380 (2022b).

Modelling thermodiffusion in aqueous sodium chloride solutions – best performing water models for predicting inversion temperatures

Alice J. Hutchinson[1,2], Juan F. Torres[1], Ben Corry[2]

[1]School of Engineering, Australian National University, Canberra, Australia, felipe.torres@anu.edu.au,
[2]Research School of Biology, Australian National University, Canberra, Australia, ben.corry@anu.edu.au

Introduction

Thermodiffusion is the migration of a species due to a temperature gradient and is the driving phenomenon in many applications ranging from early cancer detection to uranium enrichment. Molecular dynamics (MD) simulations can be a useful tool for exploring the rather complex thermodiffusive behaviour of species, such as proteins and ions. Thermodiffusive behaviour of a species can be described by the Soret coefficient S_T, which indicates the magnitude and direction of species migration under a temperature gradient, and the inversion temperature T_0, which is the temperature at which a species switches from displaying thermophilic to thermophobic behaviour. Current MD models of thermodiffusion in aqueous ionic solutions struggle to quantitatively predict S_T and T_0. In this work, we aim to improve the accuracy of MD thermodiffusion models by assessing how well different water models can recreate thermodiffusion in a benchmark aqueous NaCl solution. Beyond this, we aim to use the best performing water model to explore how the inversion temperature T_0 of a NaCl solution changes with concentration of the solution.

Which water model is best?

To improve predictions of thermodiffusion, the accuracy limitations of MD modelling must be considered. MD is based on classical mechanics and, therefore, inherently approximates real-world molecules and their behaviour. In an aqueous electrolyte MD simulation, the major approximations lie upon the choice of the ion and water models (force fields), which define the structure and interactions of these molecules. While the exact mechanism of thermodiffusion is not well understood, multiple sources emphasise the importance of hydrogen bond structures, solute–water interactions, and hydration entropy in defining thermodiffusive behaviour (Duhr & Braun 2006, Di Leece et al. 2017, Niether & Wiegand 2019). The water model and its associated ion parameters define the molecule structure and the water–water, ion–ion, and water–ion interactions in the solution and, hence, are integral to accurately recreating thermodiffusion.

In this work, the thermodiffusive behaviour of three- and four-point models from two of the best performing water model families were tested (**Figure 1**). TIPnP-FB approximates water from on experimental reference data (Wang et al. 2014) and OPCn approximates water from quantum mechanically calculated reference data (Izadi et al. 2014, Izadi et al. 2016). We also tested two commonly used models: TIP3P (Huang et al. 2013), an old but regularly used water model that is expected to perform more poorly, and SPC/E (Berendsen et al. 1987), the three-point model commonly used in other MD thermodiffusion works (Römer et al. 2013, Di Leece et al. 2017). Specifically, we sought to compare the performance of the chosen water models in reproducing T_0 of 0.5M aqueous NaCl solutions and S_T of 0.5, 2, and 4M aqueous NaCl solutions, as compared to the experimental values obtained by Römer et al. (2013).

We directly observe the thermally driven diffusion of the ions in solution, by developing a quasi-linear temperature profile over the simulation. The temperature profile is achieved via two spatially defined thermostats controlled to different temperatures (one hot, one cold). Molecules diffuse across the temperature profile to reach a steady state distribution where thermally driven diffusion is opposed by Fickian diffusion. T_0 are found by a maximum in the steady state concentration profile of the ions. The Soret coefficient is derived by fitting the concentration profile versus temperature. Each water model predicted a different ion distribution yielding different T_0 and S_T (**Figure 2**). By comparing the modelled S_T with published experimental values, we determined TIP3P-FB to be the water model that best recreates thermodiffusion in aqueous NaCl solutions (Hutchinson et al. 2022).

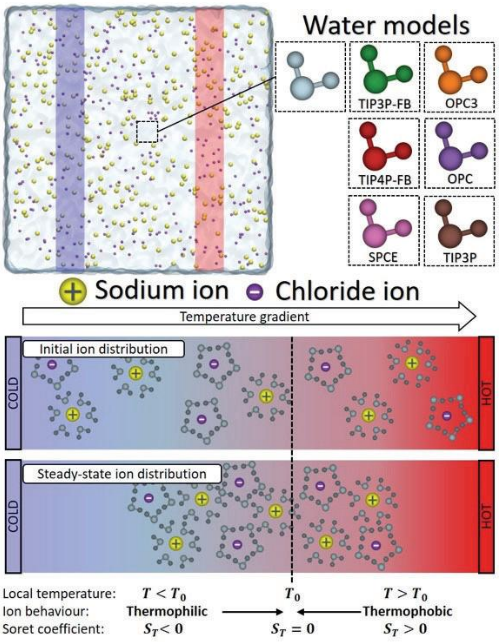

Figure 1: *Top*: Depiction of MD model of aqueous NaCl solution. The model volume is occupied by water molecules (light grey), sodium ions (yellow), and chloride ions (purple). Six different tested water models are represented on the right hand side by different colours. A cold and hot thermostat (highlighted blue and red areas, respectively) are spaced symmetrically within the simulation to create a linear temperature profile over the system. Ions diffuse within the temperature profile. *Bottom*: Depiction of thermophilic and thermophobic behaviour of an aqueous NaCl solution under a linear temperature profile that encompasses an inversion temperature. The direction of thermally driven ion diffusion is indicated by the sign of the Soret coefficient, S_T, and depends on whether the local temperature of the solution, T, is greater or less than the inversion temperature, T_0.

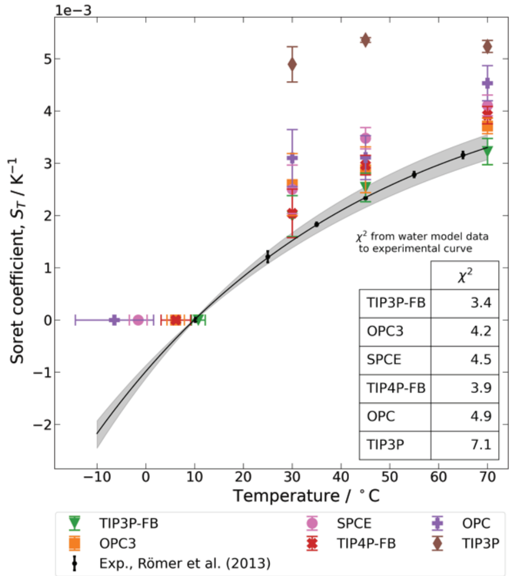

	χ^2
TIP3P-FB	3.4
OPC3	4.2
SPCE	4.5
TIP4P-FB	3.9
OPC	4.9
TIP3P	7.1

Figure 2: MD results for Soret coefficient and inversion temperature in 0.5M NaCl solutions as a function of temperature for each tested water model (Hutchinson et al. 2022). Experimental data from Römer et al. (2014) is shown in black for the comparable concentration of 0.5 mol kg^{-1} NaCl. A measure of distance between the predictions of each water model and the experimental curve is quantified by a χ^2 value in the right-hand side table, where smaller values imply the water model predictions are closer to the curve.

How does the inversion temperature of an aqueous NaCl solution depend on ion concentration?

Following the results in Hutchinson et al. (2022) outlined above, the same general MD simulation set-up is used to explore how T_0 of aqueous NaCl solutions depend on ion concentration in the range of 0.05–2.0M.

It has been proposed that the Soret coefficient is determined by two competing, temperature dependent values – the entropy of hydration and the entropy of ionic shielding (Duhr and Braun, 2006). The entropy of hydration is defined for a single ion in solution. Our preliminary MD simulations suggest that hydration entropy alone cannot cause inversion. A competing entropy of ionic shielding is required for T_0 to be defined, a value that is not defined for single ions in solution. Therefore, we hypothesise that in the infinite dilution limit (concentration, $c \rightarrow 0$), solutions can only behave thermophobically (i.e. T_0 is not defined).

Initial MD modelling of NaCl aqueous solutions of concentrations 0.1, 0.2, 0.5, 1, and 2M supported this hypothesis with a seemingly asymptotic drop in T_0 at the lowest concentration of 0.1M (**Figure 3**). The preliminary results reproduce the known T_0 at moderate concentrations, and the known reduction in inversion temperature with increasing concentration of NaCl. However, the simulation error was too large to be certain of these results and hence further simulations are to be undertaken.

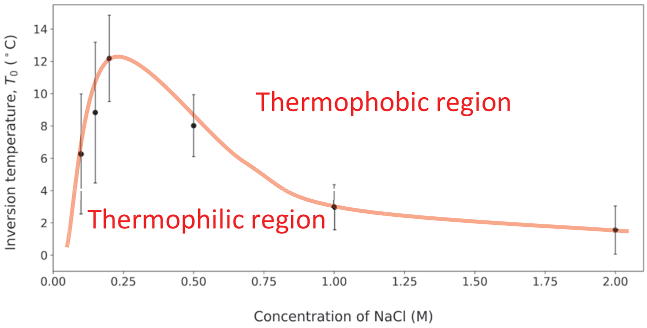

Figure 3: Inversion temperature of aqueous NaCl of varying ion concentrations predicted by MD simulations. Measured inversion temperatures (black dots) are displayed as an average with standard deviation amongst replicates of the simulation. Red line is drawn as a guide to the eye, supporting the hypothesis of a lack of inversion in single solute solutions and proposing a defined thermophobic and thermophilic behavioural region for NaCl solutions.

Conclusions

All tested rigid non-polarisable water models qualitatively reproduced thermodiffusive behaviour. Simulations using TIP3P-FB, followed by TIP4P-FB and OPC3, resulted in the most accurate quantitative predictions of thermodiffusion for a 0.5M NaCl solution. More accurate thermodiffusion properties were obtained by using combined water and ion models that accurately recreate standard properties of the ion–water interactions, such as hydration free energy and ion–oxygen distance, rather than standard properties of water.

The results provide further confidence that MD simulations can capture molecular scale details of the interactions between ions and water molecules to achieve a better understanding and predictions of thermodiffusion. We further applied such MD simulations to explore the relationship between inversion temperature and ion concentration in NaCl aqueous solutions. Preliminary results support the hypothesis that single solute solutions do not exhibit inversion behaviour and that complex thermodiffusion of NaCl solutions, and likely other aqueous solutions, cannot be described by single solute properties alone.

Acknowledgements

The authors acknowledge funding from the Foundation for Australia-Japan Studies. This research was undertaken with the assistance of resources and services from the National Computing Infrastructure, which is supported by the Australian Government.

References

H. J. C. Berendsen, J. R. Grigera, and T. P. Straatsma, "The missing term in effective pair potentials", *J. Phys. Chem.*, 91, 6269–6271, (1987)

S. Di Leece, T. Albrecht, and F. Bresme, "The role of ion–water interactions in determining the Soret coefficient of LiCl aqueous solutions," *Phys. Chem. Chem. Phys.*, 19, 9575–9583, (2017)

S. Duhr, and D. Braun, "Why molecules move along a temperature gradient," *Proc. Natl. Acad. Sci. U. S. A.*, 103, 19678–19682, (2006)

J. Huang, and A. D. MacKerell, Jr., "CHARMM36 all-atom additive protein force field: Validation based on comparison to NMR data," *J. Comput. Chem.*, 34, 2135-2145, (2013)

A. J. Hutchinson, J. F. Torres, and B. Corry, "Modeling thermodiffusion in aqueous sodium chloride solutions – Which water model is best?", *J. Chem Phys.* 156, 164503, (2022)

S. Izadi, R. Anandakrishnan, and A. V. Onufriev, "Building water models: A different approach," *Am. Chem. Soc.*, 5, 3863–3871, (2014)

S. Izadi, and A. V. Onufriev, "Accuracy limit of rigid 3-point water models", *J. Chem. Phys.*, 145, 074501, (2016)

D. Niether, and S. Wiegand, "Thermophoresis of biological and biocompatible compounds in aqueous solution," *J. Phys.: Condens. Matter*, 31, 503003, (2019)

F. Römer, Z. Wang, S. Wiegand, and F. Bresme, "Alkali halide solutions under thermal gradients: Soret coefficients and heat transfer mechanisms," *J. Phys. Chem. B*, 117, 8209–8222, (2013)

L. P. Wange, T. J. Martinez, and V. S. Pande, "Building force fields: An automatic, systematic, and reproducible approach," *J. Phys. Chem. Letters*, 5, 1885–1891, (2014)

Einstein-Helfand and Green-Kubo expressions in isothermal and energy conserving Dissipative Particle Dynamics.

D. C. Malaspina[1], M. Lísal[2], J. P. Larentzos[3], J. K. Brennan[3], A. D. Mackie[1] and J. Bonet Avalos[1]

[1] Departament d'Enginyeria Química, ETSEQ, Universitat Rovira i Virgili, Tarragona 43007, Spain, [2]Department of Molecular and Mesoscopic Modelling, The Czech Academy of Sciences, Institute of Chemical Process Fundamentals, Prague 165 01, Czech Republic, [3]U.S. Army Combat Capabilities Development Command (DEVCOM) Army Research Laboratory, Aberdeen Proving Ground, MD 21005, USA

Introduction

Einstein-Helfand (EH) and Green-Kubo (GK) formulas [1,2] have been widely used to calculate the values of macroscopic transport coefficients from equilibrium molecular dynamics simulations [3]. Transport coefficients, such as diffusion coefficients, shear viscosities or thermal conductivities, are obtained from expressions containing time correlation functions of microscopic fluxes (e.g. particle flux, stress tensor or heat flow), which are sampled from the dynamic simulations. Compared to non-equilibrium simulations, which reproduce the experimental setup in which e.g. a temperature gradient produces a heat flux across the sample, EH and GK are calculated from equilibrium simulations. The EH and GK approaches do not require specific boundary conditions to create the density, velocity or temperature gradients suitable to generate the conjugated flow. Therefore, one single equilibrium simulation can provide a set of transport coefficients. In this presentation we show that the standard GK and EH formulas can be applied to Dissipative Particle Dynamics (DPD) models, whose dynamics is expressed in terms of Langevin-like equations, containing dissipative and random contributions, contrary to the general belief.

Shear viscosity

Despite its generalised use in standard molecular dynamics simulations, concerns have been expressed about whether the presence of irreversible and random interactions forbids the use of EH and GK formulas in DPD. For such systems with stochastic and dissipative interactions, Ernst and Brito [4] proposed modifications of the GK formulas in which the transport coefficient is expressed as a summation of different contributions, which include conservative and dissipative interactions, but not the random contributions. For the shear viscosity, they propose

$$\eta = \eta_\infty + \frac{1}{k_B T V}\int_0^\infty dt\ \left\langle \left(\Pi^C_{xz}(t) + \Pi^D_{xz}(t)\right)\left(\Pi^C_{xz}(0) - \Pi^D_{xz}(0)\right)\right\rangle \qquad (1)$$

The first term is the effect of the random contribution and the second term (inside the integral) is affected by a negative sign, which is at least striking. Using this approach, Jung and Schmid [5] applied the GK relation of Eq. (1) for the calculation of viscosity for Dissipative Particle Dynamics (DPD) models.

However, in this presentation, we show that the standard EH and GK formulas are in fact valid for DPD-like models which satisfy only two fundamental conditions, namely, i) the model preserves the conservation of the given property (in the case of the viscosity, DPD models preserve momentum conservation) and ii) the random contributions satisfy detailed balance. Extensive simulations show that the standard expressions are consistent if the appropriate form of the fluxes is introduced in the formulas, i.e. the dissipative and random contributions are also included. For the sake of comparison with Eq. (1), we can prove that the expression

$$\eta = \frac{1}{k_B T V}\int_0^\infty dt\ \langle \Pi_{xz}(t)\Pi_{xz}(0)\rangle = \eta_\infty + \frac{1}{k_B T V}\int_0^\infty dt\ \left\langle \left(\Pi^C_{xz}(t) + \Pi^D_{xz}(t)\right)\left(\Pi^C_{xz}(0) + \Pi^D_{xz}(0) + \Pi^R_{xz}(0)\right)\right\rangle \ (2)$$

is theoretically equivalent to Eq. (1). In Fig. (1) we show the numerical comparison between the two expressions.

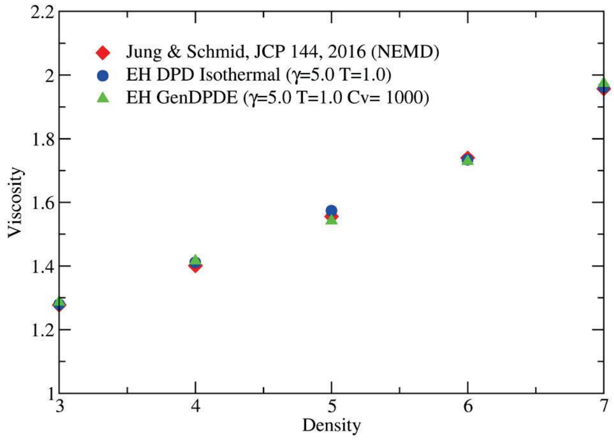

Figure 1: Comparison between values of the viscosity obtained from our proposed EH formula and non-equilibrium simulation results of Figure 5 in Ref. [5]. Blue circles correspond to simulations performed with the isothermal DPD with γ = 5, T = 1, and the same time step as in the original reference, δt = 0.01. The errors are of the size of the symbols. Green triangles stand for the values obtained from GenDPDE simulations with large heat capacity Cv = 1000 and an interparticle thermal conductivity κ = 50.

Thermal conductivity

DPD with energy conservation (DPDE) [6-9] is a particular type of DPD model that includes an internal energy and particle temperature along with conservative, dissipative and random interactions. DPDE, and its generalisation to complex systems (GenDPDE [10-12]), is of particular interest in mesoscopic fluid simulations and has applications in several areas of interest including fluids with chemical reactions, multiphase flow and heat transport under complex conditions.

Following the same line of reasoning, we present the derivation of the formulas for the EH and GK relations for the thermal conductivity (Figure 2) in DPDE and GenDPDE. The calculation of the transport coefficients from equilibrium simulations was also contrasted with non-equilibrium calculations [13]. We observe very good agreement of the proposed equilibrium EH and GK relations under different parameter ranges, proving the validity of the expressions. In overall, we present an extensive analysis of the validity of EH and GK formulas in DPD models and we extend its application to DPDE and GenDPDE models.

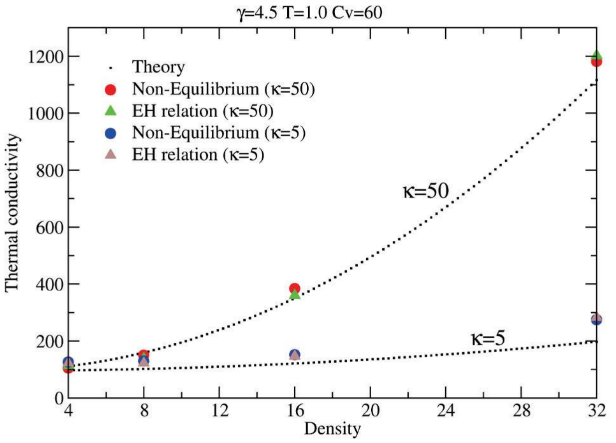

Figure 2: Thermal conductivity as a function of the density for values of the particle thermal conductivity κ = 5 and 50. The circles represent the results obtained from non-equilibrium DPDE simulations (blue circles κ = 5 and red circles κ = 50), the triangles from equilibrium DPDE simulations using our proposed EH relation (grey triangles κ = 5 and green triangles κ = 50), and the predicted theoretical value from mean-field approximation (dotted black line).

Conclusions

Our theoretical analysis, together with the broad range of parameters studied, are a strong case against the false belief that DPD-like systems cannot be treated on the same grounds as conservative systems. The random contributions in the dynamics introduce some peculiar behaviours, which are not present in conservative systems. However, the general principles of conservation and detailed balance suffice to set the appropriate framework for the analysis of transport in dissipative and stochastic systems, with no ambiguity.

Acknowledgements

D. C. Malaspina, A. D. Mackie and J. Bonet Avalos acknowledge support from the grant PID2021-122187NB-C33, funded by MCIN/AEI/10.13039/501100011033 and “ERDF A way of making Europe”. Research performed by J. Bonet Avalos and A. D. Mackie was sponsored by the Army Research Office, and was accomplished under Cooperative Agreement Number W911NF-20-2-0227. Research performed by M. Lísal was also sponsored by the Army Research Office, and was accomplished under Cooperative Agreement Number W911NF-20-2-0203. J. K. Brennan and J. P. Larentzos acknowledge support in part for a grant of computer time from the DoD High Performance Computing Modernization Program at the Army, Navy, and Air Force Supercomputing Resource Centers.

References

[1] A. Einstein, Ann. Phys., 1905, 322, 549–560.
[2] E. Helfand, Phys. Rev., 1960, 119, 1.
[3] M. P. Allen and D. J. Tildesley, Computer Simulation in Chemical Physics, Springer, ISBN: 978-0-7923-2283-2 (1993).
[4] M. H. Ernst and R. Brito, Europhys. Lett. 73 2, 183-189 (2006).
[5] G. Jung and F. Schmid, J. Chem. Phys. 144, 204104 (2016).
[6] J. Bonet Avalos and A. D. Mackie, Europhys. Lett. 40, 141 (1997).
[7] P. Español, Europhys. Lett. 40, 631 (1997).
[8] J. Bonet Avalos and A. D. Mackie, J. Chem. Phys. 111, 5267-5276 (1999).
[9] J. Bonet Avalos and A. D. Mackie, Phys. Chem. Chem. Phys., 1, 2039-2049 (1999).
[10] J. Bonet Avalos, M. Lísal, J. P. Larentzos, A. D. Mackie, and J. K. Brennan, Phys. Chem. Chem. Phys. 21, 24891 (2019).
[11] J. Bonet Avalos, M. Lísal, J. P. Larentzos, A. D. Mackie, and J. K. Brennan, Phys. Rev. E 103, 062128 (2021).
[12] M. Lísal, J. P. Larentzos, J. Bonet Avalos, A. D. Mackie, and J. K. Brennan, J. Chem. Theory Comput. 18, 4, 2503 (2022).
[13] D.C. Malaspina, M. Lísal, J. P. Larentzos, J. K. Brennan, A. D. Mackie, and J. Bonet Avalos, Phys. Chem. Chem. Phys. (2023) (submitted).

Optical measurement of thermodiffusion inversion temperature in binary solutions using digital interferometry

Shuqi Xu[1] and Juan F. Torres[1*]

[1] School of Engineering, Australian National University, Canberra, ACT 2601, Australia
[*] Email: felipe.torres@anu.edu.au

Introduction

Thermodiffusion may induce non-homogenous concentration distributions due to temperature gradients. Despite being discovered more than 150 years ago and having a rich history of observation, no universal explanation has been found for the physics behind thermodiffusion. For many species, including ions (Römer *et al.*, 2013), colloids (Putnam, Cahill and Wong, 2007), polymers (Qian *et al.*, 2018), and biomolecules (Duhr and Braun, 2006), the Soret coefficient S_T can either be positive (thermophobic) or negative (thermophilic). The temperature at which species changes thermophobicity (i.e. migration direction) is termed the inversion temperature T_0 and its value depends on the concentration and temperature. Note that T_0 is generally low for most species in aqueous solutions, e.g. < 25°C in salt solutions and polymers (Putnam, Cahill and Wong, 2007; Römer *et al.*, 2013). T_0 occurs due to the interaction between the species and effects of its thermal environment (De Miguel and Rubí, 2019). Data on T_0 could help understand the underlying physics of thermodiffusion. However, measuring T_0 may be challenging because the required low temperature control, negligible thermodiffusive transport around T_0, i.e. the measurable ΔC is very small (Römer *et al.*, 2013), and limitations in some optical methods such as beam deflection which only give limited one-dimensional information (Kolodner, Williams and Moe, 1988). Here, we demonstrate a fast and sensitive digital interferometric technique that can measure T_0 in a transparent aqueous solution. Furthermore, S_T can be extracted for a temperature range at a given concentration from a single experiment using this technique.

Proposed experimental methods

A transparent binary or multi-component solution is placed inside a Soret cell (**Figure 1**) whose upper and lower boundary temperatures are controlled with Peltier modules, thermistors and a proportional-integral-derivative control system. A temperature stability of 3 mK is achieved. The heat extracted by the Peltier modules when cooling the Soret cell is effectively removed with a water circulation system.

Phase-shifting interferometry (PSI) is a temporal digital interferometry technique that can resolve the phase difference $\Delta\psi$ between the test and the reference beams; see more details in our recent work (Torres *et al.*, 2020). In the experiments, phase-shifted data (as those shown in **Figure 2**) is obtained from three interferograms acquired within 100 ms, which is much shorter than the time taken for the temperature and concentration fields to fully develop in a 4 mm high Soret cell. The experimental procedure is shown in **Figure 2**. First, we set a no-fringe condition for an isothermal and iso-concentration solution, as shown in (**a**). Since the Lewis number is in the order of 100, the fringes that appeared in the first 1 min since applying a temperature difference, e.g. ΔT of 5 K in (**b**), can be suppressed by adjusting a test beam mirror (Torres *et al.*, 2013), as shown in (**c**) for a quasi-homogeneous solution having a linear temperature profile. After 30 min, the concentration field has fully developed, such that phase differences in (**d**) are due to concentration gradients only.

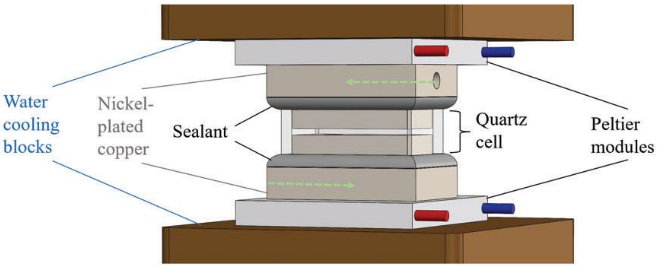

Figure 2: Soret cell. Green dashed arrows indicate the embedded temperature sensor in the copper blocks.

In the unwrapped phase difference (i.e. phase map), the phase ψ for all pixels is available and the horizontal average yields the phase map as a function of height, $\psi(y)$. The phase map just after adjusting the mirror is ψ_0 (**Figure 2c**) and after the concentration field has fully developed is ψ_{end} (**d**). Furthermore, in a convectionless environment with a linear temperature gradient across the cell height, we consider that there is only mass flux in the vertical direction, meaning that the horizontal mass flux is neglected within the field of view that captures the top and bottom boundaries. Note that ψ is directly related to the vertical concentration profile, which satisfies conservation of mass, i.e. $\int_0^H \psi_0 = \int_0^H \psi_{end}$. The mean vertical values of ψ_0 and ψ_{end} are then subtracted from

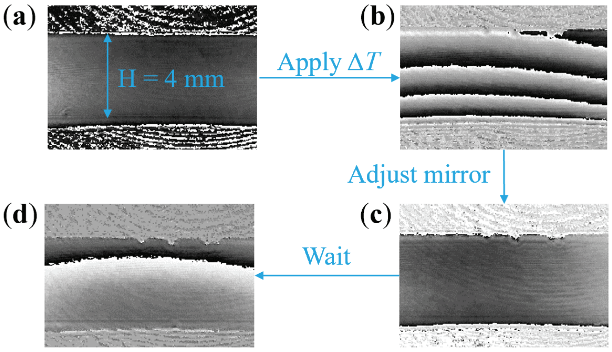

Figure 1: Experimental procedures. (**a**) First, T_{top} and T_{btm} are set to T_{mean} thus homogenous temperature and concentration is achieved in the solution. The test beam is adjusted to set a no-fringe condition. (**b**) T_{top} and T_{btm} are set to $T_{mean}+\Delta T$ and $T_{mean}-\Delta T$, respectively. Fringes start to appear quickly within the Soret cell due to temperature gradients. The development is less than 1 min. (**c**) Once the temperature field has reached steady state, the test beam is quickly adjusted to remove all fringes. (**d**) After 30 min when the cell height H is 4 mm, the thermodiffusive concentration field becomes fully develop. Fringes/gradients in the unwrapped phase-shifted data are the result of the concentration field.

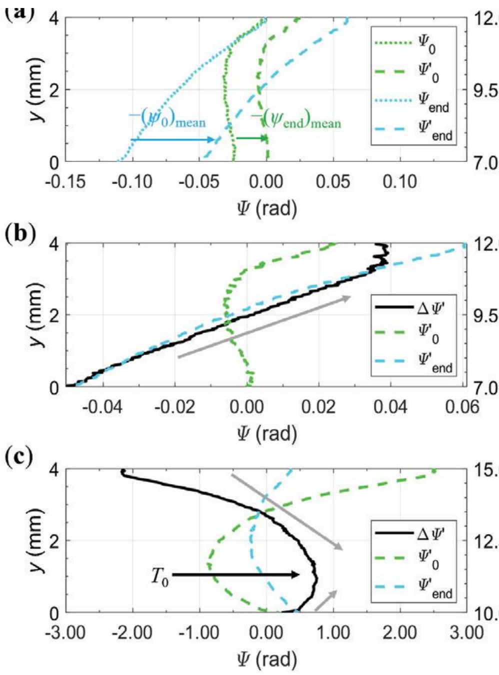

:e 3: ψ as a function of y and T for NaCl concentration 0.5 M. he mean values of ψ_0 and ψ_{end} are subtracted from the ψ_0 and espectively to obtain ψ'_0 and ψ'_{end}. (**b**) $\Delta\psi' = \psi'_{end} - \psi'_0$. Grey 's indicate the direction of NaCl migration and $\partial\Delta\psi'/\partial h$ is proportional to the magnitude of mass flux. Between 12 °C (T_{top}) and 7 °C (T_{btm}) NaCl shows thermophobic behaviour. (**c**) When T_{top} = 15 °C and T_{btm} = 10 °

thermophilic behaviour. Direct inspection yields $T_0 \approx 11.3$ °C.

$\psi_0(y)$ and $\psi_{end}(y)$, respectively, to reflect mass conservation (ψ'). This process is depicted in **Figure 3a**. Since the contrast factor can be assumed to be constant in a small concentration range (expected in a thermodiffusion experiment with $S_T \approx 0$), the obtained $\Delta\psi'$ is a direct measurement of the local concentration change. In addition, with the assumption of linear temperature gradient across the channel height, the vertical coordinate y can be transformed into temperature T by interpolation using the top T_{top} and bottom T_{btm} temperatures. In the experiment of **Figure 3b**, based on literature values (Caldwell, 1973; Römer *et al.*, 2013), we first estimated that T_0 for 0.5 M NaCl aqueous solution should be between 7 and 12 °C and used these temperature as T_{btm} and T_{top}, respectively. However, NaCl demonstrated thermophilic behaviour when $T < 11$ °C as $\partial\Delta\psi'/\partial h$ is positive (**b**). Between 11 and 12 °C, $\partial\Delta\psi'/\partial h$ is close to zero, suggesting near-zero S_T, i.e. T_0 is around this location. In (**c**), the boundary temperatures are re-set to confirm the previous observation. A maximum $\Delta\psi'$ is obtained at the location corresponding to $T \approx 11.3$ °C. Above 11.3 °C, NaCl is thermophobic ($\partial\Delta\psi'/\partial h > 0$), and below 11.3 °C NaCl is thermophilic ($\partial\Delta\psi'/\partial h < 0$). With known contrast factors, $C(y)$ can be obtained and based on a steady-state condition, the local S_T (i.e. at a given temperature and location) can be calculated as $-\frac{\partial C}{C(1-C)\partial T}$. Thus, the dependence of S_T on T can be precisely measured.

Results

Following the procedures outlined in **Figure 2** and data processing steps in **Figure 3**, T_0 as a function of concentration was measured for both aqueous NaCl and KCl from multiple experiments, with the results shown in **Figure 4**. We can

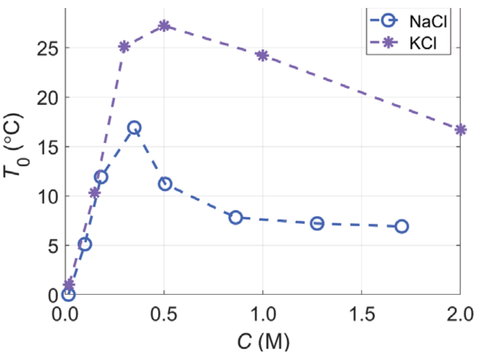

aqueous solutions.

obs

alw

sharply with C until a certain value, which is around 0.35 M for NaCl and 0.5 M for KCl. Beyond these values, T_0 starts dropping slowly with increasing concentration. Experimental data on T_0 for the investigated solutions is only available for NaCl/H_2O at 0.5 M in literature (Caldwell, 1973) for which a good agreement was obtained. $S_T(T)$ was also extracted from concentration profile obtained using PSI.

nclusions

ough PSI and post-data processing, a steady concentration file in a Soret cell can be extracted with high accuracy. asured T_0 for both investigated binary solutions seems to follow an interesting common trend with increasing C: beginning with a sharp increase, reaching a maximum T_0 and then followed by a gradual decrease. Further work on quantifying errors in this measurement is required.

Acknowledgements

We thank the Foundation for Australia-Japan Studies and the Australian Department of Foreign Affairs and Trade for their financial support, and the valuable support from the Australian National University through an international PhD student scholarship.

References

D. R. Caldwell, 'Thermal and Fickian diffusion of sodium chloride in a solution of oceanic concentration', *Deep-Sea Research and Oceanographic Abstracts*, 20, pp. 1029–1039, (1973)

S. Duhr, and D. Braun, 'Why molecules move along a temperature gradient', *Proceedings of the National Academy of Sciences of the United States of America*, 103, pp. 19678–19682, (2006)

P. Kolodner, H. Williams, and C. Moe, 'Optical measurement of the Soret coefficient of ethanol/water solutions', *The Journal of Chemical Physics*, 88, pp. 6512–6524, (1988)

R. De Miguel, and J. M. Rubí, 'Negative Thermophoretic Force in the Strong Coupling Regime', *Physical Review Letters*, 123, p. 200602, (2019)

S. A. Putnam, D. G. Cahill, and G. C. L. Wong, 'Temperature dependence of thermodiffusion in aqueous suspensions of charged nanoparticles', *Langmuir*, 23, pp. 9221–9228, (2007)

Y. Qian *et al.* 'Dynamic Pattern Formation of Microparticles in a Uniform Flow by an On-Chip Thermophoretic Separation Device', *Physical Review Applied*, 9, p. 24035, (2018)

F. Römer *et al.* 'Alkali halide solutions under thermal gradients: Soret coefficients and heat transfer mechanisms', *Journal of Physical Chemistry B*, 117, pp. 8209–8222, (2013)

J. F. Torres *et al.* 'Measurement of Soret and Fickian diffusion coefficients by orthogonal phase-shifting interferometry and its application to protein aqueous solutions', *Journal of Chemical Physics*, 139, (2013)

J. F. Torres *et al.* 'Optical Method for Simultaneous High-Resolution Measurement of Heat and Fluid Flow: The Case of Rayleigh-Bénard Convection', *Physical Review Applied*, 14, pp. 1–13, (2020)

Modelling the thermodiffusion of lone cations and anions in dilute aqueous solutions

Kasimir P. Gregory*, Lincoln D. Hall, Rosemary Zielinski, Alice J. Hutchinson, Juan F. Torres, Ben Corry†

Australian National University, Canberra, Australia, *kasimir.gregory@anu.edu.au, †ben.corry@anu.edu.au

Introduction

The thermodiffusion of ions in liquids is difficult to predict due to an an incomplete understanding of its microscopic origins. It is widely hypothesised that thermodiffusion is driven by changes in solvation and ionic shielding entropy, creating an entropic force (Duhr & Braun, 2006; Niether et al., 2017). Duhr and Braun (2006) suggest that large negative ionic shielding entropies account for thermophobicity at high temperatures, whilst large positive hydration entropies explain thermophilicity at low temperatures. In the case of aqueous solutions, structural changes in the hydrogen bond network are also thought to contribute to the direction of thermodiffusion (Niether et al., 2017). It is argued that structure formation at low temperatures minimises the free energy, whilst structure breaking due to larger translational entropic gains minimises the free energy at high temperatures (Wang, Kriegs, & Wiegand, 2012). This free energy change determines the probability of particle diffusion under equilibrium thermodynamics.

Alternatively, some authors attribute the mechanism of thermodiffusion of molecules in ionic solution to the creation of local and global electric fields, reducing this to an electrophoretic effect (A. Putnam & G. Cahill, 2005; Reichl, Herzog, Götz, & Braun, 2014; Würger, 2008). In particular, Reichl et al. (2014) propose extra contributions to thermodiffusion arising from the Seebeck effect and the capacitor model of Debye screening. Crucially, their model suggests thermophoresis is a property of bulk solutions, rather than being singularly dependent on molecule-solvent interactions.

Whilst the Soret effect has been extensively studied in mixtures and alkali halide solutions, the literature conspicuously lacks thermodiffusion experiments involving single ionic particles. Such experiments could resolve whether thermophoresis only occurs in bulk solutions. Further, single-ion studies would remove ionic shielding effects, allowing direct studies of the solvation entropy and free energy on inversion alone.

Molecular dynamics (MD) simulations can accurately model the atom scale interactions essential to thermophoresis and have been shown to reproduce thermophoretic behavior (Artola & Rousseau, 2013; Belkin, Chao, Giannetti, & Aksimentiev, 2014; Di Lecce, Albrecht, & Bresme, 2017; Hutchinson, Torres, & Corry, 2022). Such simulations also provide a viable avenue to study single-particle thermophoresis, although this is yet to be pursued.

This study uses alchemical free energy perturbation (FEP) methods to isolate the ion hydration free energy in silico, for individual cations and anions. This will indicate if thermodiffusive behavior is solely a property of bulk solution. Isolation of a single ion in a water box removes ion-ion interactions, thereby allowing the study of thermodiffusion caused purely by solute-solvent effects. This investigation tests whether the entropic force mechanism of thermodiffusion is validated for single ionic species over a range of temperatures. Significant emphasis is also placed on determining whether a thermophilic to thermophobic inversion point exists for single particles, a transition observed in bulk alkali halide solution (Di Lecce et al., 2017; Hutchinson et al., 2022). Investigation of this effect for a variety of cations and anions also allows an investigation into the fundamental ion properties governing these effects.

Section 1 – Free Energy Perturbation

Simulations investigating the free energy of ion hydration with respect to temperature and ion identity have been performed. The hydration free energy at each respective temperature was calculated via alchemical FEP methods. The TIP3P-FB forcefield has been used here, as it has been shown to be reliable for modelling thermodiffusive behaviour (Hutchinson et al., 2022). Figure 1 shows a comparison of the hydration free energy of each ion at each temperature is compared to that ion's hydration free energy at 270K. In all case, the ions exhibit thermophobic character, having more favourable hydration free energies at lower temperatures in this infinitely dilute reigime. By comparison, 0.5M NaCl has an inversion temperature at 10°C, becoming thermophilic below this temperature (Römer, Wang, Wiegand, & Bresme, 2013), something that is reproduced using MD simulations with the same parameters (Hutchinson et al., 2022). Furthermore, this model system shows that thermodiffusive force, given by the slope of the hydration free energy, is ion specific (Figure 1), indicating thermodiffusion might be utilised in the separation of different ion species.

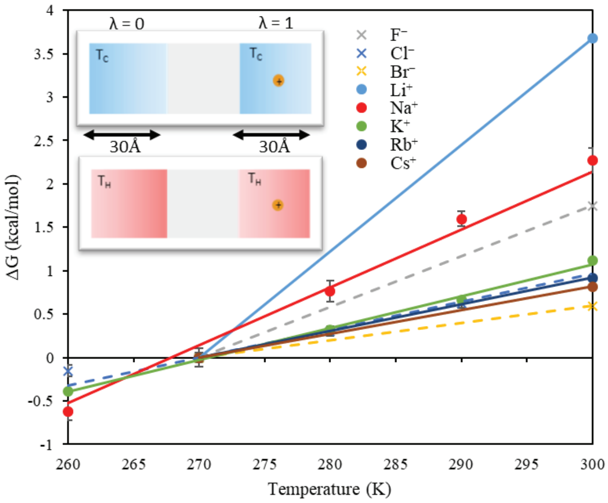

Figure 1: The temperature dependence of the hydration free energy of ions.

Section 2 – Ion parameters

The ion-specific nature of this temperature dependence effect in the hydration free energy has strong correlations with the ion's radial charge density (Gregory, Wanless, Webber, Craig, & Page, 2021) for the monatomic ions presented here (Figure 2). This suggests that the thermophobic character observed might be predicted by knowing the properties of the solute involved, and that the charge density is fundamentally important, at least in the case of monatomic ions.

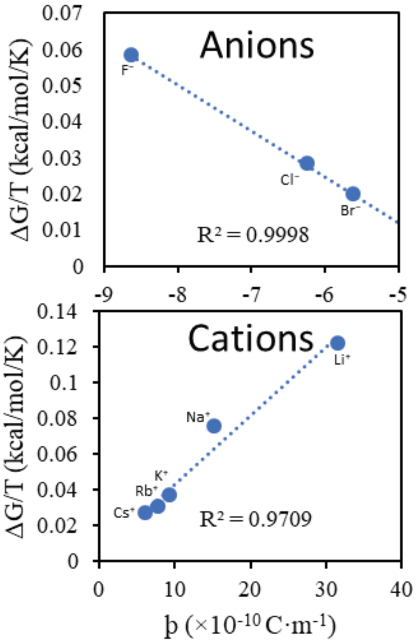

Figure 2: The temperature dependence of the free energy of ion solvation correlates with the ion's radial charge density, þ.

Conclusions

Lone ions at infinite dilution (achievable via simulation but difficult to achieve in experiments) appear to exhibit thermophobic character at all temperatures investigated here. This contrasts to concentrated electrolytes in bulk solution that exhibit a temperature inversion, having both thermo-phobic and -philic character. Furthermore, the nature of the thermophobicity appears to be dependent on the identity of the ion (i.e., ion-specific), correlating with the ion's radial charge density. By using simulations, we have been able to isolate some of the key factors governing thermophobicity of ions in water, providing a framework for predicting the thermodiffusion of aqueous ions in dilute aqueous environments.

Acknowledgements

The authors acknowledge funding from the Foundation for Australia-Japan Studies and the Australian Department of Foreign Affairs and Trade. This research was undertaken with the assistance of resources and services from the National Computational Infrastructure (NCI), which is supported by the Australian Government. The authors declare no competing interests.

References

A. Putnam, S., & G. Cahill, D. (2005). Transport of Nanoscale Latex Spheres in a Temperature Gradient. *Langmuir*, *21*, 5317–5323.

Artola, P.-A., & Rousseau, B. (2013). Thermal diffusion in simple liquid mixtures: what have we learnt from molecular dynamics simulations? *Molecular Physics*, *111*, 3394–3403.

Belkin, M., Chao, S.-H., Giannetti, G., & Aksimentiev, A. (2014). Modeling thermophoretic effects in solid-state nanopores. *Journal of Computational Electronics*, *13*, 826–838.

Di Lecce, S., Albrecht, T., & Bresme, F. (2017). The role of ion–water interactions in determining the Soret coefficient of LiCl aqueous solutions. *Physical Chemistry Chemical Physics*, *19*, 9575–9583.

Duhr, S., & Braun, D. (2006). Why molecules move along a temperature gradient. *Proceedings of the National Academy of Sciences*, *103*, 19678–19682.

Gregory, K. P., Wanless, E. J., Webber, G. B., Craig, V. S. J., & Page, A. J. (2021). The electrostatic origins of specific ion effects: quantifying the Hofmeister series for anions. *Chemical Science*, *12*, 15007–15015.

Hutchinson, A. J., Torres, J. F., & Corry, B. (2022). Modeling thermodiffusion in aqueous sodium chloride solutions—Which water model is best? *The Journal of Chemical Physics*, *156*, 164503.

Niether, D., Kawaguchi, T., Hovancová, J., Eguchi, K., K. G. Dhont, J., Kita, R., & Wiegand, S. (2017). Role of Hydrogen Bonding of Cyclodextrin–Drug Complexes Probed by Thermodiffusion. *Langmuir*, *33*, 8483–8492.

Reichl, M., Herzog, M., Götz, A., & Braun, D. (2014). Why Charged Molecules Move Across a Temperature Gradient: The Role of Electric Fields. *Physical Review Letters*, *112*, 198101.

Römer, F., Wang, Z., Wiegand, S., & Bresme, F. (2013). Alkali Halide Solutions under Thermal Gradients: Soret Coefficients and Heat Transfer Mechanisms. *The Journal of Physical Chemistry B*, *117*, 8209–8222.

Wang, Z., Kriegs, H., & Wiegand, S. (2012). Thermal Diffusion of Nucleotides. *The Journal of Physical Chemistry B*, *116*, 7463–7469.

Würger, A. (2008). Transport in Charged Colloids Driven by Thermoelectricity. *Physical Review Letters*, *101*, 108302.

Generalised Energy-Conserving Dissipative Particle Dynamics with Mass Transfer: Coupling between Energy and Mass Exchange

G. Colella[1], A. D. Mackie[1], J. P. Larentzos[2], J. K. Brennan[2], M. Lísal[3,4], and J. Bonet Avalos[1]

[1]Department of Chemical Engineering, Universitat Rovira i Virgili, Tarragona, 43007 Spain, giuseppe.colella@urv.cat
[2]U.S. Army Combat Capabilities Development Command (DEVCOM) Army Research Laboratory, Aberdeen Proving Ground, MD, 21005 USA
[3]Research Group of Molecular and Mesoscopic Modelling, The Czech Academy of Sciences, Institute of Chemical Process Fundamentals, Prague, 165 01 Czech Republic
[4]Department of Physics, Faculty of Science, J. E. Purkyně University, Ústí n. Lab., 400 96 Czech Republic

Introduction

The coupling between heat and mass transport at the nanoscale is a generic problem found in several physicochemical scenarios, ranging from molecular motors to heterogeneous catalysis, among others, and includes relevant chemical engineering applications. The analysis of these scenarios may be challenging using molecular dynamics simulations, whose computational cost is prohibitive for systems with large characteristic time and length scales. Coarse-grain (CG) modelling represents a valid alternative for such cases where molecular simulations are computationally limiting.

GenDPDE and GenDPDE-M

Dissipative Particle Dynamics (DPD) was originally introduced as a CG Lagrangian method to describe isothermal fluid dynamics with thermal fluctuations (Hoogerbrugge et al. 1992). Heat transport was soon included through energy conservation in what is referred to as the energy-conserving DPD (DPDE) model (Bonet Avalos et al. 1997). In recent years, both methods have been increasingly used in different areas, ranging from biology to engineering applications.

The Generalised Energy-Conserving Dissipative Particle Dynamics method, GenDPDE, (Bonet Avalos et al. 2019) has been introduced as an extension of DPDE, based on the definition of a mesoscopic thermodynamic description at the particle level. Within this framework, the particles carry internal energy and have variable volumes, which permit the definition of a fluctuating, locally-defined temperature and pressure. Differences in particle temperatures induce heat fluxes between the particles, following Onsager's Linear Theory at the mesoscale. The particle pressure is directly related to the forces exerted between the particles, leading to temperature-dependent particle potentials that are relevant when capturing non-equilibrium phenomena present in chemically reacting systems (Lísal et al. 2022) and systems undergoing shock compression (Lee et al. 2023).

Recently, GenDPDE has been further extended to include particles of variable composition. The new method, GenDPDE-M, (Bonet Avalos et al. 2022; Lísal et al. 2022) can describe also interparticle material exchange by simulating diffusive fluxes between particles by virtue of differences in chemical potentials, thus allowing the method to deal with a greater variety of systems.

The algorithms of GenDPDE-M are expressed as Langevin equations for the relevant dynamic properties, which are, in this case, momentum, internal energy, and particle composition.

Coupling between energy and mass exchange

The original formulation of GenDPDE-M assumes that material exchange between mesoparticles is not coupled with energy exchange, which represents a limitation. In the present work, coupling between these two properties is introduced, taking into account that Detailed Balance not only fixes the amplitude of the random contributions, but also imposes Onsager's Reciprocal Relations at the mesoscopic level. Equilibrium simulations employing the *van der Waals Mixture* model for a two-component system for the particle internal thermodynamics are used to validate the internal consistency of the stochastic model (Figure 1). Furthermore, simulations at non-equilibrium conditions are conducted to demonstrate that the model is capable of reproducing and controlling the *Ludwig-Soret Effect*, which depends precisely on the coupling between energy and matter transported at the mesoscale (Figure 2).

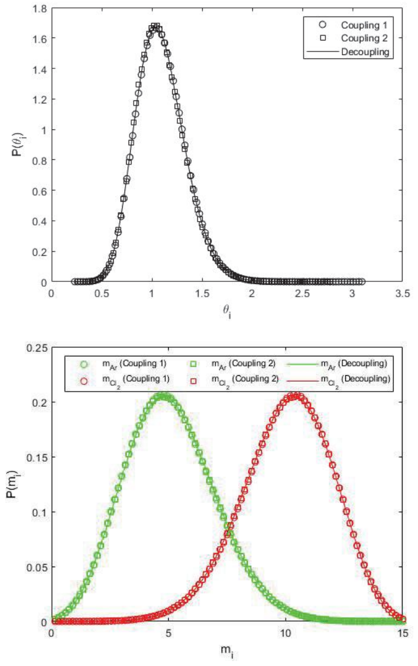

Figure 1: Equilibrium distributions of the particle temperature (top) and masses of the embedded species, Ar and Cl_2 (bottom) (T=1.081, ρ=0.3152). The dotted and squared curves refer to coupled systems characterised by different values of the mesoscopic Onsager coefficients, whereas the continuous line refers to a decoupled configuration. Superimposition of the distributions indicates consistency of the proposed model.

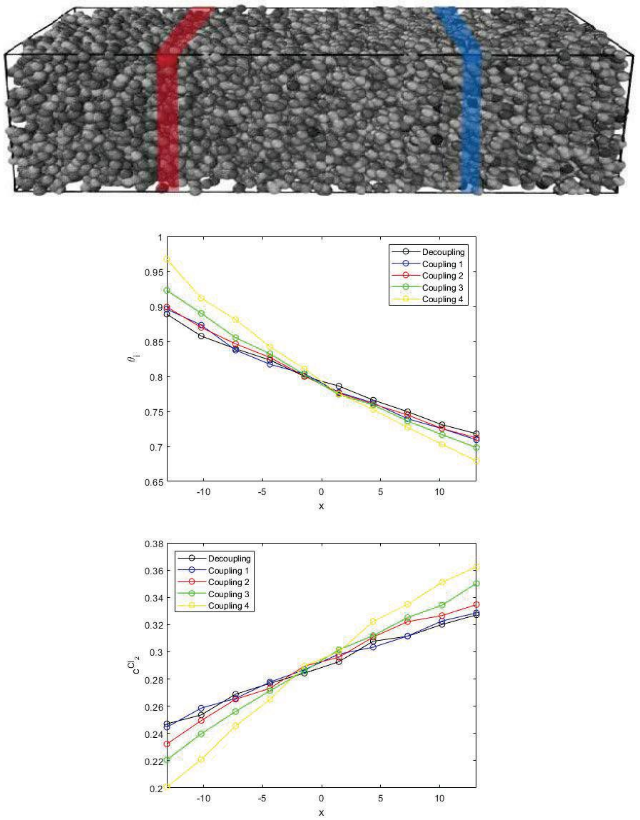

Figure 2: Simulation box (top) and average profiles for the particle temperature (middle) and number concentration of one of the embedded species, Cl_2 (bottom). The imposed temperature gradient along the x-axis between the hot (red) and cold (blue) slabs induces a concentration gradient in the system. The slope of these profiles is determined by the strength of the coupling between energy and mass transport, as shown by the differently coloured lines in the diagrams, which refer to configurations considering different values of the mesoscopic Onsager cross-coefficient.

Conclusions

In this work, we present the stochastic set of governing equations for the GenDPDE-M model when coupled energy and material exchanges occur, and show the consistency of the method together with several non-equilibrium results for the test system. With the addition of the coupling between energy and mass transfer, GenDPDE-M can be considered as the most general model for the simulation of complex fluids at the mesoscale when thermal fluctuations are relevant.

Acknowledgements

G. Colella acknowledges funding from the European Union's Horizon 2020 research and innovation programme under the Marie Skłodowska-Curie grant agreement No. 945413 and from the Universitat Rovira i Virgili (URV). G. Colella, A. D. Mackie and J. Bonet Avalos also acknowledge support from the grant PID2021-122187NB-C33, funded by MCIN/AEI/10.13039/501100011033 and "ERDF A way of making Europe". Research performed by J. Bonet Avalos and A. D. Mackie was sponsored by the Army Research Office, and was accomplished under Cooperative Agreement Number W911NF-20-2-0227. Research performed by M. Lísal was also sponsored by the Army Research Office, and was accomplished under Cooperative Agreement Number W911NF-20-2-0203. J. K. Brennan and J. P. Larentzos acknowledge support in part for a grant of computer time from the DoD High Performance Computing Modernization Program at the Army, Navy, and Air Force Supercomputing Resource Centers.

Disclaimer

This work reflects only the authors' view and the Agency is not responsible for any use that may be made of the information it contains. The views and conclusions contained in this document are those of the authors and should not be interpreted as representing the official policies, either expressed or implied, of the Army Research Office or the U.S. Government. The U.S. Government is authorized to reproduce and distribute reprints for Government purposes notwithstanding any copyright notation herein.

References

P. J. Hoogerbrugge and J. M. V. A. Koelman, "Simulating Microscopic Hydrodynamic Phenomena with Dissipative Particle Dynamics", *Europhys. Lett.*, 19, 155-160, (1992)

J. Bonet Avalos and A. D. Mackie, "Dissipative Particle Dynamics with Energy Conservation", *Europhys. Lett.*, 40, 141-146, (1997)

J. Bonet Avalos, M. Lísal, J. P. Larentzos, A. D. Mackie, and J. K. Brennan, "Generalised Dissipative Particle Dynamics with Energy Conservation: Density- and Temperature-Dependent Potentials", *Phys. Chem. Chem. Phys.*, 21, 24891–24911, (2019)

M. Lísal, J. P. Larentzos, J. Bonet Avalos, A. D. Mackie, and J. K. Brennan, "Generalized Energy-Conserving Dissipative Particle Dynamics with Reactions", *J. Chem. Theory Comput.*, 18, 2503-2512, (2022)

B. H. Lee, M. N. Sakano, J. P. Larentzos, J. K. Brennan, and A. Strachan, "A Coarse-Grain Reactive Model of RDX: Molecular Resolution at the μm Scale", *J. Chem. Phys.*, 158, 024702, (2023)

J. Bonet Avalos, M. Lísal, J. P. Larentzos, A. D. Mackie, and J. K. Brennan, "Generalized Energy-Conserving Dissipative Particle Dynamics with Mass Transfer. Part 1: Theoretical Foundation and Algorithm", *J. Chem. Theory Comput.*, 18, 7639-7652, (2022)

M. Lísal, J. Bonet Avalos, J. P. Larentzos, A. D. Mackie, and J. K. Brennan, "Generalized Energy-Conserving Dissipative Particle Dynamics with Mass Transfer. Part 2: Applications and Demonstrations", *J. Chem. Theory Comput.*, 18, 7653-7670, (2022)

Non-monotonic dependence of the Soret coefficient in fluid mixtures: insights from non-equilibrium molecular dynamics simulations

F. Bresme[1], Oliver Gittus[1], Silvia di Lecce[1]

[1]Department of Chemistry, Molecular Sciences Research Hub, Imperial College, London, United Kingdom, email: f.bresme@imperial.ac.uk

Introduction

The Soret coefficient of electrolyte solutions features a non-monotonic dependence on the salt concentration. Early studies of alkali halides reported a minimum below 1 M LiCl concentration and 0 oC [J. Colombani, 1999]. The existence of minima has remained a matter of discussion for several years. More recently, non-equilibrium simulation studies reported minima in LiCl [di Lecce et al. 2017a, di Lecce et al 2017v], verifying previous experiments. Moreover, these simulations established correlations between the heat transport and the observation of minima and the possible impact of these minima on thermoelectric effects.

Very recently, a new set of experimental studies of iodide salts, amongst other electrolytes, provided convincing evidence for the minimum at a specific concentration, 1 M. A phenomenological explanation was proposed to rationalize these results [Mohanakumar et al., 2022].

The studies discussed above have focused so far on aqueous systems. However, non-monotonic dependencies might be expected in non-aqueous systems, and some experimental evidence supports this idea. Interestingly, minima in the Soret coefficient have recently been reported using non-equilibrium molecular dynamics simulations in combination with simple binary liquid mixtures modelled with the Lennard-Jones potential. That work shows convincing evidence for a minimum at near 50:50 composition. Furthermore, a correlation was proposed between the observation of the minimum and the non-ideality of the liquid mixture.

This presentation will provide an overview of current studies of the non-monotonic dependence of the Soret coefficient with the composition of liquid mixtures and solutions and discuss possible microscopic mechanisms responsible for this observation.

Acknowledgements
We thank the Leverhulme Tust for Grant No. RPG-2018-384, and EPSRC fro grant EP/N509486/1. We acknowledge the ICL RCS High Performance Computing facility and the UK Materials and Molecular Modelling Hub for computational resources, partially funded by the EPSRC (Grant No. EP/P020194/1 and EP/T022213/1).

References

J. Colombani, J. Bert, J. Dupuy-Philon, Thermal diffusion in (LiCl, RH2O), *J. Chem. Phys.,* 110, 8622, (1999).

S. di Lecce, T. Albrecht, F. Bresme, A computational approach to calculate the heat of transport of aqueous solutions, *Sci. Rep.,* 7, 44833, (2017a).

S. di Lecce, T. Albrecht, F. Bresme, The role of ion-water interactions in determining the Soret coefficient of LiCl aqueous solutions, *Phys. Chem. Chem. Phys.,* 19, 9575, (2017b).

S. Mohakumar, H. Kriegs, W.J. Briels and S. Wiegand, Overlapping hydration shells in salt solutions causing non-monotonic Soret coefficients with varying concentration, *Phys. Chem. Chem. Phys.,* 24, 27380, (2022) .

Mass transport phenomena of hydrocarbon ternary system MN|Tol|*n*C$_{10}$

A. Errarte[1], E. Lapeira[1], M. Larrañaga[1],V. Shevtsova[1,2], M. M. Bou-Ali[1]

[1]Fluid Mechanics Group, Mondragon University, Mondragon, Spain, aerrarte@mondragon.edu
[2]Ikerbasque, Basque Foundation for Science, Bilbao, Spain

Introduction

The DCMIX project is a milestone in the research of thermodiffusion phenomenon in multicomponent mixtures, and the key to develop an on-ground nucleus for diffusion and thermodiffusion research. Nevertheless, the lack of knowledge of the phenomenon in different types of mixtures raises the need for further analysis of the transport properties of binary mixtures coupled to ternary systems. The former are key to understand the fundamental mechanisms governing mass transport phenomena in multicomponent liquid mixtures, as the initial link to study several properties such as the density, viscosity, the shape and size of molecules etc., or the development and validation of both theoretical and numerical models.

In this context, this work presents isothermal and non-isothermal transport properties as molecular diffusion, thermodiffusion and Soret in a hydrocarbons system of unequal molecular shape are analysed; the polycyclic aromatic hydrocarbon methylnaphthalene (MN), the monocyclic aromatic hydrocarbon toluene (Tol) and a chain shape alkane *n*-decane (*n*C$_{10}$). Experiments were conducted in 15 binary and 10 ternary mixtures. Thus, an integral and transversal study of the system was carried out, characterising first and second order thermophysical properties from binary to ternary mixtures, covering the whole pool of concentration. In short, thermodiffusion, molecular diffusion and Soret coefficients of twenty-five binary and ternary mixtures of MN|Tol|*n*C$_{10}$ system at 25 ºC are analysed together with all necessary thermophysical properties.

Analysed systems

Constituents of the system are arranged by the hydrodynamic principle on the descending order of density. Hereinafter, MN (c_1), Tol (c_2) and *n*C$_{10}$ (c_3). For each pair of components, 0.20, 0.40, 0.50, 0.60, 0.80 in mass fractions were analysed.

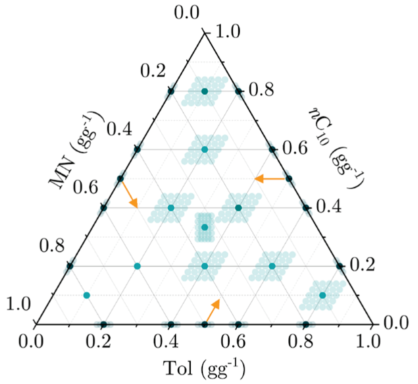

Figure 1: Ternary diagram of MN|Tol|*n*C$_{10}$ system. Light and dark green state points indicate the 10 ternary and 15 binary mixtures under study, while the blurred light blue refer to additional measurement points for the determination of thermophysical properties. Arrows determine the components direction within the triangle.

For the ternary mixtures, in turn, we focused on the following concentrations: 0.80|**0.10**|0.10, 0.60|**0.20**|0.20, 0.40|**0.40**|0.20, 0.40|**0.20**|0.40, 0.33|**0.33**|0.33, 0.20|**0.60**|0.20, 0.20|**0.40**|0.40, 0.20|**0.20**|0.60, 0.10|**0.10**|0.80, 0.10|**0.80**|0.10.

Experimental setups

The thermophysical properties measured were the following: density, thermal and mass expansion coefficients, dynamic viscosity, thermal conductivity and thermal diffusivity. The former three were measured using the Anton Paar DMA 5000 M density meter, changing either sample concentration or mean working temperature. On the other hand, the AMVn micro viscometer from Anton Paar was used to study the viscosity of mixtures, and the Thermtest THW-L1 instrument to measure thermal conductivity and thermal diffusivity, based on the transient hot-wire technique. The data on refractive index and derived solutal contrast factors were obtained by the Anton Paar Abbemat Multi-Wavelength refractometer. The instrument is operating at seven different wavelengths of visible light, λ = 435.8-656.3 nm.

The steady-state concentration separation in a thermogravitational column (TGC), together with aforementioned thermophysical properties, permits straightforward determination of the thermodiffusion coefficients. In this work, the extraction column and the thermogravitational micro-column were used. In the first one, samples are extracted from intakes at different column heights and the concentration is determined by density and/or refractive index measurements. In the second one, optical digital interferometry is used to track the constituents' separation during the entire experiment. This method, allows determining the relaxation time of the mixture at the same time, and thus, the molecular diffusion coefficient in the case of binary mixtures. Molecular diffusion coefficients of the three symmetric binary-subsystems and ternary systems was determined by the Sliding Symmetric Tubes (SST) technique. Further information about the TGC and SST techniques can be found elsewhere (Larrañaga et al. 2015, Šeta et al. 2022).

The Soret coefficients were determined by the indirect method, given by the following expressions for both binary and ternary mixtures,

$$S_T = D_T / D, \tag{1}$$

$$S'_{T,i} = \frac{D'_{T,i} D_{jj} - D'_{T,j} D_{ij}}{D_{ii} D_{jj} - D_{ij} D_{ji}}. \tag{2}$$

The analysis of a binary mixture in the TGC makes it possible to calculate the Soret coefficient by, combining the separation in the transient and steady state regimes. In the case of ternary mixtures, experiments in the SST were combined with the coefficients measured in the extraction column.

Results

The thermodiffusion experiments in binary subsystems reveal positive thermodiffusion coefficient for all mixtures. In the case of the ternary mixture, MN moves towards the cold wall and is enriched in the bottom of the column. On the contrary, $n\mathrm{C}_{10}$ moves towards the hot wall and concentrates at the top. The thermodiffusion coefficient of the toluene, intermediate component, varies depending on the concentration analysed. Figure 2 shows the variation of concentration 0.20|**0.20**|0.60 in mass fraction ternary mixture.

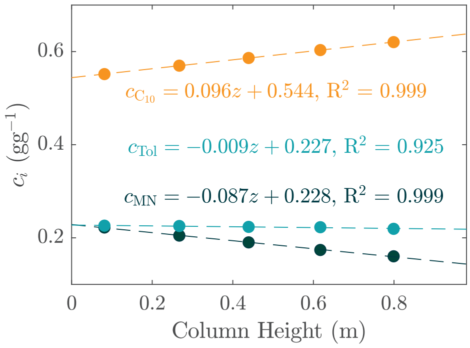

Figure 2: Variation of constituents' concentration along the height of the TGC for MN|Tol|$n\mathrm{C}_{10}$ mixture at 0.20|**0.20**|0.60 mass fraction at 25 °C.

The transient separation and steady-state analysis (Figure 3) reveals the relaxation time and concentration variation of the mixtures, and therefore, the thermodiffusion, molecular diffusion and Soret coefficients of binary mixtures.

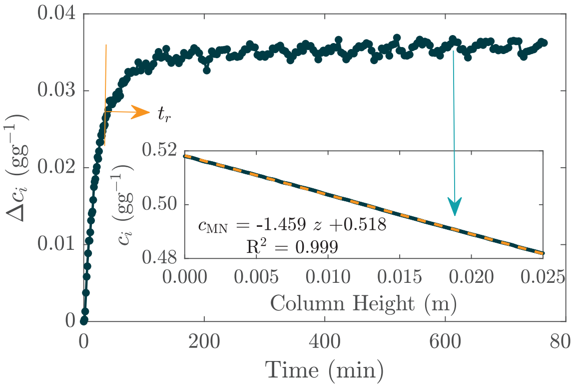

Figure 3: Result of a thermodiffusion experiment of MN|Tol 0.50 gg^{-1} in the thermogravitational microcolumn. Relaxation time and separation in the steady state at 25 °C. The inset shows the change in the MN concentration with TGC height.

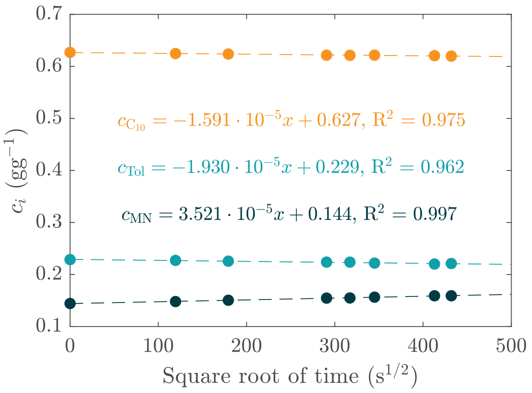

Figure 4: Concentration variation in the SST experiment for MN|Tol|$n\mathrm{C}_{10}$ mixture at 0.20|**0.20**|0.60 mass fraction at 25 °C.

In the case of the ternary mixtures, the concentration variation of the two independent components under two different initial conditions allows the determination of the four coefficients that make up the diffusion matrix. Figure 4 shows an example of an SST experiment.

Our experiments revealed that the Soret coefficients of MN are positive for all the analysed ternary mixtures while the ones corresponding to $n\mathrm{C}_{10}$, are all negative. The Soret coefficients of toluene can be either positive or negative depending on the mixture.

Conclusions

The objective of this research is to determine the transport properties along the three binary borders, which allow generating knowledge about the ternary mixtures. In order to validate these predictions, the properties have to be measured experimentally. In the case of the thermodiffusion coefficient, Blanco et al. 2010 developed a combination rule, which predicted the thermodiffusion coefficients of ternary mixtures from binaries:

$$D'_{T,i}\frac{\nu_m}{\alpha_m} = D_T^{ij} c_i c_j \frac{\nu_{ij}}{\alpha_{ij}} + D_T^{ik} c_i c_k \frac{\nu_{ik}}{\alpha_{ik}},$$

where $D'_{T,i}$ is the thermodiffusion coefficient of component i of a ternary mixture, ν_m is the corresponding dynamic viscosity and α_m is the thermal expansion coefficient. D_T^{ij} and D_T^{ik} are the thermodiffusion coefficients, ν_{ij} and ν_{ik} are the kinematic viscosities and α_{ij} and α_{ik} the thermal expansion of the corresponding binary mixtures. c_i, c_j and c_k correspond to the mass fraction of each constituent in the ternary mixture. Thus, considering the number of mixtures measured around the system, the combination rule was tested and validated with a mean deviation of 15 % in this system.

In the case of the Soret coefficients, following the work presented by Mialdun et al. 2021 the Soret vector model was used to verify the Soret coefficients of the ternary mixture. It was concluded that MN|Tol|$n\mathrm{C}_{10}$ ternary system can be considered a nearly ideal mixture as THN|IBB|$n\mathrm{C}_{12}$.

Acknowledgements

The team from Mondragon Unibersity thanks the support by KK-2021/00082 (micro4IloT), PRE_2022_2_0229 and EP_2022_1_0026, IT1505-22 from the Basque government Research Group Program, the Gipuzkoa Provincial Council under the Hoztikor project 2022-CIEN-000052-01 and PID2020-115086GB-C33 financed by MCIN/FEDER of the Spanish Government.

References

M. Larrañaga, M. M. Bou-Ali, D. et al., Contribution to the benchmark for ternary mixtures: Determination of Soret coefficients by the thermogravitational and the sliding symmetric tubes techniques, *Eur. Phys. J. E*, 38, 28 (2015).

B. Šeta, J. Gavalda et al., Determining diffusion, thermodiffusion and Soret coefficients by the thermogravitational technique in binary mixtures with optical digital interferometry analysis, *Int. J. Heat Mass Transf*, 147, 118935 (2020).

P. Blanco, M. M. Bou-Ali, et al. Thermodiffusion coefficients of binary and ternary hydrocarbon mixtures. *J Chem Phys*, 132, (2010).

A. Mialdun, et al., Soret vector for description of multicomponent mixtures, Sci. Rep., 11, 17735, (2021).

Measurement of the Soret coefficient in liquid Al–Ag alloys using X-ray radiography

A. T. Krüger, E. Sondermann, A. Meyer

German Aerospace Centre (DLR), Cologne, Germany (Asbjorn.krueger@dlr.de)

Introduction

Thermodiffusion, also called the Soret effect, is observed to influence all kinds of matter, from gases, liquids, to solids. In metals, the effect has been employed for nuclear enrichment and crystal growth, it is relevant for solder and manufacturing of integrated circuits, and has recently been shown to be of use in creating metallic nanowires.

There exist several theoretical models attempting to predict binary thermodiffusion, but there is still no comprehensive model able to predict the Soret coefficient for a wider range of systems, as recently shown by (Hoang et al. 2022). The authors of such models often voice the need for more experimental data, which is very scarce in the case of metallic melts. The same holds for modeling thermodiffusion using computational simulations, where the dynamics of thermodiffusion in the simulations (dependence of thermodiffusion on mixture size ratio, dependence of Soret coefficient on concentration, etc.) should be compared with measurements.

Almost all previous publications on liquid alloys are on binary systems where the atomic mass ratio of the two components is around two or less. The only exceptions so far are measurements on carbon and trace amounts in a solvent.

The experimental data so far indicate that the Soret coefficient is generally dependent on the relative molecular weights of the species in the mixture. Measuring the thermodiffusion in liquid Al–Ag for different concentrations therefore provides a new insight into the dynamics of thermodiffusion in an atomic fluid with a high mass ratio (Srinivasan et al. 2013).

Here, we study thermodiffusion in the liquid alloy Al–Ag as a function of composition using a newly developed experimental setup.

Method

Using X-ray radiography (XRR), we have measured the thermodiffusion in liquid Al–Ag, with compositions ranging from $Al_{80}Ag_{20}$ to $Al_{50}Ag_{50}$. The samples are around 10 mm long and have a diameter of 1.3 mm in the liquid state.

The setup that is used supports four samples, of which two samples are reference samples to calibrate the relation between image brightness and sample concentration. The two reference samples are chosen at 5 percentage points higher and lower than the main samples. This also means that reference sample data for each X-ray image are available, which are beneficial in case of fluctuations in the X-ray source over the time of the experiment.

The samples were melted by heating to 1023 K. After homogenization for about two hours in an isothermal state, a temperature gradient of around 10 K/cm was established by switching off the heater at the bottom of the samples.

Results and discussion

Figure 1 shows the concentration difference for an $Al_{75}Ag_{25}$ sample over time with the hot end fixed at 1023 K. The figure, displaying the concentration difference of silver between the hot end and the cold end of the sample, shows that the silver concentration is reduced in the hot end, and increasing at the cold end, meaning that silver migrates to the cold side.

Using the concentration gradient data from the non-isothermal equilibrium phase (highlighted on the right in the aforementioned figure) together with the last data of the isothermal phase (highlighted on the left in the aforementioned figure), the Soret coefficient can be calculated directly using

$$S_\mathrm{T} = -\frac{\Delta c_\infty}{\Delta T c_0(1-c_0)}.$$

The Soret coefficient is determined to be $(0.9\pm0.3)\times10^{-3}$ K^{-1} (Krüger et al. 2023).

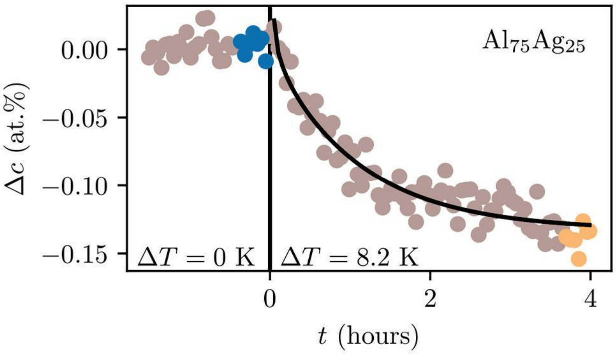

Figure 1: Concentration difference across a sample of $Al_{75}Ag_{25}$. The vertical line indicates when the temperature gradient was initiated. The exponential curve is the fit of the equation for the time-dependent concentration separation to the experimental data after the temperature gradient had stabilized. The colors indicate the basis for the averaged data used in calculation of the Soret coefficient.

Thanks to the time-resolved information from in situ XRR, the interdiffusion coefficient can simultaneously be measured (Sondermann et al. 2019). By looking at the total concentration difference Δc over time, its time-dependence can be fitted to the data in figure 1, where the equation is given by

$$\Delta \mathrm{c(t)} = \Delta \mathrm{c}_\infty \left(1 - \frac{8}{\pi^2}\sum_{n=0}^{\infty}\frac{e^{-(2n+1)^2 t/\theta}}{(2n+1)^2}\right)$$

with the characteristic time $\theta = \frac{L^2}{\pi^2 D}$ for a sample of length L and of a material with diffusion coefficient D. We then get a diffusion coefficient of $(3.8\pm1.5)\times10^{-9}$ m^2/s. This is in good agreement with previous measurements by (Engelhardt et al. 2016) on the diffusion coefficient for the Al–Ag system.

The similarity in the diffusion coefficients corroborates the measured Soret coefficient, as the observed process goes at the speed predicted by theory.

Using thermophysical values from the literature, we can calculate the predicted Soret coefficient by the current theoretical models (Eslamian et al. 2010, Shukla et al. 1998). The predicted Soret coefficients of the two models are presented in figure 2.

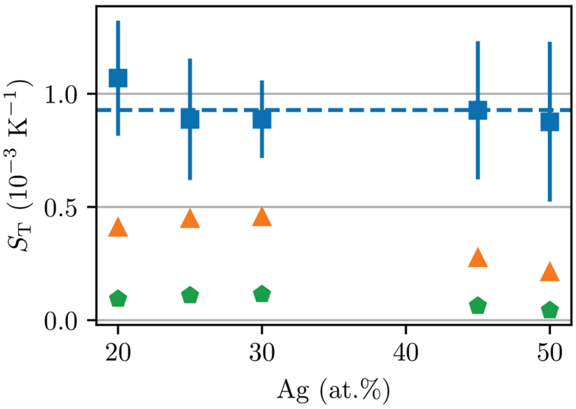

Figure 2: Soret coefficients accumulated from all experiments, measured at a mean temperature of 1018 K and with temperature differences of around 10 K. Error bars show one standard deviation for the Soret coefficient for each concentration. The dashed line shows the weighted mean of all our measurements. The predicted values by the models of (Eslamian et al. 2010) and (Shukla et al. 1998) are shown in orange triangles and green pentagons respectively.

Both models predicted the same sign for the Soret coefficient of liquid Al–Ag alloys as found in our experiments, i.e., correctly predicted the direction of thermodiffusion for the two components in the alloy. But the numerical values were off by at least a factor of two with respect to our measured values, and also the strong concentration dependence predicted by the models was not observed. This shows that there is still need for a theory to describe thermodiffusion even in binary atomic liquids.

Conclusions

Using X-ray radiography (XRR), the Soret and interdiffusion coefficients can be measured in binary liquid alloys. It also allows several samples to be analyzed simultaneously as well as several times in succession, with relative ease. We investiaged the liquid Al–Ag system with compositions ranging from $Al_{80}Ag_{20}$ to $Al_{50}Ag_{50}$. A Soret coefficient of $(0.9\pm0.3)\times10^{-3}$ K^{-1} was found over the entire measured composition range, with silver migration to the cold side, which is of the same order of magnitude as previous measurements on similar binary systems. Using experimental data from the literature, models to predict the Soret coefficient were tested. The closest model is off by a factor of two with respect to our measured values. The method of XRR for in situ measurements at different times also allows the measurement of the interdiffusion coefficient, which was found to be in accordance with previous interdiffusion measurements on the Al–Ag system. In the future, we want to analyse thermodiffusion in liquid Al–In, which has a miscibility gap, where the derivative of the chemical potential with respect to concentration (a crucial parameter in models for thermodiffusion) is sensitive to concentration/temperature changes. Ternary alloys will also be investigated.

References

H. Hoang, G. Galliero, Predicting thermodiffusion in simple binary fluid mixtures. *Eur. Phys. J. E*, 45, 42, (2022)

S. Srinivasan, M. Z. Saghir, *Thermodiffusion in Multicomponent Mixtures*, Springer, (2013)

A. T. Krüger, E. Sondermann, A. Meyer, Measurement of the Soret coefficient in liquid Al–Ag alloys using X-ray radiography, *Phys. Rev. B*, 107, 064301 (2023)

E. Sonderman, F. Kargl, A. Meyer, In situ measurement of thermodiffusion in liquid alloys, *Phys. Rev. Lett.*, 123, 255902, (2019)

M. Engelhardt, A. Meyer, G. G. Simeoni, F. Kargl, Self and chemical diffusion in liquid Al–Ag, *Defect Diffus. Forum*, 367, 157 (2016)

M. Eslamian, F. Sabzi, M. Z. Saghir, Modeling of thermodiffusion in liquid metal alloys, *Phys. Chem. Chem. Phys.*, 12, 13835, (2010)

K. Shukla, A. Firoozabadi, A new model of thermal diffusion coefficients in binary hydrocarbon mixtures, *Ind. Eng. Chem. Res.*, 37, 3331, (1998)

Thermodiffusion of CO_2 in Saline Solutions by Non-Equilibrium Molecular Dynamics Simulations

F. M. Coelho[1,2], L. F. M. Franco[1], A. Firoozabadi[2]

[1]University of Campinas, Campinas, Brazil, lmfranco@unicamp.br; [2]Reservoir Engineering Research Institute, Palo Alto, USA, af@rerinst.org

Introduction

The geothermal gradient within deep saline aquifers used for carbon sequestration may result in an uneven spatial distribution of CO_2 molecules. Nonetheless, the investigation of thermodiffusion of CO_2 in aqueous mixtures remains to be thoroughly pursued The first attempt to quantify the thermodiffusion in CO_2-H_2O mixture has been made by Windisch et al. (2012). The authors applied Raman spectroscopy to quantify the concentration gradient of CO_2 due to a temperature gradient within a temperature range between 288 and 318 K and at pressures to 10 MPa. They did not observe detectable Soret effect, within the uncertainty of the measurements. Guo et al. (2018) have also performed experiments using UV Raman spectroscopy in a temperature gradient established between 295 and 353 K and pressures of 20 and 30 MPa. The authors have examined a saturated mixture of CO_2, and the observed concentration gradient established was probably due to the temperature dependency on solubility rather than the thermodiffusion.

Thermodiffusion can also be investigated by molecular dynamics (MD) techniques (Galliero et al. 2008, Nieto-Draghi et al. 2005, Perronace et al. 2002). With Boundary-Drive Non-Equilibrium Molecular Dynamic (BDNEMD) simulations, heat flux or a temperature gradient is generated in the simulation box, and, by the system response, a concentration profile is established. The thermal diffusion factor $\alpha_{T,i}$ can be computed to quantify the phenomenon. For a binary system, $\alpha_{T,i}$ is defined as:

$$\alpha_{T,i} = -\Gamma \frac{T}{x_i(1-x_i)} \frac{dx_i}{dT} \tag{1}$$

where T is the absolute temperature, x_i is the composition in mole fraction of component i, and Γ is the thermodynamic factor that should be accounted for in non-ideal liquids ($\Gamma \neq 1$) because diffusion is driven by chemical potential gradient. For multicomponent mixtures, the thermal diffusion factor definition is not straightforward, and there is dependency on the transport diffusion coefficients.

In this work, we evaluate the thermodiffusion of CO_2 in saline solutions using non-equilibrium molecular dynamics simulations. First, the Soret effect for CO_2-H_2O mixture is computed. Then, salts are added to the system, and the thermodiffusion in the ternary mixture is investigated.

Methods

The eHeX method is the BNEMD method chosen (Wirnsberger et al. 2015). The heat flux is generated by scaling up and down the velocities of particles that are located, respectively, in the hot and cold predefined regions of the simulation box as illustrated by Fig. 1.

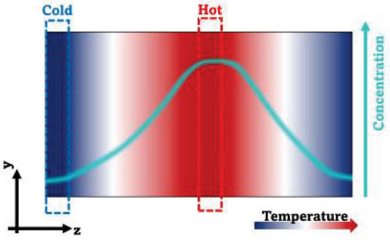

Figure 1: Representation of the simulation box with cold and hot regions.

Different combinations of force fields are selected to investigate the sensitivity of the results. Water molecules are represented by the SPC/E and TIP4P/2005 models, whereas CO_2 by EPM2 and TraPPE. The simulation box is set with 5000 molecules, and a density of ρ = 1000 kg.m^{-3}. The CO_2 composition in mole fraction is set at 0.02; a value below the solubility at the specified pressure and temperature. The mean temperature and the temperature difference between the cold and hot regions are 350 K, and 50 K, respectively. All simulations are performed in LAMMPS. First, an NVT equilibration is performed for 1 ns to keep the system close to the desired mean temperature, and then, the eHeX method is turned on for 80 ns. The thermodynamic factor is computed from equilibrium molecular dynamics simulations through the Kirkwood-Buff integrals using the method from Dawass et al. (2019). The saline effect on CO_2 thermodiffusion is investigated by adding NaCl in the mixture at a composition of 2 molal, and then evaluating the segregation of the components in the presence of the temperature gradient.

Results

Under the analyzed conditions, for the binary CO_2-H_2O mixture, CO_2 accumulates in the cold region ($\alpha_{T,CO2} > 0$), and the thermal diffusion factor is around 1 (Coelho et al. 2023). The same result is reproduced by all force field combinations; hence only the conventional SPC/E + EPM2 combination will be presented (Figure 2).

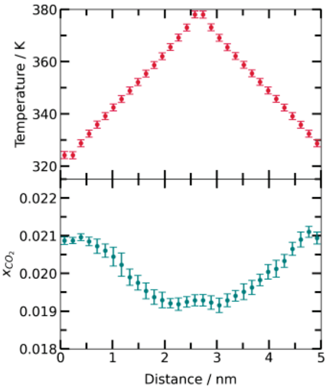

Figure 2: Temperature and CO_2 composition profile in the simulation box at T = 350 K, ρ = 1000 kg.m^{-3}, x_{CO2} = 0.02.

Water molecules interact through highly directional hydrogen bonds. The hydrogen bond network is disturbed by increasing the temperature. CO_2 molecules do not have a net dipole moment, but they interact through van der Waals and quadrupole-quadrupole interactions. For CO_2, the higher the temperature, the higher are these interactions. The cross-interactions between CO_2-H_2O molecules could be through tetrel bonds or hydrogen bonds. From the radial distribution functions, the tetrel bonds are more significant than the weak hydrogen bonds for this mixture and are decreased by temperature, whereas the hydrogen bonds are enhanced.

The $\alpha_{T,CO2}$ dependency on temperature is evaluated by performing simulations at various mean temperatures at the same pressure as the initial condition (400 bar). The thermal diffusion factor decreases by almost 50% by increasing the temperature from 300 to 350 K, and is almost negligible at 400 K, where there may be a sign change (Figure 3). The pressure effect is evaluated by equilibrating the mixture at 200 bar; however, the pressure influence on the Soret effect is not as pronounced as the temperature ($\alpha_{T,CO2}$ decreases by 28% by decreasing the pressure from 400 to 200 bar).

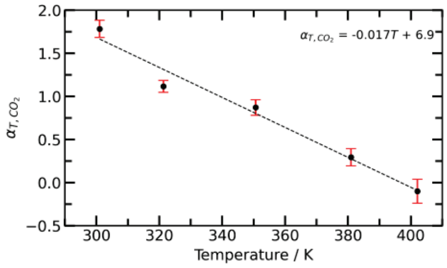

Figure 3: Thermal diffusion factor of CO_2-H_2O vs. temperature at P = 400 bar, and $x_{CO2} = 0.02$. The dashed line represents the linear interpolation.

Overall, the separation between CO_2 and water molecules due to a temperature gradient is enhanced by increasing the mixture density (lower temperature and higher pressure). CO_2 accumulates in the cold region where its interactions with other CO_2 molecules are reduced, whereas water accumulates in the hot region where it has reduced self-association. This indicates a CO_2 accumulation in the top region of the aquifers.

In brine mixtures with CO_2, NaCl salt accumulates in the cold region. The repulsive interactions between CO_2-NaCl leads to a less thermophobic behavior of CO_2. At 350 K, there is almost no detectable Soret effect, and at 400 K, CO_2 accumulates in the hot region.

Conclusions

The focus of our work is the investigation of the thermodiffusion of the CO_2-H_2O mixture at subsurface conditions. Under a temperature gradient, CO_2 accumulates in the cold region, where the hydrogen bond network is more established. The Soret effect for CO_2 in water is enhanced as density increases by decreasing the temperature or increasing the pressure. The temperature effect on the thermal diffusion factor is pronounced. The electrolytes have a pronounced influence on CO_2 distribution, changing the thermal diffusion factor sign at a lower temperature.

Acknowledgements

We thank São Paulo Research Foundation (FAPESP) for the project funding (grant #2018/02713-8, #2020/13300-6, and #2021/13068-9), and the “Centro Nacional de Processamento de Alto Desempenho em São Paulo” (CENAPAD-SP) for providing computational resources.

References

F. M. Coelho, L. F. M. Franco, A. Firoozabadi. Thermodiffusion of CO_2 in Water by Non-Equilibrium Molecular Dynamics Simulations, *J. Phys. Chem. B*, 2023 (*in press*)

N. Dawass, P. Kruger, S.K. Schnell, J.M. Simon, T. Vlugt. Kirkwood-Buff integrals from molecular simulation. *Fluid Phase Equilib.* 486, 21–36 (2019)

G. Galliero, S. Volz. Thermodiffusion in model nanofluids by molecular dynamics simulations. *J. Chem. Phys.* 128, 064505–8 (2008)

H. Guo, Q. Zhou, Z. Wang, Y. Huang. Soret effect on the diffusion of CO2 in aqueous solution under high-pressure. Int. *J. Heat Mass Transfer.* 117, 966–971 (2018).

C. Nieto-Draghi, J. B. Avalos, B. Rousseau. Computing the Soret coefficient in aqueous mixtures using boundary driven nonequilibrium molecular dynamics. *J. Chem. Phys.* 122, 114503–7 (2005)

A. Perronace, C. Leppla, F. Leroy, B. Rousseau, S. Wiegand. Soret and mass diffusion measurements and molecular dynamics simulations of n-pentane–n-decane mixtures. *J. Chem. Phys.* 116, 3718–3729 (2002)

C. Windisch, G. Maupin, B. McGrail. Ultraviolet (UV) Raman spectroscopy study of the Soret effect in high-pressure CO_2-water solutions. *Appl. Spectrosc*. 66, 731–739, (2012).

P. Wirnsberger, D. Frenkel, C. Dellago. An enhanced version of the heat exchange algorithm with excellent energy conservation properties.*J. Chem. Phys.* 143, 124104–8 (2015).

Separation stability in binary TEG-water mixtures observed by digital interferometry

C.I.A.V. Santos[1], M.M. Bou-Ali[2], A. Mialdun[3] and V. Shevtsova[2]

[1] CQC-IMS, Department of Chemistry, University of Coimbra, Coimbra, Portugal, ceciliasantos@qui.uc.pt,
[2]Mechanical and Manufacturing Department, Mondragon University, Loramendi 4, Mondragon 20500, Spain mbouali@mondragon.edu, valentina.chevtsova@ulb.be;
[3]MRC, CP165/62, Université libre de Bruxelles, 50, av. F.D. Roosevelt, Brussels 1050, Belgium, aliaksndr.mialdun@ulb.be;

Introduction

Introduction

Most mixtures in nature and industry are commonly multicomponent and subject to non-equilibrium conditions, thus the knowledge of the transport phenomena occurring in them is of great interest for many applications. When a liquid mixture is subject to a temperature gradient, its constituent species move, and a concentration gradient is generated. The complex interaction between heat and mass transfer processes can result in a variety of dynamical behaviors due to instability, being the coupling between temperature and concentration gradients, also known as thermodiffusion or the Ludwig-Soret effect (Soret, 1879), one of the mechanins that can drive convective instability. Soret effect is quantified by the Soret coefficient S_T, the ratio between the thermodiffusion coefficient D_T and the molecular diffusion coefficient D (Kohler et al., 2016). Past years brought a great development on optical methods for the measurements of both molecular and thermal diffusion coefficients for binary mixtures (Mialdun et al, 2011) motivated by their high accuracy allied to a non distressing feature on the diffusive process. However, the fact that the sign of the Soret coefficients of the various species in a mixture can be different, disturbing the system, makes the study thermodiffusion in complex mixtures more challenging. Consequently, only a limited number of thermodiffusion coefficients for binary and ternary mixtures are available in literature and, often, data are not consensual. In this work, we examined the Soret coefficient of the mixture composed of a nonpolar hydrocarbon solute triethylene glycol (TEG) and water, exploring the full concentration region of the mixture at 25 ºC. Experimental method for the determination of Soret coefficients is based on the optical digital interferometry (ODI) technique (Mialdun et al, 2011). Research on triethylene glycol is particularly important due to its applications as a dehydration agent in natural gas streams to prevent corrosion in pipelines (Trueba et al., 2022). Moreover, this is a non-ideal mixture, and thus, it has a potential to demonstrate a complex dependence of the Soret coefficient on concentration, including its sign change.

Experimental

A. Materials

The reagent grade triethylene glycol (purity 0.99%, CAS Number: 112-27-6) and water extra pure, deionized (CAS Number: 7732-18-5) were obtained from Acros Organics and were used as received, with no further purification. Liquid samples of ≈15 g were prepared in mass fraction, by weighing each component using the Sartorius 1712 analytical balance with a resolution/capacity of 0.1 mg/160 g and then remixed by a magnetic stirrer during several hours.

B. Experimental setup: Optical digital interferometry

The experimental setup for the measurement of the Soret effect used in this work was optical digital interferometry (ODI), a validated and reliable optical method very well described in literature (Mialdun et al, 2011; Santos et al. 2022).

Results

A. Overview of the component separation

The study of the separation in the TEG–water mixtures was done over the complete composition range of TEG, using a 0.1 mass fraction step. In the low TEG concentration range, the mixtures featured stable separation, well accessible by ODI, with the maximum optical signal found at c ≈ 0.2 mass fraction. A further increase of the TEG concentration resulted in a gradual decrease of the optical signal corresponding to steady-state separation, which was found unstable (negative) in the experiment at c = 0.5 mass fraction. Several experiments, made at even higher concentrations of TEG (at c = 0.75 and 0.98 mass fraction), confirmed the instability of the separation over all regions of high TEG concentrations, until c = 1. The summary plot of the observed concentration dependency of the optical separation is shown in Fig. 1.

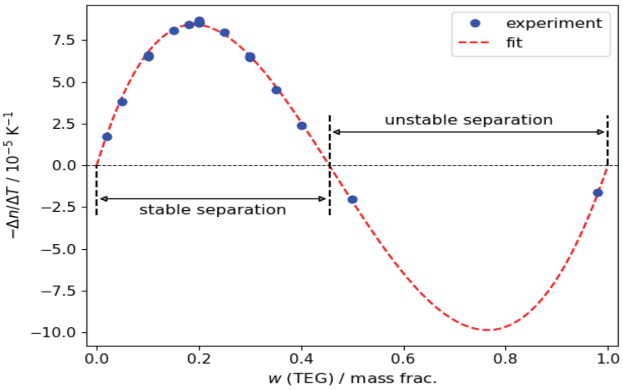

Figure 1: General trend of separation for the mixture TEG–water (dots represent the experimental data, and the dashed line is the fit).

Fitting of the results with a first-order R–K polinomia, which considers the disappearance of the separation at the diluted limits, (Redlich et al, 1948) provides a reasonable description of the explored region and a satisfactory guess about the unexplored one. The obtained fitting curve, represented by the dash line in Fig. 1, allowed to precisely locate the concentration specific to the sign change of the separation, at a 0.45 mass fraction of TEG. Until this point, the separation of components is stable and develops normally, having the point of maximum separation at 0.2 mass fraction of TEG. In an attempt to improve the accuracy of the dependence of separation, new measurements at intermediate concentrations in the region of stable separation, with a smaller step of 0.05 mass fraction, were added.

While the ODI setup configuration is optimized for the measurement of mixtures with the positive Soret separation it was still possible to measure two extra data points that belong to the region with unstable separation, and the extraction of data is explained with detail in next point.

B. Unstable separation

When running the experiments with mixtures featuring small unstable separation (e.g., at c = 0.50 and 0.98 mass fraction), we made an important observation. At first, the separation, even being generally unstable, develops in accordance with the analytical solution. At later time, when enough amount of the heavier component (TEG) has accumulated at the top of the cell, the 1-D character of the developing separation breaks, and a hydrodynamic instability develops (Santos et al., 2022). The instability should start after a certain threshold and may take either long-wave or finger-type character, with both the threshold and the character being dependent on thermophysical and transport properties of the mixture, as well as on the applied temperature difference and the cell size. The most important feature here was the duration of the step of the stable development of the separation. In the two most interesting cases, at c = 0.5 and 0.98 mass fraction, this duration was found as 2–3 h. The separation development in the case of c = 0.5 is shown in Fig. 2.

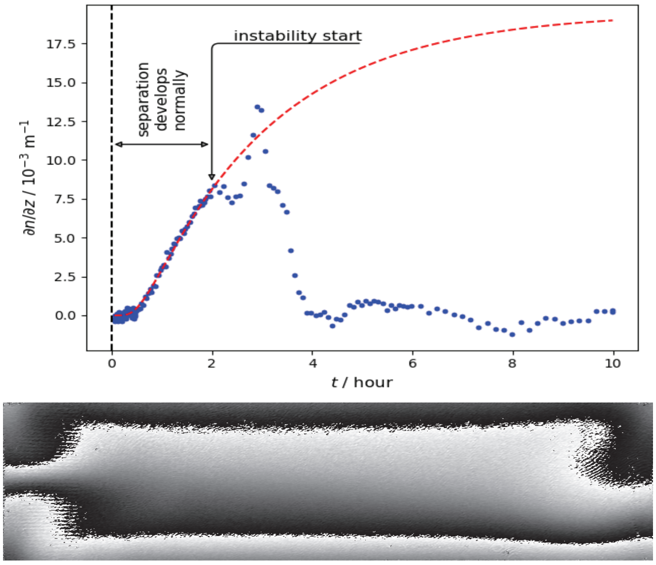

Figure 2: General trend of separation for the mixture TEG–water of c = 0.5 (dots are experimental data, and the dashed line is the fit). The wrapped optical phase map shown below corresponds to the beginning of instability development.

It is seen in the plot that, during the first hours, the separation develops in a perfect agreement with the 1-D analytical solution and that due to the faster image acquisition at the beginning of the experiment, this time interval is quite densely covered by interferograms.

It appeared that this amount of data is enough for fitting and extracting the separation magnitude and diffusion coefficient, despite that the separation does not reach even a half of the steady-state level. The 2-D phase map specific to the end of the short period of the stable separation development is shown in Fig. 2, below the separation curve. There are visible traces of the developing instability in the corners of the cell, while in the liquid bulk in the center of the cell, the distribution resembles the steady one (Santos et al., 2022). Thus, in certain cases of unstable separation, the data allow access to the transport properties in the same manner as for fully stable separation. This, however, is not always the case. For example, the experiment with the mixture of c = 0.75 mass fraction concentration did not allow one to apply this approach since the instability development started after 0.5 h, obstructing a further extraction of meaningful data. Nevertheless, this possibility let us add two additional points to our results, having a reliability comparable with all other cases featuring the stable separation.

Conclusions

Soret coefficients S_T were determined for the TEG–water mixture with ODI setup, showing that S_T changes its sign at 0.1 mol fraction of TEG (0.45 mass fraction of TEG) and that the separation of the components at high concentration of TEG is unstable.

Acknowledgements

C.I.A.V.S. is grateful for funding from "The Coimbra Chemistry Centre," supported by the Fundação para a Ciência e a Tecnologia (FCT), Project No. UID/QUI/UI0313/2013 and COMPETE Program and for the funding granted by FEDER through the COMPETE Programme and FCT for the KIDIMIX Project No. POCI-01-0145-FEDER- 030271. A.M. acknowledges support from the PRODEX program of the Belgian Federal Science Policy Office. V.S. acknowledges support from micro4IloT (Grant No. KK-2019/00101) from the Basque government and M.M.B.-A. acknowledges support from Project No. PID2020-115086GB-C33 financed by MCIN/AEI of the Spanish Government.

References

[1] C. Soret, "Sur l'état d'équilibre que prend au point de vue de sa concentration une dissolution saline primitivement homogène dont deux parties sont portées à des températures différentes.," *Arch. Sci. Phys. Nat. Geneve*, 2(3) 48–61 (1879)

[2] W. Köhler and K. I. Morozov, "The Soret Effect in Liquid Mixtures- A Review," *Journal of Non-Equilibrium Thermodynamics*, 41 (3) (2016).

[4] A. Mialdun, V. Shevtsova, "Digital interferometry as a powerful tool to study the thermodiffusion effect", *C. R. Mécanique*., 339, 362 (2011).

[3] L. Trueba, T. Gaston, J. Brackin, J. Miller, and B.-H. You, Effective strategies to reduce triethylene glycol consumption in natural gas processing plants, *Case Stud. Chem. Environ. Eng.* **5**, 100196 (2022).

[5] C. I. A. V. Santos, M. C. F. Barros, A. C. F. Ribeiro, M. M. Bou-Ali, A. Mialdun, and V. Shevtsova, "Transport properties of n-ethylene glycol aqueous solutions with focus on triethylene glycol–water", *J. Chem. Phys*. 156, 214501 (2022)

[6] O. Redlich and A. T. Kister, Algebraic Representation of Thermodynamic Properties and the Classification of Solutions, *Ind. Eng. Chem*. 40, 345 (1948).

Forced convection in two sided lid-driven horizontal cavity filled with a binary fluid: Optimal species separation

Mojtabi A. [1], Charrier-Mojtabi M.C.[1], Costeseque P.[1], Mojtabi M. [2]

1. Université de Toulouse, I.M.F.T. UMR CNRS/INP/UPS, 31400 TOULOUSE, France.
2. SUPii Mécavenir. Puteaux, Ile-de-France, France

Introduction

In the gravity field or under microgravity, pure thermo-diffusion leads to very weak species separation. To increase the species separation in the presence of gravity, many authors use thermo-gravitational diffusion in vertical or inclined columns (TGC), (Platten et al. 2003), (Charrier-Mojtabi et al. 2007) and (Seta et al. 2019). The flow velocity strongly depends on the temperature difference, *ΔT*, imposed between the two walls facing each other, and also on the thickness, *H*, between them. Indeed, an optimum species separation cannot be obtained in relation to *ΔT* and *H* simultaneously. This problem admits an optimum which is only function of *H* for fixed *ΔT* or function of *ΔT* for fixed *H*, (Mojtabi et al. 2019).

The coupling between shear-driven convection and thermo-diffusion is a complex phenomenon due to the interactions between the different forces applied to the fluid mixture.

Up to now, the species separation obtained in vertical columns has been limited. The convective flow velocity depends on the temperature difference *ΔT*, maintained on the vertical surfaces of the column and the thickness *H* separating these two surfaces. For a given thickness, to increase the importance of thermodiffusion the temperature difference *ΔT* imposed on the two vertical surfaces must be increased. This results in an increase in the convective velocity of the fluid resulting in a decrease in species separation.

For a fixed *ΔT* value, the optimum species separation is obtained for a vertical column thickness less than one millimeter.

In this work, the authors sought to dissociate the fluid flow allowing the species separation from the temperature difference imposed on the two parallel surfaces of the cavity. In addition, appropriate thermal boundary conditions were determinated in order to increase the temperature difference without generating natural convection for a positive or negative Soret coefficient of the binary fluid.

It was shown that it is possible to significantly increase the importance of the species separation for a binary mixture, using forced convection obtained with a uniform translation displacement of the horizontal isothermal walls maintained at T_{top} and T_{bot} respectively, with $\Delta T = T_{top} - T_{bot}$.

We verified that it is possible to obtain a significant species separation whatever the sign of the thermodiffusion coefficient of the binary fluid and this procedure can be extended to multi-constituant fluids. In addition, this procedure can be used with cell thickness greater than the vertical column thickness leading to optimal separation.

This procedure would also make it possible to obtain measurements of negative thermodiffusion coefficients, in the earth laboratory, without using microgravity experimentation (Schraml et al. 2021)

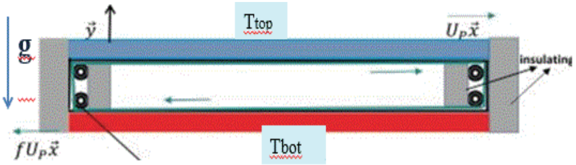

Figure1: Schematic of the rectangular cavity

1. Analytical solution in the case of shallow cavity

We considered a rectangular cavity of large aspect ratio *A=L/H>>1*, where *H* is the height of the cavity along the y axis and *L* is the length along the x axis. The cavity was filled with a binary mixture of density ρ and dynamic viscosity μ. The corresponding dimensional boundary conditions are:

$$x = 0, L: \vec{V} = 0, \frac{\partial T}{\partial x} = \frac{\partial C}{\partial x} = 0, \quad \forall\, y \in [0, H]$$
$$y = 0, H:$$
$$\vec{V} = fUp\vec{e}_x, Up\vec{e}_x, T = T_{bot}, T_{top}, D\frac{\partial C}{\partial y} + D'_T\frac{\partial T}{\partial y} = 0$$

where $D'_T = C_0(1 - C_0)D_T$, C_0 and D_T are respectively the reference mass fraction and the thermodiffusion coefficient.

In the case of a shallow cavity $A \gg 1$, the parallel flow approximation, used by many previous authors, was considered. The streamlines are all parallel to the x axis throughout the cavity except for the vicinity of the insulated walls $x = 0$ and $x = L$, which gives:

$$\boldsymbol{\vec{V}_b = U_b(y)\vec{e}_x , T_b = bx + g(y) \ and \ C_b = mx + f(y)}$$

The constants b and m represent respectively the temperature and mass fraction gradients along the x axis. The constant b is zero since constant temperatures are imposed on the walls $y = 0, H$. Replacing in the mathematic formultation of the problem, the velocity, the temperature and the mass fractions by their expression $U_b, T_b \ and \ C_b$, we obtained the analytical solution of the simplified equations. The mass fraction gradient was obtained by writing that the mass flux associated with the constituent of mass fraction C_b through any cross-section of the rectangular cavity perpendicular to the x-axis is equal to zero:

$$\int_0^H (U_b C_b - D\frac{\partial C_b}{\partial x} - C_0(1 - C_0)\frac{\partial T_b}{\partial x})dy = 0$$

The extremum of m, with respect to U_b and the coefficient f is obtained for $f = -1$. U_b and m are the solutions of fourth degree algebraic equations leading to two real solutions and two complex solutions for the binary mixture studied. The two real solutions are opposed (U_b, *-m*) and (-U_b, *m*) and lead to the same physical solution.

We also conducted a numerical study of this problem, without using any restrictive hypothesis. A comparison between analytical and numerical solutions was performed for two binary mixtures, one with $D_T > 0$and the other with $D_T < 0$. These comparisons showed a good agreement between the analytical and numerical results.

2. Results obtained for two binary mixtures with $D_T > 0$ and $D_T < 0$

How to obtain forced convection alone, within a horizontal binary fluid layer, in the presence of the gravity field? A distinction should be made between binary fluids with a positive thermodiffusion coefficient D_T and negative D_T.

a- Ethanol water mixture with 60.88% water, with $D_T > 0$
For the Water-Ethanol mixture, the densest constituent, namely water, has a $D_T > 0$. In this case, it would be necessary to operate with a layer of fluid heated from above. Indeed the densest constituent migrates towards the cold bottom wall, the binary fluid layer is thermally infinitely stable. As U_b values leading to optimal separations are of the order of 10^{-5} *m/s*, forced convection flow will remain stable even for U_b values well above 10^{-5} *m/s*.
The displacement along the x-axis of the walls maintained at T_{bot} and T_{top}, combined with the thermodiffusion leads to species separation between the two ends of the cell $(x = 0 \; and \; x = L)$, for $\Delta T = T_{top} - T_{bot} > 0$ and for *H≥1mm*.

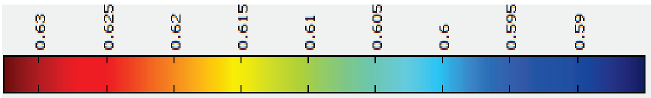

Figure 1: Mass fraction field, $\boldsymbol{C_b}$, for Water-Ethanol binary mixture.

We present some results obtained for Water-Ethanol, 60.88% water for $H = 2.10^{-3}$ m, L = 0.5m and $\Delta T = 10^{\circ}$C:
Numerical: $U_b = +3.2\ 10^{-5}$m/s ; $m = -0.521\ \mathrm{m}^{-1}$
Analytical: $U_b = +3.2\ 10^{-5}$m/s ; $m = -0.514\ \mathrm{m}^{-1}$
When increasing ΔT, the velocity U_b and the mass fraction gradient C_b increase. When H increases at fixed value of ΔT, the mass fraction gradient decreases.

b- Water-Isopropanol mixture with 90% water with $D_T < 0$
For the Water-Isopropanol mixture, the densest constituent, namely water, has a $D_T < 0$. In this case, this constituent migrates to the warmer wall. Then it would be necessary to operate with a layer heated from below, in order to prevent the onset of natural convection. This corresponds to the thermal configuration of Rayleigh-Bénard, but here the densest constituent is more concentrated at the bottom of the horizontal layer. Natural thermal convection can only occur for thermal Rayleigh values greater than the linear thermal critical Rayleigh number, $Ra_c = 1708$. Natural convection, for the Rayleigh-Bénard configuration in the presence of binary mixture, can only occur for temperature differences $\Delta T = T_{bot} - T_{top} > \Delta T_c$ associated with $Ra_c = 1708$, (Charrier-Mojtabi et al. 2007).

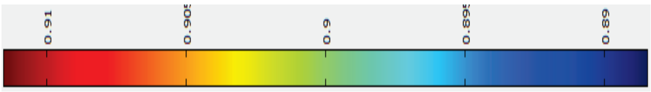

Figure 3: Mass fraction field, $\boldsymbol{C_b}$, for Water-Isopropanol binary mixture.

We present some results obtained for water-isopropanol mixture with 90% water for $H = 1.10^{-3}$ m and $\Delta T = 10^{\circ}$C:
Numerical: $U_b = 7.81.10^{-6}\frac{\mathrm{m}}{\mathrm{s}}$; $m = -0.462\mathrm{m}^{-1}$
Analytical: $U_b = 7.81.10^{-6}\frac{\mathrm{m}}{\mathrm{s}}$; $m = -0.467\ \mathrm{m}^{-1}$
When increasing ΔT, the velocity U_b and the mass fraction gradient, C_b increase.
For $H = 2.10^{-3}$ m and according to the values of the thermophysical characteristics of binary mixture studied, the thermal Rayleigh number could become much higher than $Ra_c = 1708$ leading to the onset of mixed convection.

Conclusions

This procedure of species separation using forced convection in the presence of the gravity field allows us to:
-considerably improve the species separation (several orders of magnitude greater than the one obtained in vertical columns, TGC).
- to be able to measure, in the Earth laboratory, not only diffusion and thermodiffusion coefficients for mixtures with positive thermodiffusion coefficient but also for mixtures with negative Soret coefficients. The measurement of the Soret coefficient for these mixtures is extremely difficult to obtain in the earth laboratory. This led several teams within the framework of the ESA DCMIX project to measure these coefficients in the ISS.

Acknowledgements

The authors acknowledge the support of CNES, the French National Space Agency, which provided access to results obtained in microgravity.

References

A. Mojtabi, A. Khouzam, L. Yacine and MC. Charrier-Mojtabi, Analytical and numerical study of Soret mixed convection in two-sided lid-driven horizontal cavity: optimal species separation, Int. J. of Heat and Mass transfer, V. 139, P.1037-1046 (2019).

B. Seta, E. Lapeira, D. Dubert, F. Gavalda, M.M. Bou-Ali, X. Ruiz, Separation under thermogravitational effects in binary mixtures, Eur. Phys. J.E. 42, 58 (2019).

J.K. Platten, M.M. Bou-Ali, J.F. Dutrieux, Enhanced molecular separation in inclined thermogravitational columns, J. Phys. Chem. B, 107(42), 11763–11767 (2003).

M.C. Charrier-Mojtabi, B. Elhajjar, A. Mojtabi, Analytical and numerical stability analysis of Soret driven in a horizontal porous layer, Physics of fluids, 19, 124104 (2007).

M. Schraml, H. Bataller, C. Bauer, MM. Bou-Ali, F. Crocolo, E. Lapeira , A. Mialdun, P. Mockel, AT. Ndjaka, V. Shevtsova, W. Kohler, The Soret coefficients of the ternary system water/ethanol/triethylene glycol and its corresponding binary mixtures, Eur. Phys. J.E. 44, 10 (2021).

Thermo-osmosis: Theory and Simulations

Z. Filiberti[1], P. Anzini[1], A. Parola[1]

[1]Dipartimento di Scienza e Alta Tecnologia, Università degli Studi dell'Insubria, Via Valleggio 11, 22100 Como, Italy

Introduction

Fluid flow in macroscopic systems is always driven by pressure gradients or by external forces and is accurately described by continuum approaches, like the Navier-Stokes equation. However, starting from the investigations led by Derjaguin, it became clear that in sub-micron systems interfacial effects become relevant and additional mechanisms leading to a mass flow are possible (Derjaguin 1941).

A remarkable example is provided by thermo-osmosis, a surface-induced phenomenon, where the external "field" driving the fluid flow is a temperature gradient.

Thermo-osmotic flows are expected to be minute on a macroscopic scale because the bulk fluid is set into motion due to an interfacial effect. However, the mass transport arising from any surface phenomenon becomes relevant every time one of the system's dimensions becomes comparable to the correlation length or to the mean free path of the fluid. This situation occurs in several systems of technological and biological interest (Barragán 2017): Industrial miniaturization has made available a large variety of nano-channels, paving the way to the development of nano-fluidics and many natural systems, such as membranes and gels, are characterized by porous networks with sub-micron diameters, where thermo-osmosis play an important role.

State of the art

Thermo-osmotic effects have been known since over a century and were investigated in rarefied gases starting from the studies by Maxwell (Maxwell 1879) and Reynolds (Reynolds 1879). The microscopic understanding of this out-of-equilibrium phenomenon in gases, first formulated by Maxwell within kinetic theories, is quite subtle: The flow, named thermal creep within this context, originates from the tangential stress on the gas layer near the confining surface due to the applied temperature gradient and is directed from the cold to the hot side. The effect is strongly related to the properties of the scattering event of a gas molecule on the wall and disappears for an ideal gas confined by purely reflective hard walls.

Conversely, in the liquid regime, the phenomenological descriptions usually adopted rely on macroscopic approaches, such as non-equilibrium thermodynamics and Navier-Stokes equations (Derjaguin 1941). However, the use of continuum theories can be justified when the relevant physical quantities vary on a length scale much larger than the typical range of the interaction: In the presence of a confining surface this condition is no longer satisfied, because, near the interface, the fluid properties eventually driving the phenomenon may display strong but short-ranged, modulations. Therefore, it is not surprising that the classical macroscopic paradigm can fail to predict even the direction of the induced flows (Piazza et al. 2008).

Towards a microscopic theory of thermo-osmosis

Recently, the interest on thermo-osmosis has been revived by molecular dynamics simulations aimed at a microscopic understanding of this effect (Wold et al. 1999, Galliero et al. 2002, Fu et al 2017, Ganti et al. 2018).

Stimulated by these findigs, the authors proposed a first-principle and unitary theory of thermo-osmosis (Anzini et al 2019, Anzini et al. 2022). This approach, valid both for gases and for liquids, is based on a generalization of the linear response theory formalism to the case of an inhomogeneous fluid close to a surface. This theory sheds light on the microscopic mechanisms driving thermo-osmosis and quantitatively relates the fluid flow to the properties of the fluid-wall interface via suitable dynamical correlation functions at equilibrium.

In this contribution we present a general *analytical solution* of these equations, which expresses the mass flow induced by a thermal gradient in terms of the mass current-heat current correlation function. This solution allows to confirm the interpretation of thermo-osmosis as an effect of the variation of the local enthalpy density induced by the presence of the wall, making contact with previous phenomenological approaches.

To validate the theoretical predictions in a controlled environment, we performed extensive non equilibrium molecular dynamics simulations for a simple model of one component fluid and few wall-particle interactions. In most of the examples we will present, the walls are "passive", i.e., they just act as an external force on the fluid molecules, orthogonal to the surface, thereby conserving the particle momentum parallel to the surface in a scattering process.

The same microscopic theory allows to derive an analytical form of the velocity profile in the low-density regime when the confining surfaces violate the momentum conservation during the wall-molecule scattering. In this case, the comparison between numerical and analytical results is encouraging.

Conclusions

Thermo-osmosis is an interesting effect *per se*, being the simplest example of thermal force, and is expected to play a relevant role in different physical frameworks, from engineering to biophysics.

In addition, one of the most important effects of thermo-osmosis probably occurs at the surface of colloidal particles immersed in a liquid or a gas, where the ensuing fluid flow pushes the colloidal particles through the fluid, giving rise to thermophoresis.

A microscopic study of thermo-osmosis is also instrumental for defining the correct boundary conditions (*i.e.* the slip velocity) for effective macroscopic approaches, based on hydrodynamics and the Navier-Stokes equation, describing fluid flow in confined systems.

Acknowledgements

We gratefully thank Roberto Piazza for constant encouragement and illuminating discussions.

References

V. Derjaguin, N. V. Churaev, and V. M. Muller, Surface Forces in Transport Phenomena (*Springer*, 1987)

V. M. Barragán and S. Kjelstrup, Thermo-osmosis in Membrane Systems: A Review, *J. Non-Equilib. Thermodyn*, 42, 217, (2017).

J. K. Maxwell, VII. On stresses in rarified gases arising from inequalities of temperature, *Philos. Trans. R. Soc. London*, 170, 231, (1879)

O. Reynolds, XVIII. On certain dimensional properties of matter in the gaseous state., *Philos. Trans. R. Soc. London*, 170, 727, (1879)

B. V. Derjaguin and G. P. Sidorenkov, *Dokl. Akad. Nauk SSSR*, 32, 622, (1941).

I. Wold and B. Hafskjold, Nonequilibrium Molecular Dynamics Simulations of Coupled Heat and Mass Transport in Binary Fluid Mixtures in Pores, *Int. J. Thermophys*, 20, 847 (1999).

R. Piazza and A. Parola, Thermophoresis in colloidal suspensions, *J. Phys. Condens. Matter*, 20, 153102 (2008).

G. Galliéro, J. Colombani, B. Duguay, J.-P. Caltagirone, and F. Montel, Evaluation de la thermodiffusion en milieu poreux nanométrique intégré par dynamique moléculaire hors équilibre directe, *Entropie*, 239/240, 98-102, 2002.

L. Fu, S. Merabia, and L. Joly, What Controls Thermo-osmosis? Molecular Simulations Show the Critical Role of Interfacial Hydrodynamics, *Phys. Rev. Lett.*, 119, 214501 (2017)

R. Ganti, Y. Liu, and D. Frenkel, Hamiltonian Transformation to Compute Thermo-osmotic Forces, *Phys. Rev. Lett.*, 121, 068002 (2018)

P. Anzini, G. M. Colombo, Z. Filiberti, and A. Parola, Thermal Forces from a Microscopic Perspective, *Phys. Rev. Lett.*, 123, 028002 (2019)

P. Anzini, Z. Filiberti, and A. Parola, Fluid flow at interfaces driven by thermal gradients, *Phys. Rev. E*, 106, 024116 (2022)

Optothermal heating effects on the structure and dynamics of a soft disordered solid

Roberto Piazza, Vincenzo Ruzzi, and Stefano Buzzaccaro

Dipartimento di Chimica, Materiali e Ingegneria Chimica “G. Natta”, Politecnico di Milano

Piazza Leonardo da Vinci 32, 20133 Milano, Italy

Polymer solutions can be driven by temperature-dependent attractive interactions to organize into highly porous and tenuous gels displaying a very low elastic modulus. In this work, we investigating the optothermal effects generated by the weak adsorption of an IR laser beam on Mebiol, a block-copolymer hydrogel whose strength and elastic modulus grow with T that is extensively used as a substrate for cell growth. Structural changes induced the induced spatially-localized thermal gradient are detected by Photon Correlation Imaging (PCI), an optical technique that provides space-resolved information on the microscopic dynamics, allowing one to detect at the same time the presence of displacement and strain field. A schematic view of our PCI apparatus is shown in the figure. Preliminary measurements show that, even for moderate heating, a dramatic change of the microscopic gel dynamics, accompanied by the evidence of consistent strain effects, takes place. On switching off the laser, the gel slowly reverted to its original state, but only if the IR irradiation is kept for a limited time: For longer exposure, structural deformation became permanent, hence the gel displayed a plastic behavior.

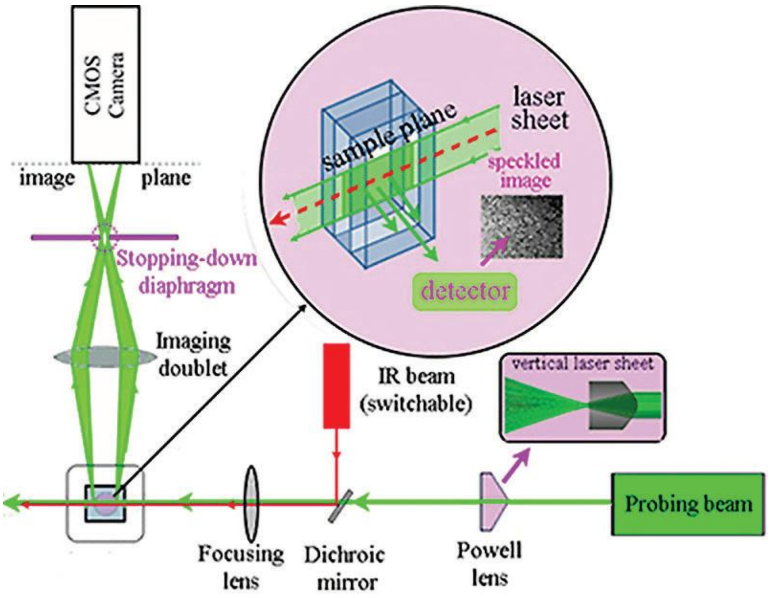

Photon Correlation Imaging setup, including an IR laser beam
operating at 980 nm for local sample heating

Thermal Marangoni effects, thermodiffusion, and thermo-osmosis in slit pores

B. Hafskjold[1], D. Bedeaux[1], S. Kjelstrup[1], Ø. Wilhelmsen[1], E. Ditaranto[1]

[1]PoreLab, Department of Chemistry, Norwegian University of Science and Technology – NTNU, Trondheim, Norway
bjorn.hafskjold@ntnu.no, dick.bedeaux@ntnu.no, signe.kjelstrup@ntnu.no, oivind.wilhelmsen@ntnu.no, ekditara@stud.ntnu.no

Introduction

The thermal Marangoni effect, also called thermo-capillary convection, is fluid creep flow along a surface caused by a temperature gradient. The actual driving force is the gradient in surface tension. When a temperature gradient is applied to a fluid mixture in a porous medium, thermo-capillary convection and thermodiffusion may occur simultaneously. We investigate how the two processes couple and why thermo-capillary convection must be considered in measurements of Soret effects in porous media.

If the permeability of the porous medium is low and the medium has sufficient mechanical strength, thermo-osmosis can generate a pressure gradient in the fluid. This pressure gradient can amount to several bars per degree [1]. We show how thermo-osmosis can be included in the theory for thermodiffusion.

Combinations of type of fluid, type of porous medium, and effects of a temperature gradient are shown in Table 1.

Table 1. Effects driven by a temperature gradient in different systems.

Fluid / Medium	One component	Mixture
Low permeability	Thermo-osmosis	Thermo-osmosis Thermodiffusion
High permeability, bulk fluid	No effect	Thermodiffusion

Theory

The flux equations for a binary fluid mixture in a porous medium may be expressed as [2,3]

$$J'_q = L_{qq}\nabla\left(\frac{1}{T}\right) - L_{qV}\frac{1}{T}\nabla P - L_{qD}\frac{x_1}{T}\nabla\mu_{1,c} \tag{1a}$$

$$J_V = L_{Vq}\nabla\left(\frac{1}{T}\right) - L_{VV}\frac{1}{T}\nabla P - L_{VD}\frac{x_1}{T}\nabla\mu_{1,c} \tag{1b}$$

$$J_D = L_{Dq}\nabla\left(\frac{1}{T}\right) - L_{DV}\frac{1}{T}\nabla P - L_{DD}\frac{x_1}{T}\nabla\mu_{1,c} \tag{1c}$$

where J'_q is the measurable heat flux and J_V and J_D are the volume flux and diffusion flux, respectively, defined as

$$J_V = J_1V_1 + J_2V_2 \tag{2a}$$

$$J_D = \frac{J_1}{x_1} - \frac{J_2}{x_2} \tag{2b}$$

were J_i is the mass flux, V_i the partial molar volume, and x_i the mole fraction of component i, respectively. Furthermore, the L-coefficients are the Onsager coefficients, P is pressure, T is temperature, and $\mu_{1,c}$ is the compositional contribution to the chemical potential from component 1.

For a binary fluid mixture in a porous medium, we define the Soret coefficient as

$$S = \left(\frac{1}{x_1x_2}\frac{\nabla x_1}{\nabla T}\right)_{J_V=J_D=0} \tag{3a}$$

$$= \frac{1}{x_1x_2RT^2}\left(\frac{L_{DV}L_{Vq} - L_{VV}L_{Dq}}{L_{DD}L_{VV} - L_{DV}^2}\right)\left(1 + \frac{\partial\ln\gamma_1}{\partial\ln x_1}\right)^{-1} \tag{3b}$$

where R is the gas constant and γ_1 is the activity coefficient of component 1. The condition $J_V = J_D = 0$ means no net flow through any cross section of the porous medium. This is achieved in molecular simulations by restricting the flow through the ends of the simulation box to keep a stationary state.

The thermo-osmotic coefficient quantifies the thermo-osmotic effect. It is defined as

$$D_P = \left(\frac{\nabla P}{\nabla T}\right)_{J_V=J_D=0} \approx \left(\frac{\Delta P}{\Delta T}\right)_{J_V=J_D=0} \tag{4a}$$

$$= \frac{1}{T}\left(\frac{L_{DV}L_{Dq} - L_{DD}L_{Vq}}{L_{DD}L_{VV} - L_{DV}^2}\right) \tag{4b}$$

where the differences ΔP and ΔT between properties in the bulk phases are used as an approximation.

NEMD Simulations

We will report results for thermodiffusion and thermo-osmosis in slit pores. Examples of the system layout for a one-component fluid of Lennard-Jones/spline particles is shown in Figure 1 (top). Non-equilibrium molecular dynamics (NEMD) simulations were done with the LAMMPS software [4]. Temperature gradients were established by heating the parts of the “hot fluid” and cooling parts of the “cold fluid”. The particle momenta of the left and right boundaries of the MD box were set to zero in order to ensure zero net mass fluxes in *x*-direction. The temperature gradients were the only external forces on the system.

Preliminary results

Result for the case shown in Figure 1 include the velocity profiles in the bottom panel of the figure. The wide pore has a distinct flow pattern with creep flow along the walls in the direction of high temperature. A consequence of the zero net mass flow is that the fluid is forced in the opposite direction in the center of the pore. The four pores show the same feature, but the narrower channels restrict fluid back-flow. The consequence is that pressure builds up in the hot bulk regions, which is the thermo-osmotic effect. Preliminary data for ΔP and D_P for this one-component fluid are given in Table 2. These results are for a one-component fluid, so there is no Soret effect here. We will present results for various porosities and permeabilities for one- and two-component fluids at IMT15.

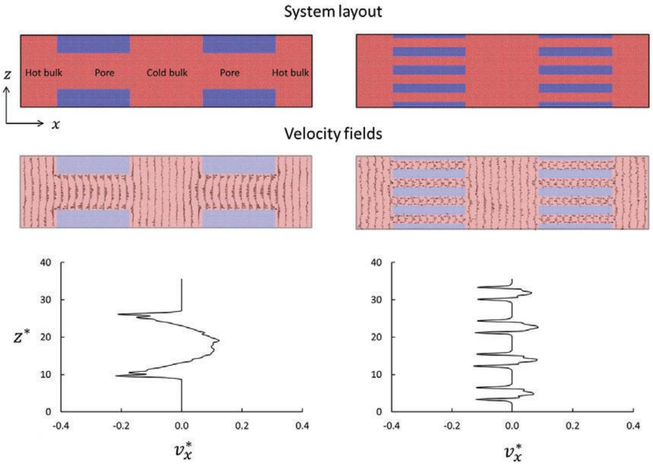

Figure 1. Top: Side view of two slit pore configurations used in this work, one wide pore (left) and four narrow pores (right). The blue regions are pore walls of Lennard-Jones/spline particles in a solid state. The red regions contain the same type of particles in a one-component liquid state. A temperature gradient is set up in the fluid between the hot and cold bulk compartments. Middle: Convective flow fields in the pores as illustrated by the velocity vectors. The velocity is towards the hot bulk along the walls and in the opposite direction in the pore centers. Bottom: x-components of the fluid velocity in the left pores as function of z.

Table 2. Preliminary results for ΔP^* and D_P^* (in Lennard-Jones units) for the two pores shown in Figure 1. The thermo-osmotic effect in the wide pore is very small because of the low resistance to fluid backflow in the center of the pore. The pressure build-up on the hot side is significant in the system with narrow pores.

Case	ΔP^* (hot-cold)	D_P^*
Wide pore	0.016	0.008
Narrow pores	0.174	0.087

Acknowledgements

The authors are grateful to the Research Council of Norway, for the Center of Excellence Funding Scheme, project no 262644, PoreLab. The NEMD simulations were performed on resources provided by UNINETT Sigma2—the National Infrastructure for High Performance Computing and Data Storage in Norway, project NN5092K, and by HPC resources at The Norwegian University of Science and Technology—NTNU.

References

[1] M. T. Rauter, S. K. Schnell, B. Hafskjold and S. Kjelstrup, *Thermo-osmotic pressure and resistance to mass transport in a vapor-gap membrane,* Phys. Chem. Chem. Phys. (2021) 23: 12988 doi: 10.1039/docp06556k

[2] A. Katchalsky, P.F. Curran, *Nonequilibrium Thermodynamics in Biophysics* (Harvard University Press, Cambridge, 1975)

[3] B. Hafskjold, D. Bedeaux, S. Kjelstrup, and Ø. Wilhelmsen, "Soret separation and thermo-osmosis in porous media", Eur. Phys. J. E (2022) 45:41, DOI: 10.1140/epje/s10189-022-00194-2

[4] S. Plimpton, "Fast parallel algorithms for short-range molecular dynamics", *J. Comput. Phys.* 117, 1–19 (1995).

Complementary Experimental Methods to Obtain Thermodynamic Parameters of Protein Ligand Systems

S. Mohanakumar[1], N. Lee[2], S. Wiegand[3,4]

[1]Forschungszentrum Jülich, Jülich, Germany, s.mohanakumar@fz-juelich.de, [2] Department of Mechanical Engineering, Yonsei University, Seoul, Korea, nk.lee@yonsei.ac.kr, [3]Forschungszentrum Jülich, Jülich, Germany, s.wiegand@fz-juelich.de,
[4]Chemistry Department – Physical Chemistry, University Cologne, D-50939 Cologne, Germany,

Introduction

Motion of solutes in a solvent induced by a thermal gradient is termed as thermophoresis. Ratio of the established concentration gradient to the temperature gradient is quantified using Soret coefficient S_T (Köhler *et al.*, 2016). Since this phenomenon is very sensitive to the nature of solute-solvent interactions, it is used as a tool for quantifying biomolecular interactions, especially protein-ligand interactions (Niether *et al*. 2020). Although, a change in the thermophoretic behaviour of protein once the ligand binds is often attributed to the change in the hydration layer, underlying microscopic physical effect is not understood. To gain deeper insight into the interactions involved, we investigate whether the non-equilibrium coefficient measured can be related to equilibrium properties. The same, thermophoretic data measured using thermal diffusion forced Rayleigh scattering (TDFRS) (which is a non-equilibrium process) are compared with the thermodynamic data obtained by isothermal titration calorimetry (ITC) (which is an equilibrium method). To connect these parameters, we start from an early work by Eastman (Eastman 1928) which connects S_T to Gibb's free energy ΔG as follows

$$S_T = \frac{1}{k_B T}\frac{dG}{dT} \qquad (1)$$

Integrating Eq. 1 with temperature gives us access to a relation between S_T and ΔG for the individual compounds of the system (free protein, free ligand, and complex). These individual contributions calculated are then used to establish a relation between ITC and TDFRS measurements, as shown in Fig. 1. We hypothesize that $\Delta G_{T_{high}}$ can be calculated from the free energy change at a low temperature $\Delta G_{T_{low}}$ measured by ITC and the differences in $\Delta\Delta G$ corresponding to two temperatures for the individual components probed by TDFRS using the following equation

$$\Delta G_{T_{high}} = \Delta G_{T_{low}} + \Delta\Delta G_{AB} - \Delta\Delta G_A - \Delta\Delta G_B \qquad (2)$$

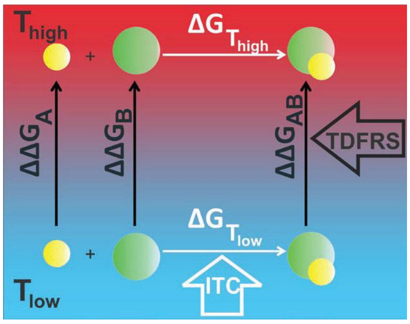

Figure 1: Schematic illustration of the calculation of ΔG and ΔΔG from ITC and TDFRS, respectively.

Choice of systems

To test our hypothesis, EDTA-$CaCl_2$ reaction in MES buffer is used as reference system. This is a well-known chelation reaction which is used as a validation standard for ITC measurements (Ràfols *et al.* 2016). Once the validation is done, Eq. 2 is tested for protein Bovine Carbonic Anhydrase I (BCA I) with two different ligands which belong to the group of arylsulfonamides. In our study, we used 4 fluorobenzenesulfonamide (4FBS) and pentafluorobenzenesulfonamide (PFBS). We carry out TDFRS and ITC measurements for these systems over a wide temperature range between 20°C to 45°C.

Results

1. TDFRS measurements

1.1 EDTA-$CaCl_2$

S_T of EDTA shows an abrupt drop between 25°C and 30°C. Although, there are several literature reports, which report a change in properties of several systems in the presence of EDTA in a similar temperature range, there exists no clear explanation for this behavior (Sugiyama *et al.* 2014, Minkevich *et al.* 2006, Yilmaz *et al.* 2011). Also, the temperature sensitive polymer poly(N-isoproplacrylamide) (PNiPAM) in water (*Kita* et al. 2005), which is influenced by the hydrogen bonds, shows an abrupt variation in S_T with temperature. Distinctive thermodiffusive properties exhibited by EDTA and the complex might have the same origin as in case of PNiPAM as it happens in similar temperature range. This also supports the hypothesis that a change in hydration has an effect on thermophoretic behavior.

1.2 Protein-ligand system

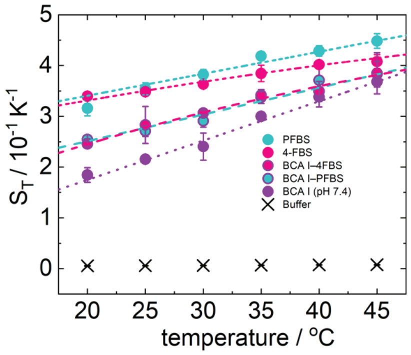

Figure 2: Temperature dependence of S_T for BCA I, 4FBS, PFBS, buffer and complexes formed.

Temperature dependence of S_T for protein-ligand systems is shown in Fig. 2. From TDFRS measurements, it can be concluded that the hydration shells of both complexes formed are very similar, but different from free BCA I. For both protein–ligand systems the difference between S_T of free protein and complex decreases with temperature, so that it is almost negligible at high temperatures. This is an indication that the binding of both ligands should become weaker with increasing temperature. A larger change in S_T with temperature for free BCA I indicate a higher hydrophilicity for the free protein in comparison to the protein-ligand complex formed. It has been reported that arylsulfonamides bind to the active site of different variants of carbonic anhydrase protein by replacing a water molecule from the active site (Krishnamurthy *et al.* 2007, Olander *et al.* 1973, Abbate *et al.* 2002). This implies that the complex is less hydrophilic than the free protein which is confirmed by TDFRS measurements.

2. Validation of relation between S_T and ΔG

The calculated values listed in Table 1 correspond to T_{high} = 30°C and T_{low} = 20°C. Mathematical expression is first applied to the EDTA-$CaCl_2$ system. With the S_T values of EDTA, CaCl2 and the complex measured at T_{high} and T_{low}, we have access to the change in Gibb's energy ($\Delta\Delta G$) of the individual components. Later, the same procedure is used for protein-ligand systems.

Table 1: Comparison of ΔG that has been calculated and that has been measured with ITC

System	$\Delta G_{calculated}$ (kJ/mol)	ΔG_{ITC} (kJ/mol)
EDTA-$CaCl_2$	-36.5±1.2	-36.4±0.8
BCA I-4FBS	-40.5±1.1	-40.4±1.3
BCA I-PFBS	-39.9±3.9	-38.2±1.5

For all the three systems that have been studied, ΔG that has been calculated agrees with the measured values within the error limits.

Conclusions

One of the main goals of this work was to investigate whether it is possible to connect thermodynamic parameter obtained with ITC to thermodiffusion parameter measured with TDFRS. A mathematical relation connecting S_T and ΔG was derived which is tested for three different systems; low molecular weight reference system, EDTA–$CaCl_2$ and the protein BCA I with two ligands 4FBS and PFBS. For all the temperature pairs that have been studied for aforementioned systems, ΔG values calculated agreed with the measured values within the error limits. This implies that S_T measured at different temperatures can be used to predict the ΔG value at particular temperature. This newly developed connection can be utilized to open promising gates in the accurate acquisition of the underlying binding and molecular dissociation mechanisms from the studied systems.

Acknowledgements

We thank Mona Sarter and Andreas Stadler for fruitful and helpful discussions. We are grateful to Peter Lang and Jan Dhont for inspiring ideas and their generous support of our work. SM acknowledges the support by the International Helmholtz Research School of Bio-physics and Soft Matter (BioSoft) and NL acknowledges the support by the Humboldt foundation.

References

W. Köhler, K. I. Morozov, The Soret Effect in Liquid Mixtures—A Review. J., *Non-Equil. Thermody*., 41, 151 (2016)

D. Niether, M. Sarter, B. W. Koenig, J. Fitter, A. M. Stadler, S. Wiegand, Thermophoresis: The Case of Streptavidin and Biotin, *Polymers*, 12, 376 (2020)

E.D. Eastman, Theory of the Soret effect., J. Am. Chem. Soc., 50, 283 (1928)

C. Ràfols, E. Bosch, R. Barbas, R. Prohens, The Ca2+-EDTA chelation as standard reaction to validate Isothermal Titration Calorimeter measurements (ITC), *Talanta*, 154, 354 (2016)

T. Sugiyama, A. H. A. Dabwan, H. Katsumata, T. Suzuki, S. Kaneco, Optimization of Conditions for the Photocatalytic Degradation of EDTA in Aqueous Solution with Fe-Doped Titanium Dioxide, *Open J. Inorg. Non met. Mater.*, 4, 28 (2014)

I. G. Minkevich, A. D. Satroutdinov, E. G. Dedyukhina, T. I. Chistyakova, E. N. Kaparullina, A. V. Koshelev, O. N. Okunev, The effect of temperature on bacterial degradation of EDTA in pH-auxostat, *World J. Microbiol. Biotechnol.,* 22, 1205 (2006)

Z. Yılmaz, S. Aktemur, H. D. Buzoglu, M. Gümüsderelioglu, The Effect of Temperature and pH Variations on the Surface Tension of EDTA Solutions, *J. Endod.,* 37, 825 (2011)

R. Kita, S. Wiegand, Soret coefficient of poly(N-isopropylacrylamide)/water in the vicinity of coil-globule transition temperature, *Macromolecules*, 38, 4554 (2005)

V. M. Krishnamurthy, B. R. Bohall, C.-Y. Kim, D. T. Moustakas, D. W. Christianson, G. M. Whitesides, Thermodynamic parameters for the association of fluorinated benzenesulfonamides with bovine carbonic anhydrase II., *Chem. Asian J.*, 2, 94 (2007)

J. Olander, E. T. Kaiser, Binding of 4-hydroxy-3-nitrobenzenesulfonamide, a reporter group labeled inhibitor, to carbonic anhydrases. *J. Am. Chem. Soc.,* 92, 5758 (1970)

F. Abbate, C. T. Supuran, A. Scozzafava, P. Orioli, M. T. Stubbs, G. Klebe, Nonaromatic sulfonamide group as an ideal anchor for potent human carbonic anhydrase inhibitors: Role of hydrogen-bonding networks in ligand binding and drug design, *J. Med. Chem.*, 45, 3583 (2002)

Thermocapillary-driven melting of PCMs in microgravity: performance enhancement strategies

P. Salgado Sánchez, J. Jimenez, A. Borshchak Kachalov, U. Martinez, D. Gligor, J. M. Ezquerro, J. Porter

E-USOC, Center for Computational Simulation, Universidad Politécnica de Madrid, Spain, pablo.salgado@upm.es

Introduction

Phase Change Materials (PCMs) are of interest in thermal management for their ability to store (and release) large amounts of energy, in the form of latent heat, near the phase change temperature. Space exploration is an especially fitting area for PCM applications because significant variations in temperature can result from cycles of radiation exposure or the heat generated by onboard systems. Although organic PCMs are a stable and attractive choice for many situations, their effectiveness can be limited by low thermal conductivity.

One straightforward strategy for improving performance is to modify the (effective) thermal conductivity of the PCM device by adding a more conductive material — metallic structures or nanoparticles, for example. Alternatively, encouraging convective flows in the liquid phase can significantly enhance the heat transfer rate. On ground, gravity can promote natural convection if the PCM device has a suitable orientation. In microgravity environments, the thermocapillary effect can similarly drive convective flow and has been proposed as an alternative strategy since, in the presence of a free surface, the temperature gradient inherent to PCM operation will naturally generate surface tension gradients.

In recent years, the topic of thermocapillary-driven melting of PCMs in microgravity has been the subject of growing research. The seminal parabolic flight experiments of Ezquerro et al. (2020) were the first to confirm the potential of the thermocapillary effect to enhance heat transport during melting in microgravity. Since then, several numerical studies have looked at this problem from the perspectives of heat transport (see, e.g., Salgado Sánchez et al. 2020, Varas et al. 2021, and reference therein) and pattern selection during the phase change. In fact, the relevance of this research line for space exploration was recently recognized by the European Space Agency with the approval of the ‘‘Effect of Marangoni Convection on Heat Transfer in Phase Change Materials’’ (MarPCM) experiment (Porter et al. 2023) for its future execution on board the International Space Station.

In this work, we review the state of the art available in the literature and discuss different strategies that can be implemented in microgravity to improve the performance of thermocapillary-enhanced PCM devices: selecting an adequate geometry, using (nano-enhanced) NePCM, or a combination of both.

Selecting PCM geometry

The types of PCM containers that been analyzed in thermocapillary-driven melting can (to the best of our knowledge) be placed into three general categories: quadrilateral (rectangular and trapezoidal cross-section), cylindrical and spherical (i.e., liquid bridges and drops when melted).

In rectangular containers, the effect of thermocapillary flow was shown to depend crucially on aspect ratio $\Gamma = L/H$ and the Marangoni number

$$\mathrm{Ma} = \frac{\gamma\, L\, \Delta T}{\mu\, \alpha},$$

which quantifies the relative importance of thermocapillary- and conductive transport during the phase change. Here, γ is the thermocapillary coefficient, L is the container length, H is its height, ΔT is the applied temperature difference, and μ and α are the viscosity and thermal diffusivity of the liquid phase, respectively. The enhancement factor $G = \tau_{\mathrm{ref}}/\tau_{\mathrm{Ma}}$, defined as the ratio between the melting time with purely conductive transport τ_{ref} and with the thermocapillary effect τ_{Ma}, ranges from approximately 2 to 25 (Salgado Sánchez et al. 2020). For fixed ΔT, there exists an optimal Γ that maximizes this enhancement.

With rectangular containers, the phase change often includes a final stage that is dominated by conduction, where the PCM near the cold boundary melts slowly. Recently, the use of trapezoidal containers was proposed to accelerate the melting process. By inclining the cold lateral wall, in particular, melting can be substantially speed up with respect to the rectangular case, with an optimal reduction of τ_{Ma} by a factor of 3 in the limiting case of a right triangle (Borshchak Kachalov et al. 2022).

In liquid bridge geometry, on the other hand, the contribution of the thermocapillary effect during the phase change was shown to be approximately 50% greater than in the rectangular case (Varas et al. 2021). Note that, for a fixed heat storage capacity (i.e., PCM volume), this geometry increases the ratio of free surface area to PCM volume compared to the most trapezoidal (or rectangular) containers. With this criteria, the optimal geometries are spherical shapes, for which the free surface driving the thermocapillary flow is maximized for a given PCM volume.

Using NePCM with thermocapillary effects

The use of dispersed nanoparticles has also been proposed for improving PCM performance with the (so-called) nano-enhanced phase change materials (NePCM) (Madruga et al. 2021).

The addition of nanopartciles modifies the thermo-physical properties of the pure PCM, increasing thermal conductivity (diffusivity) and the viscosity of the liquid phase, and slightly reducing the heat storage capacity; note that part of the original PCM volume is taken by particles that do not undergo a phase change. The extent of this modification depends on the concentration C and size of the particles, and their thermo-physical properties. Compared to the response of the pure PCM at a given ΔT, the associated NePCM will experience a smaller Marangoni number and possess lower latent heat.

However, the interplay between these two opposite effects in rectangular geometry could result in an overall enhancement ranging from 1 to 10%, depending essentially on nanoparticles properties and concentration C, and on Γ and ΔT.

Combining strategies

For applications, one may consider combining the aforementioned strategies: selecting an adequate (optimal) geometry for an NePCM. In this case, the contribution of each strategy would be complementary. A rectangular container with NePCM can provide values of G ranging from 1% to 10% greater than with the pure PCM.

In cylindrical geometry, the factor of 1.5 achieved by the greater free-surface-area-to-volume ratio would be increased by an additional factor of approximately 1.1, resulting in a final enhancement of roughly 1.65. Compared to the case of purely conductive transport, the overall enhancement would include contributions from: the thermocapillary flow, with a G factor on the order of 10, the container geometry and the NePCM, which provide additional improvements of 50% and 10%, respectively. Overall, an NePCM in a liquid bridge geometry would melt roughly 17 times faster than the same configuration of a pure PCM without a free surface.

Conclusions

The present and future of space exploration requires improved thermal control systems. Organic phase change materials (PCMs), with their large latent heat, suitable melting temperatures and chemical stability, represent an attractive option for passive thermal control.

Recently, the use of thermocapillary flows has been shown to be a viable strategy for improving the low heat transfer rate of organic PCMs, whose performance is otherwise hampered by long melting/solidification cycles. In this work, we summarize the basic options that have been proposed to accelerate the thermocapillary-driven melting of PCMs in microgravity: an appropriate selection of container geometry and the use of dispersed nanoparticles to increase the effective conductivity of the PCM. Compared to the case of pure conduction, the complementary improvments from the thermocapillary effect, container geometry and the addition of nanoparticles can increase the melting rate by an order of magnitude.

Acknowledgements

This work was supported by the Ministerio de Ciencia e Innovación under Project No. PID2020-115086GB-C31, and by the Spanish User Support and Operations Centre (E-USOC), Center for Computational Simulation (CCS).

References

J. M. Ezquerro, P. Salgado Sánchez, A. Bello, J. Rodríguez, V. Lapuerta and A. Laverón-Simavilla, Experimental evidence of thermocapillarity in phase change materials in microgravity: measuring the effect of Marangoni conbvection in solid/liquid phase transitions, *International Communications in Heat and Mass Transfer*, 113, 104529 (2020)

P. Salgado Sánchez, J. M. Ezquerro, J. Fernández and J. Rodríguez, Thermocapillary effects during the melting of phase change materials in microgravity: heat transport enhancement, *International Journal of Heat and Mass Transfer*, 163, 120478 (2020)

R. Varas, P. Slagado Sánchez, J. Porter, J. M. Ezquerro and V. Lapuerta, Thermocapillary effects during the melting in microgravity of phase change materials with a liquid bridge geometry, *International Journal of Heat and Mass Transfer*, 178, 121586 (2021)

J. Porter, A. Laverón-Simavilla, M. M. Bou-Ali, X. Ruiz, F. Gavalda, J. M. Ezquerro, P. Salgado Sánchez, U. Martínez, D. Gligor, I. Tinao, J. Gómez, J. Fernández, J. Rodríguez, A. Borschak Kachalov, V. Lapuerta, B. Seta, J. Massons, D. Dubert, A. Sanjuan, V. Shevtsova and L. García-Fernández, The “Effect of Marangoni Convection on Heat Transfer in Phase Change Materials” experiment, submitted to *Acta Astronuatica*, under review.

A. Borshchak Kachalov, P. Salgado Sánchez, U. Martínez, J. Fernández and J. M. Ezquerro, Optimization of thermocapillary-driven melting in trapezoidal and triangular geometry in microgravity, *International Journal of Heat and Mass Transfer*, 185, 122427 (2022)

S. Madruga and C. Mendoza, Heat transfer performance and thermal energy storage in nano-enhanced phase change materials driven by thermocapillarity, *International Communications in Heat and Mass Transfer*, 129, 105672 (2021)

On the potential of thermodiffusion as means for large-scale desalination

Shuqi Xu[1] and Juan F. Torres[1*]

[1] School of Engineering, Australian National University, Canberra, ACT 2601, Australia
* Email: felipe.torres@anu.edu.au

Introduction

Thermodiffusion (TD) has found use in few yet essential engineering applications, such as enrichment of nuclear material (Nier, 1989) and analysing protein binding (Wienken *et al.*, 2010). Despite TD being a phenomenon first discovered by Soret in 1879 through a desalination process (Soret, 1879), it has never been used as means of desalination because it is a weak phenomenon that may not meet the requirements of purity (<500 ppm) and yield (>100 m^3/day) for large-scale desalination. A facile method for removing salt ions from water could be key in alleviating water scarcity, which is one of the most pressing issues of our time (World Bank, 2019). Conventional desalination methods such as distillation and reverse osmosis are either very energy intensive or have membrane fouling issues. To the best of our knowledge, there are only two theoretical papers exploring the possibility of thermodiffusive desalination (TDD) including our preliminary work (Abdeljabar, 2011; Xu *et al.*, 2022). TDD is appealing because it is a membrane-free method that can be driven by low-grade thermal energy from industrial waste heat, solar energy or the surrounding environment. Here, we explore the possibility of scaling up TDD and reflect on its challenges and prospects. First, we provide experimental results showing that TD is able to achieve a concentration drop (C_{drop}) of 450 ppm and 700 ppm from a NaCl concentration of 30,000 ppm (seawater) and 60,000 ppm (brine), respectively, when passing the solution through a channel. Since C_{drop} is relatively small after a single pass, multiple passes are implemented to increase it. However, the recovery rate for that concentration drop is reduced to 6% (i.e. the percentage of low salinity water extracted from a high salinity water volume). A cascaded microfluidic structure that can potentially overcome this challenge and scale up TDD is proposed and theoretically assessed.

Single-pass TDD

The concept of TDD is depicted in **Figure 1a**. A laminar flow of an initially homogeneous saline solution passes through a rectangular channel with its upper and lower walls kept at constant high and low temperatures, respectively. NaCl is thermophobic in water above 12°C (Caldwell, 1973), thus the salt migrates to the cold side in our thermodiffusion experiment. Together with the thermal stratification, solute density stratification stabilises the flow. TDD is potentially a low-energy consumption desalination methods as it does not involve phase change (as in distillation) and can be driven by low-temperature heat from the sun or industrial processes. Phase-shifting interferometry (PSI) (Torres *et al.*, 2013) is used to accurately measure the concentration difference ΔC between the top and bottom streams, which come from an equally bifurcated flow at the end of the rectangular channel. As shown in **Figure 1b**, we control the flow rate while degassing the saline solution to avoid bubble-induced mixing. A smaller channel height means faster thermodiffusive separation but also larger heat flux. Discussion on the channel dimensions and other control parameters can be found in our previous numerical work (Xu *et al.*, 2022).

ΔC between the two streams was precisely measured using PSI and the results are shown in **Figure 2**. ΔT_{meas} is obtained from the mean measured temperatures from thermocouples placed along the channel, while ΔT_{set} refers to that set in the two water baths. The effect of ΔT_{meas} on separation is shown together with CFD results assuming a fully-developed velocity field. For the same mean temperature T_{mean}, we could confirm that the larger the ΔT_{meas}, the larger the ΔC. In addition, since the Soret coefficient S_{T} is larger at higher temperatures (Caldwell, 1973), ΔC increases with T_{mean} for the same ΔT_{meas}. The effect of flow rate was also explored. For a flow rate less than 5 mL/min, saline water stays in the 1 mm-high channel for more than 2 min, achieving a near maximum ΔC. Larger flow rates drop ΔC as there is not enough residence time of the solution in the channel for thermodiffusion to fully separate the NaCl species before reaching the bifurcation.

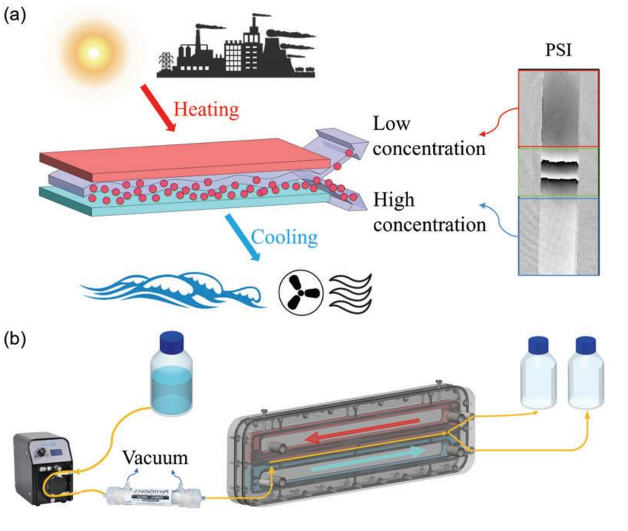

Figure 1: Concept demonstration and experimental setup of the TDD unit. (**a**) Seawater flows through the TDD channel with a positive temperature gradient across its height, then separates into two streams bifurcated at the exit. ΔC between bifurcated water streams is indicated by digital interferometry. Here, the top-stream sample (red square) was injected into a test cell half-filled with bottom-stream sample (blue square). The fringes in the green square indicate ΔC when unwrapped. (**b**) The flow rate of the saline water in the channel is controlled by a peristaltic pump. Saline water is degassed before entering the channel. The fluid path for the saline water is indicated by orange lines. The channel is 500 mm long, 20 mm wide, and 1 mm high. The collection bottles for the two streams are at the same height, ensuring equal flow rate. Water circulating from two separate water baths (blue and red arrows) creates the ΔT. Six pairs of thermocouples were distributed 100 mm apart on both sides of the channel.

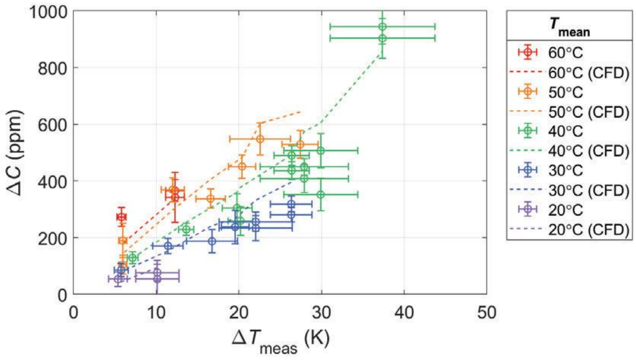

Figure 2: Single-pass TDD quantified by the ΔC between the two water streams with different T_{mean} and ΔT_{meas}.

Multiple passes

As shown in the single-pass case (**Figure 2**), the maximum ΔC between the top and lower flow streams is ca. 900 ppm for $\Delta T_{\text{set}} = 60$ K ($\Delta T_{\text{meas}} = 37$ K). Above $\Delta T_{\text{set}} = 60$ K, the heat exchange between the two water baths was too large, resulting in a marginal increase in ΔT_{meas}. Note that 900 ppm is 3% of the initial seawater concentration (relative value). Moreover, the concentration drop C_{drop} of the top stream relative to the inlet concentration is only half of that value (i.e. 450 ppm). This small drop in concentration is not enough to obtain freshwater water useful for agriculture (accounting for ca. 70% of water use worldwide), which requires 95% relative concentration drop. To amplify the thermodiffusive separation, a simple way is to accumulate the top low-concentration stream in a container and then pass it again through the channel. This experiment was done for both seawater and brine, with results shown in **Figure 3**. C_{drop} increases with the number of passes, demonstrating that TDD can be enhanced. Furthermore, it is noticed that C_{drop} is larger in brine than in seawater. This is because thermodiffusion increases with concentration (reaching a maximum at $C = 0.5$ as per thermodiffusion mass flux equation (Xu *et al.*, 2022)). This result suggests that TDD may be a potential pre-treatment method when using brine as the RO water feed because RO is more energy intensive when C is high. The significant drawback of this multiple-passes TDD is that the volume of the desalinated stream drops exponentially. In the last pass, the volume (i.e. recovery rate) was too small that the contamination in the channel and the peripherals diminished the concentration drop due to TDD.

This multiple-passes TDD is not efficient because the 'high' concentration solution from a pass may have a lower concentration than the initial saline water (seawater or brine) in the system, but it is nonetheless discarded. A scalable microfluidic thermodiffusive separation device known as the Burgers cascade was proposed for enhancing thermodiffusive separation in gases (Saiki *et al.*, 2020). It is a two-dimensional device made up of many small cells, each similar to a mini TDD channel. Different species in seawater have different S_T (Caldwell and Eide, 1981). If assuming seawater behaves as a binary mixture and has a bulk S_T of 0.005 K^{-1}, the single-pass TDD CFD model can be applied to this device. Concentration in each cell was theoretically modelled and the low concentration of 1000 ppm was predicted for a recovery rate of 10%. Future work will experimentally validate the assumption of bulk thermodiffusion in multicomponent electrolytes and improve the Burgers cascade design to maximise the recovery rate and concentration drop.

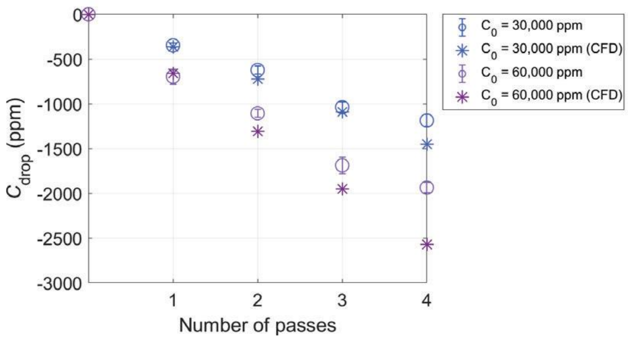

Figure 3: Multiple-pass TDD of NaCl aqueous solution. The concentration drop is plotted as a function of number of passes recirculated for two different initial concentrations (30,000 and 60,000 ppm).

Conclusions

It was experimentally shown that thermodiffusion can drop the concentration in a binary approximation of seawater (or brine) by around 450 ppm (or 700 ppm) in a single pass, which is only about 3% of the initial concentration. However, at least 95% of salt needs to be removed to obtain fresh water. In an attempt to amplify C_{drop}, multiple-pass TDD was used and $C_{\text{drop}} > 1000$ ppm was achieved, but an exponential drop in recovery rate would render TDD unfeasible. To address this problem, a scalable microfluidics device for TDD is proposed an analysed theoretically.

Acknowledgements

We thank the Foundation for Australia-Japan Studies and the Australian Department of Foreign Affairs and Trade for their financial support, the National Computational Infrastructure for providing computational resources, and the valuable support from the Australian National University through an international PhD student scholarship. We thank Mr Roelof Pottas for his work in the technical design of the TDD channel.

References

R. Abdeljabar, 'An innovative approach of salt separation using the soret effect', *Fluid Dynamics and Materials Processing*, 7, pp. 217–229, (2011)

D. R. Caldwell, 'Thermal and Fickian diffusion of sodium chloride in a solution of oceanic concentration', *Deep-Sea Research and Oceanographic Abstracts*, 20, pp. 1029–1039. (1973)

D. R. Caldwell, and S. A. Eide, 'Soret coefficient and isothermal diffusivity of aqueous solutions of five principal salt constituents of seawater', *Deep Sea Research Part A, Oceanographic Research Papers*, 28, pp. 1605–1618, (1981)

A. O. Nier, 'Some reminiscences of mass spectrometry and the manhattan project', *Journal OF Chemical Education*, 66, pp. 385–388, (1989)

T. Saiki, *et al.* 'Separation of a binary gas mixture by thermal diffusion in a two-dimensional cascade of many small cavities', *International Journal of Heat and Mass Transfer*, 163, p. 120394, (2020)

C. Soret, Sur l'état d'équilibre Que Prend, Au Point de Vue de Sa Concentration, Une Dissolution Saline Primitivement Homogène, Dont Deux Parties Sont Portées à Des Températures Différentes; Archives de Genève, 3e Periode.', *Journal de Physique Th´eorique et Appliqu´ee*, 9, pp. 331–332, (1879)

J. F. Torres, *et al.* 'Measurement of Soret and Fickian diffusion coefficients by orthogonal phase-shifting interferometry and its application to protein aqueous solutions', *Journal of Chemical Physics*, 139, (2013)

C. J. Wienken, *et al.* 'Protein-binding assays in biological liquids using microscale thermophoresis', *Nature Communications*, 1, (2010)

World Bank 'The Role of Desalination in an Increasingly Water-Scarce World', (2019)

S. Xu, *et al.* 'Scaling up thermodiffusive separation through a microchannel Scaling Up Thermodiffusive Separation through a Microchannel', *AFMC23-438*, (2022)

Numerical investigation of a pair of bubbles rising in Newtonian and shear-thinning fluids with passive scalar transfer at the interface

K. Kazemi[1], A. Vernet[1], F. X. Grau[1], S. Cito[1], A. Fabregat[1]

[1]Department of mechanical engineering, Universitat Rovira i Virgili, Tarragona, Spain, Koorosh.Kazemi@urv.cat

Introduction

Fluid systems containing bubbles are widely observed in natural phenomena such as breaking waves (Deike et al. 2016} and a wide range of engineering applications including bubble column reactors (Kantarci et al. 2005) and heat exchangers (Sadighi 2014). Momentum and heat/mass transfer between the bubbles and the surrounding fluids are common phenomena in many industrial processes including chemical reactors based on bubbly flow (Schluter et al. 2021), multiphase cooling systems (Suranjan et al. 2009), wastewater treatment (Shirai et al. 1999), metal refining (Wang et al. 1996) and also in nature such as bubbly plumes under the oceans (Boufadel et al. 2020).

Generally, buoyancy-driven bubbly flows are utilized to improve heat/mass transfer behavior in industrial applications. Heat/mass transfer across the bubble's interfaces can be affected by the flow behavior inside and around the bubbles, flow characteristics, topological changes in the bubbles, distributions of the bubbles, interactions between the bubbles, and bubble coalescence or breakup. To measure the heat/mass transfer rate, advection and diffusion within each phase and also transfer across the interface should be considered. Prediction of the heat/mass transfer can be a challenging problem due to the bubbles interactions, deformable interface, and differences between the diffusion coefficients in each phase (which could be of orders of magnitude). Interactions between the bubbles is one of the most important issues in bubbly flows which can lead to important physical processes occurring in the system such as coalescence and breakup. For example, coalescence can affect the performance of the system by changing the heat/mass transfer rate caused by altering the interfacial area. The evolution, flow dynamics and scalar transport in a system comprised of only two bubbles can be of help to better understand the nature of bubbly flows and improve the design of gas-liquid equipment. In this context, it is necessary to have sufficient knowledge of the bubbles dynamics, especially interactions between the bubbles, to predict the heat/mass transfer rate in bubbly flows.

A numerical simulation was performed to study the motion and interaction of two in-line bubbles rising in Newtonian and shear-thinning fluids and mass/heat transfer across the bubbles interface was investigated. A three-dimensional Volume-of-Fluid method (VOF) was used to capture the interface and the Carreau model was used to describe the rheological behavior of the shear-thinning fluid. The dynamical behavior of a single air bubble rising in water depends on the Galilei (Ga) and Bond (Bo) numbers shown in a Ga-Bo phase plot in Figure 1. As can be seen, there are five different regimes including I. axisymmetric, II. skirted, III. oscillatory, IV. peripheral breakup, and V. central breakup. Here, the dynamical behavior of a pair of bubbles and mass transfer across the bubbles interface in each regime have been studied both in a Newtonian fluid and a shear-thinning fluid. Moreover, the effects of the rheological properties such as flow index (n) and inelastic time constant (λ) on the mass transfer across the bubbles interface and on the bubbles dynamics have been investigated for a fixed set of (Ga,Bo).

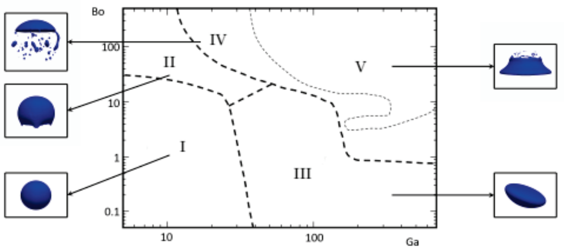

Figure 1: Ga-Bo phase plot of an air bubble rising in water.

Conclusions

It is found that the dynamical behavior of a pair of bubbles can be different from the one of a single bubble and decreasing the flow index leads to increasing local Ga. λ has a small effect on the mass transfer rate while the oscillatory behavior of the bubbles intensifies by increasing λ.

Acknowledgements

This work was funded by the Spanish Ministerio de Ciencia, Innovacion y Universidades through the grants DPI2016 75791-C2-1-P and RTI2018-100907-A-I00 (MCIU/AEI/FEDER, UE) and also by the Generalitat de Catalunya through the grant 2017-SGR-1234.

References

L. Deike, M.W. Kendall, and S. Popinet, Air entrainment and bubble statistics in breaking waves, *Journal of Fluid Mechanics*, 801, 91–129, (2016)

N. Kantarci, F. Borak, K.O. Ulgen, Bubble column reactors, *Process Biochemistry*, 40, 2263-2283, (2005)

J. Sadighi Dizaji, Heat transfer enhancement due to air bubble injection into a horizontal double pipe heat exchanger, *Automotive Science and Engineering*, 4, (2014)

M. Schlüter, S. Herres-Pawlis, U. Nieken, Ulrich, U. Tuttlies, D. Bothe, Small-Scale Phenomena in Reactive Bubbly Flows: Experiments, Numerical Modeling, and Applications, *Annual Review of Chemical and Biomolecular Engineering*, 12, 625-643, (2021)

S. Suranjan, S. R. Panneer, Direct Numerical Simulation of Heat Transfer in Spray Cooling Through 3D Multiphase Flow Modeling Using Parallel Computing, *Journal of Heat Transfer*, 131, (2009)

Y. Shirai, M. Wakisaka, O. Miyawaki, S. Sakashita, Effect of seed ice on formation of tube ice with high purity for a freeze wastewater treatment system with a bubble-flow circulator, *Water Research*, 33, 1325-1329, (1999)

L. Wang, H.G. Lee, P. Hayes, A New Approach to Molten Steel Refining Using Fine Gas Bubbles, *ISIJ International*, 36, 17-24, (1996)

M.C. Boufadel, S. Socolofsky, J. Katz, Joseph, D. Yang, C. Daskiran, W. Dewar, A Review on Multiphase Underwater Jets and Plumes: Droplets, Hydrodynamics, and Chemistry, Reviews of Geophysics, 58, (2020)

Analysis of non-equilibrium fluctuations during thermodiffusion in a binary mixture by two-wavelenght shadowgraphy

D.E. Bouyou Bouyou[1], H. Bataller[1], F. Croccolo[1]

[1] *Universite de Pau et des Pays de l'Adour, E2S UPPA, CNRS, TotalEnergies, LFCR UMR5150, Anglet, France*, fabrizio.croccolo@univ-pau.fr

Introduction

Non-equilibrium fluctuations (NEFs) are a model for investigating the diffusion processes in complex fluids. Shadowgraphy is a robust near-field scattering technique with a simple configuration and is highly sensitive to NEFs. Besides allowing the measurement of the transport properties in complex fluids (Croccolo et al. 2006a, Croccolo et al. 2012), shadowgraphy allows probing the effect of diffusion, gravity (Croccolo et al. 2006b) and confinement (Giraudet et al. 2015) on the dynamics of NEFS and the presence of propagating waves due to the coupling of the different relaxation modes (Croccolo et al. 2019; García-Fernández et al. 2019). The need for developing the two-wavelength shadowgraphy is dictated by the impossibility of separating the two solutal relaxation modes in a ternary molecular mixture with a classical one-wavelength shadowgraph (Bataller et al. 2016). Indeed, in such mixture, the eigenvalues of the diffusion matrix are almost identical, implying that the relaxation times of the NEFs of the two independent concentration fields cannot be distinguished. In such case, it is impossible to differentiate the two eigenvalues of the diffusion matrix. Using the same approach as the one implemented in the two-wavelength selectable optical digital interferometry (SODI) of the DCMIX project (Mialdun et al. 2020) to separate the two independent concentration fields of a ternary mixture, a two-wavelength shadowgraph would allow, in principle, to separate the contributions of the two concentration fields to the shadowgraph signal. Indeed, the same approach can be used to separate NEFs of temperature and concentration fields in a binary mixture subjected to a temperature gradient. The binary system is a simple and effective test for the two-wavelength shadowgraphy technique. In this case, the relaxation modes of temperature and concentration are well distinct in time and can therefore be also separated with a classical shadowgraph by fitting the structure function of the NEFs with two exponential decays. In this work, we present the principles of two-wavelength shadowgraphy and demonstrate the technique working principle by performing a thermodiffusion experiment on an equimassic binary mixture of toluene/n-hexane subjected to a temperature difference of 20 K.

Working principle of two-wavelength shadowgraphy

The shadowgraph consists of two superluminescent diodes ($\lambda = 675 \pm 13$ nm or $\lambda = 405 \pm 13$ nm) connected to a single-mode optical fiber that delivers a weakly coherent beam collimated by an achromatic lens. The intensity of the light scattered strikes the CCD sensor of an s-CMOS camera placed in the near field of the thermodiffusion cell containing the sample.

Owing to their random nature, NEFs are characterized by an autocorrelation function and static structure factor. These quantities can be calculated theoretically by fluctuating hydrodynamics (Ortiz De Zárate et al. 2006) and are directly related to the static structure factor and autocorrelation function of the refractive index fluctuations measured by shadowgraphy. The case of an ordinary binary mixture (with a large Lewis number) subjected to a temperature gradient in the Boussineq approximation (pressure fluctuations are neglected) is considered here. With a large Lewis number, all couplings between the temperature and concentration fluctuations are neglected, at least for large enough wave numbers, and the autocorrelation function of the refractive index fluctuations for a given wavelength λ can be written as:

$$S_{\lambda}(q,\Delta t) = \left(\frac{\partial n}{\partial c}\right)_{\lambda}^{2} S_{cc}(q,\Delta t) + \left(\frac{\partial n}{\partial T}\right)_{\lambda}^{2} S_{TT}(q,\Delta t) \qquad (1)$$

where q is the wave number, i.e. the modulus of the wave vector. The derivatives of the refractive index with respect to the temperature and concentration depend on the wavelength of the probe beam. Using shadowgraphy, the wave vector at which the structure factor or autocorrelation function is measured does not depend on the wavelength of the probe beam or scattering angle, as is the case in far-field scattering. Therefore, for the same wave number q, the autocorrelation function of NEFs with probe beams of different wavelengths can be easily measured. At large wave numbers, any coupling between different modes, which is responsible for the appearance of the propagating modes, disappears. The concentration and temperature signals can be easily separated if the optical contrast factor matrix is known:

$$\begin{pmatrix} S_{cc}(q,\Delta t) \\ S_{TT}(q,\Delta t) \end{pmatrix} = \begin{pmatrix} \left(\frac{\partial n}{\partial c}\right)_{\lambda_1}^{2} & \left(\frac{\partial n}{\partial T}\right)_{\lambda_1}^{2} \\ \left(\frac{\partial n}{\partial c}\right)_{\lambda_2}^{2} & \left(\frac{\partial n}{\partial T}\right)_{\lambda_2}^{2} \end{pmatrix}^{-1} \cdot \begin{pmatrix} S_{\lambda_1}(q,\Delta t) \\ S_{\lambda_2}(q,\Delta t) \end{pmatrix} \qquad (2)$$

Result and discussion

From the shadowgraph images, one can thus calculate the structure function (figure 1. a), and the static structure factor (figure 1. b), from which the autocorrelation functions (figure 1.c) of the NEFs at the two wavelengths are calculated. Having previously measured the optical contrast factors by means of a refractometer, the autocorrelation functions of the temperature and concentration NEFs can be separated (figure 1. d). On the one hand, the individual analysis of the structure functions makes it possible to determine the relaxation times of the NEFs of temperature and concentration, as well as their intensities. On the other hand, the analysis of the autocorrelation functions of the NEFs of concentration and temperature, separated optically, makes it possible to determine the relaxation times distribution of the fluctuations as well as their intensities. Preliminary analysis shows that the results obtained by the two procedures correspond for the majority of the wavenumbers. Further analysis is in progress, and the results will be presented at the IMT15.

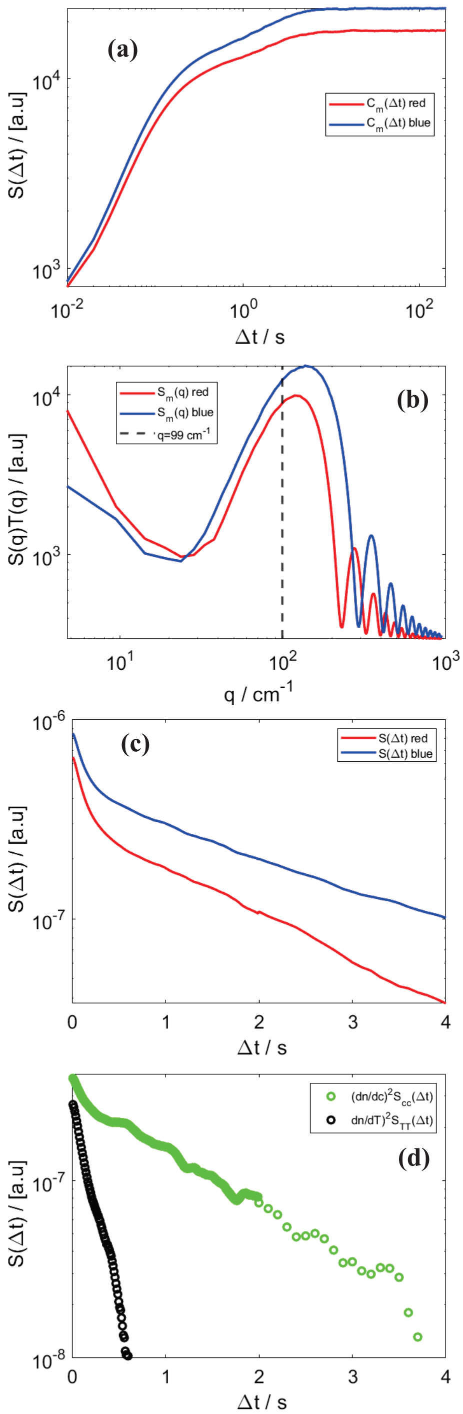

Figure 1 (a) Structure functions for both wavelengths and for q = 118 cm^{-1}. (b) Static structur factor for both wavelengths. The vertical dashed line stands for q = 118 cm^{-1} (c) Autocorrelation functions extracted from (a) and (b) and for q = 118 cm^{-1}. (d) Extraxted autocorrelation functions of the temperature and concentration NEFs as obtained by applying Eq. 2 to the data of panel (c). The distributions of the relaxation times of the temperature and concentration fluctuations are determined from the separate signals. Analysis of the distribution of the relaxation times makes it possible to determine the thermal and mass diffusion coefficients.

The procedure for separating the temperature and concentration modes in a binary system is robust enough despite a large value of the condition number of the contrast factors matrix (>400). While the analysis involved in SODI is based on fitting through a series of exponential decays, the Fourier-based analysis of Shadowgraphy is based on simple exponential decays. This actually increases the applicability of the Shadowgraph technique to a larger range of condition numbers. The large condition number obtained here, is due to the fact that the thermal contrast factor varies very little with the wavelength. This result validates the technique and promises even better results when separating solutal modes in a ternary mixture.

Conclusions

In this work, we make a first demonstration of the faiseability of the two-wavelength shadowgraphy technique to separate the signals of uncoupled fluctuating fields in a binary or ternary liquid mixture. First, we tested the ability of the technique in separating the temperature and concentration fields in a binary mixture subjected to a temperature gradient. The results obtained make it possible to validate the technique and demonstrate its robustness. The next step of our work will be to test the technique on a ternary polymer mixture and then on a ternary molecular mixture.

Acknowledgements

We acknowledge financial support from the CNES and from the E2S UPPA Hub Newpores and the Industrial Chair CO2ES supported by the Investissements d'Avenir French programme managed by ANR (ANR16IDEX0002). Work partially supported by the European Space Agency, CORAMAP TechNES Contract No. 4000128933/19/NL/PG.

References

F. Croccolo, D. Brogioli, A. Vailati, M. Giglio and D.S. Cannell, Use of dynamic schlieren interferometry to study fluctuations during free diffusion, *Applied Optics*, 45, 2166, (2006a)

F. Croccolo, H. Bataller and F. Scheffold, A light scattering study of non equilibrium fluctuations in liquid mixtures to measure the Soret and mass diffusion coefficient. *The Journal of chemical physics*, 137, 234202, (2012)

F. Croccolo, D. Brogioli, A. Vailati, M. Giglio and D.S. Cannell, Effect of gravity on the dynamics of non equilibrium fluctuations in a free diffusion experiment, *Annals of the New York Academy of Sciences*, 1077, 365, (2006b)

C. Giraudet, H. Bataller, Y. Sun, A. Donev, J. M. Ortiz de Zárate and F. Croccolo, Slowing-down of non equilibrium fluctuations in confinement, *Europhys. Lett,* 111, 60013, (2015)

F. Croccolo, L. Garcia-Fernández, H. Bataller, A. Vailati and J. M. Ortiz de Zárate, Propagating modes in a binary liquid mixture under thermal stress, *Phys. Rev. E*, 99, 012602, (2019)

L. García-Fernández, P. Fruton, H. Bataller, J. M. Ortiz de Zárate, and F. Croccolo, Coupled non-equilibrium fluctuations in a polymeric ternarymixture, *Eur. Phys. J. E*, 42, 124, (2019)

A. Mialdun et al., Data quality assessment of Diffusion Coefficient Measurements in ternary mIXtures 4 (DCMIX4) experiment, *Acta Astronautica*, 176, 204-215 (2020)

H. Bataller, C. Giraudet, F. Croccolo, et al. Analysis of non-equilibrium fluctuations in a ternary liquid mixture. *Microgravity Science and Technology*, vol. 28, p. 611-619, (2016)

J. M. Ortiz De Zárate, and Jan V. Sengers. Hydrodynamic fluctuations in fluids and fluid mixtures, *Elsevier*, Amsterdam (2006)

Integrating artificial intelligence to the structure function analysis

M. Chraga[1], F. Croccolo[1]

[1]Universite de Pau et des Pays de l'Adour, LFCR UMR5150, E2S UPPA, CNRS, TotalEnergies, Anglet, France
mohammed.chraga@univ-pau.fr

Introduction

Fluctuations occur spontaneously in a fluid and are amplified by a gradient of at least one thermodynamic variable (concentration, temperature or pressure). The resulting non-equilibrium fluctuations (NEFs) can be studied by means of several optical techniques, such as Dynamic Shadowgraphy, Dynamic Schlieren and Differential Dynamic Microscopy (DDM). The spatio-temporal evolution of NEFs, can be represented by the structure function (Croccolo et al. 2007, Croccolo et al. 2012, Schulz-DuBois and Rehberg 1981) over a wide range of wave numbers, as calculated by means of the differential dynamic algorithm (DDA). The structure function is obtained using a series of images obtained by one of the optical techniques cited above (Croccolo et al. 2007, Norouzisadeh et al. 2021). At each wave number, the structure function can be analyzed after providing a theoretical model (fitting equation) to extract the transport properties of the fluid under study, such us the mass diffusion coefficient, critical cut-off vector, and eventually from those values, the Soret and thermodiffusion coefficients can be derived. The applicable model varies depending on the nature and conditions of the experiment as well as the wavenumber. The best model should be used for each wave number in order to obtain a suitable fitting, which can be a challenge for the analysis of large amounts of data, especially when different physical phenomena dominate at different wavenumbers.

In this study, we take advantage of artificial intelligence (AI) to analyse the experimental structure function. We developed a program based on neural networks that chooses the best model to fit the structure function for each wave number thus allowing an automatic, fast and efficient analysis independent of the amount of data to be treated.

Structure function analysis

Fitting theoretical models to experimental data is important in all scientific fields. It aims at estimating unknown parameters of models from data using a variety of statistical methodologies. In our case, the experimental structure function should be fitted with a theoretical model to extract the transport properties of the fluid under study. The basic theoretical equation of the structure function is given by:

$$SF = 2\{T(q)S(q)[1 - ISF(q,\Delta t)] + BG(q,\Delta t)\}, \quad (1)$$

where q and Δt represent the wave number and the correlation time, respectively. T(q) is the optical transfer function of the shadowgraph, S(q) the static power spectrum of the fluid density fluctuations and $ISF(q,\Delta t)$ is the Intermediate Scattering Function. The latter corresponds to the dynamic part of the structure function that can be modelled by a sum of exponential decays:

$$ISF(q,\Delta t) = \sum_{i=1}^{n} a_i \exp\left(-\frac{\Delta t}{\tau_i(q)}\right), \quad (2)$$

where n is the number of relaxation modes in the system (e.g. concentration and temperature), a_i are the relative amplitudes of the different modes such as $\sum_i a_i = 1$ and the $\tau_i(q)$ represent the decay times.

At small wave number, in the presence of propagating modes, a sinusoidal term needs to be included to describe the oscillations in the SF originated by the presence of propagating modes (Croccolo et al. 2019):

$$ISF(q,\Delta t) = a_1\, exp\left(-\frac{\Delta t}{\tau_1(q)}\right) + \frac{a_2}{\cos[\phi(q)]} \times \cos[\Omega(q)\Delta t + \phi(q)]\exp\left(\frac{\Delta t}{\tau_2(q)}\right), \quad (3)$$

where Ω and ϕ depend on q and represent the oscillation frequency and phase.

In Eq. 1, $\mathrm{BG}(\mathrm{q},\Delta t)$ represents the optical background that can take different forms depending on the experimental conditions. Here, we take two possible forms, constant or quadratic:

$$BG_1(q,\Delta t) = A(q), \quad (4)$$

$$BG_2(q,\Delta t) = A(q) + B(q)\Delta t^2, \quad (5)$$

where A describes the experimental noise, while B is related to the stability of the background itself.

Automatic analysis

The experimental structure function can be fitted using different models, depending on the investigated system. Manual or non-automatic analysis of a large amount of data is time consuming and may lack accuracy. Indeed, in a thermo-diffusion experiment, the propagation modes are expected at small wave numbers and both the concentration and temperature modes are expected at different wave number ranges. In addition, the optical background can take different shapes from one wave number to another. In this study, we show how we can leverage the power of the deep learning, especially convolutional neural networks (CNN) (Albawi et al. 2017) to automatically analyze the experimental structure functions. Six possible fitting equations were considered, ISF in the propagation modes, ISF with one or two exponentials ($n = 1$ or $n = 2$), and constant or quadratic background. The output coefficients are: $T(q)S(q)$, $a_i(q)$, $\tau_i(q)$, $A(q)$ and $B(q)$.

As shown in Fig. 1, our approach consists in passing the image pixel values of the structure function shape through several convolutional layers looking for patterns and creating feature maps that represent the inputs of a fully connected artificial neural network (ANN), to finally obtain the best theoretical model for analyzing the structure function. To do so, three steps were followed. First, a "learning phase" allows creating learning classes containing different representative structure function shapes. Homogeneity within each class should be maximized while homogeneity between classes should be minimized in order to reach high accuracy results.

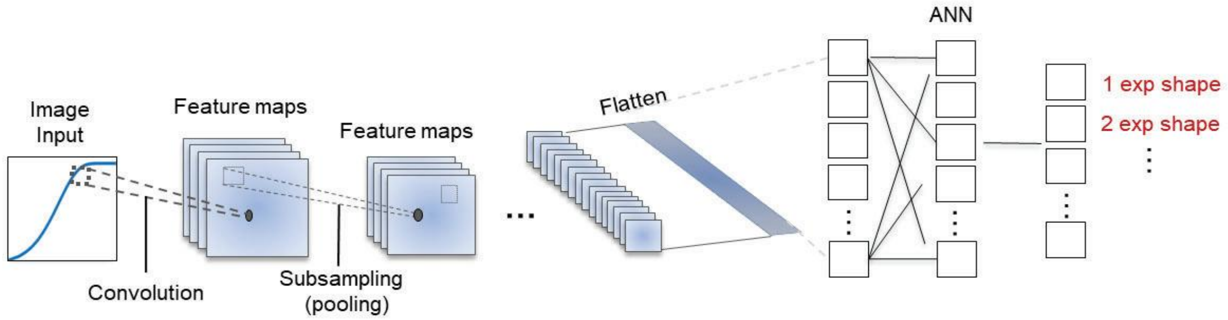

Figure 1: A typical CNN architecture scheme applied on recognizing the more adequate fitting model to analyze the experimental structure function.

Second, “data smoothing” allows maximizing the software accuracy by making the new data shape as similar as possible to the learning data before choosing its best fitting equation. Third, “data clustering” predicts the more appropriate fitting equation of the experimental structure functions using a CNN. The number of possible fitting equations can be easily increased by adding more homogeneous-learning-classes in the learning phase. The approach is based on full-connected neural networks, which implies a voluminous calculation and very expensive computing time. Therefore, high-performance computing techniques using graphics processing unit (GPU) are highly recommended to obtain results in an optimal time. Once the software has selected the right model, an implemented Levenberg-Marquad non-linear least square fitting routine is used to extract the amplitudes and the decay times of the fluctuations.

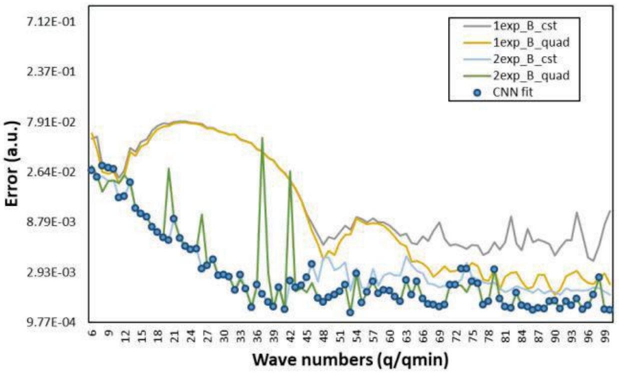

Figure 2: Error between thermodiffusion experimental data and SF model as a function of the wave number using different fit equation, one exponential with constant and quadratic background, two exponentials with constant and quadratic background, represented by the gray, yellow, blue and green lines, respectively. The blue points represent the choice of the CNN program.

Results

In Fig. 2 the errors (averaged absolute value of the differences) between the experimental data and the fitting equations using four fit models (one exponential with constant or quadratic background and two exponentials with constant or quadratic background) are shown. The experimental data were obtained from Shadowgraph visualization of a thermodiffusion experiment on a polystyrene (PS)-toluene binary mixture. We used the concatenated angular average of bi-dimensional structure functions of three series of images acquired at 1Hz, 10Hz and 100Hz.

Our approach shows high performance on choosing the best-fit equations of the experimental structure function for each wave number. We notice that the software chooses the best fitting equation as compared to the minimum error for most of the wave numbers.

Conclusions

In this study, we present a new approach for automatically analyzing the experimental structure function using AI, particularly, artificial neural networks. Automatic selection of the fitting equation for each wave number greatly facilitates data analysis. It offers better performance in terms of result quality and analysis time, particularly in the presence of different physical phenomena and when analyzing a large amount of data.

Acknowledgements

The authors express their gratitude to CNES and ESA for their support to the Giant Fluctuations project, as well as to the partners of the CO2ES Industrial Chair: E2S-UPPA, TOTAL, CNES and BRGM.

References

F. Croccolo, D. Brogioli, A. Vailati, M. Giglio, and D. S. Cannell, “Nondiffusive decay of gradient-driven fluctuations in a free-diffusion process,” *Phys. Rev. E*, vol. 76, no. 4, p. 041112, Oct. 2007.

F. Croccolo, H. Bataller, and F. Scheffold, “A light scattering study of non equilibrium fluctuations in liquid mixtures to measure the Soret and mass diffusion coefficient,” *The Journal of Chemical Physics*, vol. 137, no. 23, p. 234202, Dec. 2012.

E. O. Schulz-DuBois and I. Rehberg, “Structure function in lieu of correlation function,” *Appl. Phys.*, vol. 24, no. 4, pp. 323–329, Apr. 1981.

M. Norouzisadeh, M. Chraga, G. Cerchiari, and F. Croccolo, “The modern structurator: increased performance for calculating the structure function,” *Eur. Phys. J. E*, vol. 44, no. 12, p. 146, Dec. 2021.

F. Croccolo, L. García-Fernández, H. Bataller, A. Vailati, and J. M. Ortiz de Zárate, “Propagating modes in a binary liquid mixture under thermal stress,” *Phys. Rev. E*, vol. 99, no. 1, p. 012602, Jan. 2019.

S. Albawi, T. A. Mohammed, and S. Al-Zawi, “Understanding of a convolutional neural network,” in *2017 International Conference on Engineering and Technology (ICET)*, Antalya, Aug. 2017, pp. 1–6.

Study of salts free-diffusion by shadowgraphy

C.O. Oko[1], A.T. Ndjaka[1,2], F. Croccolo[1], H. Bataller[1]

[1]Universite de Pau et des Pays de l'Adour, E2S UPPA, CNRS, TotalEnergies, LFCR UMR5150, Anglet, France, henri.bataller@univ-pau.fr
[2]ENTENT, Aix-en-Provence, France

Introduction

The injection of CO_2 into deep saline aquifers has been endorsed as one of the most promising pathways to reduce CO_2 emissions in the atmosphere, as CO_2 being considered as one of the major causes of the greenhouse effect (Bachu et al. 2003). However, various studies on Carbon Capture, transport and geological Storage (CCS) have shown that injection of supercritical CO_2 in a deep saline aquifer perturbs the physio-chemical equilibrium of the medium, leading to highly coupled Thermal-Hydrodynamical-Mechanical-Chemical processes (Kolditz et al. 2012). All these coupling effects are not yet well understood and formally implemented into the numerical models. In this framework, we are investigating the coupling between the thermal gradients and the reactive transport taking place in a diffusion cell, in order to model what happens in a saline aquifer. For this, an already developed diffusion cell is used (Ndjaka et al. 2022), where we put in contact two saline solutions and investigate the fluctuations happening during the mixing process. In this diffusion cell, the observations are performed in the direction parallel to the concentration gradients by means of shadowgraphy. Here, we present the results of the validation of the device, as well as the analysis method, on the free-diffusion of sodium chloride NaCl, sodium sulphate Na_2SO_4 and calcium chloride $CaCl_2$ into water at 25 °C. By analysis of non-equilibrium fluctuations (NEFs), mass diffusion coefficients can be measured. A free diffusion experiment was carried out under homogeneous and stabilizing inhomogeneous temperature conditions and the impact of the temperature gradient on the mass diffusion process was investigated. After comparison of our results with literature, we were able to validate the experimental setup and methodology with the binary salt solutions.

Experimental procedure

The shadowgraph apparatus involves two main parts: a free diffusion cell, allowing to superimpose two layers of two different solutions and a precise differential temperature control through the liquid column, and the optical setup aimed at acquiring shadowgraph images of the density fluctuations (Croccolo et al. 2012). A light beam at wavelength (675±13) nm passes trought the sample in the vertical direction parallel to the imposed concentration gradients. The images acquired in real time by the camera (a CCD PIKE camera with a pixel side of $l_{pix} = 7.32\ \mu m$.) are saved on a workstation. In the absence of convective instabilities, we study the dynamics of fluctuations by calculating the Structure Function (SF) of the images by means of a differential dynamic Algorithm (Cerchiari et al. 2012). The expression of the normalized correlation function in the SF fitting equation, that describes the time evolution of concentration fluctuations, has been modified in order to integrate the thickness of the sample. Series of $N = 2500$ images of $1024 \times 1024\, pix^2$ have been recorded at frequency $f = 7.8\, Hz$, every 5 minutes (after closing the valves) over the first 20 minutes of each experiment, and then every 10 minutes until the equilibrium state.

Free-diffusion experiments with binary mixtures

The cell filling protocol entails filling the diffusion cell completely with a less dense solution after which the bottom half of the cell is filled with a denser solution. This is achieved with the help of a syringe pump by filling the cell simultaneously with the two fluids from the bottom and the top inlets, while the remixed fluid is let out through the two outlets positioned at the mid-height of the cell. Once this is achieved, a relatively flat horizontal interface between the two solutions is formed. Then, inlet and outlet valves are simultaneously closed and the free-diffusion process starts. In order to validate setup, procedure and the adjustment model, we carried out a first series of measurements by superimposing two solutions of different concentrations but of the same salt. c is the mean molar concentration of dissolved salt between the two layers, which corresponds to the equilibrium concentration. Δc is the molar concentration difference between the bottom and the top layers. The average temperature of the sample was set at $T = 25°C$. Experiments were performed at atmospheric pressure. In Fig. 1, we plot the mean mass diffusion coefficient D as a function of the normalised time (i.e. time divided by the characteristic diffuvise time τ_d) for the three binary mixtures studied in this work, obtained after analysis of the NEFs decay times.

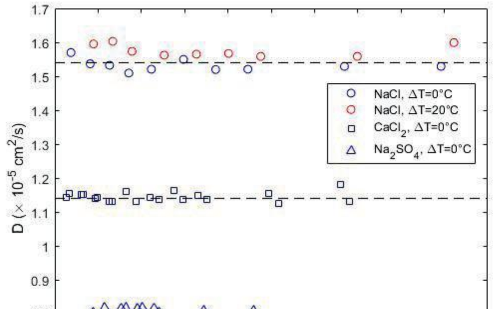

Figure 1: Mass diffusion coefficient D as a function of the normalized time for the free-diffusion experiments carried out at $T = 25°C$, blue and red circles for NaCl ($c = 2.7\, mol/L$, $\Delta c = 2.0\, mol/L$), blue squares for $CaCl_2$ ($c = 0.46\, mol/L$, $\Delta c = 0.8\, mol/L$) and blue triangles for Na_2SO_4 ($c = 0.5\, mol/L$, $\Delta c = 0.7\, mol/L$).

Literature values (Rard et al. 1979a, Rard et al. 1979b) are represented by the horizontal dashed lines in Fig. 1 for each binary mixture of interest. The agreement is pretty good in the three cases. Red points in Fig. 1 correspond to a series of measurement carried out at the average temperature of $T = 25°C$ and a temperature difference between the top and the bottom of the column of $\Delta T = 20°C$. The impact of the thermal gradient on the concentration NEFs was considered negligible.

Conclusion

We have studied by shadowgraphy the free-diffusion of the main salts representative of saline aquifers. An experimental setup has been developed and a first experimental procedure tested with saline solutions. We incorporated fluid column thickness effects into the fitting equation for the analysis of the measured structure functions. The procedure and the equation proved to be sufficient for the study of the free-diffusion process.

Acknowledgements

This work has been developed with the financial support from the Centre National d'Etudes Spatiales (CNES), the E2S UPPA Hub Newpores and the Industrial Chair CO2ES, the last two being supported by the Investissements d'Avenir French program managed by ANR (ANR16IDEX0002).

References

S. Bachu, J. J. Adams, Sequestration of CO2 in geological media in response to climate change: capacity of deep saline aquifers to sequester CO2 in solution, *Energy Convers. Manag*., 44, 3151–3175, (2003)

O. Kolditz, U.-J. Görke, H. Shao, and W. Wang, Eds., *Thermo-Hydro-Mechanical-Chemical Processes in Porous Media: Benchmarks and Examples*, vol. 86. Berlin, Heidelberg: Springer Berlin Heidelberg, (2012)

A. T. Ndjaka, L. García-Fernández, D. E. Bouyou Bouyou, A. Lassin, M. Azaroual, F. Croccolo, H. Bataller, Mass diffusion and Soret coefficient measurements of triethylene glycol/water binary mixtures by dynamic shadowgraphy, *Eur. Phys. J. E,* 45, 20, (2022)

F. Croccolo, H. Bataller, and F. Scheffold, A light scattering study of non-equilibrium fluctuations in liquid mixtures to measure the Soret and mass diffusion coefficient, *J. Chem. Phys.*, 137, 234202, (2012)

G. Cerchiari, F. Croccolo, F. Cardinaux, F. Scheffold, Note: Quasi-real-time analysis of dynamic near field scattering data using a graphics processing unit, *Rev. Sci. Instrum.*, 83, 106101, (2012)

J. A. Rard, D. G. Miller, The mutual diffusion coefficients of $NaCl/H_2O$ and $CaCl_2/H_2O$ at 25°C from Rayleigh interferometry, *J. Solution Chem.*, 8, 701–716, (1979a)

J. A. Rard D. G. Miller, The mutual diffusion coefficients of Na_2SO_4/H_2O and $MgSO_4/H_2O$ at 25°C from Rayleigh interferometry, *J Solution Chem.*, 8, 755–766, (1979b)

Oscillations and internal gravity waves in a stratified fluid – an engaging experiment to introduce advanced physics

Marina Carpineti[1], Irene Spongano[1], Fabrizio Croccolo[2] and Alberto Vailati[1]

[1] Dipartimento di Fisica Aldo Pontremoli, Università degli Studi di Milano, I-20133 Milano, Italy
[2] Universite de Pau et des Pays de l'Adour, E2S UPPA, CNRS, TotalEnergies, LFCR UMR5150, Anglet, France

Introduction

We propose a simple experiment that can be performed with household equipment, aimed at introducing students of all grades to the rich phenomenology of liquids stratified by diffusion, including processes such as levitation, Brunt–Väisälä oscillations and internal gravity waves.

Stratification in fluids is often observed in the presence of density gradients controlled by diffusion and thermal diffusion and has a great relevance in many natural systems such as the atmosphere, the oceans, and the stars.
A volume of fluid, or a body, with density in the same range as the stratification, can be in equilibrium at the appropriate height where the density coincides exactly with its own.
A slight displacement from the equilibrium position causes the body to oscillate due to an elastic recovery force originating from the density umbalance. This oscillation, whose frequency depends on the density gradient and is known as Brunt–Väisälä, can transmit its motion to the surrounding fluid and produce internal gravity waves. These phenomena are difficult to visualize as they only produce refractive index variations within the fluid.
The physics involved can be quite easily understood and has many relevant links with diffusion, hydrostatic, physics of stratified fluids and internal gravity waves. For that reason, an experiment able to evidence these aspects has demonstrated to be a very good candidate for an engaging activity for students (Carpineti et al, 2021).

In this new work, we propose a further experiment able to catch levitation, oscillations and gravity waves, but also the evolution of a density gradient through diffusion. The new experiment is a variant of the well-known Cartesian Diver experiment. In the traditional experiment, a hollow object is immersed in a sealed bottle containing a uniform liquid: when the applied pressure is varied the diver's density increases and the diver sinks, but when the original external pressure is restored, it goes back to the top of the liquid.
In our experiment, the diver floats in a density stratified liquid obtained by pouring coarse kitchen salt inside a jar of water. The salt grains initially sink to the bottom of the jar, where they start to dissolve into water. The diffusion of the salt determines the formation of a gravitationally stable density gradient, which slowly evolves in time. By varying the applied pressure, the diver's density changes and it moves to a different height accordingly. In contrast to the original version of the experiment where the diver can only sink or float, in this case the diver can stop in a stable equilibrium position within the fluid, at the height where its density is matched. When a sudden pressure pulse is applied, the diver, pushed off its temporary equilibrium position, starts oscillating due to a restoring force. Moreover, by changing the pressure on the container, students can span different heights and, performing measurements at different times, they can map different density gradients and observe the evolution in time of the diffusion process with a single non-invasive experiment.
It is also possible to make visible the internal gravity waves produced by the oscillating diver, by putting in suspension small fragments of a material of appropriate density, which localize in a fluid layer and oscillate when the gravity waves pass. With a simple experiment that students can project and realize by themselves with easy-to-find objects and by following all the steps, it is possible to let them experience how a simple diffusion process leads to complex phenomena of general interest.
Thanks to the use of simple free educational programs, which allow recording the diver oscillations, plotting and fitting the data, students can perform quantitative analysis of the results, and therefore enhance their understanding of the physics issues.

Figure 1 - A small glass bottle partially filled floats in equilibrium inside a density stratified liquid. Small plastic fragment with a known density are localized at a height where their density is matched and allow visualizing the internal gravity waves originated by the diver's oscillations.

Acknowledgements

Work supported by the European Space Agency

References

M. Carpineti; F. Croccolo; A. Vailati, Levitation, oscillations, and wave propagation in a stratified fluid, *Eur. J. Phys.,* 42, 055011, (2021) DOI: 10.1088/1361-6404/ac0fba2021

Chiral symmetry breaking induced by energy dissipation

A. Arango-Restrepo[1], O. Arteaga[2], D. Barragán[3], and J.M. Rubi[1]

[1]Departament de Física de la Materia Condensada, Universitat de Barcelona, Avinguda Diagonal 647, 08028 Barcelona, Spain, aarangor@unal.edu.co, [2]Departament de Física Aplicada, Universitat de Barcelona, Avinguda Diagonal 647, 08028 Barcelona, Spain, [3]Escuela de Química, Universidad Nacional de Colombia, Carrera 65 No 59A-110, 050034 Medellín, Colombia.

Introduction

Chiral structures are frequently found in nature, on scales as diverse as those of elementary particles and living beings. These structures present mirror images known as enantiomers. In some situations, the ratios of these enantiomers are similar, but in others there is an excess of one over the other, resulting in chiral symmetry breaking. Explaining why this is so is a problem of great current interest (Hegstrom et al. 1990, Viedma 2005, Kondepudi et al. 2001).

At equilibrium, the free energy ΔG_{rev} required for the formation of the possible enantiomers is practically the same so the corresponding probabilities $p_s \sim e^{-\frac{\Delta G_{rev}}{k_B T}}$ with k_B the Boltzmann constant and T the temperature, are very similar, resulting in weak or none chiral symmetry breaking. Experiments have shown that the actuation of external factors such as temperature gradients (Ribó et al. 2013) and in general external forces driving the system out of equilibrium can lead to a significant disproportion in the concentrations of the homochiral structures (enantiomers) or even prevent their formation (Buhse et al. 2021, Szurgot 2012).
In this paper, we demonstrate by modelling and experiments that the energy required to generate an enantiomeric crystal excess must be equal to the energy dissipated in the irreversible processes involved in crystallisation: heat exchange and salt phase change. This energy causes an increase in the free energy barrier of one of the enantiomeric crystals and, consequently, a decrease in the enantiomer formation rate which explains the enantiomeric excess. In the experiments performed, we have measured for the first time the enantiomeric excess of $NaClO_3$ along the crystallisation process of this substance, for different non-equilibrium conditions. We have found that the enantiomeric excess becomes more important when the actuating forces, temperature and activity differences, increase and therefore when energy dissipation, measured in terms of the entropy production rate, is larger.

Chiral symmetry breaking induced by entropy production

The existence of an enantiomeric excess has been attributed to the disparity in the activation energies of both enantiomers which causes different formation rates (Ribó et al. 2017, Kondepudi et al. 2001). In Fig. 1, we illustrate the different stages of crystallisation in which the two driving forces, temperature difference ΔT between the system and its surrounding and activity difference Δz between the solid and liquid phases reach different values.

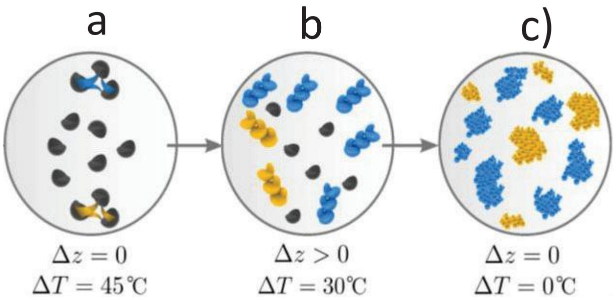

Figure 1: Enantiomer formation process. The system is initially an under-saturated mixture of salt, denoted by small black semicircles, and glycerol. Temperature decrease leading to stage a) characterised by stronger interaction among salt compounds (yellow and blue lines) thus reaching saturation. Small nuclei of both enantiomers are formed (L- and D-nuclei represented by gold and blue agglomerates respectively) in the process of phase change in which one of the enantiomers is dominant, as represented in stage b). Finally, crystals emerge and the system reaches a state of chemical and thermal equilibrium c) with an enantiomeric excess.

Theory

Heat transfer

The heat that the system exchanges with the environment which is at constant temperature T_s causes the temperature varies according to the equation

$$c_0 c_p \frac{\partial T}{\partial t} = \frac{2U}{d}(T_s - T) + \kappa \frac{\partial^2 T}{\partial y^2} \tag{1}$$

Where c_p is the specific heat of the mixture at constant pressure, U the convective heat transfer coefficient, c_0 the total molar concentration, d the test tube diameter, and κ the thermal conductivity.

Crystallisation kinetics

The evolution equation of the average L-crystal size a_L is

$$\frac{da_L}{dt} = -\frac{D_l l_0^2}{\kappa_B T}\left(\frac{\partial \phi_L}{\partial a_L}\right) n_L + \vartheta a_L \frac{l_0 T}{\kappa_B}\left(\frac{\partial k_v}{\partial T}\right)(\Delta T)^2 \tag{2}$$

With ϕ_L the potential energy to form a crystal of size a_L, D_l the diffusivity in the l space (Reguera et al. 2005), l_0 the minimum size of the nucleus, n_L the amount of salt in L-configuration, k_v the thermal expansion coefficient for the solid salt and ϑ the coupling constant. An analogous evolution equation can be written for D-crystals.

Results

We obtain Fig. 2 for one initial and cooling condition. We observe that heat transfer and nuclei formation are the most dissipative processes and that the supersaturation gradient is the main driving force for crystal formation (Szurgot 2012b), as it causes the most dissipation. This conclusion is reached in all the cases studied.

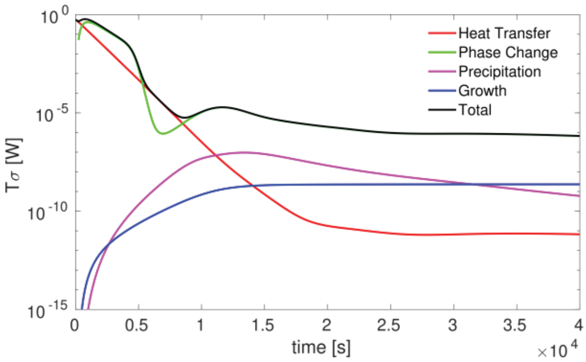

Figure 2: Energy dissipation rate corresponding to the different irreversible processes occurring in crystal formation as a function of time.

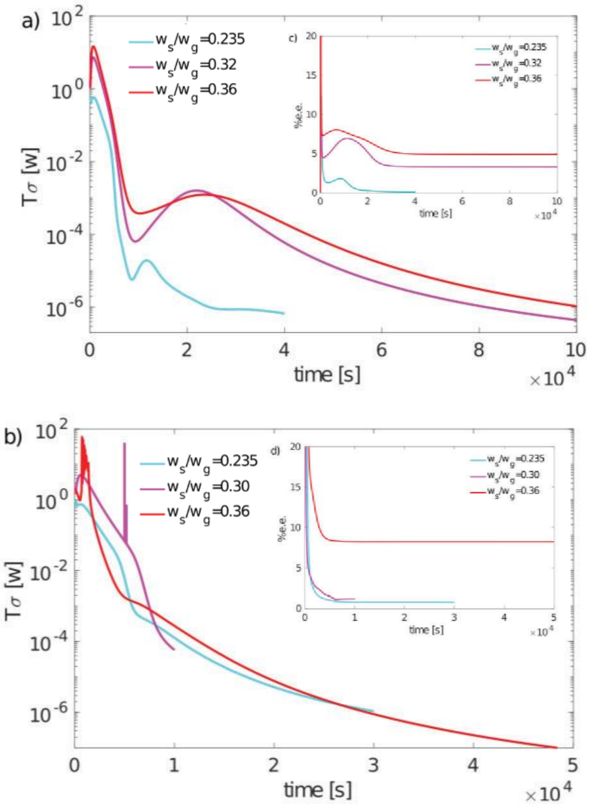

Figure 3: Energy dissipation rate corresponding to the different irreversible processes occurring in crystal formation as a function of time

In Fig. 3(a-b), we represent the energy dissipation rate of: i) heat transfer with the environment due to a temperature difference; ii) solid nuclei formation driven by the over-saturation force; iii) crystal growth caused by surface and volume energy differences. Fig. 3(a) shows the presence of two peaks and one minimum whereas in Fig. 3(b) there is only one peak for each salt/solvent concentration ratio. We also observe that for enhanced cooling the peaks are slightly higher than those for natural cooling which is a consequence of the fact that in the former case, the energy barrier is higher and consequently the barrier crossing rate diminishes which leads to an increase of the enantiomer population difference, as shown in Fig. 3(c-d). The final enantiomeric excess percentage is higher in the case of enhanced cooling, as the energy dissipation rate is initially higher. Therefore, the early excess of one of the enantiomers, with a lower redissolution rate, causes the enantiomeric crystals to persist over time (A. Arango-Restrepo et al. 2023).

Conclusions

The minimum values of the energy dissipation are found when the dissipation due to phase change decreases and heat exchange becomes the most dissipative process. This is connected with local maximum of the enantiomeric excess which means that temperature gradients might amplify the symmetry breaking.

The enantiomeric excess depends on the cooling rate and temperature gradients. The path in which the cooling process takes place, inducing supersaturation of the mixture, affects the intermediate states in the nucleation, thus leading to chiral symmetry breaking.

Acknowledgements

A.A-R. and J.M.R. are grateful for financial support of MICIU (Spanish Government) under grant No. PID2021-126570NB-I00. O.A. recognises the financial support of MICIU (Spanish Government under grants No. RYC2018-024997-I and RTI2018-098410-J-I00.

References

R. A. Hegstrom and D. K. Kondepudi, The handedness of the universe, *Scientific American*, 262, 108–115, (1990).

C. Viedma, Chiral symmetry breaking during crystallization: complete chiral purity induced by nonlinear autocatalysis and recycling, *Phys. Rev. Lett.*, 94, 065504, (2005).

D. K. Kondepudi and K. Asakura, Chiral autocatalysis, spontaneous symmetry breaking, and stochastic behavior, *Accounts of Chemical Research*, 34, 946–954, (2001).

J. M. Ribó, J. Crusats, Z. El-Hachemi, A. Moyano, C. Blanco and D. Hochberg, Spontaneous Mirror Symmetry Breaking in the Limited Enantioselective Autocatalysis Model: Abyssal Hydrothermal Vents as Scenario for the Emergence of Chirality in Prebiotic Chemistry, *Astrobiology,* 13, 132–142, (2013).

T. Buhse, J.-M. Cruz, M. E. Noble-Terán, D. Hochberg, J. M. Ribó, J. Crusats and J.-C. Micheau, Spontaneous deracemizations, *Chemical Reviews*, 121, 2147–2229, (2021).

M. Szurgot, in *Crystallization and Materials Science of Modern Artificial and Natural Crystals*, InTech, Rijeka, Croatia, (2012). Parity Violation in Unstirred Crystallization from Achiral Solutions.

J. M. Ribó, D. Hochberg, J. Crusats, Z. El-Hachemi and A. Moyano, Spontaneous mirror symmetry breaking and origin of biological homochirality, *Journal of The Royal Society Interface*, 14, 20170699, (2017).

D. Reguera, J. M. Rubí and J. M. G. Vilar, Mesoscopic non-equilibrium thermodynamics, *The Journal of Physical Chemistry B*, 109, 21502–21515, (2005).

M. Szurgot, Chiral symmetry breaking in unstirred crystallization, *Crystal Research and Technology*, 47, 109–114, (2012).

A. Arango-Restrepo, O. Arteaga, D. Barragán, J.M. Rubi, Chiral symmetry breaking induced by energy dissipation, *PCCP*, submitted (2023).

Simultaneous appearance of fingers and overstable instability in isothermal ternary systems

Berin Šeta[1], Jon Spangenberg[1], Fina Gavalda[2], M. Mounir Bou-Ali[3], Xavier Ruiz[2], Valentina Shevtsova[3,4]

[1]Department of Civil and Mechanical Engineering, Technical University of Denmark, Lyngby, Denmark
[2]Department of Physical and Inorganic Chemistry, Universitat Rovira I Virgili, Tarragona, Spain
[3]Fluid Mechanics Group, Mondragon University, Arrasate/Mondragon, Spain
[4]IKERBASQUE, Basque Foundation of Science, Bilbao, Spain

Introduction

Buoyancy can be generated by multiple driving forces simultaneously, as in the cases of temperature and concentration gradients or gradients of two or more species in multicomponent mixtures. The convective movements due to density inversion caused by different rates of diffusion are called double-diffusive convection. Double-diffusive convection appears in many natural processes, most notably in form of salt fingers causing water mixing in oceans (Stern 1960). However, the convective motion caused by different diffusion rates of species disturbs experimental measurements in many different setups, most notably the ones with a sharp interface between solutions, like Sliding Symmetric Tubes (SST), Counter-Flow Cell (CFC) or Open Capillary Tubes (OECT) (Seta et al. 2019).

In ternary mixtures, it is well established that two different types of instability can occur: fingers-like, where "fingers" of one mixture are transported into another mixture and overstable type of instability, where the sharp interface is maintained through experiments, but convective structures are formed on the edges of interface. Static limits for the onset of previously mentioned instabilities can be obtained either by taking derivatives of the analytical solution of the diffusion transport equation in the ternary mixture or applying linear stability analysis (Seta et al. 2019, Vitagliano et al. 1992). Nevertheless, it must be mentioned that the inversion density pockets are sufficient, but not required for the appearance of finger-like instability.

The experiments conducted in the aforementioned setups are designed to maintain a small concentration difference between the top and bottom mixtures. This is done to ensure that the constant diffusion coefficient assumption is valid. However, some experiments have been carried out with a concentration difference of up to 0.1 (Mialdun et al. 2013, Larranaga et al. 2014). This difference is significant enough to result in distinct diffusion coefficients across the concentration gradient, as demonstrated by the ternary diagram in Figure 1 for the Toluene (Tol) – Methanol (Meth) – Cyclohexane (Cyl) mixture in the case of D_{12}.

By using a set of constant diffusion coefficients, stability graphs can be created based on the initial concentration difference between independent components toluene and methanol. These graphs can indicate the initial conditions that will result in convective motion. However, if we account for the concentration-dependent nature of diffusion coefficients, it is possible that the top and bottom mixtures will have different coefficients. In this case, the stability graph for each mixture may differ, leading to uncertainty in predicting the occurrence of instability during the experiment.

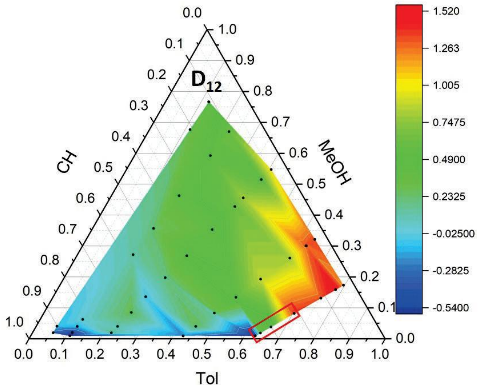

Figure 1: Concentration-dependent variation of D_{12}. Red rectangular shows a region of interest, where, for a relatively small variation of concentration, cross-diffusion term D_{12} shows big differences.

Methodology

The system is initialized as two superimposed layers of ternary mixture with slightly different concentration and hence different diffusion coefficients. The Navier-Stokes equations, along with the transport equations for independent components w_1 (toluene) and w_2 (methanol), are solved using the open-source software OpenFOAM. The mixture is assumed to be incompressible, with the exception of the Boussinesq approximation, where the density depends on the mass compositions. The governing equations can be expressed as follows:

$$\frac{\partial \boldsymbol{u}}{\partial t} + \boldsymbol{u} \cdot \nabla \boldsymbol{u} = -\frac{1}{\rho_0} \nabla p + \nu \Delta \boldsymbol{u} + \boldsymbol{g} \rho^* \qquad (1)$$

$$\frac{\partial w_1}{\partial t} + \boldsymbol{u} \cdot \nabla w_1 = \nabla \cdot (D_{11} \nabla w_1) + \nabla \cdot (D_{12} \nabla w_2) \qquad (2)$$

$$\frac{\partial w_2}{\partial t} + \boldsymbol{u} \cdot \nabla w_2 = \nabla \cdot (D_{21} \nabla w_1) + \nabla \cdot (D_{22} \nabla w_2) \qquad (3)$$

Where $\mathbf{u}$ is velocity vector, D_{ij} are concentration-dependent diffusion coefficients, ρ_0 is mean density, $\rho^* = \rho_0 (1 - \beta_{w1}(w_1 - w_{10}) - \beta_{w2}(w_2 - w_{20}))$ is mixture density dependent on concentration of species, β_{w1} and β_{w2} are mass expansion coefficients of toluene and methanol and $\mathbf{g}$ is gravity vector. The stability graphs are obtained from limits given in (Seta et al. 2019) for constant diffusion coefficients. Simulations were conducted in Hele-Shaw cell.

Results

The initial difference in diffusion coefficients between the top and bottom solutions in the Hele-Shaw cell results in an asymmetric solution (Bratsun et al. 2022). However, the influence of cross-diffusion in this work was neglected, which is crucial mechanism to obtain simultaneously two different types of instability. Furthermore, previous research (Bratsun et al. 2015) suggested that another coupling mechanism, such as a reaction, was necessary to produce two different instabilities simultaneously in different parts of the diffusion front. In this study, we demonstrate that if the diffusion coefficients are such that the stability pattern undergoes a complete change in the top and bottom solutions, meaning that the regions of overstable and fingers switch places, it is possible to observe two instabilities occurring simultaneously. For example, if we initialize system with $w_{1,bot}=0.67$ and $w_{2,bot}=0.015$ and $w_{1,top}=0.65$ and $w_{2,top}=0.065$, maps of stability will look like in Fig. 2. Based on the work of Grossmann (Grossmann et al. 2009), polynomial equations are used to fit the diffusion coefficients as a function of concentration. The regions of overstable and fingers have evidently shifted, resulting in distinct movements in different areas of the domain.

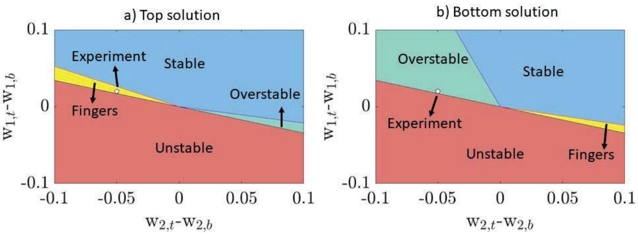

Figure 2: a) Stability map for top solution, b) Stability map for bottom solution.

Once the conditions for different types of instability are reached at the top (fingers) and bottom (overstability), the resulting fluid motion differs, as shown in Figure 3. The resulting structure is asymmetric, with small fingers forming in the upper part and large structures forming in the bottom, far from the center and hindering movement, which helps to maintain a sharp interface.

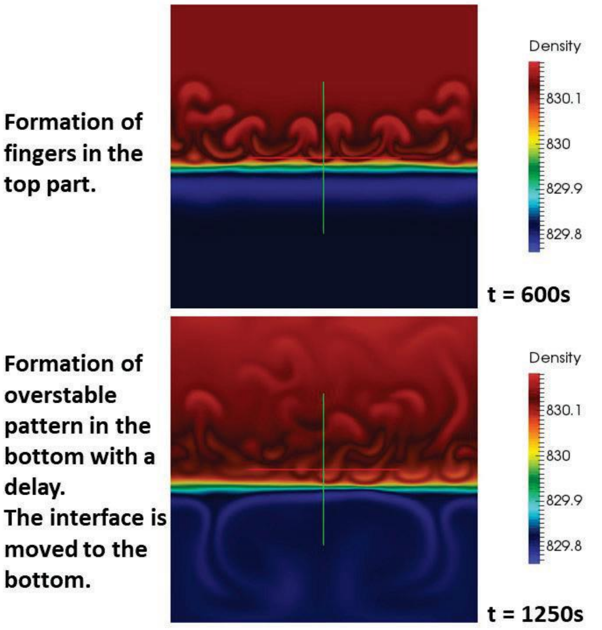

Figure 3: Formation of two different instabilities in a ternary mixture with diffusion coefficients depending on the composition.

As seen in the later stages of the process (t=1250s), the entire interface moves downward, as the upper part is mixed due to convective motion of the fingers, while the bottom remains blocked. Furthermore, the onset of instabilities is time-dependent and differs at early stages, suggesting that one instability may evolve into another once the field is sufficiently mixed.

Conclusions

This study presents, for the first time in literature, the simultaneous appearance of two types of instability in an isothermal ternary system. The primary mechanism behind the asymmetric solution is the concentration-dependence of the diffusion coefficients. This concentration-dependence allows for the emergence of various patterns, such as finger-overstable, finger-stable, stable-overstable, and others. Additionally, the onset of these patterns may occur at different times and be transient in nature, causing certain instabilities to emerge and disappear during the course of the experiment.

Acknowledgments

The present work has been supported by grants 2021PFR-URV-74 (Rovira i Virgili University).

References

Stern, M. E. (1960). The “salt-fountain” and thermohaline convection. *Tellus*, *12*(2), 172-175.

Šeta, B., Errarte, A., Dubert, D., Gavaldà, J., Bou-Ali, M. M., & Ruiz, X. (2019). Gravitational stability analysis on double diffusion convection in ternary mixtures. *Acta Astronautica*, *160*, 442-450.

Vitagliano, P. L., Ambrosone, L., & Vitagliano, V. (1992). Gravitational instabilities in multicomponent free-diffusion boundaries. *The Journal of Physical Chemistry*, *96*(3), 1431-1437.

Mialdun, A., Yasnou, V., & Shevtsova, V. (2013). Measurement of isothermal diffusion coefficients in ternary mixtures using counter flow diffusion cell. *Comptes Rendus Mécanique*, 341(4-5), 462-468.

Larrañaga, M., Rees, D. A. S., & Bou-Ali, M. M. (2014). Determination of the molecular diffusion coefficients in ternary mixtures by the sliding symmetric tubes technique. *The Journal of chemical physics*, *140*(5), 054201.

Grossmann, T., & Winkelmann, J. (2009). Ternary diffusion coefficients of cyclohexane+ toluene+ methanol by Taylor dispersion measurements at 298.15 K. Part 1. Toluene-rich area. *Journal of Chemical & Engineering Data*, *54*(2), 405-410.

Bratsun, D. A., Oschepkov, V. O., Mosheva, E. A., & Siraev, R. R. (2022). The effect of concentration-dependent diffusion on double-diffusive instability. *Physics of Fluids*, *34*(3), 034112.

Bratsun, D., Kostarev, K., Mizev, A., & Mosheva, E. (2015). Concentration-dependent diffusion instability in reactive miscible fluids. *Physical Review E*, *92*(1), 011003.

Soret effect on viscous dissipation thermal instability of Poiseuille flows in binary mixtures; Part I: Linear stability

K. Ali Amar1[1], S. Hirata2[1], M.N. Ouarzazi3[1]
[1]Unité de Mécanique de Lille, URL 7512, Université de Lille, Bd. Paul Langevin, CEDEX,
59655 Villeneuve d'Ascq, France;
email1 katia.ali-amar@univ-lille.fr,
email2 silvia.hirata@univ-lille.fr,
email3 mohamed-najib.ouarzazi@univ-lille.fr

Introduction

The aim of the present paper is to investigate the linear stability of the Poiseuille flow of binary fluids by taking into account both the effects of viscous heating and thermodiffusion. Both boundaries are considered impermeable. The upper boundary is assumed isothermal while the lower one is adiabatic. Therefore, this work may be seen as an extension to binary fluids of the linear stability analysis conducted by [Barletta et al. 2011] for a one-component fluid. As no external temperature or concentration difference is imposed on the layer, the cause of thermal instability is the flow rate through the volumetric heating induced by the viscous dissipation and the Soret effect inherent to binary mixtures.

Physical problem and the basic state

We consider a binary fluid mixture contained between two horizontal plates of infinite extension in the horizontal directions x and y, separated by a height H in the vertical direction z, so that the lower wall is in $z=0$ and the top wall in $z=H$. A constant pressure gradient is imposed in the x -direction, generating a Poiseuille velocity profile. The thermal boundary conditions are such that the lower wall is adiabatic while the upper wall is isothermal. No slip for the velocity field and no mass flux conditions are imposed on the horizontal walls (Fig. 1).

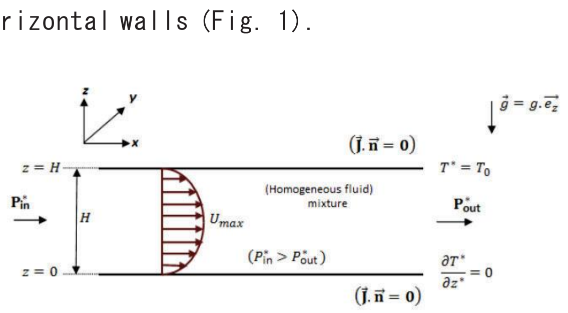

Figure 1: Geometry problem

The basic state solutions may be written in dimensionless form as:

$$\vec{u}_b = Re\ \Pr f(z)\vec{e}_x,\quad T_b=\Lambda\ g(z),\quad C_b=-\ \psi\ T_b$$

The functions $f(z)$ and $g(z)$ are defined as follows:

$$f(z)=6z(1-z),\qquad g(z)=6(\frac{2}{5}-3z^2+4z^3-2z^4)$$

where Re is the Reynolds number, $\Pr$ is the Prandtl number, Λ is the viscous dissipation Rayleigh number defined as $\Lambda = Ge\,Re^2\Pr^2$ with Ge the Gebhart number, a parameter that measures the intensity of the viscous dissipation and the parameter ψ is the separation ratio which represents the ratio between the mass contribution and the temperature contribution to buoyancy forces.

The above basic solutions state that in the presence of an imposed Poiseuille flow, a negative basic temperature nonlinear vertical gradient exists due to the viscous dissipation contribution. A basic vertical nonlinear concentration stratification is then generated by the Soret effect.

Linear stability of the basic state

A linear stability analysis of the above basic solutions has been carried out in [Ali Amar et al. 2022] by solving the eigenvalue problem numerically using the shooting method for arbitrarily oriented convective rolls. The results indicated that the most unstable disturbances are longitudinal rolls independently of the Soret effect. In addition to Lewis number (Le) and Prandtl number $\Pr$, the onset of convection in the form of longitudinal rolls depends on the viscous dissipation Rayleigh number Λ.

Results for $\psi \succ 0$

It is interesting to note that both the basic temperature and the basic concentration gradients are negative, meaning that the system may be unstable under some conditions. We present in Fig. 2(a) the linear stability diagram in the (ψ,Λ) plane.

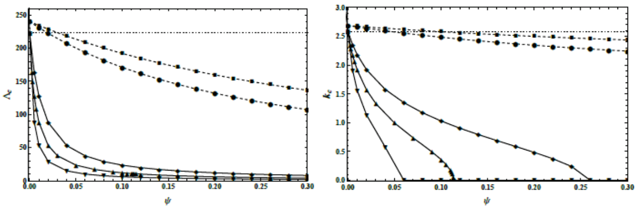

(a) (b)

Figure 2: Stability diagram for $\psi \succ 0$

The stability diagram depends on the values of the Lewis and Prandtl numbers. The plot in Fig. 2(a) was obtained for $\Pr = 10$ and different values of Lewis number $Le = 50$, $Le = 100$ and $Le = 200$, values which are typical for liquid mixtures. The same figure shows the stability diagram for $\Pr = 1$ and two values of Lewis number $Le = 1$ and $Le = 2$, representing gas mixtures. As can be seen in this figure, the instability appears at a lower Λ_c than in the case of a mono-constituent fluid ($\psi = 0$) for a liquid mixture and for a gas mixture. The difference is that the destabilizing is more important for a liquid mixture than for a gas mixture. Moreover, this figure shows a drastic drop of the critical threshold Λ_c as the Lewis number increases. Numerical results indicate that instability appears with zero frequency, indicating that the emerging longitudinal rolls are stationary. As shown in Fig. 2(b), for a fixed $\psi \neq 0$ the instability appears with a wave number k_c that deviates weakly from its value for $\psi = 0$ in the case of a gas mixture, while it decreases strongly for a liquid mixture as ψ increases. We remark that the decrease in the wave number is drastic for a liquid mixture with a high Lewis number. In that case, there exists a particular value of the separation ratio ψ_{mono} such that a finite critical wave number is observed for $\psi \prec \psi_{mono}$ and zero wave number for $\psi \succ \psi_{mono}$.

Results for $\psi \prec 0$

For $\psi \prec 0$, the basic temperature and concentration fields are of the same sign and the densest constituent migrates toward the hot wall, that is, the lower wall, stabilizing the system. Figure 3(a) illustrates the evolution of the threshold Λ_c at the onset of convection as a function of ψ for different values of Le and $\Pr$. For fixed Le and $\Pr$, two types of instability may exist depending on the value of ψ. On one hand, the instability appears with a non-zero wave number and non-zero frequency if ψ is below a particular value ψ_{CT}. Thus, the instability mechanism is an oscillatory periodic Hopf bifurcation, leading to symmetry degenerating left and right traveling wave patterns in the y direction. At the onset of convection, their corresponding threshold Λ_c and frequency ω_c are plotted as functions of separation ratio by the dashed lines of Fig. 3. The dashed lines of Fig. 3(a) show that Λ_c increases very weakly with $|\psi|$.

.

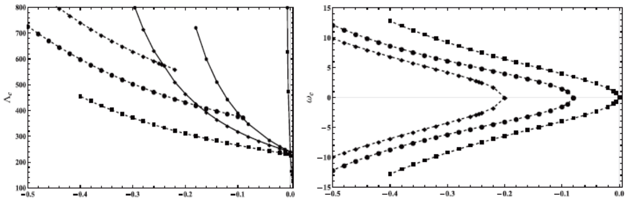

(a) (b)

Figure 2: Critical values at the onset of stationary longitudinal rolls (solid line) and oscillatory longitudinal rolls (dashed line): (a) Λ_c, (b) ω_c vs ψ for $Le = 100$, and $\Pr = 10$ (square symbols), $Le = 2$ and $\Pr = 1$ (dot symbols) and $Le = \Pr = 1$ (diamond symbols).

We now restate the results obtained in terms of the critical Reynolds number that can be easily evaluated from the relationship $\Lambda = Ge\, Re^2 \Pr^2$, namely,

$$\mathrm{Re}_c = \frac{1}{\Pr}\sqrt{\frac{\Lambda_c}{Ge}}$$

We note that Re_c is proportional to the inverse of the Prandtl number, which means that the more we increase the Prandtl number, the more the critical Reynolds number decreases. This may allow us to observe the effect of viscous dissipation on experimentally affordable Reynolds number for highly viscous fluids. Figure 4 presents the stability diagram in the (ψ, Re) plane for fixed $\Pr$ and Ge. We observe in Fig. 4 that the larger the positive separation ratio, the smaller the critical Reynolds number needed to trigger stationary convection, which confirms once again the destabilizing role of the Soret effect with positive separation ratios. Inversely for negative separation ratios, the Soret effect has a stabilizing influence.

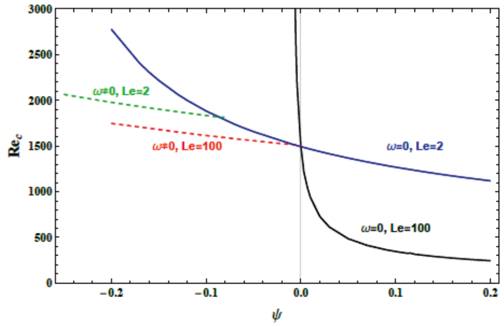

Figure 4: Critical value Re_c vs ψ for $Le = 2,\ 100$, $\Pr = 10$ and $Ge = 10^{-4}$ at the onset of longitudinal rolls: stationary mode (solid line) and oscillatory mode (dashed line)

Conclusions

The linear stability analysis is performed for the convective instability induced by viscous dissipation for a Poiseuille flow of a binary fluid mixture by taking into account the Soret effect. It is found that

(i) For positive ψ, the bifurcation is stationary, and the

Soret effect precipitates the appearance of stationary longitudinal rolls. Moreover, a drastic drop of the critical wave number is observed for liquids such that it becomes zero if ψ exceeds a particular value ψ_{mono}. This means that longitudinal rolls have an infinite wavelength or are structured as a mono-cellular flow in a real channel bounded in the y direction;

(ii) For negative ψ, the system exhibits a Hopf bifurcation, if $\psi \prec \psi_{CT}$. Otherwise, the bifurcation is stationary.

References

A. Barletta, M. Celli, D.A. Nield. On the onset of dissipation thermal instability for the Poiseuille flow of a highly viscous fluid in a horizontal channel. J. Fluid Mech., 681, 499-514 (2011).

K. Ali Amar, S. C. Hirata, M. N. Ouarzazi, Soret effect on the onset of viscous dissipation thermal instability for Poiseuille flows in binary mixtures, Phys. Fluids, 34, 114101 (2022).

Analysis of the thermogravitational behaviour of binary liquid mixtures for positive and negative Soret coefficients

A. Sanjuan[1], B. Šeta[2], V. Shevtsova[1,3], M. Mounir Bou-Ali[1] and C. Santamaria[4]

[1]Fluid Mechanics Group, Mondragon University, Mondragon, Spain, asanjuan@mondragon.edu
[2]Department of Mechanical Engineering, Technical University of Denmark, Kongens Lyngby, Denmark
[3]IKERBASQUE, Basque Foundation for Science, Bilbao, Spain
[4]Department of Applied Physics II, University of Basque Country, Bilbao, Spain

Introduction

In recent years, the interest and study in the phenomenon of thermodiffusion that describes the separation of species under a temperature gradient has grown significantly due to its applicability in different sectors (W. Köhler et al. 2016). The representative magnitude of this phenomenon is the Soret coefficient (S_T) which in a binary mixture is the fraction between the thermodiffusion (D_T) and diffusion (D) coefficient. When S_T is positive, the denser component of the binary mixture moves to the cold region. Otherwise, in a less common scenario, the denser component goes to the hot part. Regarding the experimental process, the thermogravitational column (TGC) technique was one of the first methods applying the D_T effect under thermogravitational conditions to separate uranium isotopes (K. Clusius et al. 1939). The analytical solution to the problem was presented by W. H. Furry, R. Clark Jones and L. Onsager and is known as Fury-Jones-Onsager (FJO) theory (W. H. Furry et al. 1939), who succeeded in associating the thermodiffusion coefficient D_T of a binary mixture from stationary separation measurements Δc, between two points ΔL_z using the following Eqn. (1).

$$\Delta c = 504 \, \frac{\nu}{\alpha g} D_T c_0 (1 - c_0) \frac{\Delta L_z}{L_x^4} \tag{1}$$

where ν is the kinematic viscosity of the sample, α the thermal expansion coefficient, g is the gravity force, c_0 the initial mass fraction and L_x the gap of the column.

Binary mixtures of positive Soret coefficient have been studied in detail both numerically and experimentally using the cartesian configuration TGC technique (Šeta, B. et al. 2020). While in the case of the negative ones, the context is more complex. There is an experimental work where an adverse density gradient was stabilised in a TGC of cylindrical configuration (M. M. Bou-Ali et al. 1999), including the determination of negative D_T coefficients in different binary mixtures (M. M. Bou-Ali et al. 2000). Later, (Kozlova, S. et al. 2020) analysed the thermohydrodynamic stability problem under the same conditions as (M. M. Bou-Ali et al. 1999) stabilising an adverse density gradient by considering a larger gap in the cyclindrical configuration. This problem was also analysed for multicomponent mixtures (Ryzhkov, I. I. et al. 2009), pointing out that the long-wave perturbations were less invasive than for the binary case. Moreover, (Zebib, A et al. 2008) concluded that transversal waves (in third dimension) were more dangerous than longitudinal ones. Recently (Berin Šeta et al. 2020) investigated the stability analysis under thermogravitational effect concluding that the third dimension (not considered in the FJO theory) has a significant effect on the stability of an adverse density gradient in the cartesian configuration TGC. In this work, a numerical analysis was carried out to determine the best geometrical conditions of the cartesian TGC configuration to stabilise a negative binary mixture. A new TGC installation was designed and fabricated to verify and validate the numerical results.

Numerical model

As a starting point, the thermogravitational microcolumn (micro-TGC) existing in our laboratory was used. This has a gap of 0.509 mm (L_x), a width of 3 mm (L_y) and a height of 30 mm (L_z). Ansys Fluent 2022 R1 software was used considering the species transport model to simulate the species separation of a binary sample in the micro-TGC. The boundary conditions were defined in such way that a horizontal temperature gradient was applied between two parallel walls, while rest of the walls were considered adiabatic. As for the properties of the mixture, it was defined that the density of the sample changes due to temperature and concentration considering the Boussinesq approximation Eqn. (2) where ρ_0 is the initial density of the sample, T_0 is the mean temperature and β is the mass expansion coefficient.

$$\rho = \rho_0 [1 - \alpha(T - T_0) + \beta(c - c_0)] \tag{2}$$

For the validation of the numerical model, the mixture tetrahydronaphthalene-dodecene (THN-C_{12}) at 50 % in the mass fraction and at 25 ºC was considered as a reference (Platten, J. K. et al. 2003). The variation of the concentration of the denser component (THN) along the micro-TGC was analysed for ΔL_z = 25 mm. As can be seen (Table 1), the deviation between literature, experimental and numerical results do not exceed 5 %.

Table 1 : Stationary Δc values sample THN-C_{12} 50 % at 25ºC.

$\Delta c_{Ref} = 0.0576$	$\Delta c_{Exp} = 0.0583$	$\Delta c_{Num} = 0.0579$

Once numerical model was validated, the thermogravitational behaviour was analysed in the case of a mixture with a negative Soret coefficient, toluene-cyclohexane (tol-Ch) 50 % mass fraction at 25ºC. Different widths of the column were analysed, Ly = 3, 1.75, 1.5 and 1 mm, always maintaining the height and the gap of the micro-TGC as constant (L_x = 0.509 mm and L_z = 30 mm). The numerical results provided that the effect of the third dimension stabilizes the system for the widths of 1mm and 1.5 mm. (see Figure 1). The simulation used the value of the Soret effect given in the literature (Lapeira et al., 2017). It was noted that separation in a column with a width of 1 mm had a higher value when compared to FJO theory (literature), so the cartesian configuration of a 1.5 mm window was considered the optimum for that mixture.

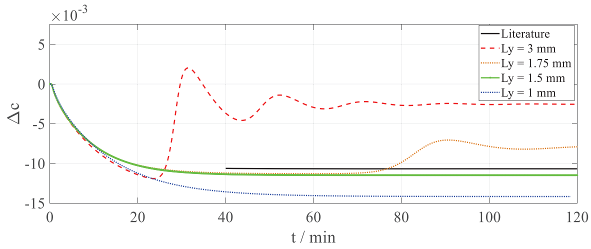

Figure 1: Separation of the sample Tol-Ch 50 % at 25ºC. Numerical results for different geometrical configurations.

Experimental setup and preliminary results

Based on the numerical results, a new micro-TGC was designed, fabricated, and adapted to the optical installation in the laboratory, see Figure 2 a). The blue laser (473 nm) was used in the experiments, which has shorter wavelength when compared to the red one (633 nm) and allows us to obtain a higher phase separation. An optical sensor based on a Mach-Zehnder interferometer was used to measure the change in concentration between two selected points. The experimental results shown in figure 2 b), confirm that, for the first time, an adverse density gradient was experimentally stabilised in a binary mixture validating the results shown in the numerical section corresponding to the mixture tol-Ch 50 % at 25ºC.

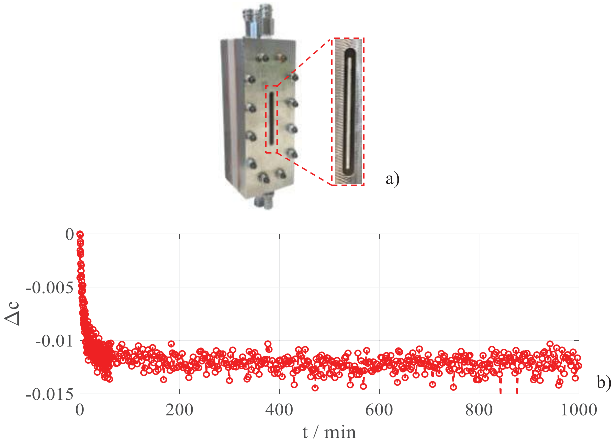

Figure 2: New fabricated micro-TGC a) and experimental results, separation of the mixture tol-Ch 50 % (stable) at 25ºC b).

Conclusions

In this work, the effect of the third dimension on the stability of a separation with an adverse density gradient under thermogravitational effect in a cartesian configuration was analysed. For the first time, it has been numerically and experimentally demonstrated that an optimal choice of TGC width allow to measure a binary system with a negative Soret effect otherwise unstable. To do so, a new micro-TGC was designed, fabricated and set up by changing the column width, also known as third dimension.

Acknowledgements

In memory of Prof. Jean Karl Platten, Prof. Abdelfattah Zebib and Prof. Jose Antonio Madariaga. A.S. wants to thank the Basque Government for funding under an FPI grant (PRE_2022_1_0136). MMB and VS would like to thank the financial support from the Basque Government under the Research Group Programme IT1505-22, the Gipuzkoa Provincial Council under the Hoztikor project (2022-CIEN-000052-01) and PID2020-115086GB-C33 financed by (MICINN/FEDER) of the Spanish Government.

References

W. Köhler and K. I. Morozov, The Soret Effect in Liquid Mixtures – A Review, J. Non-Equilibrium Thermodynamics, 41, (2016).

K. Clusius and G. Dickel, Das Trennrohrverfahren bei Flüssigkeiten, Naturwissenschaften, 27, 148, (1939).

W. H. Furry, R. C. Jones, and L. Onsager, On the Theory of Isotope Separation by Thermal Diffusion, Phys. Review, 55, 1083–1095 (1939).

Šeta, B., Gavalda, J., Bou-Ali, M. M., Ruiz, X., & Santamaria, C., Determining diffusion, thermodiffusion and Soret coefficients by the thermogravitational technique in binary mixtures with optical digital interferometry analysis, J. Heat Mass Transfer, 147, 118935, (2020).

Bou-Ali, M. M., Ecenarro, O., Madariaga, J. A., Santamaría, C. M., & Valencia, J. J., Stability of convection in a vertical binary fluid layer with an adverse density gradient, Phys. Review E, 59, 1250–1252, (1999).

M. M. Bou-Ali, O. Ecenarro, J. A. Madariaga, C. M. Santamaría and J. J. Valencia, Measurement of negative Soret coefficients in a vertical fluid layer with an adverse density gradient, Phys Review E, 62, 1420–1423, (2000).

Kozlova, S. v., Ryzhkov, I. I., & Bou-Ali, M. M.,Modeling of Separation in a Binary Mixture with Negative Soret Effect in a Cylindrical Thermogravitational Column, J.Non-Equilibrium Thermodynamics, 46, 109–120, (2020).

Ryzhkov, I. I., & Shevtsova, V. M. Long-wave instability of a multicomponent fluid layer with the Soret effect, Phys. Fluids, 21, 014102, (2020).

Zebib, A., Stability of ternary and binary mixtures in a vertical slot including the Soret effect, J.Chemical Physics, 129, 134711, (2008).

B. Šeta, J. Gavalda, M. M. Bou-Ali, and X. Ruiz, Stability analysis under thermogravitational effect, Int. J.Thermal Sciences, 156, 106464, (2020).

Platten, J. K., Bou-Ali, M. M., Costesèque, P., Dutrieux, J. F., Köhler, W., Leppla, C., Wiegand, S., & Wittko, G., Benchmark values for the Soret, thermal diffusion and diffusion coefficients of three binary organic liquid mixtures, Philosophical Magazine, 83, 1965–1971, (2003).

Lapeira, E., Gebhardt, M., Triller, T., Mialdun, A., Köhler, W., Shevtsova, V., & Bou-Ali, M. M.,Transport properties of the binary mixtures of the three organic liquids toluene, methanol, and cyclohexane, J. Chem. Phys., 146, 094507, (2017).

Convective Plume Spreading in Model Transparent Porous Media

H. Imuetinyan[1], P. Fruton[1], C. Giraudet[1], F. Croccolo[1]

[1]Laboratoire des Fluides Complexes et leurs Réservoirs-IPRA, UMR 5150, E2S-Univ Pau & Pays de l'Adour/CNRS/TotalEnergies, France, himuetinyan@univ-pau.fr

Introduction

Carbon dioxide (CO_2) long-term storage has been identified as one of the most relevant strategies to achieve the 2015 Paris Agreement objectives (Rogelj *et al.*, 2021). Although the main physico-chemical processes have been well characterised (Emami-Meybodi *et al.*, 2015; De *et al.*, 2022), several open questions remain regarding the 3D convective dissolution of CO_2 in brine. This is mainly because of the lack of experimental data close to process-relevant conditions.

As a first step towards the understanding of convective dissolution of CO_2 in brine, we investigated the convective patterns in a 3D system in free medium (Fruton *et al.*, 2023). More recently, we started preliminary study to observe the same phenomena in a model transparent porous medium. In this context, we developed an experimental setup using the shadowgraph method for the dynamic spreading of convective plumes in saturated transparent porous media, whose permeability ranged between 6 and 60 × 10^{-10} m^2. The first studies were performed close to the refractive index matching (RIM) conditions without fluorescent dyes using fluid mixtures with density gradients similar to those involved during the dissolution of CO_2 in brine.

Experimental Methodology

Here, the optical technique is shadowgraphy. The optical apparatus consists of a super-luminous diode (SLD) and a high-resolution s-CMOS camera from Hamamatsu. The light beam is passing through the sample cell which is a 3500 µL precision cuvette (Thorlabs). It contains a 3D model porous medium filled with a matching solution of 1-hexanol and toluene as shown in figure 1. The porous medium consisted in borosilicate glass beads (Sigma-Aldrich) of 1 or 3 mm diameter.

A denser fluid was injected through a syringe pump by allowing a drop of 16.7 µL volume to fall at the liquid-gas interface. The drop is prepared to have a density higher than the solution saturating the porous medium. Three density differences ($\Delta\rho$=13.6, 7.7, and 4.9 kg/m^3) were tested to investigate the convective process through the transparent porous medium.

During the experiment, we ensured that the drop was injected very slowly and that the injection needle was placed at the centre of the cuvette. Pure fluid density and viscosity data were obtained from the supplier and compared to literature data (Wu *et al.*, 2019; Almasi, 2021). Series of images were acquired at a frequency of 20 Hz and the experiments typically lasted for about 5 minutes. We defined Z=0 for each experiment at the liquid-gas interface as shown in Fig. 1. To test the reliability of our setup, each experiment was repeated at least three times.

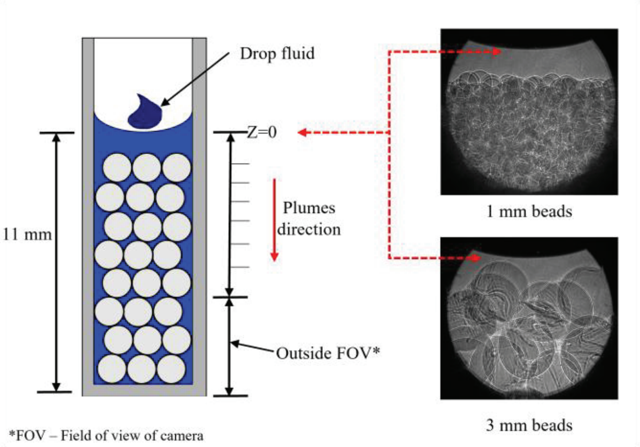

Figure 1: Schematic representation of the cuvette filled with a porous medium saturated with the RIM solution. The free liquid-gas interface is chosen as the origin of the vertical axis. On the right-hand side, the shadowgraph images show the position of the porous medium and liquid-gas interface.

Results and Discussions

For each density difference, we analysed the convective front velocity (CFV) defined as the velocity of the first plume travelling downwards to the bottom of the sample cell. We computed the variance of the lines of each image difference at different times after injection. Using a threshold variance, we were able to determine the position of the first plume, Z_0, see figure 2.

For both porous media, the CFV increases as $\Delta\rho$ increases. While average CFV doubles when $\Delta\rho$ increases from 7.7 kg/m^3 to 13.6 kg/m^3 for the 1 mm beads (0.29 mm/s to 0.59 mm/sec), the speed increase was less than 20% for 3 mm beads (3.43 mm/s to 4.18 mm/s). For the experimental dissolution of CO_2 in brine at a density difference of 0.29 kg/m^3, the maximum vertical velocity of the leading fingers in a Hele-Shaw cell is approximately 0.029 mm/s (Li, Zhong and Jiang, 2023).

Our results show that when a large $\Delta\rho$ is achieved (1.5%), the plumes travel faster, but when $\Delta\rho$ is small (0.9% and 0.6%), the spreading velocity is affected by the tortuosity pathway of the porous media. The density difference attained during convection substantially influences the CFV.

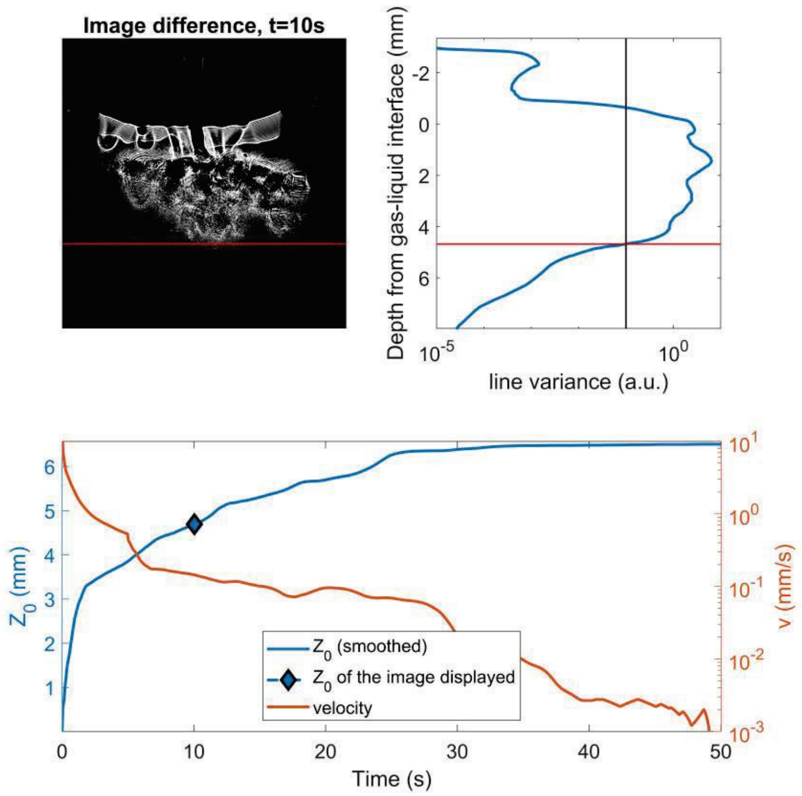

Figure 2: CFV analysis for the 1 mm porous medium and a density difference of 4.9 kg/m^3. Top left: image difference at t=10 s. Top right: variance of each line of the image difference. The intersection of the line variance curve (blue) and a threshold variance (black line) determines the position of the plumes, Z_0, at a given time. Bottom: plume position (blue), Z_0, and velocity profile (orange). The average CFV of this system's early plumes was 0.27 mm/s.

Conclusions

In this study, we developed an experimental methodology to study density-driven convection in a model transparent porous medium where we could experimentally determine the convective front velocity for three values of $\Delta\rho = (4.9, 7.7$ and 13.6 kg/m^3) and two permeabilities of 6×10^{-9} and 6.6×10^{-10} m^2. The CFV analysis shows consistency and repeatability. We show that when a high $\Delta\rho$ is achieved, the early plume velocity is significantly affected by the density difference, but at $\Delta\rho$ lower than 1 %, the early spreading velocity of the plume considers other factors of the porous media (e.g. pore spaces). These results can be used as input parameters for simulations of convective mixing in porous media. The relationship between the laboratory experimental data and its implications for CO_2 sequestration will be explored in the near future.

Acknowledgements

This research was carried out under the framework of the E2S UPPA Hub Newpores and Industrial Chair CO2ES supported by the Investissements d'Avenir French program managed by ANR (No. ANR16IDEX0002). We also acknowledge the support from PTDF Nigeria.

References

Almasi, M., 2021. Molecular interactions and structural studies of toluene and (C5 − C10) 1-alkanol; mutual diffusion and virial coefficients. J. Mol. Struct. 1230.

De, N., Singh, N., Fulcrand, R., Méheust, Y., Meunier, P., Nadal, F., 2022. Two-dimensional micromodels for studying the convective dissolution of carbon dioxide in 2D water-saturated porous media 22, 4645–4655.

Emami-Meybodi, H., Hassanzadeh, H., Green, C.P., Ennis-King, J., 2015. Convective dissolution of CO2 in saline aquifers: Progress in modeling and experiments. Int. J. Greenh. Gas Control 40, 238–266.

Fruton, P., Nauruzbaeva, A., Bataller, H., Giraudet, C., Vailati, A., and Croccolo, F. (2023) 'Convective dissolution of carbon dioxide into brine in a three-dimensional free medium', *Physical Review Fluids*, 8(2), p. 023503.

Li, D., Zhong, Y. and Jiang, X. (2023) 'Experimental study of impurity effects on convective mixing in Hele-Shaw cell with application to CO2 geological sequestration', *Advances in Water Resources*, 172, p. 104379.

Rogelj, J., Geden, O., Cowie, A., Reisinger, A., 2021. Net-zero emissions targets are vague: three ways to fix. Nature 591, 365–368.

Wu, W., Klein, T., Kerscher, M., Rausch, M.H., Koller, T.M., Giraudet, C., Fröba, A.P., 2019. Diffusivities in 1-Alcohols Containing Dissolved H2, He, N2, CO, or CO2 Close to Infinite Dilution. J. Phys. Chem. B 123, 8777–8790.

Marangoni convection in a surfactant solution containing micelles

A. A. Nepomnyashchy

Department of Mathematics, Technion – Israel Institute of Technology, Haifa, Israel, nepom@technion.ac.il

The Marangoni convection in a heated layer of a surfactant solution in the presence of Soret effect has been a subject of research during past decades; for review, see (Shklyaev et al. 2017). Typically, it is assumed that the concentration of the surfactant is below the critical micelle concentration. It is known that the influence of the micelle development on the Marangoni stresses is significant (Edmonstone et al. 2006, Craster et al. 2009).

We consider the development of the Marangoni convection in a heated layer of a surfactant. The Soret effect, the kinetics of adsorption and desorption of the surfactant on the liquid surface, and the kinetics of micelle formation are taken into account. The polydispersity of micelles is neglected. The main attention is payed to the cases where a longwave Marangoni instability is developed (moderate Galileo number or small Biot number). The longwave expansions are used for the derivation of strongly nonlinear equations for active variables. The linear stability theory is developed for monotonic and oscillatory instability modes, and the pattern selection is discussed.

Acknowledgements

The research was partially supported by the Israel Science Foundation (grant No. 843/18).

References

S. Shklyaev, A. Nepomnyashchy, Longwave Instabilities and Patterns in Fluids, Birkhauser, New York, (2017)

B.D. Edmonstone, R.V. Craster, O.K. Matar, Surfactant-induced fingering phenomena beyond the critical micelle concentration, J. Fluid Mech., 564, 105-138, (2006)

R.V. Craster, O.K. Matar, D.T. Papageorgiou, Breakup of surfactant-laden jets above the critical micelle concentration, J. Fluid Mech., 629, 195-219, (2009)

Thermal diffusion experiments in CO_2-1-hexanol mixtures at different gravity levels
Design and data overview of a parabolic flight campaign

P. Fruton[1,*], E. Lisoir[1], F. Croccolo[1], C. Giraudet[1]

[1]Universite de Pau et des Pays de l'Adour, E2S UPPA, CNRS, TotalEnergies, LFCR UMR5150, Anglet (France)
*paul.fruton@univ-pau.fr

Introduction

By applying a temperature gradient to a binary fluid mixture, a concentration gradient is generated by the Soret effect. In a non-associative system, like the binary mixture of 1-hexanol and carbon dioxide (CO_2), the Soret coefficient is negative which can lead to hydrodynamic instabilities in the form of convective rolls. Before convection sets-in, non-equilibrium fluctuations (NEFs) spontaneously emerge in the presence of a density gradient and can be additionally amplified by buoyancy, thus originating convection (Giavazzi and Vailati 2009). The Shadowgraph method allows to visualize and analyze both NEFs and convective patterns (Croccolo and Brogioli 2011). The signal stemming from convective patterns, however, overwelhms the one from NEFs. Thus, studying this process under reduced gravity conditions can provide a deeper understanding of the behaviour of NEFs in conditions close to the onset of convection.

In this work, we present the set-up specifically developed for the 61st CNES parabolic-flight campaign VP161. Then, we describe the analysis method and the results obtained during thermodiffusion experiments at different gravity levels (1g, 1.8g and 0g). The samples are mixtures of 1-hexanol and CO_2 at different molar concentrations. Positive and negative temperature gradients are applied to the system to study both stable and unstable conditions. The influence of the different gravity levels on convection is investigated.

Materials and Method

The sample under study is prepared in a vapour-liquid-equilibrium (VLE) vessel by mixing CO_2 with 1-hexanol at a given pressure. The vessel is strongly shaked to reach a VLE quickly with the concentration of CO_2 in the 1-hexanol phase determined by the thermodynamic conditions of temperature and pressure.

Thereafter, the liquid phase of the mixture is transferred to a sample cell that mainly consists of a stainess-steel annulus sandwiched between two thermally-controled sapphire windows. The thermal gradient is applied by two Peltier elements featuring a 13 mm-diameter hole for the optical access. The cell is placed in a Shadowgraph apparatus consisting in a beam, provided by a superluminescent diode (SLD) and collimated by a lense, passing through the sample cell towards a high-speed sCMOS camera. The latter can record intensity maps of 2048x2048 pixels at a maximum frequency of 100 Hz, thus providing information about the variations of the refractive index and, thus, of the density variations inside the cell.

During an experiment, we first apply a thermal gradient, and, once the macroscopic thermal equilibrium is reached, we record series of images at a constant frame rate.

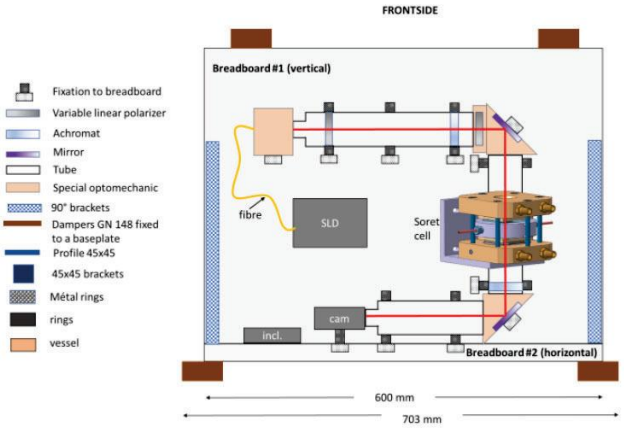

Figure 1: Illustration of the experimental set-up: two breadboards mounted at 90° with the vertical one hosting most of the elements of the setup (SLD, camera, achromats, mirrors, polarizers, optomechanic items, tubing, cell, inclinometer).

The NEFs are studied using a dynamic differential algorithm (DDA) that computes the spatial Fourier transform of image differences for each pair of images (Croccolo et al. 2012). Thus, we obtain the structure functions (SFs) containing information on the static and dynamic behaviour of the process. When the thermal gradient is destabilizing, the convective rolls emerge inside the bulk and prevent us from analysing the NEFs. In this case, we focus on the temporal evolution of the contrast of the patterns, quantified by the computation of the variance of the images.

Ground-based results

Preliminary investigations have been performed to define the experimental conditions of parabolic-flight experiments. It was found that the strength of convective rolls increases with increasing CO_2 concentration and pressure.

When x_{CO_2} is smaller than about 10%, no convective rolls could be observed on ground independently of the distance from the bubble pressure. Nonetheless, NEFs feature a very limited optical contrast, so that smaller concentrations were discarded. For $x_{CO_2} = 40\%$, we rapidly observed convection for pressures in the range 6 - 24 MPa, thermal gradients of 15 and 18 K and a mean temperature of 303 or 313 K. We observed convective rolls that are more contrasted at high pressures and vanish at low pressure. These results suggest that at these temperatures, the Soret coefficient increases with decreasing x_{CO_2} and approaching first-order fluid-phase transition.

Results during parabola

During the CNES parabolic flight campaign VP161, we investigated two molar fractions, $x_{\mathrm{CO}_2} = 26$ and 56 %. We applied both positive and negative thermal gradients in the range -6 to +6 K (the negative sign means heating from below). At the largest molar fraction, we observed convection for every thermodynamic condition during the terrestrial gravity phase. The contrast of the patterns increases during the hyper-gravity period, while it decreases in micro-gravity (Fig.4).

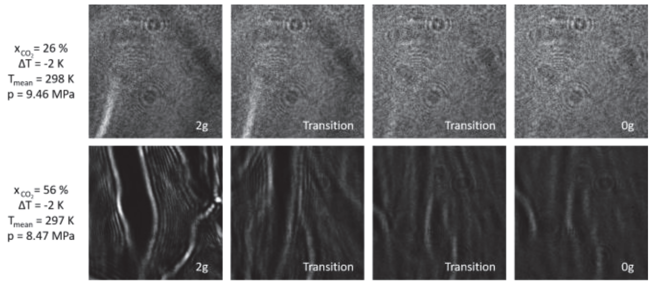

Figure 2: Shadowgraph images of two experiments for a temperature difference $\Delta T = -2$ K and two molar fractions of $x_{\mathrm{CO}_2} = 26$ (top) and 56 % (bottom).

In some experiments convection was totally removed during the reduced-gravity phase; see top row of figure 2. This provides us periods to study the NEFs. Unfortunately, the SFs computed with the DDA do not provide appropriate data. Indeed, the vibrations of the plane and the g-jitters induce large perturbations of the thermally stratified layers inside the sample. This is especially amplified during the transition from hypergravity to micro-gravity.

Despite this, we are still able to provide quantitative results from the analysis of the image variance. The variance of the raw images (*var2*) provides information on the presence of local variation of the contrast, i.e. convective patterns. The variance of the difference of successive images (*var1*) provides information on the movement of the patterns.

We observe that the convective patterns are stabilized during the reduced gravity phase, which is illustrated with the decrease of *var1* in figure 3. In the same period, we observed that the patterns are losing contrast and tend to vanish diffusively, which is demonstrated by the decrease of *var2* in figure 3. From this, we are able to link the characteristic time decay of *var2* with the thermal diffusivity of the mixture.

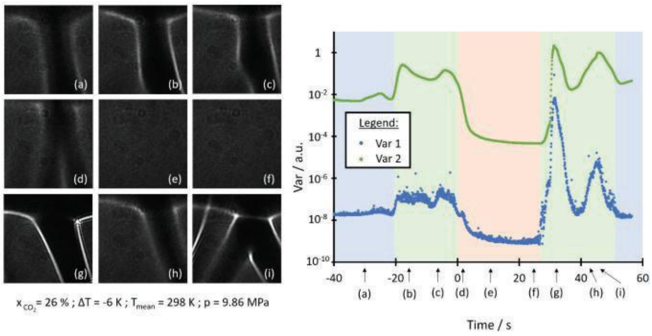

Figure 3: (left) Sample images during a parabola. **(right)** Temporal evolution of the variance of the difference of the image with the previous one (*var1*) and the variance of raw images (*var2*) over an entire parabola. The blue area corresponds to the terrestrial gravity phase, the green one to the hyper gravity phases, and the orange one to the reduced gravity phase.

Conclusions

We developed an experimental set-up to study the establishment of convection in a mixture of CO_2 and 1-hexanol stressed by a thermal gradient. We could highlight the effects of the gravity levels, from 1.8g to close to microgravity conditions, on the intensity of convection. This can vary depending on the molar fraction of the mixture and on the applied thermal gradient. During reduced gravity phases, we observed that the convective patterns are vanishing diffusively. The analysis of the transitory allowed us to measure the value of the thermal diffusivity that is in good agreement with literature.

However, we were not able to study the NEFs because of the strength of g-jitters and vibrations of the plane. The latter induce a lost of the autocorrelation plane of the NEFs. In further campaigns, we would need to develop a better vibration removal apparatus, or perform the experiments in other microgravity facilities, like e.g. sounding rockets or sattelites.

Acknowledgements

We acknowledge financial support from the CNES for the parabolic flight campaign. We thank Novespace and especially A. Jacquemet for her support during the preparation phase. This work received also financial support from the E2S UPPA Hub Newpores and the Industrial Chair CO2ES, supported by the Investissements d'Avenir French program managed by ANR (ANR16IDEX0002).

References

J. Oh, J. M. Ortiz de Zárate, J. V. Sengers, G. Ahlers, Dynamic of fluctuations in a fluid below the onset of Rayleigh-Bénard convection, *Physical Review E* **69**, 021106, (2004)

F. Croccolo, C. Giraudet, H. Bataller, R. Cerbino, A. Vailati, Shadowgraph analysis of non-equilibrium fluctuations for measuring transport properties in micro-gravity in the GRADFLEX experiments, *Microgravity Sci. Tecnol.*, 28:647-475, (2016)

C Croccolo, D. Brogioli, Quantitative Fourier analysis of shlieren masks: the transition from shadowgraph to schlieren, *Appllied Optics*, vol. 50, No. 20, 3419-3427, (2001)

F. Croccolo, H. Bataller, F. Scheffold, A light scattering study of non-equilibrium fluctuations in liquid mixtures to measure the Soret and mass diffusion coefficient, *The Journal of Chemical Physics*, 137, 234202, (2012)

F. Giavazzi, A. Vailati, Scaling of the spatial power spectrum of excitations at the onset of solutal convection in a nanofluid far from equilibrium, *Physical Review E* **80**, 015303(R), (2009)

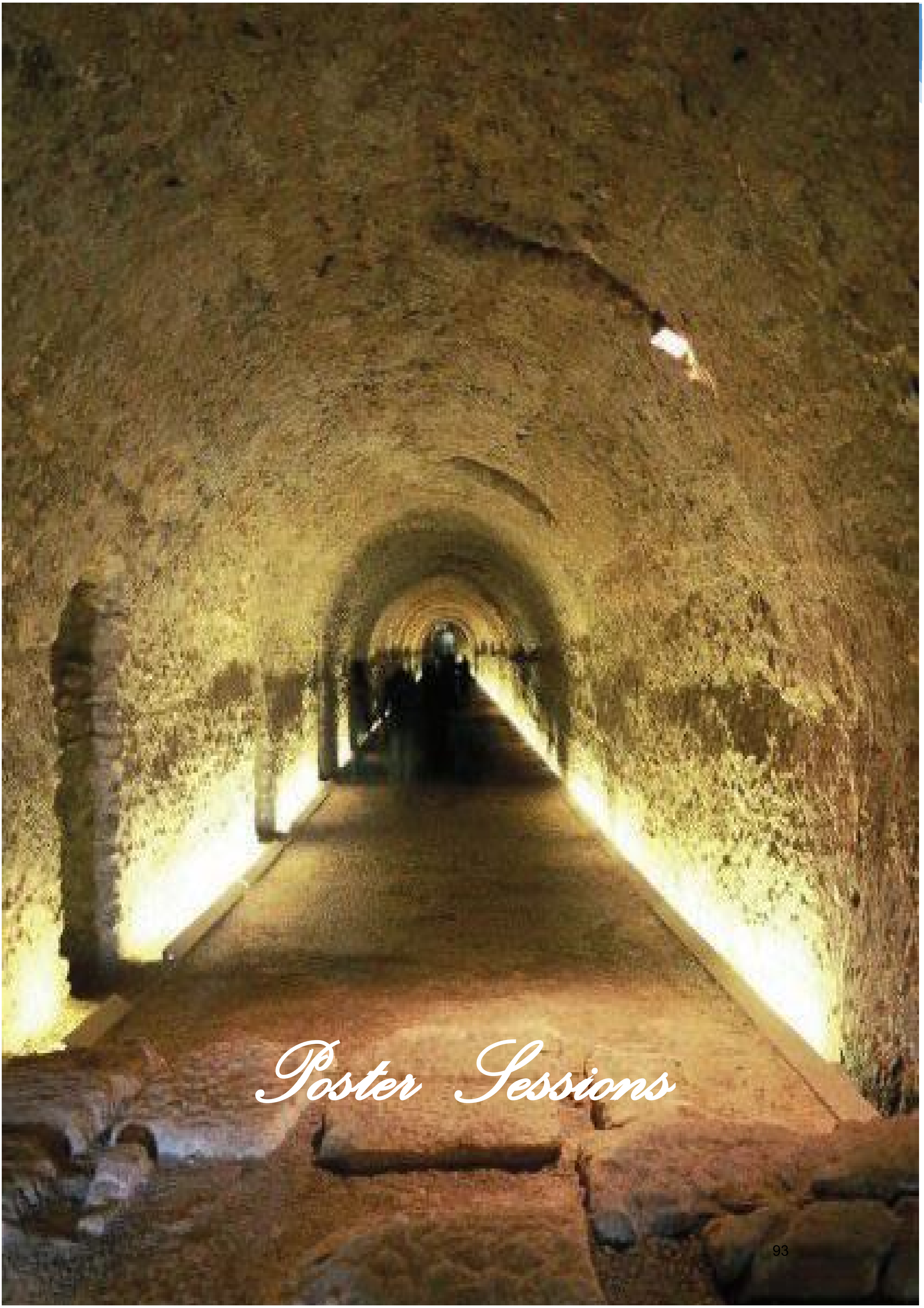

Poster Sessions

Soret effect on viscous dissipation thermal instability of Poiseuille flows in binary mixtures; Part II: Nonlinear stability

K. Ali Amar1[1], S. Hirata2[1], M.N. Ouarzazi3[1]
[1]Unité de Mécanique de Lille, URL 7512, Université de Lille, Bd. Paul Langevin, CEDEX,
59655 Villeneuve d'Ascq, France;
email1 katia.ali-amar@univ-lille.fr,
email2 silvia.hirata@univ-lille.fr,
email3 mohamed-najib.ouarzazi@univ-lille.fr

Introduction

The weakly nonlinear stability analysis of plane Poiseuille flow when viscous dissipation is taken into account is considered as a second part of our contribution to the IMT 15. As we are dealing with a binary fluid mixture, the aim is to study the effect of thermodiffusion on the nonlinear properties of the instability near the onset of convection. The impermeable lower boundary is considered adiabatic, while the impermeable upper boundary is isothermal. The linear stability of this problem has been carried out in [Ali Amar et al. 2022] by solving the eigenvalue problem numerically using the shooting method for arbitrarily oriented convective rolls. The results indicated that the most unstable disturbances are longitudinal rol**ls** independently of the Soret **e**ffect. Therefore the current study focuses on the near-threshold behaviour of longitudinal rolls by using a weakly nonlinear analysis. We determine numerically up to third order the coefficients of the Landau amplitude equation and investigate in detail the influences on bifurcation characteristics of the different dimensionless parameters present in the system. These parameters are namely, the Reynolds number Re, the Prandtl number $\Pr$, the viscous dissipation Rayleigh number Λ defined as $\Lambda = Ge\, Re^2 \Pr^2$ with Ge the Gebhart number, a parameter that measures the intensity of the viscous dissipation, the separation ratio ψ which represents the ratio between the mass contribution and the temperature contribution to buoyancy forces and the Lewis number Le which is defined here as the ratio between the thermal diffusivity and the solutal diffusion coefficient. In the case of a mono-constituent fluid ($\psi = 0$), [Requilé et al] carried out a linear and a weakly nonlinear stability analysis of the viscous dissipation induced instability both for Poiseuille and Couette flows. Consequently, the current study may be seen as an extension of [Requilé et al] to binary fluids.

Amplitude equation of the most unstable mode

The linear stability analysis can be used to predict when a particular flow becomes unstable, thus providing a marginal stability curve and critical values at the onset of the instability. However, linear stability theory cannot describe the evolution of unstable modes above the instability threshold. Nonlinear theories are used in order to study the further development of the instability. The spatiotemporal dynamics of complex flows is often described in fluid mechanics by relatively simple amplitude evolution equations. One of the most popular dynamic models is the Landau equation governing weakly nonlinear instability. This is of course not the only one. The attractiveness of the Landau equation is based on the fact that is a relatively simple model that allows the inclusion of physical effects. Without entering into mathematical details, we have proceed as in (Requilé et al) to derive amplitude equation that describes the evolution of the vertical velocity component in near threshold region (i.e. the viscous dissipation Rayleigh number Λ near its linear critical value Λ_c determined in [Ali Amar et al. 2022]. For positive separation ratio ψ this equation reads,

$$\gamma \frac{\partial A}{\partial t} = \frac{\Lambda - \Lambda_c}{\Lambda_c} A - \lambda A \left| A \right|^2 \qquad (1)$$

in which appear the characteristic time of instability γ and the Landau coeffcient λ. Computations indicate that the coefficient γ is real and always positive, while the nonlinear coefficient λ is real and is positive or negative depending on the values of ψ, Le, $\Pr$ and Ge considered.

The stationary amplitude of convection reads,

$$\left| A_s \right| = \left[\frac{\Lambda - \Lambda_c}{\Lambda_c \lambda} \right]^{1/2} \qquad (2)$$

Results of the weakly nonlinear stability

1. Supercritical/subcritical bifurcation

The sign of λ determines whether we are dealing with a subcritical or a supercritical bifurcation. For $\lambda \succ 0$, the bifurcation is supercritical, otherwise it becomes subcritical. Figure 1 shows the dependence of λ on ψ for different values of Ge with $\Pr = 10$ and $Le = 100$.

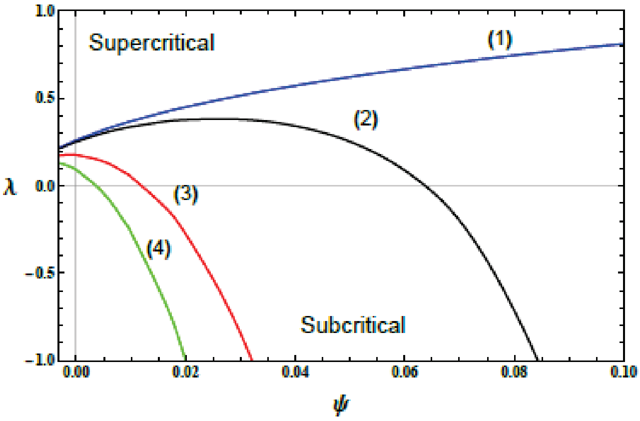

Figure 1: λ as a function of ψ at $\Pr = 10$, $Le = 100$ for : (1) $Ge = 10^{-4}$, (2) $Ge = 10^{-1}$, (3) $Ge = 1$, (4) $Ge = 2$

As can be seen from figure 1, for reasonable values of the separation ratio $0 \prec \psi \prec 0.1$, the Landau coefficient λ is always positive for $Ge = 10^{-4}$ indicating the supercritical nature of the bifurcation. Moreover, λ increases with ψ which means, according to Eq. (2), that the stationary amplitude of convection decreases with the increase of the Soret effect. However, for $Ge = 10^{-1}$, $Ge = 1$ and $Ge = 2$, the sign of λ may change and the system observes a transition from supercritical to subcritical bifurcation at a particular value of ψ, say $\psi = \psi^*(Le, Ge, \Pr)$. From figure 1 we observe that the more we increase the Gebhart number, the more the ψ^* decreases. For these prescribed values of Ge, figure 1 also shows that λ decreases with ψ indicating that thermodiffusion reinforces the convective motions, and hence increases the heat and mass transfer in the fluid layer. As the Gebhart number plays a key role in determining the supercritical or subcritical nature of the bifurcation, it is necessary to consider its realistic numerical values. From the physical point of view, high values of Ge can occur only in geophysical or in atmospheric flows, so one can expect the occurrence of subcritical bifurcation for such flows. In contrast to these flows, if the fluid flow is on a typical laboratory scale, then Ge can hardly be greater than 10^{-4}. Results of practical relevance to experiments are presented in Table 1 for liquid mixtures involving ethanol/water and methanol/water for which the thermo-physical properties are well documented respectively in [Platten et al.] and [Lizarraga et al.]. As can be seen from Table 1, the minimum viscous dissipation parameter $Ge^* = Ge(\lambda = 0)$ needed to trigger a subcritical bifurcation is $Ge^* = 0.2316$ for ethanol/water mixture and $Ge^* = 0.4902$ for methanol/water. As these values are not realistic in real experiments, we expect that for these particular mixtures, the convection may set up via a supercritical bifurcation.

liquid properties	Water-Ethanol	n-dodecane/n-hexane
C_a^*	0.10 (water)	0.50
T_a^* (C)	37.5	25
Pr	16.5	8.1
Le	59.71	32.5
ψ	0.071	0.076
Nonlinear instability results		
Λ_c	27.49	44.36
γ	0.267	0.216
λ	$0.5788 - 2.4988\ Ge$	$0.4753 - 0.9697\ Ge$
$Ge^*(\lambda = 0)$	0.2316	0.4902

Table 1

.II. Nonlinear effects on the convective spatial distribution

To illustrate the influence of the nonlinearities on the spatial distribution of the emerging longitudinal rolls, figure 2 presents the streamlines in the (y, z) plane at the onset of the instability (Fig. 2a) and at 10% far from the criticality (Fig. 2b). The parameters are $\psi = 0.01$, $Le = 100$, $Ge = 10^{-4}$ and $\Pr = 10$ and the length in the y direction is fixed to the wave-length of longitudinal rolls at $\psi = 0$, i.e. two rolls . As seen from Fig. 2a, the number of rolls decreases from 2 for $\psi = 0$ to 1.5 for $\psi = 0.01$. Moreover, according to linear theory, Fig. 2a shows a perfect mid-plane reflection symmetry of convection cells. In the nonlinear domain, it can be seen from Fig. 2b that the mid-plane symmetry is broken and the center of the convection rolls is shifted towards the upper plate, while the fluid motion is significantly reduced near the lower boundary. We also note that the nonlinearities increase the number of rolls.

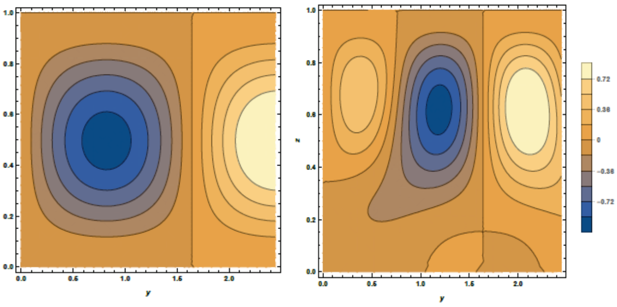

(a) (b)

Figure 2: Streamlines: (a) Linear theory, (b) weakly nonlinear approach

Conclusions

A weakly nonlinear stability analysis of mixed convection in a plane parallel channel has been carried out for positive values of the separation ratio ψ . The effect causing the unstable thermal stratification and, as a consequence, the emergence of convection cells is the viscous dissipation. This effect is the sole cause of the vertical temperature gradient in the basic state, as no thermal forcing is imposed through the boundary walls. We determined numerically up to third order the coefficients of the Landau amplitude equation and discussed the bifurcation nature. The main result obtained through this analysis is that the viscous dissipation, the Lewis number and thermodiffusion act in a concert to promote a transition from supercritical to subcritical bifurcation. However, for realistic values of the parameters in real laboratory experiments, we found that the bifurcation in mixed convection of binary fluids induced by viscous heating is always supercritical. In this case, some nonlinear properties of convection cells were identified in this work.

References

K. Ali Amar, S. C. Hirata, M. N. Ouarzazi, Soret effect on the onset of viscous dissipation thermal instability for Poiseuille flows in binary mixtures, Phys. Fluids, 34, 114101 (2022).

Y. Requilé, S. C. Hirata, M. N. Ouarzazi, Weakly nonlinear analysis of viscous dissipation thermal instability in plane Poiseuille and plane Couette flows, J. Fluid Mech., 886, A26 (2020).

J. K. Platten, M. M. Bou-Ali, , P. Blanco J. A. Madariaga, C. Santamaria, Soret coefficients in some water-methanol, water-ethanol, and water-isopropanol systems. J. Phys. Chem.B, 111,11524-11530 (2007).

I. Lizarraga, F. Croccolo, H. Bataller, M. M. Bou-Ali, Soret coefficient of the n-dodecane-n-hexane binary mixture under high pressure. Eur. Phys. J. E, 40, 36:1-9(2017).

Non-isothermal water treatment technology using green polymeric membranes

L. García-Fernández[1], O.B. Ferreiro[1,2], R. Guerrero[1], L.R. De la Rosa[1], M. Khayet[1,3], M.C. García-Payo[1]

[1]Department of Structure of Matter, Thermal Physics and Electronics, Faculty of Physics, Complutense University of Madrid, Madrid, Spain, loreto.garcia@ucm.es, [2]Facultad de Ciencias Químicas, Universidad Nacional de Asunción, San Lorenzo, Paraguay, [3]Madrid Institute for Advanced Studies of Water (IMDEA Water Institute), Alcalá de Henares, Madrid, Spain

Introduction

Water treatment technologies are at the forefront of scientific research to address the problem of water scarcity, which represents one of the worldwide unsolved issues today. Membrane distillation (MD) is a non-isothermal water treatment technology of emerging interest because of its environmentally-friendly benefit other than its ability to treat extremely high saline solutions. The MD driving force is the transmembrane temperature difference which induces the water vapor pressure difference through a porous hydrophobic membrane (Khayet and Matsuura 2011). One of the main challenges of MD is the design and preparation of membranes with suitable characteristics and improved MD performance (L. García-Fernández et al. 2015). Nonsolvent induced phase separation (NIPS) is the most commonly used technique for the preparation of polymeric membranes. However, a greener alternative is needed to mitigate the involved contamination of wastewaters during membrane preparation due to the discharge of toxic solvents, commonly used in industrial membrane fabrication. Membrane engineers are currently endeavoring to find proper green solvents (i.e. problematic and recommended) such as Triethyl phosphate (TEP), γ-Valerolactone (GVL), Cyrene (CYR), Dimethyl sulfoxide (DMSO), and Ethyl acetate (ETAC) among others to replace the most toxic ones (i.e. hazardous) such as N-Methyl-2-pyrrolidone (NMP), N,N-Dimethylacetamide (DMAC), N,N-Dimethylformamide (DMF); classified according to the CHEM21 guideline criteria (see Table 1) (Jiang et al. 2020, Wang et al. 2019, Prat et al. 2016).

MD membranes must meet some exigent requirements in order to achieve excellent separation performance. Therefore, the membrane morphology should be specifically designed for MD, which represents a current breakthrough in the field of membrane science. In this research study, polymeric flat-sheet membranes were prepared via NIPS using the eco-friendly solvents shown in Table 1 together with a prior analysis of the thermodynamics and kinetics mechanisms.

Table 1. Classification of solvents according to the CHEM21 guideline criteria (Prat et al. 2016)

Solvent	Safety score	Health score	Environmental score	Ranking
NMP	🟩	🟥	🟥	Hazardous
DMAc	🟩	🟥	🟨	Hazardous
DMF	🟩	🟥	🟨	Hazardous
TEP	🟩	🟩	🟥	Problematic
GVL	🟩	🟨	🟥	Problematic
CYR	🟩	🟩	🟥	Problematic
DMSO	🟩	🟩	🟨	Recommended
ETAC	🟨	🟩	🟩	Recommended

Membrane preparation via NIPS

Firstly, an homogeneous polymer solution was prepared by dissolving the hydrophobic copolymer, poly(vinylidene fluoride-co-hexafluoropropylene) (PVDF-HFP) in different green solvents (DMSO, TEP, ETAC, CYR and GVL) and some mixed solvents. Flat-sheet membranes were prepared by casting followed by immersion in a coagulation bath composed by pure water and different nonsolvent aqueous mixtures (60 wt% ethanol (EtOH60), 40 wt% tetraethylenglycol (TetraEt40)). Finally, the membranes were dried at room temperature before characterization.

The effects of the solvent type and the coagulation bath composition on the membrane structure were studied.

NIPS thermodynamics and kinetics analysis

Looking for the best MD performance (i.e. efficient heat and mass transfer through the membrane), a global knowledge of the membrane morphological structure is needed. Therefore, before membrane fabrication, the polymer solutions must be characterized by studying the polymer (P)/solvent (S)/nonsolvent (NS) interactions (calculated via Hansen solubility parameter distance, R_{HSP}), viscosity, together with both NIPS thermodynamic and kinetic experiments in order to analyze and correlate the relationship with the membrane morphological structure (L. García-Fernández et al. 2014, 2017).

The P/S affinity is determined by R_{HSP} (P-S), which informs about the solvent quality for PVDF-HFP. The solvent power increases for lower R_{HSP} (P-S) values, and consequently the viscosity of the dope solutions decreased. This effect was observed when 40 wt% of TEP or ETAC was added to DMSO in the solvent mixture, respectively (see Fig. 1).

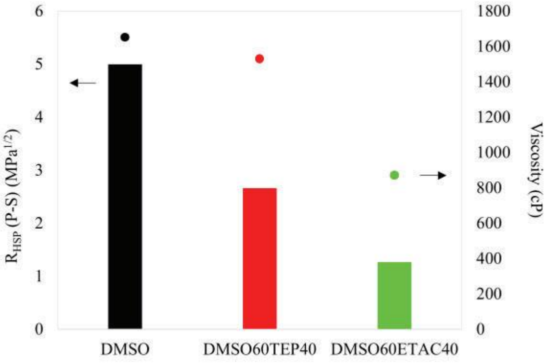

Figure 1: R_{HSP} (P-S) and viscosity of the PVDF-HFP casting solutions prepared with DMSO, DMSO 60 wt%/TEP 40 wt%, and DMSO 60 wt%/ETAC 40 wt%.

The NIPS thermodynamic analysis was determined by turbidimetric titration method. The maximum quantity of the nonsolvent admitted by the polymeric solution is denominated cloud point. It is represented in the ternary phase diagram (Fig. 2) and it is a useful parameter to understand the thermodynamic behavior at the beginning of the phase inversion process occurred during membrane formation. The kinetic experiment showed the S-NS exchange rate during membrane formation. This can be studied via the evolution of the light transmittance during the formation of the flat-sheet membrane.

By means the polymer solution characterization and NIPS thermodynamics and kinetics analysis, it is possible to predict the resultant membrane morphological structure, selecting therefore, the most adequate green solvent.

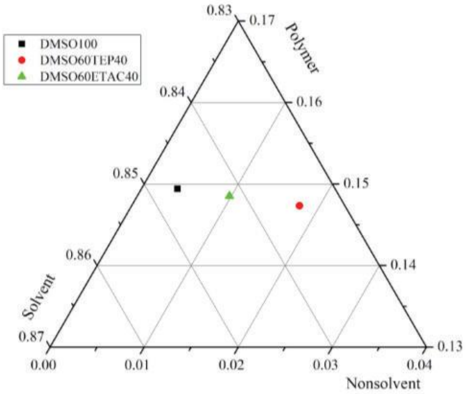

Figure 2: Ternary phase diagram of PVDF-HFP/DMSO mixed solvent/water system.

Membrane characterization and water treatment application

Various characterization techniques are used to analyze the suitability of the prepared membranes for MD. These are the thickness, contact angle, morphological structure (SEM cross-section and top surface), pore size distribution and liquid entry pressure (*LEP*).

By keeping constant the solvent used for the casting solution preparation (DMSO 100wt%), and changing the coagulation bath composition, it is possible to study the coagulation mechanism of the different nonsolvent mixtures during the NIPS process. R_{SHP} (S-NS) informs about the S-NS interaction, then, lower R_{SHP} (S-NS) values mean higher S-NS affinity, leading to different mean pore sizes and pore size distributions. As it can be seen in Fig. 3, the mixtures EtOH60 or TetraEt40 acted as weaker nonsolvents than water (lower R_{SHP} (S-NS) values). The reduced coagulation power induced the formation of membranes with narrower pore size distribution and smaller mean pore size.

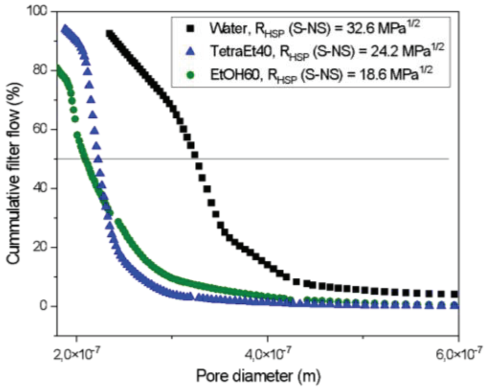

Figure 3: Cumulative filter flow of the membranes determined by porometry method, and the corresponding R_{HSP} (S-NS) parameters obtained for different nonsolvent mixtures.

The morphology of the prepared membranes as well as their morphological structure properties can be explained according to the thermodynamics and kinetics characterization analysis. According to the membrane characteristics, the most suitable ones were tested in desalination by direct contact MD (DCMD). The obtained results (permeate flux and salt rejection factor) could be explained well with the analyzed membrane characteristics.

Conclusions

Polymeric flat-sheet membranes were successfully prepared using green solvents. These membranes exhibited suitable properties for MD desalination. The adopted approach, for the selection of the adequate green solvent through polymeric membrane characterization together with NIPS thermodynamic and kinetic analysis, proved to be interesting to achieve adequate MD membranes with a sustainable water management.

Acknowledgements

The authors acknowledge the support of the Madrid Government (Comunidad de Madrid-Spain) under the Multiannual Agreement with University Complutense of Madrid (Research Incentive for Young PhDs, V PRICIT, Regional Programme of Research and Technological Innovation, PR27/21-060). LGF, MCGP and MK are also thankful to the Spanish Ministry of Science, Innovation and Universities for the financial support of the I+D+I project RTI2018-096042-B-C22. OBF also thanks BECAL Paraguay for the scholarship (Contract No. 221/2021). RG gratefully acknowledges Spanish Ministry of Education for the Department Collaboration grant (22CO1/005909). LRDR thanks Comunidad de Madrid-Spain for the contract Programa Investigo (CT36/22-26).

References

D. Prat, A. Wells, J. Hayler, H. Sneddon, C. Robert McElroy, S. Abou-Shehada and P.J. Dunn, CHEM21 selection guide of classical-and less classical-solvents*, Green Chemistry,* 18, 288-296, (2016).

H.H. Wang, J.T. Jung, J.F. Kim, et al., A novel green solvent alternative for polymeric membrane preparation via nonsolvent-induced phase separation (NIPS), Journal of Membrane Science, 574, 44–54, (2019)

L. García-Fernández, M Khayet y MC García-Payo, Membranes used in membrane distillation: preparation and characterization., Chapter 11, Elsevier, 317-359 (2015).

L. García-Fernández, M.C. García-Payo, M. Khayet, Effects of mixed solvents on the structural morphology and membrane distillation performance of PVDF-HFP hollow fiber membranes. *Journal of Membrane Science*, 468, 324-338, (2014).

L. García-Fernández, M.C. García-Payo, M. Khayet, Mechanism of formation of hollow fiber membranes for membrane distillation: 2. Outer coagulation power effect on morphological characteristics. Journal of Membrane Science, 542, 469-481 (2017).

M. Khayet, T. Matsuura, Membrane Distillation: Principles and Applications. Elsevier, The Netherlands, (2011).

S. Jiang, B.P. Ladewig, Green synthesis of polymeric membranes: Recent advances and future prospects, *Current Opinion in Green and Sustainable Chemistry*, 21, 1–8, (2020).

Measurement of Thermodiffusion in Molten Al-Cu-Ag

E. Sondermann[1], A. T. Krüger[1], A. Meyer[1]

[1] German Aerospace Centre (DLR), Cologne, Germany (elke.sonderamann@dlr.de)

Introduction

Thermodiffusion in liquid alloys influences the homogeneity of doped semiconductors and grown crystals as well as the microstructure formation during solidification. The calculation of thermodiffusion by molecular dynamic simulation can be very sensitive to the specific potential (Levchenko et al. 2016). Recently improved theories were proposed but the database to validate models for thermodiffusion in liquid alloys is scarce. Therefore, reliable measurements are needed.

For binary alloys with sufficient contrast in x-ray absorption x-ray radiography can be used for in-situ measurement of thermodiffusion (Sondermann et al. 2019). This technique excludes disturbances by solidification and reveals possible error sources as e.g. free surfaces.

It has been reported that in liquid Al-Cu the copper migrates to the cooler end of the sample (Bhat 1973) and in Al-Ag the silver atoms migrate to the cooler end (Krüger et al. 2023). Here, we study thermodiffusion in the ternary Al-Cu-Ag melt.

Method and Results

In a ternary alloy it is not possible to determine the concentration distribution from the grey values of the x-ray image. It is necessary to analyze the concentration distribution of the processed samples after solidification. However, x-ray radiography is employed as process control.

The setup for the measurement of thermodiffusion in multicomponent liquid alloys is very similar to the setup described in (Krüger et al. 2023). It consists of a furnace made out of graphite and boron-nitrite which is placed inside a vacuum chamber. The alloy samples have the form of a cylinder with 1.3 mm in diameter and 10 mm in height. The crucible that holds the samples in vertical position is made of boron-nitrite. It can be separated into six parts of 1.5 mm height.

During an experiment, the Al-Cu-Ag samples in the furnace are heated up to 973 K with a temperature gradient of 1.5 K/mm along the sample. After annealing for at least three hours the liquid alloy is separated into six parts and then cooled down to room temperature. The solidified parts are subsequently removed from the crucible and analyzed by energy dispersive X-ray spectroscopy (EDS).

For the eutectic composition $Al_{68.6}Ag_{17.6}Cu_{13.8}$ it is found that aluminum migrates to the hot end and silver migrates to the cold end. The copper concentration stays about constant along the sample. The concentration gradient of silver is comparable to measurements of thermodiffusion in liquid $Al_{80}Ag_{20}$.

Although the heaviest element in the alloy tends to diffuse to the lower part of the sample and aluminum as the lightest element diffuses to the upper part this is not due to gravity. In liquid alloys the thermal energy of an atom is larger than the gravitational energy by orders of magnitude (Sondermann et al. 2022).

Conclusions

With the newly developed setup, it is possible to measure the Soret effect in multicomponent liquid alloys. In the case of eutectic Al-Cu-Ag it was found that aluminum diffuses to the hot end while silver diffuses to the cold end.
The Soret effect in the binary liquid Ag-Cu has not yet been determined due to its low contrast in x-ray absorption. From the results in the ternary Al-Cu-Ag we expect silver to migrate to the cold end also in the binary Ag-Cu melt.

References

E. V. Levchenko, A. V. Evteev, T. Ahmed, A. Kromik, R. Kozubski, I. V. Belova, Z.-K. Liu, G. E. Murch, Influence of the interatomic potential on thermotransport in binary liquid alloys: case study on NiAl, *Philos. Mag.*, 96, 3054 (2016)

E. Sondermann, F. Kargl, A. Meyer, In situ measurement of thermodiffusion in liquid alloys, *Phys. Rev. Lett.*, 123, 255902, (2019)

A. T. Krüger, E. Sondermann, A. Meyer, Measurement of the Soret coefficient in liquid Al–Ag alloys using X-ray radiography, *Phys. Rev. B*, 107, 064301 (2023)

B.N. Bhat, Thermotransport in liquid Al-Cu alloys, *National Aeronautics and Space Administration*, Technical Report No. TR R-415, (1973)

E. Sondermann, T. Voigtmann, A. Meyer, Influence of Gravity on Atomic Mobility in a Liquid, *Microgravity Science and Technology*, 34, 93 (2022)

Temperature dependent measurements of the diffusion- and Soret-coefficient in a binary polystyrene/toluene mixture by means of a transient holographic grating technique

J. Kantelhardt[1], W. Köhler[1]

[1]Physikalisches Institut Universität Bayreuth, Bayreuth, Germany, werner.koehler@uni-bayreuth.de

Introduction

Thermodiffusion in polymer solutions has revealed a number of surprising properties, like the molar mass independence of the thermodiffusion-coefficient D_T in the dilute limit or the blindness of the Soret-coefficient against the glass transition at higher polymer concentrations. Little is known, however, about the temperature dependence of the Soret effect in polymer solutions. In this work we investigate how the diffusion- and the Soret-coefficient change with different ambient temperatures, thereby covering a temperature range from 10°C to 50°C in steps of 5°C. The investigated system is a binary mixture of polystyrene in toluene. In a similar concentration the same system was also used in the DCMIX4 microgravity campaign on ternary mixtures and is currently investigated in the ongoing GIANT FLUCTUATIONS project of ESA.

The measurements have been performed with a Thermal-Diffusion-Forced-Rayleigh-Scattering (TDFRS) set-up (Fig.1). With this heterodyne procedure one is able to directly get information of the changes in the refractive index through the measured signal (J. Rauch et al. 2003).

Experimental set-up

For the TDFRS set-up we need two laser beams with different wavelength. One is the writing beam with a wavelength of 532nm, which produces a holographic grating with a period of ~10µm inside the cell. With the addition of a negligible amount of an inert dye, which is compatible with the wavelength of the laser, absorption occurs and temperature differences well below 0.1mK appear. This periodic temperature grating leads to a superposed concentration grating and both give rise to refractive index gratings. The readout laser is 632.8nm where it is important that the wavelength is not absorbed by the dye. The signal is measured by Bragg-diffraction (W. Köhler et al. 2000).

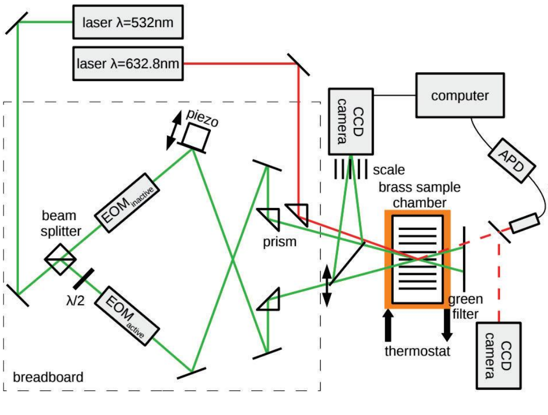

Figure 1: The TDFRS set-up.

Experiment

The liquid is a binary mixture consisting of polystyrene (PS) with a molar mass of 4840 g/mol dissolved in toluene (Tol), which is a well established and researched system. The weight fraction of PS is c_{PS}=1%.

We have measured the diffusion- and Soret-coefficient for different temperatures (10°C, 15°C, 20°C, 22°C, 25°C, 30°C, 35°C, 40°C, 45°C, 50°C) and compared them to literature data at room temperature (J. Rauch et al. 2003). Both can be seen in Fig.2 and Fig.3 respectively.

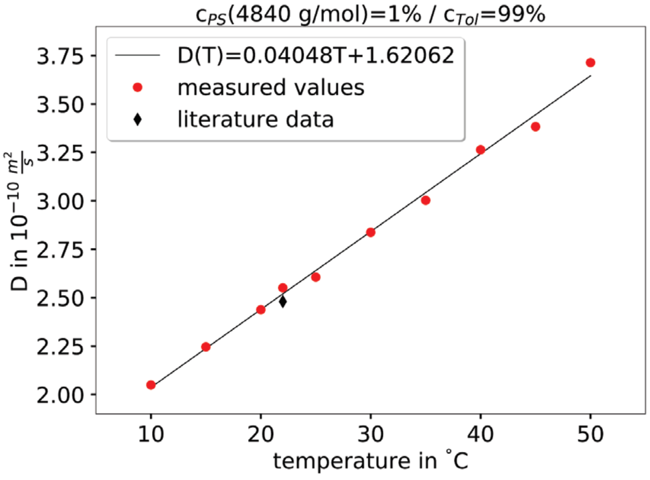

Figure 2: The diffusion-coefficient of the sample PS/Tol with c_{PS}=1% for different ambient temperatures. The measured values of the diffusion-coefficient are the red dots, the literature data (J. Rauch et al. 2003) is a black diamond.

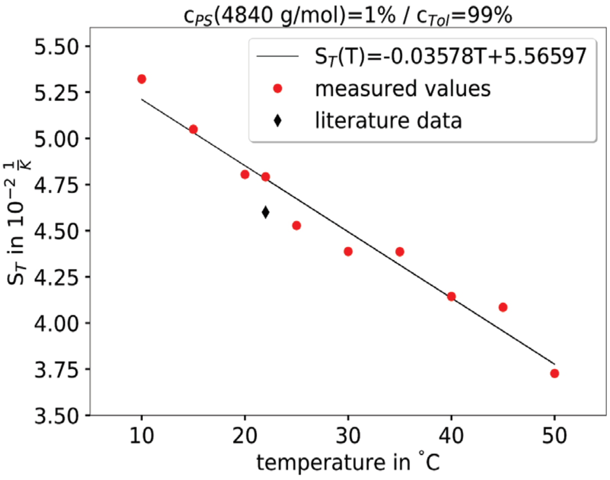

Figure 3: The Soret-coefficient of the sample PS/Tol with c_{PS}=1% for different ambient temperatures. The measured values of the Soret-coefficient are the red dots, the literature data (J. Rauch et al. 2003) is a black diamond.

Results

We found a good agreement for the literature data (black diamonds, which were also measured with TDFRS) and our measured data points (red dots). The diffusion-coefficient rises linearly with an increase in temperature while the opposite can be said about the Soret-coefficient. D_T is slightly increasing.

We also looked into the hydrodynamic radius (R_h) for the different temperatures. We calculated it with the Stokes-Einstein equation $R_h=(k_B T)/(6\pi\eta D)$ (A. Einstein 1905). k_B is the Boltzmann-constant, T the temperature in Kelvin, η the dynamic viscosity and D the diffusion-coefficient. We can approximate the value of the dynamic viscosity of the pure solvent because our sample is diluted (D. Stadelmaier et al. 2008). The equation for the approximation is (F.J.V. Santos et al. 2006):

$$ln(\overline{\eta}) = -5.2203 + \frac{8.964}{\overline{T}} - \frac{5.834}{\overline{T}^2} + \frac{2.089}{\overline{T}^3}$$

with the reduced variables $\overline{\eta} = \eta_0(T)/\eta_0(T_0)$ and $\overline{T} = T/T_0$, where T_0=298.15K and $\eta_0(T_0)$=554.2µPas. The values for the hydrodynamic radius follow a constant behaviour which can be seen in Fig.4, indicated with a horizontal black line whose value is R_h=1.51nm. As a result it can be said that the increase in temperature has no effect on the quality of the solvent and hence, on the expansion of these short polymer chains.

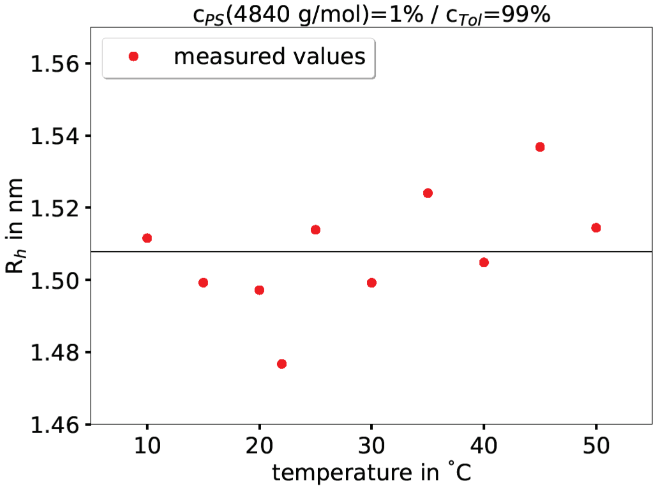

Figure 4: The hydrodynamic radius of the sample PS/Tol with c_{PS}=1% for different ambient temperatured. The values were calculated with the Stokes-Einstein equation..

Acknowledgements

This work was supported by the ESA poject GIANT FLUCTUATIONS, the ESA-MAP project TechNES (Grant 4000128933/19/NL/PG), and by Deutsches Zentrum für Luft- und Raumfahrt (DLR), Grant 50WM2147 (BTGIANTII).

References

W. Köhler, R. Schäfer, Polymer Analysis by Thermal-Diffusion Forced Rayleigh Scattering, Advances in Polymer Science, Vol. 151, (2000)

J. Rauch, W. Köhler, Collective and thermal diffusion in dilute, semidilute, and concentrated solutions of polystyrene in toluene, J. Chem. Phys 119, 11977 (2003)

A. Einstein, Über die von der molekularkinetischen Theorie der Wärme geforderte Bewegung von in ruhenden Flüssigkeiten suspendierten Teilchen, Annalen der Physik, Band 17, (1905)

D. Stadelmaier, W. Köhler, From Small Molecules to High Polymers: Investigation of the Crossover of Thermal Diffusion in Dilute Polystyrene Solutions, Macromolecules, 41, 16, 6205–6209, (2008)

F.J.V. Santos, C.A. Nieto de Castro, J.H. Dymond, N.K. Dalaouti, M.J. Assael, A. Nagashima, J. Phys. Chem. Ref. Data 35, 1 (2006)

Measurements on Diffusion and Thermodiffusion on thermoresponsive Poly(N-acryloylglycinamide) in water and polystyrene/toluene mixtures with a scaled down double-pass Optical-Beam-Deflection setup

R. Reh[1], M. Hager[1], N. Majstorovic[2], S. Agarwal[2], W. Köhler[1]

[1]Universität Bayreuth, Physikalisches Institut, Germany, werner.koehler@uni-bayreuth.de
[2]Universität Bayreuth, Macromolecular Chemistry II, Germany

Introduction

We report about measurements on Poly(N-acryloylglycinamide) (PNAGA) in aqueous solution and binary and ternary mixtures of polystyrene and toluene with a scaled down double-pass Optical-Beam-Deflection (OBD) setup. For PNAGA, Diffusion-, Thermodiffusion- and Soret coefficients were measured with the polymer in linear form and as a crosslinked microgel. Furthermore, temperature dependent turbidity measurements were done with the linear PNAGA polymer. For polystyrene in toluene, results of OBD measurements were processed with a CONTIN routine.

Experimental

Experiments on diffusion were performed with a scaled down double-pass Optical-Beam-Deflection setup. The top view of the setup is sketched in Figure 1.

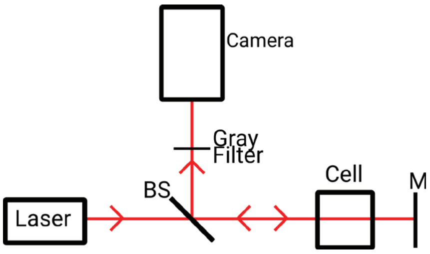

Figure 1: Sketch of the top view of the scaled down double-pass Optical-Beam-Deflection setup.

A laser beam transmitted through the sample gets back-reflected behind the OBD-cell and, thus, traverses the sample volume a second time. The cell with the path of the laser beam is sketched in Figure 2. Applying a vertical temperature gradient to the sample leads to thermodiffusion and the beam gets deflected by the resulting gradient in refractive index due to the gradients in temperature and concentration. A beam splitter guides the beam towards a camera, where the time dependent laser position is recorded. The signal then gives information about the diffusion processes. Since the laser beam propagates on the same path between the beam splitter and the cell before and after getting deflected in the sample and since the double-transmission geometry allows for a short distance between cell and camera, the whole setup could be built very compact.

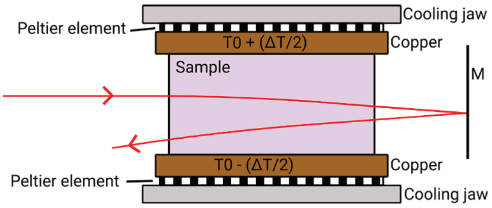

Figure 2: Side view of the cell containing the sample in the Optical-Beam-Deflection technique. The path of the deflected laser beam is drawn in red.

Results

In case of mixtures of polystyrene/toluene, the multimodal time traces were evaluated with an adapted version of the CONTIN program for the solution of inverse problems. We found that diffusion coefficients extracted in this way agree with literature data (J. Rauch et. al. 2003). The results for diffusion coefficients in the measurements with samples with two polymers of different sizes are in agreement with the data for the single components. Based on these results, polymers with a broad molar mass distribution can now be investigated. Turbidity measurements with Poly(N-acryloylglycinamide) in water show a UCST-behavior and a hysteresis in the temperature of the cloud point, depending on the direction of the temperature ramp, which is in accordance with results from other experiments (J. Seuring et. al. 2012). Thermodiffusion- and Soret coefficients at different temperatures are described with an exponential Piazza function (S. Iacopini et. al. 2006) and are comparable for the linear polymer and the microgel, showing a behaviour and a change in sign in the region of about 35 to 40 °C.

References

J. Seuring, F. M. Bayer, K. Huber, S. Agarwal, Upper Critical Solution Temperature of Poly(N-acryloyl glycinamide) in Water: A Concealed Property, *Macromolecules,* 45, 374-384, (2012)

S. Iacopini, R. Rusconi, R. Piazza, The “macromolecular tourist”: Universal temperature dependence of thermal diffusion in aqueous colloidal suspensions, *Eur. Phys. J. E*, 19, 59-67, (2006)

J. Rauch, W. Köhler, Collective and thermal diffusion in dilute, semidilute, and concentrated solutions of polystyrene in toluene, *Journal of Chemical Physics,* 119**,** 11977-11988 (2003)

Measurement of the Soret coefficient of binary mixtures in porous media

I. C. Pérez de Luco[1], P. Fernández de Arroiabe[1], V. Shevtsova[2], M. M. Bou-Ali[1], A. Mojtabi[3], P. Costeseque[3]

[1]Fluid Mechanics Group, Mondragon University, Mondragon, Spain, mbouali@mondragon.edu
[2]Ikerbasque, Basque Foundation for Science, Bilbao, Spain,
[3]Université de Toulouse, I.M.F.T. UMR CNRS/INP/UPS, 31400 Toulouse, France

Introduction

Transport mechanisms due to temperature gradients have been widely studied in fields, such as energies (Mahamoudou et al. 2022) or the oil industry (Touzet et al. 2011). Quantiy describing this process is the Soret coefficient (S_T), which is the ratio between thermodiffusion (D_T) and diffusion (D) coefficients. For the case of a binary sample, the mass flux is defined as follows:

$$\vec{J} = -\rho D \nabla c - \rho D_T c_0 (1 - c_0) \nabla T \tag{1}$$

Where $\vec{J}$ is the mass flow, ρ is the density of the mixture, c is the concentration of the densest component in the mixture; ∇c and ∇T are the concentration and temperature gradients respectively. When the mixture is in steady state ($\vec{J} = 0$) the Soret coefficient in free and porous media (Platten et al. 2004), S_T is defined as follows:

$$S_T^* = \frac{D_T^*}{D^*} = S_T = \frac{\Delta c}{\Delta T c_0 (1 - c_0)} \tag{2}$$

With the aim of studying this phenomenon in depth, several international projects have emerged, such as the Benchmark of Fontainebleau (Platten et al. 2003). Furthermore, there are various experimental techniques in free media such as the thermogravitational column (Blanco et al. 2008) or ODI (Mialdun et al. 2008) for quantifying these coefficients. In porous media, Soret cell (Costesèque et al. 2003) can be used for both positive and negative Soret coeficcients. Therefore, given the importance of thermodiffusion, the aim of this work is to set up the Soret experiment to determine its magnitude in terrestrial conditions in aqueous-salt mixtures.

The article is structured as follows. First, both the device and the experimental procedure are briefly described. Then, the numerical and experimental validation with previously analysed samples is presented. After that, new aqueous samples based on LiBr salt are analysed, due to the importance of their transport properties in absorption chillers and heat pumps. Finally, conclusions are drawn from the study carried out.

Experimental device and technique

The experimental setup consists of two stainless steel cavities through which water circulates at a controlled temperature by means of two thermostatic baths LAUDA ProLine RP 855 and RC 6. Between the two plates, there is the gap (380×90×15 mm) which is surrounded by PVC (Figure 1a). Both the stainless steel plates and the gap of constant dimensions must be perfectly horizontal to avoid disturbances in the tests. In addition, the Soret cell has 6 extraction outlets at the top and 6 at the bottom (Figure 1b). To ensure the sealing of the working space during the tests, all the parts are fixed together with a viton gasket in between.

Figure 1: a) Transverse cross-sectional view of the Soret cell. b) Whole installation of the Soret cell.

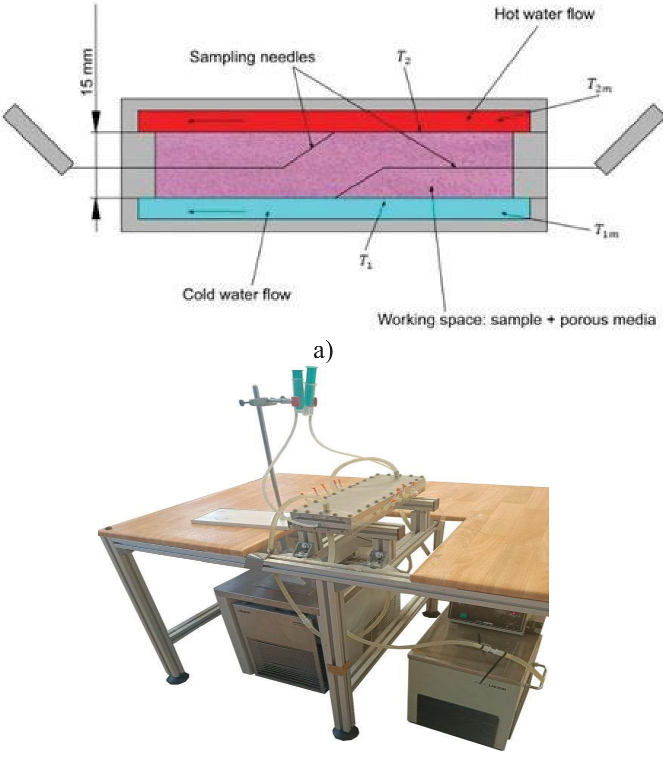

a)

b)

The experimental procedure starts by filling the gap and the porous medium with the mixture to ensure that the porous medium is completely saturated. To do so, the cell is placed in a vertical position and the mixture is circulated from the bottom upwards until the mixture comes out of the top bubble-free. After that, it is returned to a completely horizontal position and the walls are exposed to the corresponding temperatures. If the mixture has a positive Soret coefficient, the top wall is heated and the bottom one cooled. In contrast, if the Soret coefficient is negative, the other way around. This way, the denser component always migrates downwards.

Numerical and experimental validation

For the numerical validation, a 2D computational domain is used. The validation is carried out using a well-known mixture: tetralin (THN) – isobutilbenzene (IBB) with a mass fraction of 0.5. The numerical model includes the momentum, heat and mass transfer equations in the Boussinesq approximation (Naumann et al. 2012). The density changes due to temperature and concentration are taken into account by the following:

$$\rho = \rho_0(1 - \alpha(T - T_0) + \beta(c - c_0)) \qquad (3)$$

Where α and β correspond to the coefficients of thermal and solutal expansion respectively. The applied temperature difference is 10 K. **¡Error! No se encuentra el origen de la referencia.** shows the computed concentration profile on the steady state.

Figure 2: Concentration profile of THN in the THN-IBB sample with a temperature difference of 10 K.

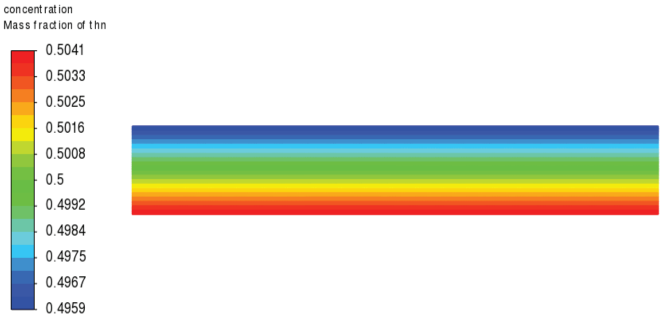

The figure shows that the denser component (THN) goes to the lower part and the less dense component (IBB) accumulates at the upper part.

For the experimental validation samples of 3 mL are extracted. In particular, the fluid from three extraction sockets is analysed together, obtaining four samples (two from the upper part and two from the lower part). In this way, enough liquid is obtained to calculate the concentration based on density, using a high-resolution density-meter. In addition, by having samples from two different points of the column, the values obtained are averaged, thus minimising experimental error.

Following this procedure, samples previously analysed by (Königer et al. 2009) have been used to perform the validation. The results obtained for a pair of mixtures THN-IBB and water-ethanol (H_2O-Eth) are shown in Table , as well as the temperature difference and the separation of the components as an example.

Table 1: Experimental results of experiments performed with the validation samples.

Sample	c_0	ΔT (°C)	Δc	$S_T/10^{-3}$ (K^{-1})	$S_T/10^{-3}$ (K^{-1}) lit
THN-IBB	0.5	14.0	0.0123	3.49	3.3
H_2O-Eth	0.9	-15.4	0.0093	-6.73	-6.75

H_2O-LiBr samples

Once the experimental device has been validated, the sample LiBr-H_2O has been measured in the temperature range of 30 to 45 °C and mass concentration range of 0.5 to 0.65. This mixture plays an important role in the field of renewable energies.

Before determining the transport coefficients of these samples, their thermophysical properties have been studied first. Then, the sliding symmetric tubes technique will be used to determinate their diffusion coefficients, and their Soret coefficients will be determined using the Soret cell with porous media.

Conclusions

The validation experiments show that the Soret cell with porous media is an adequated technique to measure the Soret coefficient of both positive and negative samples of binary mixtures in terrestrial conditions.

Acknowledgements

This work is supported by Gipuzkoa Provincial Council under Grant No. 2022-CIEN-000052-01 (Hoztikor), Research Group Program of the Basque Government under Grant No. . IT1505-22, GE-MICINN-TED of the Spanish Government Grant No. PID2021-124232OB-I00 (Treated) and by CNES, the French National Space Agency.

References

A. Königer, B. Meier, W. Köhler, Measurement of the soret, diffusion, and thermal diffusion coefficients of three binary organic benchmark mixtures and of ethanol-water mixtures using a beam deflection technique, *Philos. Mag.*, 89, 907-923, (2009).

A. Mahamoudou, J. Ramousse, N. Le Pierrès, Analysis of a falling film H_2O/LiBr absorber at local scale based on entropy generation, *Int. J. Heat Mass Transf,* 198, 123425, (2022).

A. Mialdun, V. Shevtsova, Development of optical digital interferometry technique for measurement of thermodiffusion coefficients, *Int. J. Heat Mass Transf.,* 51, 3164-3178, (2008)

J.K. Platten, M.M. Bou-Ali, P. Costeséque, J.F. Dutrieux, W. Köhler, C. Leppla, S. Wiegand, G. Wittko, Benchmark values for the Soret, thermal diffusion and diffusion coefficients of three binary organic liquid mixtures, *Philos. Mag.*, 83, 1965-1971, (2003).

J.K. Platten, P. Costesèque, The Soret Coefficient in Porous Media, *J. Porous Media*, 7, 317-329, (2004).

M. Touzet, G. Galliero, V. Lazzeri, M.Z. Saghir, F. Montel, J.C. Legros, Thermodiffusion: From microgravity experiments to the initial state of petroleum reservoirs, *Comptes Rendus – Mecanique,* 339, 318-323, (2011).

P. Blanco, M.M. Bou-Ali, J.K. Platten, P. Urteaga, J.A. Madariaga, C. Santamaria, Determination of thermal diffusion coefficient in equimolar n -alkane mixtures: Empirical correlations, *J. Chem. Phys*., 129, 174504, (2008).

P. Costesèque, S. Gaillard, Y. Gachet, P.H. Jamet, Determination of the apparent negative Soret coefficient of water-10% alcohol solutions by experimental and numerical methods in packed cells, *Philos. Mag.*, 83, 2039-2044, (2003).

P. Naumann, A. Martin, H. Kriegs, M. Larrañaga, M.M. Bou-Ali, S. Wiegand, Development of a thermogravitational microcolumn with an interferometric contactless detection system, J. Phys. Chem., 116, 13889- 13897, (2012).

The melting-solidification cycle for materials with different Prandtl numbers

D. Dubert[1], B. Seta[2], M.J. Simón[3], Jna. Gavalda[1], J. Massons[1], A. Perez-Poch[4], X. Ruiz[1]

[1]Dept. Química Física I Inorgànica, Universitat Rovira I Virgili, Tarragona, Spain
[2]Dept. of Mechanical Engineering, Technical University of Denmark. Kogens Lynaby, Denmark.
[3] Dept. Enginyeria Mecànica, Universitat Rovira I Virgili, Tarragona, Spain
[4] Dept.Computer Science, Universitat Politècnica de Catalunya, Institut d'Estudis Espacials de Catalunya (IEEC), Spain
Corresponding author: Diana Dubert: dianacristina.dubert@urv.cat

Introduction

Marangoni convection greatly affects the material's processing since it enhances heat and mass transport near a free surface. Its benefits are clearly noticed in Space due to the lack of natural convection but also on Earth, as seen in crystal growth techniques.

Currently, the effect of thermocapillary flow in heat transport during a phase change material (PCM) has risen a lot of attention. Moreover, the use of PCMs for the extraction or storage of heat is of great interest, not only for terrestrial applications but as well in Space, mainly due to the simplicity of its design and usage. In this context, the literature shows different studies of the fluid dynamics during the melting and solidification phenomena, as two separate processes (see Seta et al. 2021 and Lappa et al. 2017) and very scarce studies that analyze the complete melting-solidification cycle. This could be interesting due to the fact that these PCM devices are foreseen to work continuously with this kind of cycles. Some of the typical materials that already have been studied during melting or solidification processes are sodium nitrate ($NaNO_3$, Pr=8), succinonitrile (SCN, Pr=23), or the conventional Gallium (Ga, Pr=0.02) (Hannoun et al. 2003, Lappa et al. 2017).

Paraffin-based PCMs, such as n-octadecane, are attractive materials due to their high latent heat values. Furthermore, their low density and chemical stability make them successfully compete with other materials already in use for this purpose. From this perspective, the MarPCM ESA project investigates the effectiveness of Marangoni convection to improve the heat transfer of passive devices based on PCM materials, Porter et al. 2022. Pure and blended n-octadecane under thermodiffusive Soret effect conditions are investigated in this project (Sanjuan et al. 2022). This work aims to study the flow dynamics of the n-octadecane during a complete melting-solidification cycle. In addition, a comparison between n-octadecane and the typical PCM materials specified earlier is proposed. To do so, 2-D simulations in a rectangular box were planned and the patterns of the flow were analyzed.

Methodology

The geometry used in the simulations was a rectangular cell with the height of 0.8 mm and the length of 8 mm (aspect ratio, AR=10). Initially, the material selected was in a solid state with a temperature, Ts, one degree under the melting one (see Table 1). By applying a 20 K temperature difference, ΔT, between the opposite walls (with the high temperature above the solid one, at the right wall) the system began to melt. The melting process continued until reached a minimum of 98% of the liquid phase. The high temperature is then lowered to $Ts-\Delta T$, when the solidification process began. The upper wall was considered a free surface, where thermocapillary convection appeared, driving the liquid phase flow. All the boundary walls were assumed adiabatic and no-slip fluid velocity conditions were imposed except in the upper free border. All the simulations were carried out by using OpenFOAM tools. Entalphy-porosity method was used to model the melting-solidification cycle. In this case, the latent heat generated during the phase change was introduced as a new term in the energy equation. More details in Seta et al. 2021. For the discretization of the system, we have checked different meshes and selected a 260 x 40 points mesh refined near the free surface and lateral walls, where high gradients of the physical magnitudes were expected. The physical properties of all the materials used in the simulations are summarized in Table 1.

Table 1: Physical properties of materials used in this work: Seta et al. (2021)[1], Lappa et al (2017) [2], Hannoun et al (2003)[3].

	N-octad.[1]	SCN[2]	$NaNO_3$[2]	Ga[3]
Melting Temperature (K)	301.15	331.23	581.15	302.93
Density solid/liquid Kg/m^3	865 780	998 998	2261 1908	5910 6093
Specific latent heat (KJ/Kg)	243.5	46.9	178.0	80.2
Specific heat capacity solid/liquid J/(Kg K)	1934 2196	1955 2000	1780 1655	371 382
Conductivity solid/liquid W/(m K)	0.36 0.15	0.23 0.23	0.68 0.52	41 32
Dynamic viscosity ($x\ 10^{-3}$ Pa.s)	3.6	2.6	2.7	1.8
Thermocapillary coefficient $x\ 10^{-5}$ N/(m K)	8.44	10.63	5.83	8.99
Prandtl number	56	23	8	0.02

Results

Figure 1 shows the evolution of the liquid fraction along a melting-solidification cycle for all materials analyzed. Notice that the melting time of the n-octadecane is substantially increased (18000 s) with respect to the melting time of the rest of the materials (around 1800 s). This fact may be due to its high latent heat value which increases the melting time as well as its low conductivity and higher dynamic viscosity (high Prandtl number) that contribute to this effect.

In addition, the melting and solidification processes showed to be asymmetric, presenting higher solidification time compared to the melting one. During the cooling process, the four samples exhibited very different behavior, Gallium having the lowest solidification time.

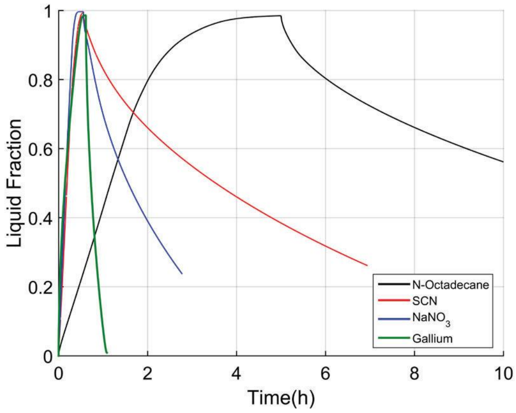

Figure 1: Liquid fraction evolution during melting/solidification cycle for different materials.

Figures 2 and 3 plot the flow pattern during the melting and solidification processes for all the materials, respectively. In both cases, the screenshots correspond to the time at which the liquid fraction reached 0.8 (80% melted).

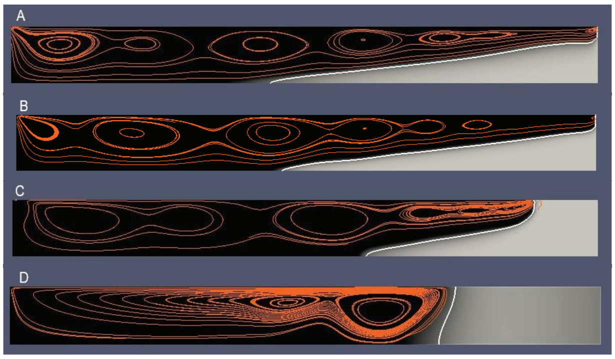

Figure 2: Screenshots of flow pattern at 0.8 liquid fraction: A) N-octadecane, B) SCN, C) $NaNO_3$, and D) Gallium.

We can differentiate three types of flow patterns. For n-octadecane and SCN, the longitudinal traveling hydrothermal waves were formed at the hot wall (right side), with multiple vortex cells (see Figs. 2a and 2b). The same traveling hydrothermal waves were seen in the case of $NaNO_3$ material though they were generated in the upper corner of the cold wall (left side, see Fig. 2c). In case of Gallium no traveling waves were detected, hence two stationary vortex cells were formed (see Fig. 2d). In addition, the above-mentioned flow patterns, due to Marangoni convection, as well conditioned the shape of the interphase liquid-solid.

Once the solidification process started, two vortex cells appeared in all cases, originated in both right and left upper corners of the box, respectively (See Figure 3). These vortices presented a clockwise and counterclockwise rotation due to the existing Marangoni forces, which have opposite signs in the left and right corners. Remark the shape of the solidification front that remained practically perpendicular on the free surface in all cases.

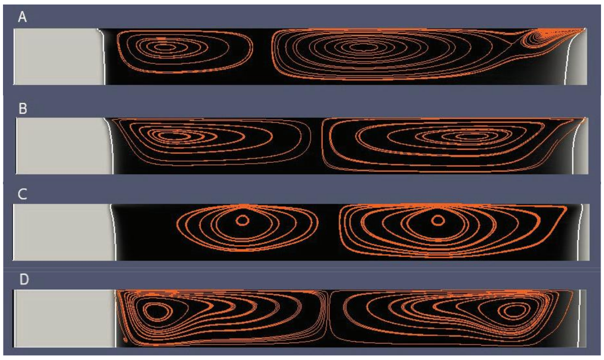

Figure 3: Screenshots of flow pattern at 20% solidification: A) N-octadecane, B) SCN, C) NaNO3, and D) Gallium

Conclusions

Generally, for all materials investigated, melting and solidification processes were not symmetric presenting longer solidification times compared to those of melting. Moreover, the flow pattern and the shape of the liquid-solid interphase strongly depend on the Prandtl number. Under the specified simulation conditions, this behavior has been observed mainly in the melting process. In particular, n-octadecane showed to have a longer solidification time compared to the melting one, so that raises the question: do we need to wait for the complete cycle or it is possible to have an optimized heat extraction just by using a partially melting-solidification cycle? Therefore, more investigations are needed to answer this question.

Acknowledgments

This work has been supported by the Ministerio de Ciencia e Innovación under Project PID2020-115086GB-C32.

References

M. Lappa, On the formation and propagation of hydrothermal waves in liquid layers with phase change, Computers & Fluids,000,1-20 (2017).

B. Seta, D. Dubert, J. Massons, Jna. Gavalda, M.M. Bou-Ali, X. Ruiz, Effect of Marangoni induced instabilities on a melting bridge under microgravity conditions, Int. J. Heat Mass Trasf., 179, 121665 (2021).

N. Hannoun, V. Alexiades, T.Zee Mai,Resolving the controversy over Tin and Gallium melting in a rectangular cavity heated from the side, Numerical Heat Transfer, part B, 44, 253-276(2003).

Sanjuan, B. Seta, F. Gavalda, X. Ruiz, V. Shevtsova, M.M. Bou-Ali, Comparativeexperimental-numerical análisis of PCM:n-hexadecane, n-octadecane and n-eicosane, Proceedings ELGRA symposium,68-69 (2022), https://www.elgra.org/?page_id=908

J. Porter et al., The effect of Marangoni convection on heat transfer in phase change materials experiment, Proceedings ELGRA symposium, 77-78 (2022), https://www.elgra.org/?page_id=908

Transport phenomena binary and ternary mixtures of Fullerene C_{60} in aromatic solvents

A. Errarte[1], D. Sommerman[2], M. Mounir Bou-Ali[1], W. Köhler[2]

[1]Fluid Mechanics Group, Mondragon University, Mondragon, Spain, aerrarte@mondragon.edu
[2]Department of Physics, University of Bayreuth, Bayreuth, Germany

Introduction

The fullerene C_{60} is an allotropic form of carbon where the 60 atoms are arranged forming a hollow sphere, *buckyball*, with 12 pentagonal and 20 hexagonal faces. Due to unique physico-chemical properties, the discovery in 1985 opened new routes in nanoscience and nanotechnology (Kroto et al. 1985). Fullerenes are promising molecules for use in composites, energy materials, lubricants, etc., but its high stability, strength and low toxicity also make it a strong candidate for biomedical use (Bakry et al. 2007). Considered as potential drug delivery system, these carbon allotropes are active molecules for transport or can even capture molecules in their cage.

Nevertheless, one of the most relevant properties that influence both the ease of extraction and purification, as well as the subsequent functionalisation and use of fullerenes, is their solubility (Ruoff et al., 1993). Even if fullerenes are the only allotropic modifications of carbon that are soluble in organic compounds, their solubility is in most cases low, and this is one of the main obstacles to progress in the study of their transport properties. Works in literature are almost non-existent; the diffusion of C_{60} through a semiconducting polymer film (polyfluorene) was analyzed using an optical method based on photoluminescence quenching (Fischer et al. 2014), whereas the Soret and diffusion coefficients of C_{60} fullerene in organic solvent o-dichlorobenzene used for photovoltaics were measured by the thermal-diffusion forced Rayleigh scattering (TDFRS) technique (Matsuura et al., 2015).

Motivated by the possibilities of fullerenes, the gap in the literature and the inherent need to determine their transport properties for the development of new applications, we present thermodiffusion (D_T), molecular diffusion (D) and Soret coefficients (S_T) of C_{60} in five aromatic solvents: Methylnaphthalene, Toluene, and Xylene isomers oXylene, mXylene and pXylene. Although the structures of the molecules are similar, all contain cyclic atom arrangements and methyl groups, the thermophysical properties are different; That is why, in this work, we analyse the effect of the number of rings in the molecular structure (MN|Tol) and the number and position of the methyl group (Tol|oXyl|mXyl|pXyl) over the mentioned transport properties. This work is considered as a continuation of the analysis of transport properties of the ternary mixture C_{60}|THN|Tol within the framework of the DCMIX project, where abovementioned properties are being measured both on ground and on-board the International Space Station (Errarte et al., 2022).

Investigated systems

We clasify the mixtures in three blocks: diluted fullerene nanofluids C_{60}+{MN|Tol|oXyl|mXyl|pXyl}, solvent-solvent binary mixtures and the ternary mixtures. In the case of the former, solute concentration range in mass composition, $c_i = 0.0010 - 0.0025$ was analysed. Solvent combinations were tested at $c_i = 0.50$. All studied ternary mixtures consisted of C_{60} at a mass fraction of 0.002, MN at a concentration of 0.499 and each of the other compounds - Tol, oXyl, mXyl or pXyl - at another 0.499.

All the mixtures, represented in Figure 1 were analysed at a mean temperature of 25 °C.

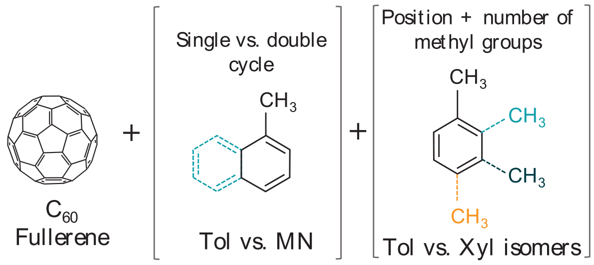

Figure 1: Schematic representation of molecules and analysis perfomed in this work.

Experimental setups

We tested all mixtures using the multiple-color Optical Beam Deflection (4-OBD) technique (Gebhardt and Köhler 2015). In order to determine the thermodiffusion coefficients, we performed supporting experiments on ternary mixtures by the thermogravitational column technique (TGC) (Larrañaga et al. 2015).

The former consists of determining the concentration variation induced by the Soret effect studying the deflection of a perpendicularly incident laser beam on a Soret cell. A mixture in thermal equilibrium is subjected to a temperature gradient. That condition induces components migration, which in turn generates a measurable refractive index gradient, as can be seen in Figure 2.

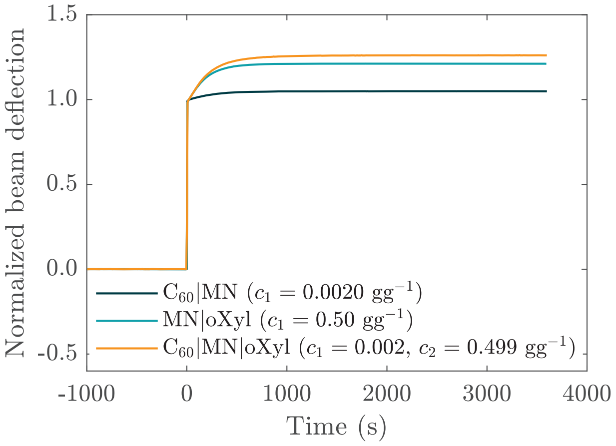

Figure 2: Normalized OBD signal from red laser (405.0 nm) for C_{60}, MN and oXyl based mixtures appliying a 1 °C difference.

Fitting analytical solutions to the OBD curves (Figure 2), the relaxation time τ and the normalized amplitude M (ratio between the value of the amplitude at the Soret plateau and the thermal plateau) can be determined, and, thus, the molecular diffusion and Soret coefficient of a binary mixture can be determined from $D = h^2/\tau$ and

$$S_T = \frac{M}{c_0(1-c_0)} \left(\frac{\partial n}{\partial T}\right)_{p,c} \left(\frac{\partial n}{\partial c}\right)_{p,T}^{-1}, \qquad (1)$$

respectively. Here, h is the cell height and c_0 the initial concentation. In the case of a ternary mixture, two eigenvalues of the diffusion matrix and two independent Soret coefficients are obtained.

In the thermogravitational technique, a mixture is confined in a narrow slot between two plates with different temperatures. The imposed horizontal temperature gradient induces separation of composition due to the Soret effect in the same direction. At this point, a counterflow that tries to homogenize the system is risen. This horizontal separation also results in convective flow driven by buoyancy forces, which in the end leads to an enhanced concentration separation between the top and bottom ends of the column. Mixture is placed inside the column until the time of equilibrium, were samples are extracted from several intakes evenly distributed along the height of the column. Getting to know the concentration variation in function of the colum height, $\partial c_i/\partial z$, the thermodiffusion coefficients are determined by

$$D'_{T,i} = -\frac{L_x^4}{504}\frac{\alpha g \rho}{\mu}\frac{\partial c_i}{\partial z}, \qquad (2)$$

where L_x corresponds to the thickness of the liquid inside the colum, ρ is the density, α the derived thermal expansion coefficient, μ the dynamic viscosity and g the gravitational acceleration. Figure 3 shows the concentration variation along the TGC of mixture C_{60}|MN|oXyl.

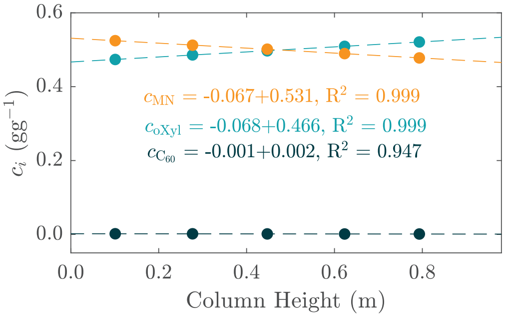

Figure 3: Concentration variation in function of the height of the LTC for C_{60}|MN|oXyl 0.002|0.499|0.499 mixture at 25 °C.

As can be seen, both techniques require the knowledge of several thermo-optical properties. The concentration effect over the refractive index $(\partial n/\partial c)$ was determined measuring the refractive index of different samples by the Abbemat WR and MW refractometers. The thermal contrast factor $\partial n/\partial T$ was measured by interferometry. Density and derived thermal expansion coefficients were determined by the Anton Paar DMA 5000M density meter and viscosity by the automated Anton Paar AMVn micro-viscometer.

Conclusions

Comparing the properties among solvents differing in the number of solvent rings of the structure (MN|Tol), we observed a decrease in both diffusion and thermodiffusion coefficient for the double ring methylnaphthalene, but Soret coefficient is symilar to that of toluene.

Regarding the effect of methyl groups, xylene isomers show slightly lower diffusion and thermodiffusion coefficients than toluene. The order of the value of the coefficients changes with the shape of the organic compound, depending on the symmetry given by the position of the methyl group. We observed the same trend in the analysis of the solvent-solvent binary mixtures composed of MN+(Tol|oXyl|mXyl|pXyl).

The eigenvalues of the diffusion matrix of ternary mixtures related to the C_{60} are small, while the ones related to the liquids agree with diffusion coefficients of the corresponding binary subsystems MN+(Tol|oXyl|mXyl|pXyl), which, again, verify the effect of the position of the methyl group in the molecules. The ill-conditioning of the solutal contrast factors hinder the determination of both thermodiffusion and Soret coefficients of the ternary systems, where in the case of the small coefficients of C_{60}, the sign is not maintained for all systems. Positive S'_T and D'_T demonstrate thermophobic behaviour of MN and negative, hence thermophilic behaviour of the third, which is in good agreement with the coefficients of the associated binary sub-systems.

Acknowledgements

The team from Mondragon Unibersity thanks the support by KK-2021/00082 (micro4IloT), PRE_2022_2_0229 and EP_2022_1_0026, IT1505-22 from the Basque government Research Group Program, the Gipuzkoa Provincial Council under the Hoztikor project 2022-CIEN-000052-01 and PID2020-115086GB-C33 financed by MCIN/FEDER of the Spanish Government. The team from Bayreuth kindly acknowledges support by Deutsches Zentrum für Luft- und Raumfahrt (DLR) (Grant 50WM2147) and DFG (Grant KO 1541/13-1).

References

H.W. Kroto, J. R. Heath, et al., C60: Buckminsterfullerene, *Nature*, 318, 162−163, (1985).

R. Bakry, R. M. Vallant, M. Najam-ul Haq, M. Rainer, Z. Szabo, C. W. Huck, G. K. Bonn, Medicinal applications of fullerenes. *Int. J. Nanomed.*, 2, 639−649, (2007).

R.S. Ruoff, D. S. Tse, R. Malhotra, D. C. Lorents, Solubility of fullerene (C60) in a variety of solvents. *J. Phys. Chem.*, 97, 3379−3383, (1993).

A. Errarte, M. Schraml et al. , Thermophysical, Optical, and Mass Transport Properties of C_{60} Fullerene Solutions in Toluene and Tetralin, *J. Chem. Eng. Data*, 67, 2160–2173, (2022).

M. Gebhardt, W. Köhler, What can be learned from optical two-color diffusion and thermodiffusion experiments on ternary fluid mixtures? , *J. Chem. Phys.*, 142, 084506, (2015).

M. Larrañaga, M. M. Bou-Ali, D. et al., Contribution to the benchmark for ternary mixtures: Determination of Soret coefficients by the thermogravitational and the sliding symmetric tubes techniques, *Eur. Phys. J. E,* 38, 28 (2015).

F. Fischer, T. Hahn, et al., Measuring Reduced C60 Diffusion in Crosslinked Polymer Films by Optical Spectroscopy. Adv. Funct. Mater. 24, 6172−6177, (2014).

H. Matsuura, S. Iwaasa, Y. Nagasaka, Mass Diffusion Coefficient and Soret Coefficient of o-Dichlorobenzene Solutions of PCBM and [60]Fullerene by the Soret Forced Rayleigh Scattering Method. *J. Chem. Eng. Data*, 60, 3621−3630, (2015).

Thermodiffusion coefficients in Polystyrene-Toluene and Polystyrene-Cyclohexane mixtures at different mass fractions

A. Sanjuan[1], V. Shevtsova[1,2] and M. Mounir Bou-Ali[1]

[1]Mechanical and Manufacturing Department, Fluid Mechanics Group, Mondragon University, Mondragon, Spain, asanjuan@mondragon.edu
[2]IKERBASQUE, Basque Foundation for Science, Bilbao, Spain

Introduction

We present the thermodiffusion (D_T) coefficients of a polymer (polystyrene (ps) 4880 g/mol) in pure solvents toluene (tol) and cyclohexane (Ch) at room temperature (25ºC), atmospheric pressure and different mass fractions of the polymer 2-5-10-15-20 %. For this purpose, all the thermophysical and optical properties of the mixtures were also measured in the Fluid Mechanics Laboratory of the University of Mondragón. The objective of this work is to use the thermogravitational column (TGC) procedure (convective technique) to determine D_T in polymeric samples and thus confirm the results obtained so far (tol solvent) using a non-convective method, thermal diffusion forced Rayleigh scattering (TDFRS) (J. Rauch et al. 2003).

Methodology

For the experimental analysis, a cartesian configuration TGC was considered. This consists of two parallel-plane plates in which the mixture to be studied is injected and a horizontal temperature difference is applied between them Figure 2 b). Regarding the method of analysis and determination of D_T, two main procedures can be differentiated. The first is the traditional method and consists of extracting different samples at distinct points of the TGC. After that, in the case of a binary mixture, the variation of the density along the TGC is determined and this is converted to concentration. By means of the slope it is possible to determine the D_T coefficient (Lapeira, E. et al. 2017). The second method of analysis is based on optical ditigital interferometry considering a thermogravitational microcolumn (micro-TGC). In this case, a Mach-Zehnder interferometer is used to generate interference patterns during the experiment. The obtained phase variation is related to the concentration difference (via the optical properties) along the micro-TGC (Lapeira, E. et al. 2018). As for the mentioned procedures, each one has its benefits and drawbacks. With respect to the traditional method, in general, the columns are larger and therefore the amount of sample and the test time is longer. However, the species separation is higher and thus the sensitivity of the measurements is improved. As for the optical method, the transient state can be studied thus providing additionaly the diffusion coefficient. As working part of the cavity is reduced it leads to the decrease of the separation.

Regarding the experimental methodology followed in this work, first the necessary thermophysical properties (for each sample) such as density (ρ), thermal expansion coefficient (α), mass expansion coefficient (β) and dynamic viscosity (μ) were determined. The Anton Paar DMA 5000 M equipment Figure 1 a) was used to determine the ρ of the samples. The same dispositive was considered to determine α and β. The density variation with respect to temperature, α, was determined according to Eqn. (1) To calculate α at 25ºC the density of the sample was measured in the range from 24ºC to 26ºC (with step of 0.5ºC). The variation of the density with regard to concentration β was calculated according to Eqn. (2) To determine β five samples of different concentrations were prepared. For example, in the case of the ps-tol 10 % mixture, samples were prepared at the following mass fractions 8-9-10-11-12 %. The dynamic viscosity of the mixtures μ was measured using the Anton Paar AMVn microviscosimeter Figure 1 b). The optical constrast factors $(\partial n/\partial c)$ of the mixtures were determined using the Anton Paar Abbemat WR MW refractometer Figure 1 c).


a) b) c)

Figure 1: Equipment used for thermophysical properties measurements: Anton Paar DMA 5000 densimeter a), Anton Paar AMVn microviscosimeter b) and Anton Paar Abbemat WR MW refractometer c).

$$\alpha = -\frac{1}{\rho}\frac{\partial \rho}{\partial T} \qquad (1)$$

$$\beta = \frac{1}{\rho}\frac{\partial \rho}{\partial c} \qquad (2)$$

Regarding TGC experiments, in this work, these were carried out both in the traditional TGC (mass fractions of 2-5 % of ps due to sensitivity) and micro-TGC based on the optical analysis (mass fractions of 10-15-20 % of ps due to the amount of sample needed). In the first case, extraction method, the large column available in our laboratory was used Figure 2 a) which consists of the following dimension: length = 980 mm (L_z), gap = 1.02 mm (L_x) and width = 50 mm (L_y). In the TGC, the samples were extracted at 5 different points as shown in Figure 2) and the density of each extracted sample was determined. This procedure allows to obtain the concentration variation $(\partial c/\partial z)$ along the height of the TGC and determine the D_T coefficient of the mixture using Eqn. (3) where c_0 is the initial mass fraction of ps and g corresponds to the gravity force.

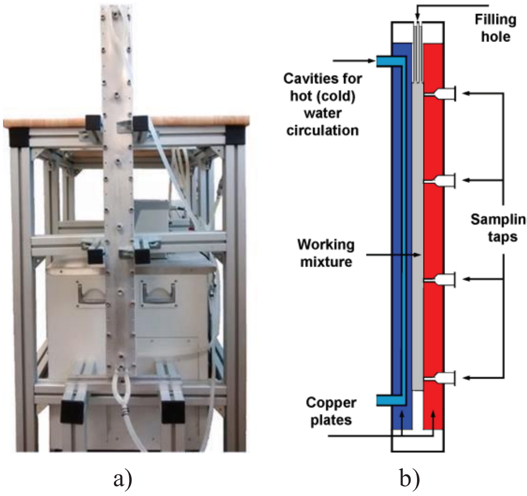

a) b)

Figure 2: TGC experiment traditional method: used large column a) and a cross-section sketch b) (Lapeira, E. et al. 2017).

$$D_T = \frac{-L_x^4}{504} \frac{c_0}{c_0(1-c_0)} \frac{\alpha g \rho}{\mu} \frac{\partial c}{\partial z} \tag{3}$$

As for the optical analysis method, the micro-TGC existing in our laboratory based on digital interferometry was used (Lapeira, E. et al. 2018). This has the following dimensions: length = 30 mm (L_z), gap = 0.509 mm (L_x) and width = 3 mm (L_y). Regarding the setup (Figure 3), the optical installation contains three lasers of different wavelengths, 473 nm, 543 nm, 633 nm. At the starting point Figure 3 (1), three pneumatic cylinders are placed. In this way, the different lasers do not interfere with each other. After that, the filters to clean the beam and the collimation lenses for expansion are located Figure 3 (2). In the final part of the configuration, the Mach-Zehnder intermerometer is placed Figure 3 (3). Matlab R2021b software was used to analyse the interference patterns acquired in the camera. In this process, the first step was to obtain the phase variation($\Delta\emptyset$) along the column from the captured images. The optical phase $\Delta\emptyset$ is directly related to the refractive index difference (Δn), see Eqn. (4) where (λ) corresponds to the laser wavelength. Finally, using the measured optical contrast factor ($\partial n/\partial c$) the variation of the concentration was obtained Eqn. (5). The thermodiffusion coefficient D_T was calculated using Eqn. (3).

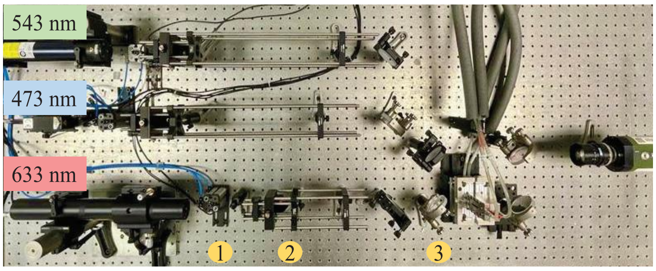

Figure 3: micro-TGC experiment. Real optical installation.

$$\Delta n(y,z) = \frac{\lambda}{2\pi L_x} \Delta\emptyset(y,z) \tag{4}$$

$$\Delta n(y,z) = \left(\frac{\partial n}{\partial c}\right)_{T_0, C_0, \lambda} \Delta c(y,z) \tag{5}$$

Preliminary results

This section presents the preliminary results obtained for the studied mixtures. Figure 4 a) shows the ρ variation along the height of the traditional TGC (sample ps-Tol 5 % at 25 ºC) when the mixture reaches steady state regime. As for the micro-TGC experiment, Figure 4 b) represents the $\Delta\emptyset$ (sample ps-tol 10 %) and in this case the three stages of the experiment can be observed.

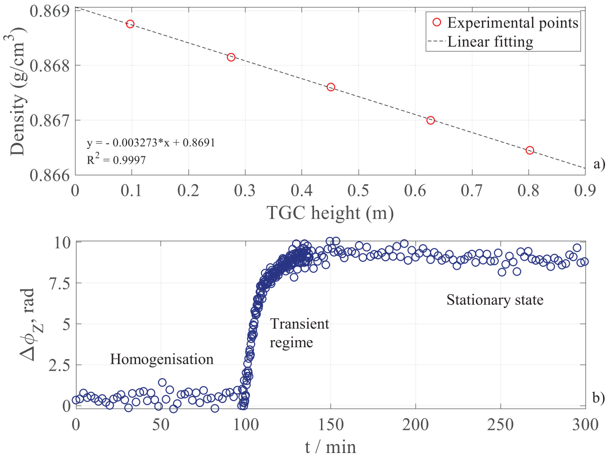

Figure 4: TGC experiment (ρ variation) mixture ps-tol 5 % at 25ºC a) and micro-TGC experiment $\Delta\emptyset$ sample ps-tol 10 % at 25ºC b).

Conclusions

The thermodiffusion coefficients D_T of ps in pure solvents Tol and Ch as a function of concetration were determined combining the traditional TGC technique and the micro-TGC method based on optical analysis. The thermophysical and optical properties were also measured. As for the experimental results obtained, the determination of the D_T coefficient is still going on.

Acknowledgements

A.S. wants to thank the Basque Government for funding under an FPI grant (PRE_2022_1_0136). MMB and VS would like to thank the financial support from the Basque Government under the Research Group Programme IT1505-22, the Gipuzkoa Provincial Council under the Hoztikor project (2022-CIEN-000052-01) and PID2020-115086GB-C33 financed by (MICINN/FEDER) of the Spanish Government.

References

J. Rauch, W. Köhler, Collective and thermal diffusion in dilute, semidilute, and concentrated solutions of polystyrene in toluene, *J. Chem. Phys*., 22, 11977-11988 (2003).

Lapeira, E., Gebhardt, M., Triller, T., Mialdun, A., Köhler, W., Shevtsova, V., & Bou-Ali, M. M., Transport properties of the binary mixtures of the three organic liquids toluene, methanol, and cyclohexane, *J. Chem. Phys.*, 146, 094507, (2017).

Lapeira, E., Mialdun, A., Yasnou, V., Aristimuño, P., Shevtsova, V., & Bou-Ali, M. M., Digital Interferometry Applied to Thermogravitational Technique, *Microgravity Science and Technology*, 30, 635–641, (2018).

Mass transport properties of C_{60}|THN|Tol mixture in ground laboratories and microgravity: Results of DCMIX4 mission.

A. Errarte[1], M. Schraml[2], A. Mialdun[3], W. Köhler[2], V. Shevtsova[1,4], M.M. Bou-Ali[1]

[1]Fluid Mechanics Group, Mondragon University, Mondragon, Spain, aerrarte@mondragon.edu
[2]Department of Physics, University of Bayreuth, Bayreuth, Germany
[3]Aéro-thermo-mécanique, Université libre de Bruxelles, Brussels, Belgium
[4]Ikerbasque, Basque Foundation for Science, Bilbao, Spain

Introduction

Most available experimental data on thermodiffusion and diffusion relate to binary mixtures of a certain class of systems such as alkanes, glycols or organic mixtures. With the advent of convection-free microgravity environments, the focus of research has strongly shifted toward ternary mixtures. Still, there is a lack of studies, equally among binary and ternary mixtures, containing nanoparticles and, in particular, fullerene. The knowledge of the transport properties of fullerene and its compounds in various organic and biological solvents is important for applications. However, such experiments are rare.

In this work, we focus on isothermal and non-isothermal mass transport of fullerene C_{60} in two organic solvents measured in the framework of the last mission of the DCMIX project. The Soret effect of C_{60}|THN|Tol mixture at 0.0007|0.6000|0.3993 mass fraction composition is investigated at four mean temperatures of 20, 25, 30 and 35 °C inside SODI, the Selectable Optical Diagnostic Instrument, installed in the MSG facility of the International Space Station (ISS) (Mialdun et al., 2019). Likewise, the mixture is characterized in three ground-laboratories by the Optical Digital Interferometry (ODI), the Optical Beam Deflection (OBD) and the Thermogravitational Columns (TGC).

We recently published first findings about the three associated binary subsystems, in which thermophysical, optical and mass transport properties such as molecular diffusion, thermodiffusion and Sore coefficients were reported (Errarte et al. 2022). This work is a continuation to the entire characterization of the mixture by experiments in both earth laboratories and microgravity.

Experimental setups

The focus of the work is placed on microgravity experiments performed in SODI, in orbit since 2009. The instrument contains a two-laser Mach-Zehnder interferometer operating at 670 nm and 935 nm, which can sequentially access five cells with ternary mixtures. The experiments consist of two stages. First, in the thermal homogenization, the temperature of the system is stabilized to the mean temperature. Second, a thermal gradient is applied across the height of the cell almost instantaneously. That temperature gradient induces component separation, from which Soret coefficients can be obtained by

$$S'_{T,i} = -\frac{1}{\Delta T}\Delta c_i^{st}. \qquad (1)$$

A brief description of the data processing pipeline is given. SODI was designed to work by the phase stepping method, even if the single interferogram analysis can also be used. The first step consists of obtaining the linear phase of the signal from the intensity of the interferograms. In order to analyse the phase variation related to the concentration variation, a reference image is selected after the gradient is completely established in the cell and is subtracted from all subsequent images. The calculated unwrapped phases are converted into 2D-refractive index maps by the expression $n(y,z) = (\lambda/2\pi L)\Delta\phi(y,z)$, where in this case the path the beam crosses through the liquid volume is of $L = 10.0$ mm. In order to fit RI data to analytic solutions that describe the separation in a Soret cell, the calculated 2D map is converted into a 1D-RI profile averaging the normalized refractive index map in the horizontal direction.

Finally, the analytical solution for the heat and mass transfer problem describing the Soret separation is attempted by the quasi-binary fitting of data, successfully tested in previous DCMIX campaigns. Even if each fitting algorithm can lead to slightly different results, all of them provide both the Soret $S'_{T,i} \propto \Delta n_\lambda^{st}$ and the effective diffusion coefficients (D_{eff}). Both full path and differences methods described in Mialdun et al. 2018 are used to determine the Soret and effective diffusion coefficients and results are compared to those determined by the novel Optical Beam Deflection based data processing method reported in Sommermann et al. 2022. Figure 1 shows the steps followed for the first two fitting methods.

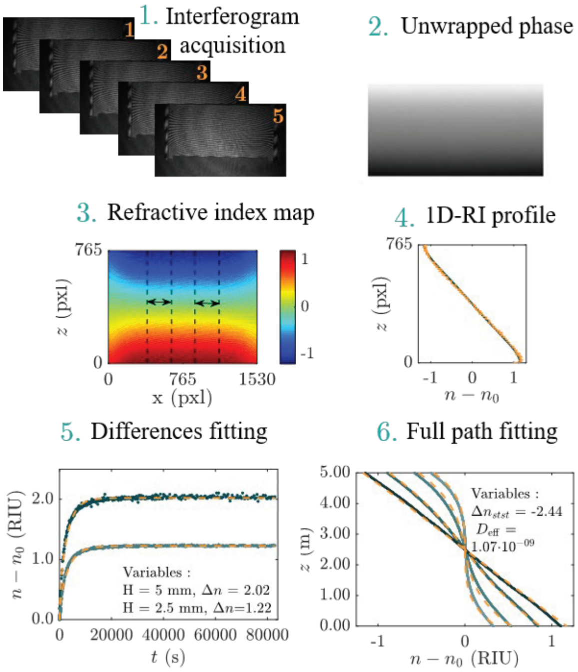

Figure 1: Processing steps followed for the analysis of SODI experiments.

In parallel to microgravity experiments, we are determining Soret and diffusion coefficients by OBD and ODI techniques and thermodiffusion coefficients by the TGC method.

The former, OBD, consists of determining the concentration variation induced by the Soret effect by studying the deflection of a monochromatic laser beam incident perpendicularly on a diffusion cell exposed to a temperature gradient (Gebhardt and Köhler, 2015). Such concentration gradient, in turn, generates a measurable refractive index gradient. ODI, as SODI, uses digital interferometry to analyse the refractive index variation at 670 and 904 nm in a Soret cell (Mialdun et al. 2015). The main features of data processing are similar to those applied in SODI. Both OBD and ODI provide the diffusion coefficients and the Soret coefficient. In order to determine the thermodiffusion coefficients, we use the TGC (Larrañaga et al, 2015). We insert a mixture between two vertical walls at different temperatures. That temperature gradient induces a horizontal separation. Because of this horizontal separation, a concentration gradient appears which in turn creates a mass flow in the opposite direction due to the phenomenon of molecular diffusion. Moreover, the effect of gravity generates convective flows that amplify the separation along the column, used for the determination of thermodiffusion coefficients.

All these techniques require thermo-optical properties such as the solutal contrast factors, that turns out to be the most critical step during the evaluation of ternary data. This sensitivity leads to very asymmetrically stretched error ellipsoids for the Soret coefficients in the 2d-space of the independent concentration variables.

Conclusions

We present evaluation of the C_{60}|THN|Tol mixture analysed in DCMIX4 campaign performed on-board the ISS. We discuss different data processing methods in order to address their effect on the transport coefficients. Likewise, we show complete mixture characterization performed in three ground laboratories and techniques. Considering the diluted nature of the mixture, comparison to the corresponding binary sub-system THN|Tol (0.60|0.40 gg^{-1}) confirms the quasi-binary behaviour of the system.

Acknowledgements

The team from Mondragon Unibersity thanks the support by KK-2021/00082 (micro4IloT), PRE_2022_2_0229 and EP_2022_1_0026, IT1505-22 from the Basque government Research Group Program, the Gipuzkoa Provincial Council under the Hoztikor project 2022-CIEN-000052-01 and PID2020-115086GB-C33 financed by MCIN/FEDER of the Spanish Government. AM acknowledges support from PRODEX program of the Belgian Science Policy Office (BELSPO). M.S. and W.K. acknowledge support by Deutsches Zentrum für Luft- und Raumfahrt (DLR) (Grants 50WM1544 and 50WM1850).

References

A. Mialdun, H. Bataller, M. M. Bou-Ali, M. Braibanti, F. Croccolo, A. Errarte, J.M. Ezquerro, J.J. Fernández, Yu. Gaponenko, L. Farcía-Fernandez, J. Rodríguez, V. Shevtsova, Preliminary analysis of Diffusion Coefficient Measurements in ternary mIXtures 4 (DCMIX4) experiment on board the International Space Station, *Eur. Phys. J. E,* 42, 87 (2019).

A. Errarte, M. Schraml, W. Köhler, V. Shevtsova, M. M. Bou-Ali, A. Mialdun, Thermophysical, Optical, and Mass Transport Properties of C_{60} Fullerene Solutions in Toluene and Tetralin, *J. Chem. Eng. Data*, 67, 2160–2173, (2022).

A. Mialdun, I. Ryzhkov, O. Khlybov, T. Lyubimova, V. Shevtsova, Measurement of Soret coefficients in a ternary mixture of toluene–methanol–cyclohexane in convection-free environment, *J. Chem. Phys.*, 148, 044506 (2018).

D. Sommerman, M. Schraml, W. Köhler, Thermodiffusion of polymer solutions and colloidal dispersions in mixed solvents, *J. Chem. Phys.*, 157, 194903, (2022).

M. Gebhardt, W. Köhler, What can be learned from optical two-color diffusion and thermodiffusion experiments on ternary fluid mixtures? , *J. Chem. Phys.*, 142, 084506, (2015).

A. Mialdun, J. C. Legros, V. Yasnou, V. Sechenyh, V. Shevtsova, Contribution to the benchmark for ternary mixtures: Measurement of the Soret, diffusion and thermodiffusion coefficients in the ternary mixture THN/IBB/nC12 with 0.8/0.1/0.1 mass fractions in ground and orbital laboratories, *Eur. Phys. J. E,* 38, 27 (2015).

M. Larrañaga, M. M. Bou-Ali, D. Alonso de Mezquia, D. A. S. Rees, J. A. Madariaga, C. Santamaría, J. K. Platten, Contribution to the benchmark for ternary mixtures: Determination of Soret coefficients by the thermogravitational and the sliding symmetric tubes techniques, *Eur. Phys. J. E,* 38, 28 (2015).

Non-Equilibrium Fluctuations during Free-Diffusion in a highly stratified solution of Glycerol and Water

S. Castellini[1], M. Carpineti[1], F. Croccolo[2], C. Giraudet[2] and A. Vailati[1]

1 Dipartimento di Fisica "A. Pontremoli", Università degli Studi di Milano, Italy

2 Universite de Pau et des Pays de l'Adour, E2S UPPA, CNRS, TotalEnergies, LFCR UMR5150, Anglet, France

Introduction

In a binary mixture at equilibrium there are small spontaneous local fluctuations in concentration, temperature and velocity fields around the average values of these variables (J. M. Ortiz de Zárate et al. 2006). For fluids at equilibrium these fluctuations are characterized by a white noise spectrum. In the presence of non-equilibrium conditions, such as those created by applying concentration or temperature gradients, the non-equilibrium fluctuations (NEFs) have a static power spectrum that diverges as a power law at large wave vectors q $S(q) \propto \frac{1}{1+\left(\frac{q}{q_{ro}}\right)^4}$ (A. Vailati et al. 1997).

These fluctuations are orders of magnitude larger than those occurring at equilibrium, and are strongly affected by the presence of gravity, which quenches them at wave vectors q smaller than a typical roll-off wave vector q_{ro} (A. Vailati et al. 1998).

Concentration NEFs are not just a small perturbation of a macroscopic process; in fact, they cause a net mass transfer that coincides with the usual Fickean diffusion. Concentration NEFs in the presence of a macroscopic concentration gradient are determined by stochastic fluctuations in the velocity field δv, which displace volume elements of the fluid into layers of different concentration. The concentration of the elements then relaxes to the local concentration of the fluid layer with a certain characteristic rate $\gamma(q)$. The relaxation is related to the wave vector by the relation:

$$\gamma(q) = Dq^2 \cdot \left(1 + \left(\frac{q_{ro}}{q}\right)^4\right)$$

where D is the diffusion coefficient. The roll-off wave vector q_{ro} also appears in this law, indicating that gravity affects the relaxation of fluctuations.

For this reason, space missions have been undertaken to characterize the fluctuations in more detail in the absence of gravity. In 2007, the GRAdient Driven FLuctuations Experiment (GRADFLEX), designed and carried out in collaboration with the European Space Agency (ESA) and NASA, confirmed that the theoretical models based on linearized hydrodynamics provide a convincing quantitative interpretation of nonequilibrium fluctuations for ideal systems (A. Vailati et al. 2011).

However, since in nature and in technological processes NEFs occur in nonideal systems, where strongly nonlinear diffusion takes place with very intense concentration gradients, it is very useful to investigate such systems. The Giant Fluctuations and TechNES projects funded by ESA will study the non-equilibrium fluctuations that occur in fluids during diffusion processes under microgravity conditions. The focus of the experiments will be the investigation of transient and stationary processes in multicomponent fluids, also in the presence of intense concentration gradient.

This is the context for the present work, in which we seek to provide an interpretation of results obtained by exploring NEFs occurring in a mixture of water and glycerol subjected to a strong concentration gradient.

The experiments are performed in the isothermal free-diffusion configuration, where two mixtures of water and glycerol at different concentrations are initially brought into contact in the stable configuration where the denser mixture is at the bottom of the sample cell. To perform these experiments, we exploit a cell called Flowing-Junction Cell (F. Croccolo 2019), which can generate an interface between the two mixing phases. The strong dependence of the thermophysical property on the glycerol concentration results in a wide range of NEFs relaxation times at a fixed wave vector.

To probe NEFs, a quantitative Shadowgraph technique was used (F. Croccolo et al. 2007). We investigate systematically diffusion processes between water-glycerol mixtures with glycerol concentrations ranging from 0% to 95%.

We develop an empirical model for the time correlation function of the scattered light and compare it to the models traditionally used to characterize polydisperse colloidal systems, such as cumulant analysis and the Schulz distribution model (A. G. Mailer et al. 2015).

We validate the effectiveness of the model with computational simulations and by its application to the experimental data. The mean square deviation between the model and the experimental data turns out to be better for our proposed model than for the others analysed.

Furthermore, with our model we have been able to extract information about the stratification of the sample by calculating the distribution of diffusion coefficients involved in the mass diffusion occurring in the sample. This important result opens-up new scenarios in which the Shadowgraph technique can be employed to characterize systems in which it is essential to characterize stratification using a non-invasive method. Finally, we have characterized the impact of gravity for systems of this type; this step is critical in view of the space missions in which we are involved, where systems strongly stratified in concentration will be characterized under microgravity conditions.

Acknowledgements

Work supported by the European Space Agency.

References

A. Vailati and M. Giglio, Giant fluctuations in a free diffusion process, *Nature* 390, 262–265 (1997)

A. Vailati and M. Giglio, Nonequilibrium fluctuations in time-dependent diffusion processes, *Phys. Rev. E* 58, 4361–4371 (1998).

J. M. Ortiz de Zárate, J. V. Sengers, Hydrodynamic fluctuations in fluids and fluid mixtures, *Elsevier*, Amsterdam, (2006)

F. Croccolo, D. Brogioli, A. Vailati, M. Giglio, and D. S. Cannell, Non-diffusive decay of gradient-driven fluctuations in a free-diffusion process, *Phys. Rev. E* 76 (2007).

A. Vailati, R. Cerbino, S. Mazzoni, C. J. Takacs, D. S. Cannell, and M. Giglio, Fractal fronts of diffusion in microgravity, *Nat. Commun*. 2, 290 (2011).

A. G. Mailer, P. S. Clegg, and P. N. Pusey, Particle sizing by dynamic light scattering: non-linear cumulant analysis, *Journal of Physics: Condensed Matter* 27, 145102 (2015)

F. Croccolo, D. Brogioli, and A. Vailati, Cylindrical flowing-junction cell for the investigation of fluctuations and pattern-formation in miscible fluids, *Rev. Sci. Instrum*. 90, 085109 (2019)

Diffusion and thermodiffusion of polymers in mixed solvents

D. Sommermann[1], W. Köhler[1], A. Sanjuan[2], M. Mounir Bou-Ali [2]

[1]Department of Physics, University of Bayreuth, Bayreuth, Germany, werner.koehler@uni-bayreuth.de
[2]Fluid Mechanics Group, Mondragon University, Mondragon, Spain, mbouali@mondragon.edu

Introduction

We present experiments on diffusion and thermodiffusion of polymers in mixed solvents. So far, most works on thermodiffusion have dealt with binary systems or ternary mixtures of small molecules. Binary samples with polymers in solvents have been studied over both a broad concentration and polymer molar mass range (Rauch et al. 2003). Only a few very recent experiments measured polymers in a binary solvent (Bataller et al. 2017, García-Fernández et al. 2019). In this work, samples made of polystyrene, toluene and cyclohexane have been analysed using multiple-color optical beam deflection (OBD) and supporting thermogravitational column (TGC) experiments, based on the traditional extraction technique (Lapeira et al. 2017) and optical digital interferometry method (Lapeira et al. 2018). While binary mixtures are readily characterized by one diffusion and one thermodiffusion coefficient, the number of coefficients increases to four plus two for ternaries. The measured signals show three well separated modes that can be assigned to the thermal diffusivity and the two eigenvalues of the mass diffusion matrix. A first analysis supports the picture of an effective solvent whose internal dynamics is decoupled from the one of the polymer.

Experimental setups

For an OBD experiment, a temperature gradient parallel to gravity is suddenly applied to a horizontal sample which was in thermal equilibrium. A laser beam which travels through the middle of the cell perpendicular to the gravity direction gets deflected over time due to the concentration and, thus, refractive index gradient as can be seen in Figure 1.

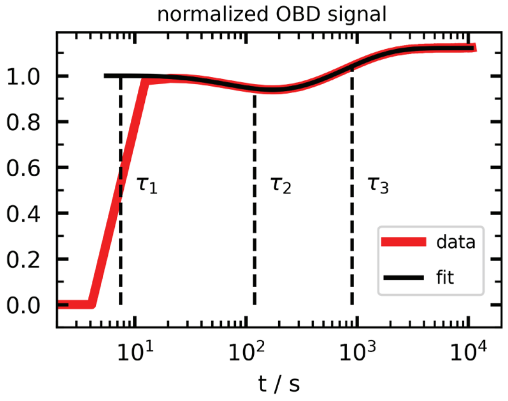

Figure 1: Ternary OBD signal normalized to the thermal amplitude together with the fit. The three indicated time constants τ describe the diffusive behavior over time of the sample. The sample consists of polystyrene/toluene/cyclohexane (2.0/39.2/58.8 in mass fraction).

In order to prevent convection, the sample height is chosen in a way to be far below the critical Rayleigh number. The temperature jump causes a fast steep change in the OBD signal due to the thermal diffusivity of the sample. At longer times, the signal evolution is driven by the Soret effect and can be characterized by a time constant for each independent concentration. In the case of a polymer dissolved in a mixed binary solvent the time constants are nicely separated. In the end the system reaches a nonequilibrium steady state, corresponding to a plateau of the OBD signal, from which the Soret coefficient can be calculated.

The TGC technique basically consists of two parallel-plane plates. The sample is introduced into the cavity generated by the two walls and the fluid is subjected to a temperature gradient perpendicular to the gravitational field. During the experiment, due to the thermodiffusion effect, a horizontal concentration difference is generated in the column. This species separation activates the phenomenon of molecular diffusion, trying to homogenise the concentration gradient in the opposite direction. At the same time, the horizontal density gradient produces a convective flow along the TGC cavity, which increases the separation of species in the vertical direction. As for the method of analysis and determination of the thermodiffusion coefficients, two main procedures can be differentiated. The first, the traditional method, consists of extracting five different samples along the height of the TGC. After that, in the case of ternary mixtures, by determining the variation of the density and the refractive index, the vertical concentration gradient is obtained and therefore it is possible to determine the thermodiffusion coefficient for each species. The second analysis is based on optical digital interferometry using a thermogravitational microcolumn (micro-TGC). In this case, by means of a Mach-Zehnder interferometer, interference patterns are acquired for each step of the micro-TGC experiment: temperature homogenisation, temperature gradient application and steady state regime. Figure 2 shows the phase variation in a micro-TGC experiment for a stable (blue) and unstable (red) sample showing each stage of the experiment.

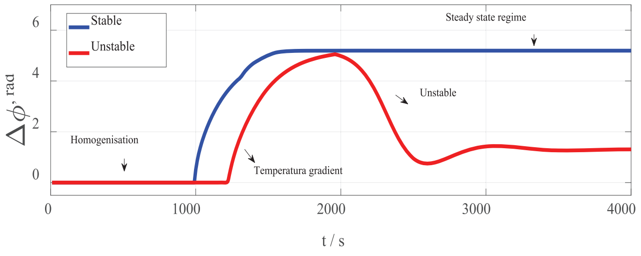

Figure 2: Phase variation over time in a micro-TGC experiment for a stable (blue) and an unstable (red) mixture.

Investigated system

As stated above, the system consisting of one polymer and one solvent has been analysed for various components over the last decades. In order to build upon the existing research and keeping the measurement time decent, polystyrene ($M_w = 4880$ g/mol) was used in combinations with toluene and cyclohexane over a broad concentration range, which can be seen in Figure 3. The polymer concentrations and solvent ratios are always based on the masses of the constituents. It turns out that the solvent ratio has a big influence on the fast mode and the polymer concentration on the slow mode (τ_2 and τ_3 in figure 1, respectively). With increasing toluene content, the amplitude of the fast mode decreases, while for increasing polymer concentration at constant solvent ratio, the amplitude of the slow mode also increases. For the measurement series with a solvent ratio toluene:cyclohexane of 80:20, the evaluation of the OBD signal gets more difficult because the fast mode is hard to distinguish from the noise of the thermal amplitude; the ternary signal almost resembles a binary one. This problem was the main reason to look for other measurement techniques in order to provide some reference data. The TGC experiments proofed to be reliable, and the evaluation is not so much affected by noise as in the case of OBD. As a downside, the Soret coefficient of the densest component must be positive in order to be measurable. Preliminary experiments with a smaller micro-TGC showed that not all samples are stable (see red and grey squares in (Figure 3), so the focus was on samples with a sufficient large polymer concentration (blue squares in Figure 3). These samples were analysed at a mean temperature of 25°C while the faster OBD measurements could also be investigated at 20°C, 30°C and 35°C.

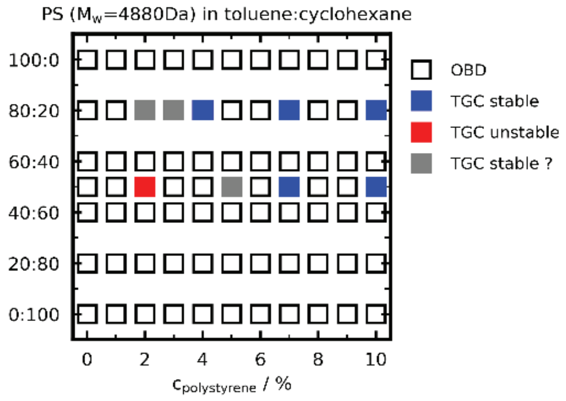

Figure 3: Measured samples in the OBD setup (open squares) and additionally with the TGC setup (filled squares). The y-axis indicates the solvent mass ratio in terms of toluene:cyclohexane. Due to instabilities not all samples are measurable in the TGC.

Data analysis

While the data evaluation is still going on, a few tendencies can already be seen. The fast mode, which corresponds to the smaller eigenvalue of the mass diffusion matrix, matches pretty well in the limit of small polymer concentrations with the diffusion constant in the pure solvent samples. The larger eigenvalue, on the other hand, scales in first order approximation linear with the polymer concentration and is confined in an area which is defined by the eigenvalue of the binary system of polymer in the two mentioned solvents. To get the thermodiffusion coefficients from an OBD measurement, the inversion of a so called contrast factor matrix is needed, which is often ill conditioned and results in a large error propagation. The analysis of the TGC uses a way better conditioned contrast factor matrix leading to significantly less noise in the results. A definite interpretation of the comparison of the thermodiffusion coefficients from both setups is still under debate.

Conclusions

The OBD technique was applied to investigate ternary samples consisting of a small polystyrene molecule in toluene and cyclohexane. It was possible to measure the system over a broad range, starting from the binary samples to ternaries with a polymer concentration up to 10%. Due to problems during the signal evaluation, experiments were also performed using TGC in order to create reference data. Concerning the well separated diffusion coefficients, they can be attributed to a solvent-solvent mode and a polymer motion in an effective solvent. The interpretation of the thermodiffusion coefficient is still going on, mainly hindered by error propagation.

Acknowledgements

The team from Bayreuth thanks the German Research Foundation (DFG, Grant KO1541/13-1) as well as the German Aerospace Center (DLR, Grant 50WM2147 (BTGIANTII)) for funding. A.S. wants to thank the Basque Government for funding under an FPI grant (PRE_2022_1_0136). MMB would like to thank the financial support from the Basque Government under the Research Group Programme IT1505-22, the Gipuzkoa Provincial Council under the Hoztikor project (2022-CIEN-000052-01) and PID2020-115086GB-C33 financed by (MICINN/FEDER) of the Spanish Government.

References

J. Rauch, W. Köhler, Collective and thermal diffusion in dilute, semidilute, and concentrated solutions of polystyrene in toluene. *J. Chem. Phys*. **22**, 11977-11988 (2003).

H. Bataller, T. Triller, B. Pur, W. Köhler, J. M. Ortiz de Zárate, F. Croccolo, Dynamic analysis of the light scattered by the non-equilibrium fluctuations of a ternary mixture of polystyrene-toluene-n-hexane. *Eur. Phys. J. E* **40**, 35 (2017).

L. García-Fernández, P. Fruton, H. Bataller, J. M. Ortiz de Zárate, F. Croccolo, Coupled non-equilibrium fluctuations in a polymeric ternary mixture. *Eur. Phys. J. E* **42**: 124 (2019).

Lapeira, E., Gebhardt, M., Triller, T., Mialdun, A., Köhler, W., Shevtsova, V., & Bou-Ali, M. M, Transport properties of the binary mixtures of the three organic liquids toluene, methanol, and cyclohexane, The Journal of Chemical Physics, 146, 094507, (2017).

E. Lapeira, A. Mialdun, V. Yasnou, P. Aristimuño, V. Shevtsova, and M. M. Bou-Ali, Digital Interferometry Applied to Thermogravitational Technique, *Microgravity Sci Technol*, 30, 635–641, (2018).

SORET-INDUCED CONVECTION OF TERNARY FLUID IN HORIZONTAL POROUS LAYER HEATED FROM BELOW

T.P. Lyubimova[1,2], I.S. Shubenkov[1,2]

[1]Institute of Continuous Media Mechanics UB RAS, Perm, Russia, [2]Perm State University, Perm, Russia, lyubimovat@mail.ru

Introduction

The paper is devoted to the investigation of the Soret-induced convection of ternary fluid in horizontal porous layer heated from below. The study of convection in horizontal porous layers is important for understanding the processes of heat and mass transfer in oil-bearing fields. Oil is a complex mixture of a large number of different fractions of hydrocarbons. In oil-bearing fields it is subjected to geothermal temperature gradient. The knowledge of peculiarities of heat and mass transfer in these conditions could allow to make the oil extraction more efficient. The problems of convection of multi-component fluids began to be considered quite recently and are not enough understood.

Problem formulation, governing equations, boundary conditions and system parameters

An infinite horizontal layer of a porous medium saturated with a multicomponent fluid is considered. As a fluid, a three-component mixture of hydrocarbons is considered: dodecane (component №1), isobutylbenzene (component №2) and tetralin (component №3) with equal mass fractions of components at an average temperature of 25℃ (I.I. Ryzhkov, 2013). These components are typical for mixtures found in natural hydrocarbon deposits. We choose the heaviest component (tetralin) as the solvent. This mixture was studied in experiments under microgravity conditions within the framework of the DCMIX 1 project (V. Sechenyh et al. 2016). The system is subjected to the gravity field. It is assumed that the boundaries of the layer are rigid, perfectly conductive and impermeable for solute. Different constant temperatures are maintained at the boundaries. It is assumed that the density of the fluid depends linearly on the temperature and concentrations of the components.

The equations of the Soret-induced convection of multicomponent fluid in a porous medium (N.I. Lobov et al. 2007) in the dimensionless form are:

$$0 = -\nabla P - \boldsymbol{V} + Ra_p(T + \widehat{\boldsymbol{\psi}}\widehat{\boldsymbol{C}})\boldsymbol{e}_y \qquad (1)$$

$$\frac{\partial T}{\partial t} + \boldsymbol{V} \cdot \nabla T = \nabla^2 T \qquad (2)$$

$$\varepsilon \frac{\partial \widehat{\boldsymbol{C}}}{\partial t} + \boldsymbol{V} \cdot \nabla \widehat{\boldsymbol{C}} = \widehat{\boldsymbol{Le}}^{-1}(\nabla^2 \widehat{\boldsymbol{C}} - \boldsymbol{I} \cdot \nabla^2 T) \qquad (3)$$

$$\nabla \cdot \boldsymbol{V} = 0 \qquad (4)$$

where $Ra_p = \frac{Kg\beta_T L \cdot \Delta T}{a\nu}$ is an analog of the Rayleigh number for a porous medium (hereinafter, we call it the "Rayleigh number"); $\widehat{\boldsymbol{\psi}} = -\widehat{\boldsymbol{C_0}}(1 - \widehat{\boldsymbol{C_0}})\beta_T^{-1}\boldsymbol{B}(\widehat{\boldsymbol{D}})^{-1}\widehat{\boldsymbol{D_T}}$ is the vector of separation ratio; $\varepsilon = \varepsilon^* \frac{(\rho c)_f}{(\rho c)^*}$ is the normalized porosity; $\widehat{\boldsymbol{Le}} = a(\widehat{\boldsymbol{D}})^{-1}$ is the diagonal matrix of the Lewis numbers, where $\widehat{Le_{11}} = \frac{a}{D_{11}}$, $\widehat{Le_{22}} = \frac{a}{D_{22}}$; $\boldsymbol{e}_y$ is the unit vertical vector. Here $a = \frac{\lambda^*}{(\rho c)_f}$ is the effective thermal diffusivity, $\boldsymbol{V}$ is the filtration velocity, P is the pressure, g is the gravity acceleration, K is the permeability of the porous matrix, ν is the kinematic viscosity, λ^* is the effective thermal conductivity of the porous medium, $(\rho c)^*$ is the effective heat capacity of the porous medium, $(\rho c)_f$ is the heat capacity of the mixture, ε^* is the porosity, $\boldsymbol{D}$ is the matrix of molecular diffusion coefficients, $\boldsymbol{J} = (1, \dots, 1)$ is the column vector, $\boldsymbol{I} = (1, \dots, 1)$ is the row vector, $\boldsymbol{C} = (C_1, \dots, C_{n-1})$ is the concentration vector, $\boldsymbol{D_T}$ is the vector of thermal diffusion coefficients.

At the layer boundaries maintained at constant different temperatures the impermeability condition and the condition of the absence of the solute flux are imposed. These conditions in the dimensionless form are:

$$y = 0, 1: \quad T = 1, 0, \quad V_y = 0, \quad \frac{\partial \widehat{\boldsymbol{C}}}{\partial y} - \boldsymbol{I} \cdot \frac{\partial T}{\partial y} = 0$$

The problem was studied for fixed values of the parameters ψ_2, $\widehat{Le_1}$, $\widehat{Le_2}$, ε : $\psi_2 = 0.120$, $\widehat{Le_1} = 147$, $\widehat{Le_2} = 91$, $\varepsilon = 0.15$. The separation ratio ψ_1 was varied in the interval $[-0.150, 0]$.

Linear stability of conductive state

To solve the linear problem of the stability of the conductive state, the Runge-Kutta method of the 5th order and the subsequent search for the zero value of the determinant of the matrix of the fundamental system of solutions using the two-dimensional secant method were used.

Fig. 1 shows the linear stability map obtained in the calculations. For heating from below only the longwave monotonic instability mode exists in the range $\psi_1 \in [-0.047; 0]$ (curve 1). At $\psi_1 = -0.047$, the longwave oscillatory instability mode branches off from the longwave monotonic instability mode and becomes more dangerous (curve 3). At $\psi_1 = -0.065$, the finite-wavelength monotonic instability mode (curve 2) branches off from the longwave monotonic instability mode. At $\psi_1 = -0.101$, the longwave oscillatory instability transforms into finite-wavelength oscillatory instability (curve 4). At $\psi_1 = -0.113$, this curve changes the slope.

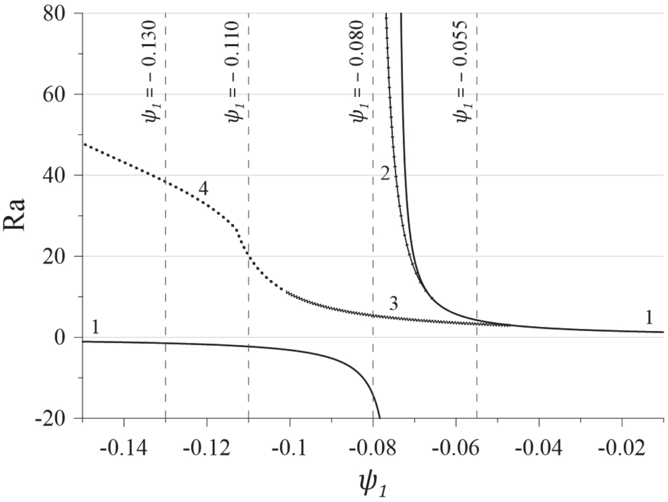

Figure 1: Linear stability map (instability curves: 1 - monotonic longwave, 2 - monotonic finite-wavelength, 3 - oscillatory longwave, 4 – oscillatory finite-wavelength)

Note that the onset of convection in the system under consideration at similar parameter values was studied earlier in (D. Mutschler et al. 2020), but in this work the longwave oscillatory mode of instability was not found.

Nonlinear regimes of convection

Nonlinear calculations were carried out for two-dimensional horizontally elongated rectangular cavity with aspect ratio 5x1. At all the boundaries, the impermeability condition and the absence of the solute flux were set. The constant different temperatures were imposed at the horizontal boundaries, and the vertical boundaries were assumed to be adiabatic. The stream function was introduced, which was determined by the relations $V_x = \frac{\partial \Psi}{\partial y}$, $V_y = -\frac{\partial \Psi}{\partial x}$.

The problem was solved in an unsteady formulation by the finite difference method. The Poisson equation for the stream function was solved by the successive over-relaxation method. A uniform grid was used. The number of grid cells was 20 vertically and 100 horizontally.

Modeling of nonlinear convection regimes was carried out for the values ψ_1, which are characteristic points on the stability map:

$$\psi_1 = \{-0.055, \quad -0.080, \quad -0.110, \quad -0.130\}$$

The calculations have shown that at $\psi_1 = -0.055$ after stability loss by the conductive state at $\text{Ra} \approx 3.26$, the regime of stationary oscillations of the longwave type is excited, via direct bifurcation. With the increase in the Rayleigh number to $\text{Ra} \approx 3.40$, this regime is transformed into the monotonic longwave regime. If, being on the curve of the monotonic regime, the Rayleigh number is lowered, then at $\text{Ra} \approx 3.10$ the convection starts to decay. Thus, the transition between different convection regimes is accompanied by hysteresis.

At $\psi_1 = -0.080$, after stability loss by the conductive state at $\text{Ra} \approx 5.26$, the longwave oscillatory regime is excited via direct bifurcation. When the Rayleigh number increases to $\text{Ra} \approx 5.95$, this regime passes into a monotonous longwave regime. If, while on the curve of the monotonic regime, the Rayleigh number is lowered, then a reverse transition to the oscillatory regime occurs.

At $\psi_1 = -0.110$, after stability loss by the conductive state at $\text{Ra} \approx 18.58$, the regime of stationary oscillations of the three-vortex structure is excited, which, with a further increase in the Rayleigh number to $\text{Ra} \approx 20.00$, transforms into a monotonous five-vortex regime. If, being on the curve of the five-vortex regime, the Rayleigh number is lowered, then at $\text{Ra} \approx 15.50$ there is a transition to the four-vortex monotonic regime, which exists up to $\text{Ra} \approx 13.20$. With a further decrease in Ra, the convection starts to decay.

At $\psi_1 = -0.130$, after stability loss by the conductive state at $\text{Ra} \approx 36.85$, a six-vortex stationary regime is excited. If, being on this curve, we reduce the Rayleigh number, then at $\text{Ra} \approx 36.00$ there is a transition to the five-vortex stationary regime, which exists up to $\text{Ra} \approx 34.08$. With a further decrease in Ra, the convection starts to decay.

Conclusions

In the investigated range of parameters, four types of instability were found in the system: long-wave monotonic, cellular monotonic, long-wave oscillatory and cellular oscillatory.

Within the framework of linear stability analysis, a new longwave oscillatory mode of instability was found, the existence of which was confirmed by nonlinear calculations using the finite difference method.

The convection threshold found in non-linear calculations agrees with the threshold predicted by linear theory.

At $\psi_1 = -0.055$, $\psi_1 = -0.080$ and $\psi_1 = -0.110$, the direct bifurcation takes place and at $\psi_1 = -0.130$, convection is excited in a finite-amplitude way.

Nonlinear calculations have shown that the transitions between different convection regimes are accompanied by hysteresis.

References

I.I. Ryzhkov, Thermal diffusion in mixtures: equations, symmetries, solutions and their stability, *SD RAS*, 200 (2013)

V. Sechenyh, J.C. Legros, A. Mialdun, J.M. Ortiz De Zárate, V. Shevtsova, Fickian diffusion in ternary mixtures composed by 1, 2, 3, 4-tetrahydronaphthalene, isobutylbenzene, and n-dodecane, *The Journal of Physical Chemistry B,* 120 (3) 535–548 (2016)

N.I. Lobov, D.V. Lyubimov, T.P. Lyubimova, Problem solving on a computer, *Perm University*, 82 (2007)

D. Mutschler, A. Mojtabi, Theoretical and numerical analysis of Soret-driven convection in a horizontal porous layer saturated by an n-component mixture: Application to ternary hydrocarbon mixture tetralin, isobutyl benzene, n-dodecane with mass fractions 0.8-0.1-0.1, *International Journal of Heat and Mass Transfer,* 162 120339 (2020)

Nonlinear regimes of Soret-induced convection in a two-layer porous system with an interface simulating a synclinal fold

T. Lyubimova[1,2], N. Zubova[1]

[1]Institute of Continuous Media Mechanics UB RAS, Perm, Russia, [2]Perm State University, Perm, Russia lyubimovat@mail.ru

Introduction

One of the variants of the structure of an oil-bearing field is a horizontal reservoir. The simplest model of such a reservoir can be a layer of porous medium (sands, limestones) saturated with oil and limited by hard-permeable rocks. Such a deposit is called lithologically limited. However, most often the structure of an oil-bearing formation is some rather complex tectonic form, where hydrocarbon-saturated layers with different porosity and permeability can alternate.

Oil is a multicomponent mutually soluble mixture of hydrocarbons of various structures with a small admixture of some other substances. The complex composition of the liquid filling the porous medium is one of the complicating factors in modeling. The properties of the mixture may be such that a positive or negative thermal diffusion effect may occur under the action of a geothermal temperature gradient. In this case, instability can occur, leading to the appearance of convection.

The aim of this work is to simulate the convection of a binary mixture of liquid hydrocarbons in a two-layer porous medium, the layers of which have different permeabilities and are separated either by a flat horizontal boundary or by a boundary that simulates a synclinal geological fold.

Problem configuration and governing equations

The considered mixture of dodecane ($C_{12}H_{26}$) and tetralin ($C_{10}H_{12}$), taken in equal proportions [Gebhardt et al. 2013], fills a horizontally elongated rectangular region of a porous medium with the dimensions $L = 200$ m and $H = 100$ m and rigid external boundaries impermeable to the matter. The computational domain consists of two horizontal layers with different constant values of permeability K_1 and K_2, but the same other properties. We study two options for the shape of the boundary between the layers: a flat boundary that divides the area into two layers of equal height (Fig. 1a), and a boundary in the form of an arc of a circle with a radius of 187.5 m, directed downwards, which imitates the boundary of a synclinal geological fold (Fig. 1b).

In the simulation, we assume that the viscosity and transport coefficients are constant and neglect the barodiffusion and the Dufour effect. Calculations of the Soret-induced convection of a binary mixture in a porous medium can be carried out within the framework of non-stationary nonlinear Darcy–Boussinesq equations [Nield 2013]:

$$0 = -\frac{1}{\rho_0}\nabla p_i - \frac{\nu}{K_i}\mathbf{V}_i - \mathbf{g}\left(\beta_T\left(T_i - T_0\right) + \beta_C\left(C_i - C_0\right)\right),$$

$$\left(\rho c\right)^* \frac{\partial T_i}{\partial t} + \left(\rho c\right)_f \mathbf{V}_i \cdot \nabla T_i = \lambda^* \nabla^2 T_i,$$

$$\varepsilon^* \frac{\partial C_i}{\partial t} + \mathbf{V}_i \cdot \nabla C_i = D\nabla^2 C_i + C_0\left(1 - C_0\right) D_T \nabla^2 T_i,$$

$$\nabla \cdot \mathbf{V}_i = 0 .$$

Here $\mathbf{V}$ is the filtration rate; p is the pressure; T is the temperature; C is the concentration of tetralin; β_T is the thermal expansion coefficient; β_C is coefficient of the concentration dependence of the density; T_0 and C_0 are the initial temperature and concentration; $\mathbf{g}$ is the acceleration of gravity; t is the time; K_1 and K_2 are the permeability of the upper and lower layers; ν is the kinematic viscosity of the mixture; λ^* is the effective thermal conductivity of the porous medium; $\left(\rho c\right)^*$ is the effective heat capacity of the porous medium; $\left(\rho c\right)_f$ is the heat capacity of the mixture; ε^* is the porosity; D is the molecular diffusion coefficient of the mixture; D_T is the thermal diffusion coefficient. Indexes $i = 1, 2$ indicate correspondence to the top or bottom layer.

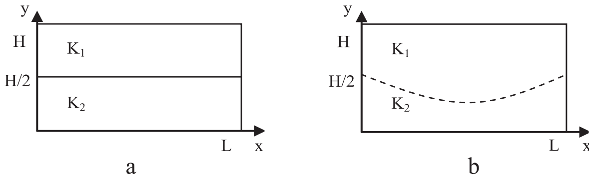

Figure 1: Problem geometry. a – system of layers of equal height, b – system imitating a synclinal fold.

At all external boundaries we set the conditions of impermeability and the absence of a diffusion flux of matter, at the upper and lower boundaries we impose constant different temperatures, on vertical ones – the absence of a heat flux; at the boundary between the layers – the continuity of pressure, heat flux and diffusion flux of matter.

At the initial moment of time, we assume the liquid to be motionless, the solute concentration in the region to be homogeneous, and the temperature to be linearly dependent on the vertical coordinate. The temperature difference at the external horizontal boundaries corresponds to the average value of the geothermal gradient: $3 \cdot 10^{-2}$ K/m.

The calculations were carried out using the ANSYS Fluent software package, which implements the finite volume method. A spatially uniform grid with square cells was used, the grid spacing was 2 m. To obtain a discrete analog of the equations, scheme of the second order of approximation in time and the third in space was used.

Numerical results

We considered the cases where the upper or lower layer was more permeable.

An analysis of the time evolution of the maximum value of the stream function in the computational domain has shown that for any considered configuration of the two-layer system, a certain non-convective period is first observed (the stream function is practically zero), the duration of which decreases with increasing permeability of any layer. The emergence of convection is accompanied by a sharp jump in the intensity of motion. Then, through a series of rearrangements, which are accompanied by smaller jumps in flow intensity, the steady state is reached. As an example, Figure 2 shows the temporal evolution of the maximum value of the stream function in a two-layer system with a curved boundary between the layers for the cases $\gamma = K_1 / \mathrm{K}_2 < 1$ (the lower layer is more permeable).

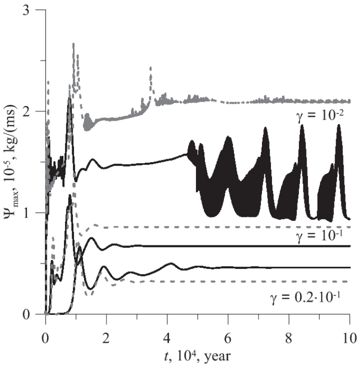

Figure 2: Temporal evolution of the maximum value of the stream function in a two-layer system with a curved boundary between the layers, $\gamma < 1$; gray dashed curves correspond to the case of a flat layer boundary and the same value of γ.

During the non-convective period, a process of separation of the mixture close to pure diffusion is observed: the concentration difference between the upper and lower boundaries tends to a value corresponding to the maximum separation of the mixture. For higher values of the medium permeability, the rapidly occurring convective motion strongly mixes the mixture, as a result of which the maximum separation of the mixture is substantially reduced.

With significantly different permeabilities of the layers (the permeability of one of the layers is ten or a hundred times higher than that in the other), a "local" occurrence and existence of convection is observed in the cavity, i.e. the flow arises and develops in a layer with a higher permeability (Fig. 3a). With a decrease in the difference in the permeabilities of the layers, a weak penetration of the flow into the less permeable layer is observed. At close values of the permeability of the layers, the emergence and existence of convection is of a "large-scale" nature: the flow arises and develops throughout the volume of the system, but is shifted to a layer of a higher permeability (Fig. 3b). It is found that at close permeabilities of the layers, one-, two-, or four-vortex stationary flow is established. For strongly different permeabilities of the layers, the appearance of quasi-periodic or irregular oscillations of complex shape is typical; the flow structure in this case is one- or two-vortex.

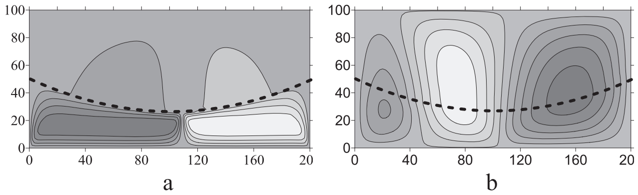

a b

Figure 3: Fields of the stream function at $t = 20000$ years. a – $\gamma = 10^{-2}$, б – $\gamma = 0.2\cdot10^{-1}$.

The distribution of the solute concentration during the "local" development of convection and significantly different permeabilities of the layers is almost uniform in the layer where convection is observed (a layer of a higher permeability) and close to a linear distribution along the vertical in a layer where the flow practically does not penetrate (a layer with a lower permeability). A decrease in the permeability difference leads to a greater penetration of the flow into a less permeable layer. In this case, the concentration isolines have a characteristic finger-like shape.

Conclusions

The simulation performed has shown a very slow development of convection (at times of the order of thousands of years) and the formation of steady-state regimes (at times of the order of tens of thousands of years). It is found that at close permeabilities of the layers, one-, two-, or four-vortex stationary flow is established. For strongly different permeabilities of the layers, the appearance of quasi-periodic or irregular oscillations of complex shape is typical; the flow structure in this case is one- or two-vortex.

It is shown that the "local" development of convection (the flow arises and exists in a layer of a higher permeability) is typical for layers that differ significantly in permeability (the permeability of one of the layers is ten or one hundred times higher than that in the other). With an increase in the permeability of the second layer, a slight penetration of the flow into this layer is observed. At even closer values of the permeabilities of the layers (less than ten times), the onset and development of convection is of a "large-scale" nature: the flow occurs in the entire volume of the system, but is shifted to a layer with a higher permeability.

The emerging convective flows have low filtration rates. However, these low velocities are sufficient to mix the fluid even in the case of weak flow penetration into the less permeable layer and to prevent its separation.

Acknowledgements

This work was funded by Russian Science Foundation (grant No. 20-71-00147).

References

M. Gebhardt, W. Kohler, A. Mialdun, V. Yasnou, V. Shevtsova, Diffusion, thermal diffusion, and Soret coefficients and optical contrast factors of the binary mixtures of dodecane, isobutylbenzene, and 1,2,3,4-tetrahydronaphthalene, *J. Chem. Phys.* 138, 114503, (2013).

D.A. Nield, A. Bejan, Convection in porous media, Springer, 778, (2013).